Wind Energy Science, Engineering and Policy

National Science Foundation

Research Experiences for Undergraduates

Symposium Proceedings

31 July 2013

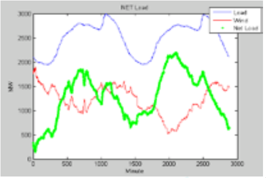

	Avg. Pressure	Avg. Wind Speed	Avg. Wind Dir.	Avg. Stability
All_Up	1009.8	23.8	232.1	0.1
All_Dwn	1008.6	25	242.5	0.03
Some_Up	1011.4	14.7	219.4	0.4
Some_Down	1011.6	16.3	221.6	0.1
Mixed	1011	20	226.4	0.02

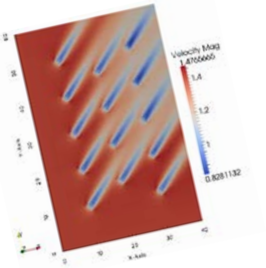

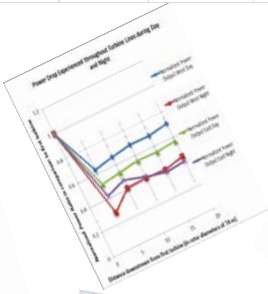

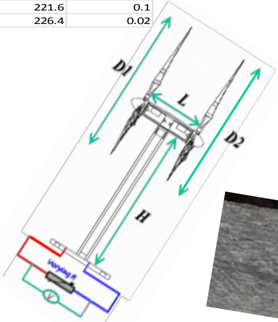

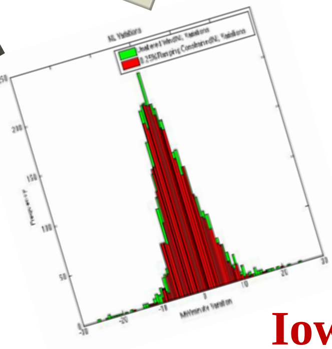

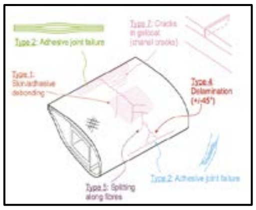

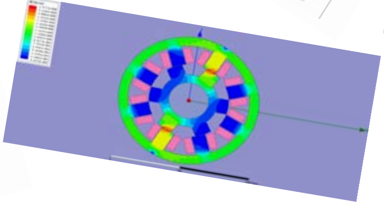

$$
\begin{aligned}
&\sum_{t\in T_k}\sum_{(i,j)\in G,T} C_{(i,j)}(t).e_{(i,j)}(t)\\
&+\sum_{t\in T_k}\sum_{(i,j)\in G} C^{sr}_{(i,j)}(t).e^{sr}_{(i,j)}(t)\\
&+\sum_{t\in T_k}\sum_{(i,j)\in G} C^{nsr}_{(i,j)b}(t).e^{nsr}_{(i,j)}(t)\\
&+\sum_{t\in T_k}\sum_{(i,j)\in G} C^{reg+}_{(i,j)}(t).e^{reg+}_{(i,j)}(t)\\
&+\sum_{t\in T_k}\sum_{(i,j)\in G} C^{reg-}_{(i,j)}(t).e^{reg-}_{(i,j)}(t)\\
&+\sum_{t\in T_k}\sum_{(i,j)\in G} [S^{X}_{(i,j)}(t).(X_{(i,j)}(t)\\
&+X^{0}_{(i,j)}(t))]\\
&+\sum_{t\in T_k}\sum_{(i,j)\in G} [S^{Y}_{(i,j)}(t).(Y_{(i,j)}(t)\\
&+Y^{0}_{(i,j)}(t))]+\sum_{t\in T_k}\sum_{(i,j)\in G} Pen_j(t).L_j(t)
\end{aligned}
$$

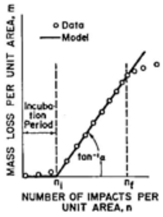

Iowa State University

Preface

This volume brings together the research results of a remarkable group of thirteen undergraduates who came together at Iowa State University for 10 weeks to develop their skills at scientific research. Without prior experience in these research areas or familiarity with each other, these students from across the US converged on the Iowa State campus in the summer of 2013 to learn about the science, engineering and policy relating to one of the most promising areas of renewable energy. As a fast-track into the science and engineering underpinning wind energy they participated in a short course, Lunch & Learn, and webinar sessions led by faculty, industry professionals, wind energy entrepreneurs and others engaged in the wind power enterprise. They toured operating utility-scale wind farms, an energy utility trading floor, turbine-components manufacturing plants, a research wind tunnel, and a meteorological field observing site in an operating wind farm.

Each student practiced and honed his or her research skill in faculty-led research program under daily guidance of faculty members, postdoctoral research associates, graduate students and laboratory supervisors. During their 10-week stay each student weekly produced an updated draft on their research project in the form of a journal paper. Their final products include the journal-targeted papers that comprise this volume and 20-minute power-point presentations of their findings in a symposium attended by mentors and other researchers and students in the Iowa State University community.

As you page though this compilation of research results you should note the diversity of topics all relating the general theme of wind energy. This permanent record of their achievements would not be possible without the dedication and assistance of the research mentors listed on their individual papers, along with the many faculty members at Iowa State, wind energy industry professionals, and support staff in the College of Engineering. And the day-to-day tasks necessary to run such a program would never have been accomplished had it not been for the tireless efforts of Ms. Barbara Brown.

Support for this research was provided by a National Science Foundation Research Experience for Undergraduates site program in Wind Energy Science Engineering and Policy (WESEP) grant number EEC-1063048 at Iowa State University.

Eugene S. Takle
Principal Investigator

James D. McCalley
Co-Principal Investigator

August 2013

A copy of this proceedings or individual papers herein can be obtained by from the College of Engineering website: http://www.engineering.iastate.edu/eri/initiatives/strategies/wei/wesep-reu/.

TABLE OF CONTENTS

Effect of Wind Energy Control on Power System Economincs
Destenie Nock ……………………………………………………………………….1/1-1/12

The Role of Demand Response in Complementing Wind on a Grid
Peter McHale ………………………………………………………………………. 2/1-2/7

Numerical Simulations of Flow Convergence Phenomenon in Wind Turbine Arrays
Angelo Jerez Chaves ……………………………………………………………. 3/1 -3/12

Meterorological Phenomena Impacting Spatial Consistency of Ramp Events in Wind Farms
Ian James Camerlin ……………………………………………………………….4/1 – 4/10

Modeling Absolute Power Rate Limitation based Wind Control Strategy in Production Costing Program
Michael F. Howland ……………………………………………………………... 5/1- 5/14

Effect of Out-of-Plane Waves on Fiber Volume Fraction in Wind Turbine Blade Composites
Victor Aiello ………………………………………………………………………. 6/1 – 6/8

A Comprehensive Approach to Health Monitoring and Management of Wind Energy Infrastructure Systems
Lindsey J. Wickman………………………………………………………………7/1 – 7/13

Measurements of Wind Turbine Wake Conditions in a Utility-Scale Midwest Wind Farm
Erin M. Jackson…………………………………………………………………..8/1 – 8/10

Analysis of the Switched Reluctance Generator for Wind Power Operations
Andrew L. Hoffman……………………………………………………………….9/1 – 9/12

Use of a Flexible Capacitive Surface Sensor for Wind Turbine Blade Condition Assessment with Comparison of Two Shape Reconstruction Algorithms
Vanessa J. Pan………………………………………………………………….10/1 – 10/9

An Experimental Investigation of Dual-Rotor Wind Turbines and the Effects of Rotation Direction
Colton Boehm……………………………………………………………………….11/1 – 11/10

Integrating an Automated Fabric Placement System into the Manufacturing of Wind Turbine Blades
P. Sam Cook ………………………………………………………..……………….12/1– 12/17

Modeling Precipitation Induced Gel-Coat Surface Erosion with Application to Wind Turbine Blades
Jenna M. Koester ………………………………………………………………….. 13/1 – 13/6

Effect of Wind Energy Control on Power System Economics

Destenie S. Nock
Wind Energy Science Engineering and Policy REU, Iowa State University, Ames, Iowa
Mentors: J. McCalley, V. Krishnan, and N. Brown.

Abstract

This paper focuses on assessing the effectiveness of methods used to address the economic issues associated with higher penetration of variable (wind) generation. Wind variability can be balanced utilizing wind control techniques and storage methods. Production costing simulations were done on IEEE 24 bus system across different wind penetration levels, and results were used to evaluate the impacts of two different wind control methods on the power grid, namely maximum power limitation and delta control. Simulations showed that these control methods have the potential to significantly lower the overall production cost of the power system. Future research will focus on having wind farms participate in the ancillary service market in the simulations, while implementing the maximum power limitation control method. Also further studies involving increased transmission limits should be performed to see how the system deals with high winds.

---

1. Introduction

Including wind generation in the energy market creates more of a need for regulation services because the high variability in wind makes it harder to predict the level at which other sources will need to generate power. The Department of Energy 20% by 2030 plan is increasing the amount of wind projects across the nation. In 2006 the installed wind capacity in the US was about 12 GW. By 2010 this number had grown to 40 GW (Wiser et al. 2010). This growth can be contributed to the Federal Production Tax Credit (PTC), state renewable portfolio standards, and the favorable economic and environmental characteristics of wind energy compared to other forms of energy (Smith et al. 2007). These fluctuations in generation impact the other generation methods that were not designed to operate under high variability conditions and therefore increase their maintenance costs. Ancillary services (AS) are needed to maintain the balance of supply and demand for power on the grid. These are capacity services, not energy services. In the context of energy markets AS refers to contingency and regulating reserves. Spinning, non-spinning, and regulation reserves are used to maintain the balance of power on the grid.

This paper examines the effects of wind control on the 48 hour energy and AS cost of operating the power system. The focus of this research is to investigate the impact of wind control on system AS requirements and system costs associated with production (i.e., fuel, AS and cycling) under four different system scenarios:

1. Increasing wind penetration
2. Presence of wind control methods
3. Presence of storage
4. Including cycling cost for conventional generators

This research will help determine if wind control is an effective way to provide AS or alleviate their need. In addition to providing energy, wind farms have the ability to provide the same AS that conventional generation currently provides, given that there is sufficient wind and the proper controlling equipment is installed. This is necessary because some conventional generation technologies, such as coal units, suffer performance degradation when they are frequently transitioned between highly loaded and lightly loaded or decommitted states, a mode of operation made necessary when they are required to follow demand variability caused by high levels of wind penetration.

Previous research by Das (2013) analyzed the integration of storage technologies to the grid and their economic value. Storage technologies store electricity in a variety of different forms. Chemical energy (batteries), kinetic energy (flywheel), and potential energy (compressed air energy storage and pumped hydro) are all being considered to meet the increase in variability of net load due to intermittent renewable generation. Storage benefits include discharging energy during peak demand times when Locational Marginal Prices (LMP) are high, and charging during off-peak times when LMPs are low, the latter conditions usually associated with wind producing excess power. This work is a continuation of the PhD research of Das (2013). This work will expand upon her dissertation by analyzing the impact of wind control.

Further increases in installed wind capacity would require the industry to move away from using maximum power point tracking (MPPT), and to a system that gives utility companies more control over the power that is being generated from the wind farms. In most markets wind power generation has exemptions from real-time deviation penalties (Botterud et al. 2010). As wind farms begin participating in the day-ahead and real-time markets they will need to consider these penalties when making offers based on a given forecast. Allowing utility companies to make day-ahead and real-time offers for different outputs of their wind farms is desirable because this will tend to decrease LMPs since the low marginal costs of wind farms allows them to offer low in the market are usually. More stability in grid operations could be provided by allowing wind farms to participate in the energy market. Their ability to make good energy and AS market offers would depend on the time they are required to submit their generation offer. Wind forecast errors significantly decrease with a shorter time horizon (Botterud et al. 2010).

Wind control methods based on Maximum Power Limitation and Delta Control were implemented to determine how power system prices would be affected. Maximum Power limitation involves limiting the peak point of a wind farm. This should lower the need for regulation in conventional generators. Delta Control involves producing and offering energy quantities lower than the wind forecast by an amount “delta” Kristoffersen (2005). So if a wind farm is able to offer 20 MW of wind in the energy market their energy quantity offered will be (20 MW – delta MW). Limiting the output of the wind farms, and offering the rest of the available power into the AS market, could lower total energy and AS cost within the market without causing a significant drop in the profit for wind farms.

2. Literature review

Wind farms with conventional MPPT control are creating a need for increased AS due to the variability in wind speeds that result in increases and decreases in real power. These AS can be divided into contingency reserves and regulation reserves. Selling AS can significantly increase the generators profits as seen in Kirby (2007). Contingency reserves can be further divided into spinning and non-spinning reserves. Spinning reserve is supplied by a generator that is online, which is synchronized to the grid. Online generators can increase output immediately in response to outages which cause power imbalance and reach their full output capacity in 10 minutes. Non-spinning reserve is similar to spinning reserve, but non-spinning reserve does not have to respond to an outage immediately. The resources supplying this reserve can be either online or offline, but they must be able to reach full output capacity within 10 minutes. The 10-minute time frame follows the North American Electric Reliability Council (NERC) standards.

Regulating reserves, which can be divided into regulation up and regulation down reserves, are required to meet the variability of the net load. The regulation up and down reserves are needed when using wind technologies to maintain the balance of the power level based on unit capability.

Regulation and load-following are used continuously to support normal grid operation, and maintain the balance of supply and demand, while spinning, non-spinning, and replacement reserves are ready to be used if equipment fails. These reserves are essential to the integration of wind turbines to the power grid due to the variability of wind generation.

In the absence of fast responding/flexible resources, conventional generators have to supply AS, and they incur cycling costs. Increasing the amount of variable renewable generation on the electric grid has resulted in increased cycling of conventional fossil generation plants. Operating conventional generation units at varying load levels causes the auxiliary components, the boiler, turbine, and steam lines to encounter large thermal and pressure stresses, which cause damage to the system (Kumar et. al 2012). Operational efficiency, operation and maintenance cost, capital cost and lifespan of conventional generation plants are all negatively affected by the increasing variable generation. Cycling in plants can be reduced by the implementation of wind control methods and storage units. Cycling costs for various generators are modeled in Das (2013).

Kristoffersen (2005) detailed the different methods used to control active and reactive power for the Horns Rev Offshore Wind Farm, in Denmark. Through absolute power limitation, balance control, power rate limitation and delta control this offshore wind farm was able to adjust the power production as needed. This is in contrast to maximum power point tracking (MPPT) control, which is currently being used in most other wind farms. MPPT controls the turbine so that at any given moment it extracts maximum electric energy from the wind resource. Being able to adjust the power production as needed provides ramp-down capability if the turbine is producing an excess of energy, and ramp-up capability if the turbine is generating below its maximum power point. This leads to less variable generation, which reduces the need for AS.

3. Experimental methods

A production cost program developed using MATLAB with the Tomlab optimization suite was used to perform the analysis. The objective was to determine if wind control can be effective in reducing the need for AS under different system conditions as mentioned in the section 1, and if it will be a cost-effective way of providing AS. A lower cost for AS will lead to lower costs for wind integration, which will lead to a more sustainable method of harvesting energy. Society benefits from this because of lower costs and the displacement of fossil-based generation by wind reduces overall power plant CO_2 emissions.

The analysis was done on the IEEE 24 bus Reliability Test System (RTS), shown in Figure 1, for different control regimes and different wind penetration levels.

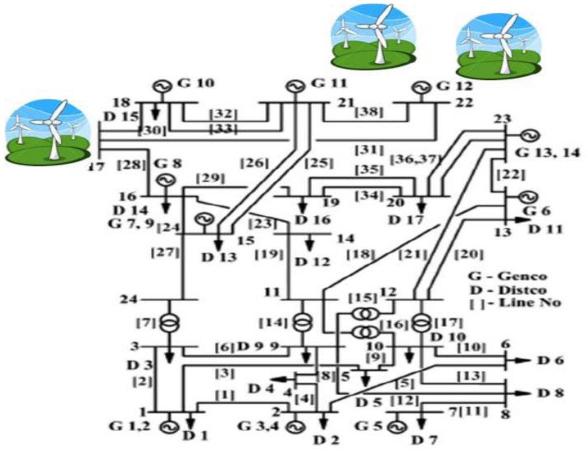

Figure 1. IEEE RTS 24 Bus System

The multi-period linear programming production cost model of Das (2013) employs a network structure which satisfies the set D of demand nodes by optimizing the set G of generation nodes. The time base for unit commitment is 1 hour, the time base for economic dispatch is 5 minutes, and the power base used this program is 1 MVA.

A simplified version of the objective is given in (1):

$$\boldsymbol{Minimize}\ \{energy\ production\ cost + ancillary\ service\ cost + load\ shedding\ penalty\} \quad (1)$$

The full objective function is provided in Appendix A1. The constraints imposed within this optimization problem are as follows: power balance, wind availability, transmission line limits, generation power and ramp limits, and DC load flow constraints. Wind is limited by hourly forecast W(t) based on historical data.

Different wind penetrations were analyzed utilizing the program. Wind capacity penetration is defined by (2) as

$$pen = 100 * \frac{\sum_{i=1}^{w} wp_i}{Gen_{cap} + \sum_{i=1}^{w} wp_i} \quad (2)$$

In this equation wp_i, $i = 1 \ldots w$ represent the name plate capacity of $w=3$ different wind farms in the system. Gen_{cap} represents the total capacity (in MW) of the other generators in the system, which is 3405 MW for the test system considered in this paper. As per (2), a 20% wind penetration level is defined as wind farms representing 20% of the total installed generation capacity in the system.

In the program wind control is being modeled in two ways.

1. Maximum power limitation: The wind farms are subjected to maximum power limitation. From a section of the 48-h forecast with high variability, a cap is determined for power production. Everything below this cap will be offered into the energy market, and the rest of the available wind capacity will be offered into the AS market.
2. Delta control: Delta control is implemented in the program in two ways. First, constant delta control is implemented by limiting wind production at every instance by a fixed amount. Second, variable delta control is implemented to accommodate the different AS requirements in different hours. This allows wind farms to participate in the energy and AS markets.

These control methods provide Independent System Operators (ISO) with less variability in dispatching energy and AS.

The system generation parameters and energy offers are provided in Table A2 of the appendix. The values for oil, coal, natural gas (NG), nuclear (Nuc), and wind generators were taken from Das (2013). Wind energy offers for different generation levels are based on the operation and maintenance cost of various wind farms.

4. Results

4.1 Progression of Load

Figures 2-5 show the graphs of the system load, wind and net load over 2880 minutes (48hr) for 0%, 20%, 40%, and 60% wind penetration levels respectively. Based on this data, hourly regulation needs were estimated (Das, 2013), and unit commitment and economic dispatch were performed. The production costing program is designed to always match the generation to hourly energy and AS requirements needed to meet the net load variations.

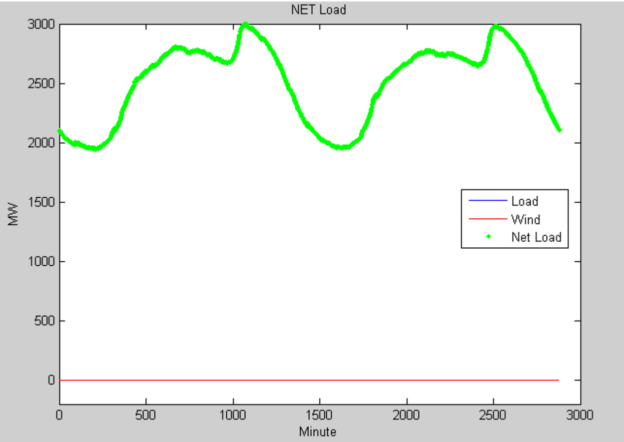

Figure 2. Progression of load, wind, and net load for 0% wind penetration

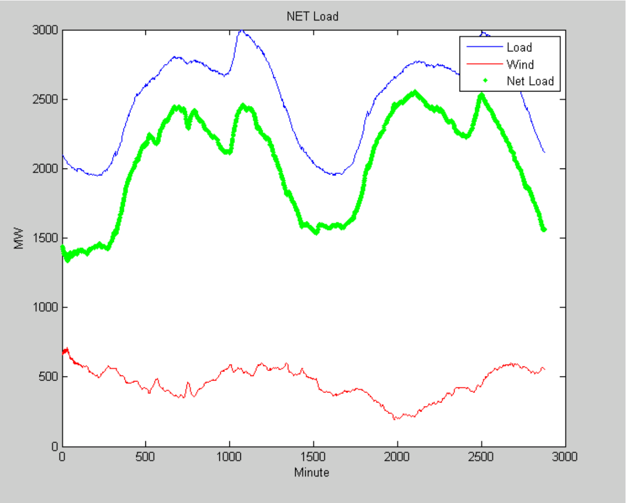

Figure 3. Progression of load, wind, and net load for 20% wind penetration

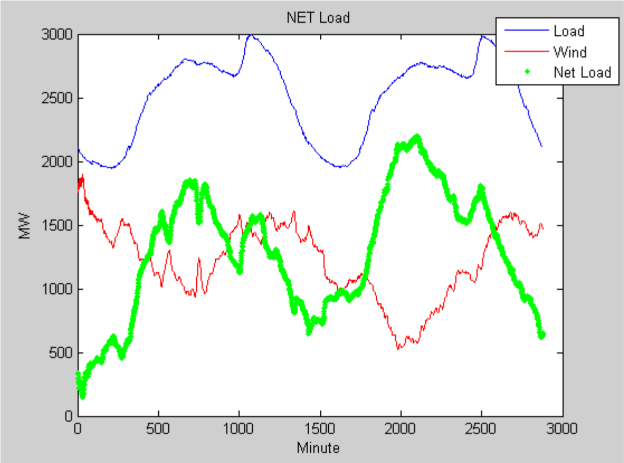

Figure 4. Progression of load, wind, and net load for 40% wind penetration

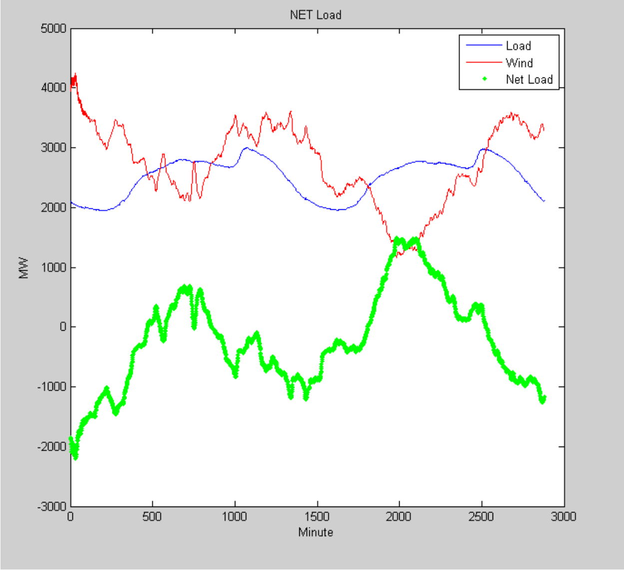

Figure 5: Progression of load, wind, and net load for 60% wind penetration

Results from the 48-h production costing simulation without modeling wind control, storage, or cycling cost are provided in Table 1. Wind is not used for AS in these simulations. These runs demonstrate that high wind penetration lowers the production cost. Production cost results from adding the total energy costs, AS costs, and load shedding penalties. The average MCP has a positive correlation with levels of wind penetration, while average LMP across the entire 24-bus system correlates negatively with wind penetration levels. This is caused by wind having lower marginal costs than other sources of power generation and will drive the LMP down. The increase in MCP could be caused by the increase in regulation requirements that result from growth in wind penetration.

Without wind control and storage, this regulation has to come from expensive conventional generators. The large amounts of wind spillage are undesirable, but this can be remedied to some extent by incorporating storage in to the power system. The percentage of wind spillage is defined in (3) below.

$$Wind\ Spillage\ \% = 1 - \frac{avg.\ amount\ of\ wind\ used}{avg.available\ wind} \quad (3)$$

In Table 1 wind spillage percentage is higher in the 40% simulation compared to the 60 % simulation. This is caused by a lack of adequate transmission to accommodate this much wind and system's lower load levels (Table 9).

Table 1: Results from Energy Bid Simulation, No Cycling, No Storage, No AS

Wind Penetration Level	0%	20%	40%	60%
Production Cost ($)	3.929e6	3.812e6	3.764e6	2.705e6
Wind Spillage Mean (MW)	0	61.62	207.80	417.75
Wind Spillage (%)	0	63.42	80.02	71.76
LMP Mean ($/MWh)	62.82	64.97	63.49	42.50
Energy MCP Mean ($/MWh)	27.51	28.53	27.56	39.44

4.2 Implementation of Maximum Power Limitation and Constant Delta Control

Maximum power limitation (Figure 6) and delta control (Figure 7) methods were implemented to determine how these wind control methods would affect production costs and LMPs.

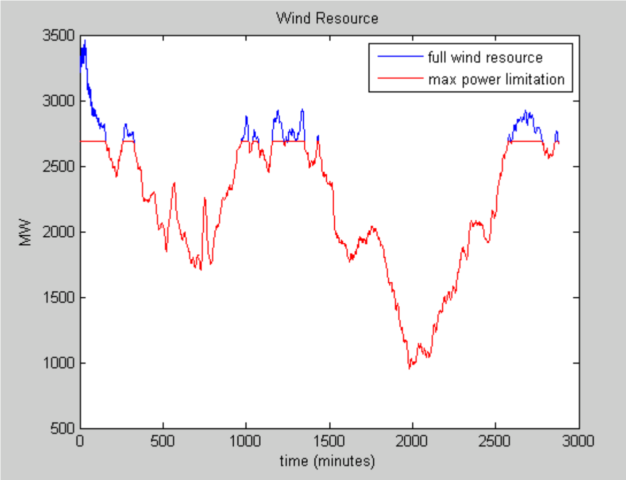

Figure 6. Implementation of maximum power limitation

In Figure 6 above the 48-h forecast was used to implement maximum power limitation. A section of high variability was selected and used to determine where to limit the amount of power production from wind farms. The section of the wind forecast between minutes 930 and 1449 appears to have short term variability prior to significant ramp down, through visual analysis. The mean wind power was estimated from this section of the forecast to determine the wind energy production cap for the entire 48-hour period. The limit was set to 2,687 MW. Everything below the maximum power limitation line was offered into the energy market. The remaining will be offered into the AS market, in future simulations. Table 2 shows the results of maximum power limitation method, where wind is used to supply only energy. During the simulations it was observed that using maximum power limitation in the 20% wind penetration simulation did not significantly increase or decrease the need for regulation. However, in the 40% and 60% simulations the need for regulation reduced by 2.7% and 6.0% respectively.

Table 2: Results from Maximum Power Limitation with no AS bidding

Wind Penetration Level	0%	20%	40%	60%
Production Cost ($)	3.930e6	3.848e6	3.756e6	2.689e6
Wind Spillage Mean (MW)	0	61.14	207.03	414.40
LMP Mean ($/MWh)	62.82	66.20	62.8256	43.06
Energy MCP Mean ($/MWh)	27.51	28.91	28.12	38.96

Comparing Tables 1 and 2, it is observed that after the 20% wind penetration level there is a reduction in the production cost of about 0.21% and 0.59% for the 40% and 60% wind penetration levels, respectively.

Constant delta control, Figure 7, involves offering capacity below the capacity inherent in the available wind resource by a fixed capacity (here it is 50 MW for each wind farm) and providing that as an offer to the AS market. Table 3 shows the results of delta control method, where wind is used to supply only energy.

Figure 7. Implementation of constant delta control, delta = 50 MW

Table 3: Results from Constant Delta Control with no AS Bidding

Wind Penetration Level	0%	20%	40%	60%
Production Cost ($)	3.93e6	3.812e6	3.764e6	2.707e6
Wind Spillage Mean (MW)	0	61.62	207.84	417.75
LMP Mean ($/MWh)	62.82	64.97	62.99	42.50
Energy MCP Mean ($/MWh)	27.51	28.53	27.56	39.73

Table 3 does not show a significant increase in the production cost, LMP, or MCP prices, compared to the base simulation in Table 1. This could be the result of the system spilling most of the wind in the high wind penetration scenarios due to transmission limits.

In Figures 8 and 9 constant delta control and maximum power limitation were implemented, without AS offers, to determine how the LMP prices at Bus 21 would be affected. The constant delta control and base case (without wind control) LMP values in Figure 8 overlapped.

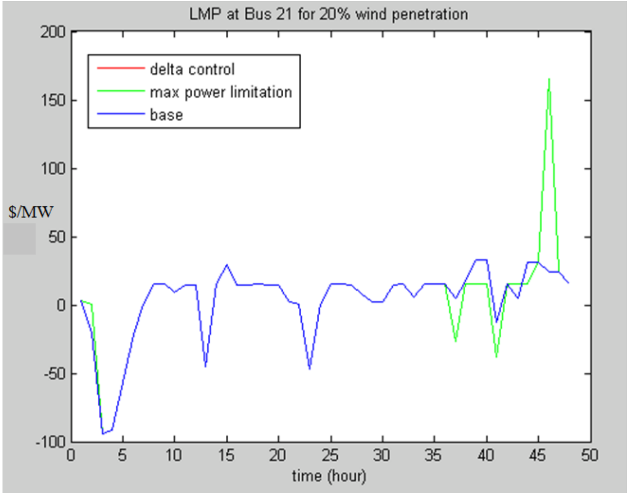

Figure 8. Comparison of LMP at Bus 21 for 20% wind penetration, with constant delta control, max power limitation, and base case.

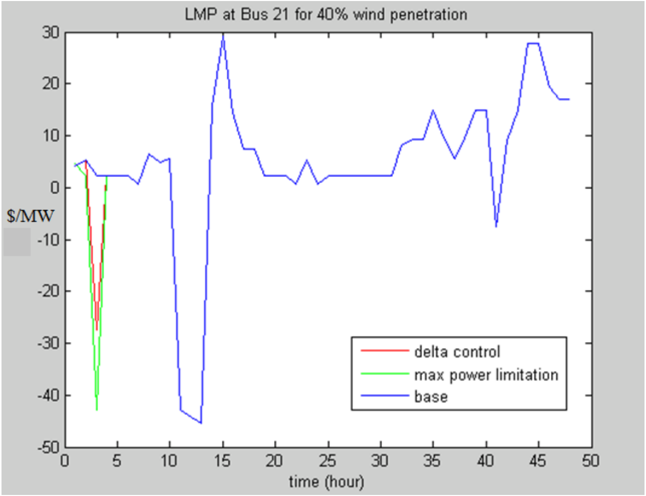

Figure 9. Comparison of LMP at Bus 21 for 40% wind penetration, with constant delta control, max power limitation, and base case.

4.3 Incorporating Storage and Variable Delta Control into the System

A 100 MW compressed air energy storage (CAES) unit was incorporated into the system at bus 21, and wind was allowed to participate in the AS market, using variable delta control. In the simulation the program will simultaneously commit wind for up/down regulation and spinning reserve. It will not commit a constant amount, such as, 50MW; but from hour to hour wind farms will commit different amounts based on the system economics and wind generator's 5-minute ramp rate. Each generation units AS offer is limited by how many MWs the unit can ramp in one hour. The capacity of wind generation offered to the AS market is calculated using the (4).

$$AS\ Wind\ Capacity\ Offer = \frac{ramp\ rate}{12} \qquad (4)$$

The wind AS offer was $15/MW for each category. Below, Tables 4 and 5 presents the results for 20% and 40% wind penetration levels, respectively. The simulation categories are as follows:

1. Case 1: Wind only participates in the energy market;
2. Case 2: Wind participates in the energy and AS market, using variable delta control;
3. Case 3: Wind participates in the energy market, and a CAES participates in the energy and the AS markets;
4. Case 4: Wind participates in the energy and AS market, using variable delta control, and CAES participates in the energy and the AS markets.

When storage participates in the energy and AS markets, there are significant reductions in the MCP for the different AS categories. Also when variable delta control is used in combination with CAES, prices drop even further. These results suggest that if wind is allowed to participate in the AS market, using variable delta control, constant delta control, or maximum power limitation, then there will be a reduction in AS MCPs if storage is present.

Table 4: Comparison of AS MCPs for 20% Wind Penetration Cases

Simulation Category	**Case 1**	**Case 2**	**Case 3**	**Case 4**
Regulation up ($/MWh)	45.48	45.48	30.03	15.68
Regulation down ($/MWh)	28.53	28.53	15.81	9.51
Spinning Reserve ($/MWh)	19.48	19.48	15.01	9.90

Table 5: Comparison of AS MCPs for 40% Wind Penetration Cases

Simulation Category	**Case 1**	**Case 2**	**Case 3**	**Case 4**
Regulation up ($/MWh)	44.97	44.21	27.78	15
Regulation down ($/MWh)	27.56	27.56	16.74	10.40
Spinning Reserve ($/MWh)	18.97	18.21	11.82	8.55

Tables 6 and 7 compare the results from the various simulations of the 20% and 40% wind penetration levels, respectively. Both penetration levels experience decreases in production cost, wind spillage, LMP, and MCP for Cases 3 and 4. Figures 10 and 11 display the results of the LMPs at Bus 21 for Case 3, where wind and CAES participate in the energy and AS markets. The result for the 20% penetration simulation is that there are fewer spikes in the drop in prices, while still having a slight reduction in the average LMP for the entire system, as indicated in Table 6. In Figure 11 there is a large spike in the increase in prices at hour 46. Referring back to Figure 4 we see that there is an increase in the load demand around this time; although the CAES operated in the discharge mode, a load shed occurred at hour 46. This means there was a load shedding penalty for unmet load requirements resulting in a spike in LMP prices.

Table 6: Comparison of 20% Penetration Cases

Simulation Category	**Case 1**	**Case 2**	**Case 3**	**Case 4**
Production Cost ($)	3.812e6	3.812e6	3.622e6	3.571e6
Wind Spillage Mean (%)	63.42	63.42	52.71	54.98
LMP Mean ($/MWh)	64.97	64.97	65.93	64.49
Energy MCP Mean ($/MWh)	28.53	28.53	15.81	9.51

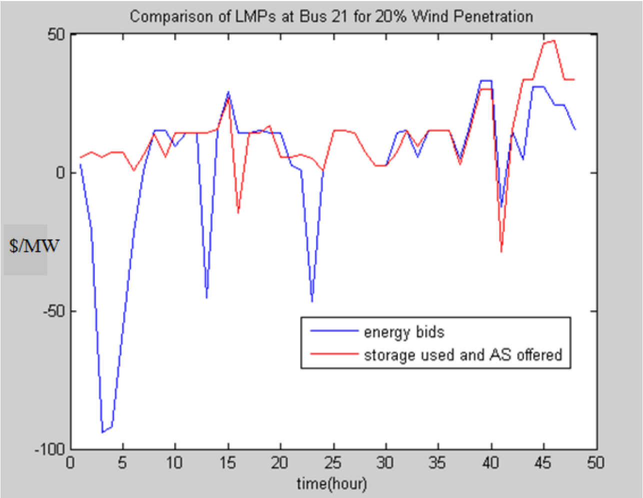

Figure 10. Comparison of LMP at Bus 21 for 20% wind penetration, with storage and wind participating in AS market

Table 7: Comparison of 40% Penetration Cases

Simulation Category	Case 1	Case 2	Case 3	Case 4
Production Cost ($)	3.764e6	3.764e6	3.471e6	3.559e6
Wind Spillage Mean (%)	80.02	80	66	68.58
LMP Mean ($/MWh)	63.49	63.00	64.65	66.44
Energy MCP Mean ($/MWh)	27.56	27.56	16.74	10.02

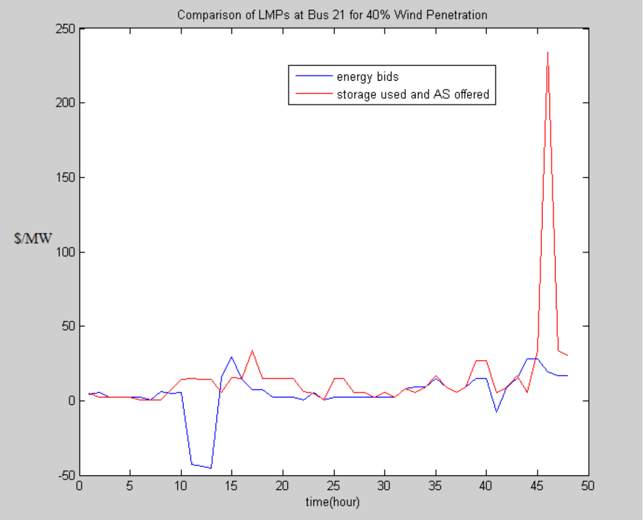

Figure 11. Comparison of LMP at Bus 21 for 40% wind penetration, with storage and wind participating in AS market

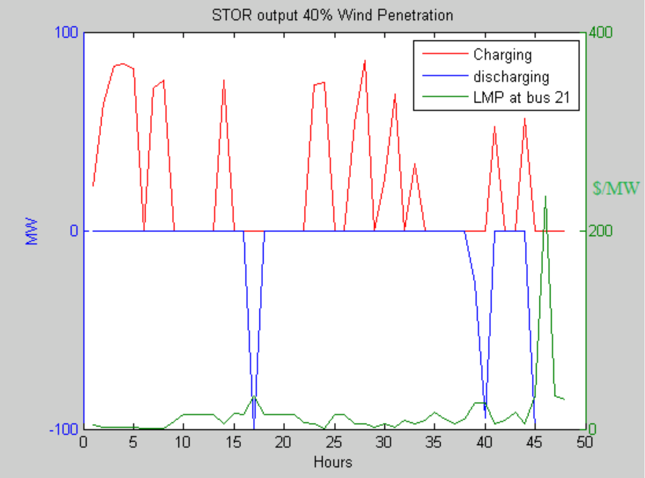

Figure 12. The storage charge and discharge results for the 40% wind penetration, compared with the LMPs at Bus 21

4.3 Increased Transmission Limits

The transmission limits were increased, so the system can accommodate high winds. The results were compared with previous simulations in Tables 8 and 9. The different simulations performed are represented as follows:

1. Case A: Wind only participates in the energy market;
2. Case B: Wind only participates in the energy market and transmission limits have been increased;
3. Case C: Wind participates in the energy and AS market, using variable delta control;
4. Case D: Wind participates in the energy and AS market, using variable delta control, and transmission limits have been increased.

In Tables 8 and 9, the wind spillage decreased for every simulation category. Since the system is accepting more electricity produced by wind farms the variable generation has increased. This increased the regulation up and down requirements by 0.05% and 1.07% for the 20% and 40 % wind penetration levels respectively. This leads to an increase in production cost, and LMPs. The MCP increased in every simulation category in both tables, except for Case D. From Case C to Case D the regulation up and down requirements decreased by 3.58% and 35.74% for the 20% and 40% wind penetration levels, respectively. This suggests that using variable delta control helps reduce the effects of high variability situations.

Table 8: 20% Wind Penetration Cases with Increased Transmission Limits

Simulation Category	Case A	Case B	Case C	Case D
Production Cost ($)	3.812e6	4.120e6	3.812e6	4.145e6
Wind Spillage Mean (%)	63.42	52.87	63.42	50
LMP Mean ($/MWh)	64.97	72.10	64.97	71.50
Energy MCP Mean ($/MWh)	28.53	49.68	28.53	15.83
Regulation up MCP ($/MWh)	45.48	54.34	45.48	17.30
Regulation down MCP ($/MWh)	28.53	49.68	28.53	15.83
Spinning Reserve MCP ($/MWh)	19.48	28.34	19.48	14.04

Table 9: 40% Wind Penetration Cases with Increased Transmission Limits

Simulation Category	Case A	Case B	Case C	Case D
Production Cost ($)	3.764e6	4.387e6	3.764e6	4.417e6
Wind Spillage Mean (%)	80.02	62.68	80	59.34
LMP Mean ($/MWh)	63.49	73.95	63.00	74.50
Energy MCP Mean ($/MWh)	27.56	36.27	27.56	15.15
Regulation up MCP ($/MWh)	44.97	63.44	44.21	15
Regulation down MCP ($/MWh)	27.56	36.27	27.56	15.15
Spinning Reserve MCP ($/MWh)	18.97	36.96	18.21	12.68

5. Analysis and interpretation

From Figures 2-5 we see that a common problem with using wind energy is that the wind resource does not always complement the load. This can be remedied by using storage and wind control methods to accommodate for the variability of wind.

The production costs, LMPs, and MCPs decreased when variable delta control and storage were implemented into the system. The same trend is projected to happen for the maximum power limitation (Figure 6) and constant delta control (Figure 7) methods when the program is able to include wind AS offers with these control methods.

In Figure 8 the mean overall LMP for the delta and base simulation was $3.60, while the mean overall LMP for the maximum power limitation was $4.92. In Figure 9, mean overall LMP for the base simulation was $4.76, delta control simulation was $4.14, and the maximum power limitation was $3.76. Higher wind penetration levels produces variability. Both control methods in the 40% wind penetration level simulation caused the LMP at Bus 21 to decrease.

When analyzing Table 4 we see that the MCP for the 20% wind penetration level does not change in any category when wind is allowed to participate in the AS market. The regulation up MCP drops by 33.97% when a 100MW storage unit becomes a participant in the AS market. This reduction in the regulation up MCP is 65.52% when both wind and storage participate in the AS market. Similar trends are seen for the 40% wind penetration level, Table 5. The 40% wind penetration level produces a slight decrease in the regulation up, and spinning reserve MCP, when the 20% wind penetration did not. This could result from the energy market using all of the available wind resource.

In Tables 6 and 7, there is a reduction in Case 4, the AS and Storage category, when comparing them to Case 1, the energy only category. These results suggest that the effects of high variability situations caused by wind can be significantly reduced by incorporating storage into the power system, and implementing variable delta control.

Tables 8 and 9 show that variable delta control helps reduce the effects of high variable generation. When more wind generation was used in the system the production cost increased. This is most likely due to the increased need for AS. When variable delta control is used The MCP for the energy and AS markets significantly decreased.

6. Conclusions

High variability in wind causes cycling in other generation plants and instability in power generation. Since MPPT requires the power grid system to use all of the power production from wind farms, other generators have to cycle more, and are susceptible to sudden changes in wind speeds. Wind control methods could provide more confidence in energy offers from wind farms and less demand variability across the power grid system. Although wind farms are operating below their maximum energy production levels, they can minimize revenue losses due to decreased energy production by offering into the AS market. In the program, wind farms offer $15/MWh in the AS market to regain the revenue that they would lose by limiting their power generation in the energy market. Section A3 of the Appendix lists the AS market offers (Das 2013).

Maximum power limitation provides a way to deal with high variability situations. Using the forecast to anticipate high variability, and then using that information to determine the limit of power production for wind farms could lead to less exposure to the penalties imposed by the market (for dispatchable intermittent resources) on wind units that cannot follow dispatch. Constant or variable delta control would allow wind to gain revenue from the energy market without significant decrease in prices, while allowing the wind farms to participate in the AS market.

When variable delta control was implemented in the system, allowing wind to participate in the AS market, for higher wind penetration levels, 40%, there were slight decreases in the overall LMP mean, spinning reserve MCP, and regulation up MCP. These reductions are increased when wind is combined with one 100 MW CAES unit.

For future work the program should be changed to include wind farms in the AS market bidding system while using the maximum power limitation control method. This will provide a way to further analyze how much revenue would be lost or gained by using maximum power limitation. Also further studies surrounding increasing the transmission limits in the system should be performed to see how the system reacts when it can accommodate high winds, and if other control methods can be used to lower production costs for the system.

Acknowledgements

Support for this research was provided by a National Science Foundation Research Experience for Undergraduates site program in Wind Energy Science Engineering and Policy (WESEP) grant number EEC-1063048 at Iowa State University.

References

Botterud, Audun, Jianhui Wang, V. Miranda, Ricardo Bessa, April 2010: Wind Power Forecasting in U.S. Electricity Markets. Electricity Journal. 71-82 pp. [Available online at http://www.ferc.gov/eventcalendar/Files/20100530130438-Botterud%20Paper,%20Wind%20Power%20Forecasating%20in%20US%20Electricity%20Markets.pdf]

California ISO, cited 2013: Market products and services help meet demand. [Available online at http://www.caiso.com/market/Pages/ProductsServices/Default.aspx]

Das, Trishna, 2013: Performance and economic evaluation of storage technologies. PhD dissertation, Iowa State University. 237 pp. [Available online at http://lib.dr.iastate.edu/etd/13047]

Kirby, Brendan, 2007: Ancillary Services: Technical and Commercial Insights. Wartsila. [Available online at http://www.science.smith.edu/~jcardell/Courses/EGR325/Readings/Ancillary_Services_Kirby.pdf]

Kristoffersen, Jesper, 2005: The Horns Rev wind farm and the operational experience with the wind farm main controller. Copenhagen Offshore Wind. [Available online at http://wind.nrel.gov/public/SeaCon/Proceedings/Copenhagen.Offshore.Wind.2005/documents/papers/Wind_power_plant_control/J.R.Kristoffersen_TheHornsRevWindFarm.pdf]

Kumar, N., P. Besuner, S. Lefton, D. Agan, D. Hilleman, April 2012: Power Plant Cycling Costs. Subcontract Report. National Renewable Energy Laboratory. [Available online at http://www.nrel.gov/docs/fy12osti/55433.pdf]

Smith, J., T. Acker, E. DeMeo, M. Milligan, B. Parsons, M. Schuerger, R. Zavadil, 2007: Best practices in grid integration of variable wind power: summary of recent US case study results and mitigation measures. Midwest Research Institute. [Available online at http://www.uwig.org/EWEC07paper.pdf]

Wiser, Ryan, Mark Bolinger, June 2011: 2010 Wind Technologies Market Report. Department of Energy. [Available online at http://www.windpoweringamerica.gov/pdfs/2010_annual_wind_market_report.pdf]

Appendices

Appendix A1

The objective function and constraints:

$$
\begin{aligned}
Minmize \sum_{t\in T_h}\sum_{(i,j)\in G,T} & C_{(i,j)}(t) * e_{(i,j)}(t) \\
& + \sum_{t\in T_h}\sum_{(i,j)\in G} C^{sr}{}_{(i,j)}(t) * e^{sr}{}_{(i,j)}(t) \\
& + \sum_{t\in T_h}\sum_{(i,j)\in G} C^{nsr}{}_{(i,j)}(t) * e^{nsr}{}_{(i,j)}(t) \\
& + \sum_{t\in T_h}\sum_{(i,j)\in G} C^{reg+}{}_{(i,j)}(t) \\
& * e^{reg+}{}_{(i,j)}(t) \\
& + \sum_{t\in T_h}\sum_{(i,j)\in G} C^{reg-}{}_{(i,j)}(t) \\
& * e^{reg-}{}_{(i,j)}(t) \\
& + \sum_{t\in T_h}\sum_{(i,j)\in G} S^{x}{}_{(i,j)}(t) * (X_{(i,j)}(t) \\
& + X^0_{(i,j)}(t)) \\
& + \sum_{t\in T_h}\sum_{(i,j)\in G} S^{y}{}_{(i,j)}(t) * (Y_{(i,j)}(t) \\
& + Y^0_{(i,j)}(t)) + \sum_{t\in T_h}\sum_{j\in D} Pen_j(t) * L_j(t)
\end{aligned}
$$

- *e(i,j)(t)* is per unit (p.u.) energy flow and *C(i,j)(t)* its cost at hour *t* across all system arcs *(i,j)*
- *esr(i,j)(t)* is p.u. spinning reserve capacity and *Csr(i,j)(t)* its cost at hour *t*, where *(i,j)*∈ *G*;
- *ensr(i,j)(t)* is p.u. non-spinning reserve capacity and *Cnsr(i,j)(t)* its cost at hour *t*, where (*i,j*)∈*G*; *ereg+(i,j)(t)* is p.u. up-regulation capacity and *Creg+(i,j)(t)* its cost at hour *t*, where (*i,j*)∈*G*;
- *ereg-(i,j)(t)* is p.u. down-regulation capacity and *Creg-(i,j)(t)* its cost at hour *t*, where (*i,j*) ∈*G*;
- *Sx(i,j)(t)* is start-up and *Sy(i,j)(t)* is shut-down costs, (*i,j*) ∈*G*;
- *X(i,j)(t)* is start-up and *Y(i,j)(t)* is shut-down indicators;
- *X0(i,j)(t)* is start-up and *Y0(i,j)(t)* is shut-down indicators for non-spinning reserves, where (*i,j*) ∈*G*;
- *Lj(t)* is p.u. energy demand not served at hour *t*, where *j*∈*D*;
- *Penj(t)* is the cost penalty for *Lj(t)*

Appendix A2

Table 8: System Generation Parameters and Energy Offers

Generator	**Min-Max (MW)**	**Offer 1 (MW)/ Price ($/MWh)**	**Offer 2 (MW)/ Price ($/MWh)**	**Offer 3 (MW)/ Price ($/MWh)**
Oil (1)	0-40	0-20/93.7	21-40/98.8	-
Coal (1)	50-152	50/26.9	51-100/32.4	101-152/41.9
Oil (2)	0-40	0-20/93.7	21-40/98.8	-
Coal (2)	50-152	50/29.6	51-100/32.4	101-152/41.9
NG (7)	100-300	100/51.8	101-200/60.8	201-300/73.8
NG (13)	200-591	200/48.6	201-400/57.6	401-591/70.6
NG (15)	0-60	0-20/48.6	21-40/54.6	41-60/66.4
Coal (15)	50-155	50/24.5	51-100/28.5	101-155/36.5
Coal (16)	50-155	50/24.5	51-100/28.7	101-155/37.1
Nuc (18)	300-400	300/10.5	300-400/17.5	-
Nuc (21)	300-400	300/10.5	300-400/17.5	-
Coal (22)	150-300	150/24.6	151-250/32.2	251-30/44.3
Coal (23)	150-310	150/20.5	151-250/28.5	251-310/41.3
Coal (23)	150-350	150/20.6	151-250/27.8	251-350/39.3
Wind 20% (17)	0-300	0-300/15	-	-
Wind 20% (21)	0-400	0-400/15	-	-
Wind 20% (22)	0-151.25	0-151.25/15	-	-
Wind 40% (17)	0-700	0-700/15	-	-
Wind 40% (21)	0-875	0-875/15	-	-
Wind 40% (22)	0-700	0-700/15	-	-
Wind 60% (17)	0-1400	0-1400/15	-	-
Wind 60% (21)	0-2300	0-2300/15	-	-
Wind 60% (22)	0-1400	0-1400/15	-	-

Appendix A3

Table 9: System AS Offers

Unit	SR ($/MWh)	NSR ($/MWh)	RU/RD ($/MWh)
Oil	7.8	-	62
Coal	8	-	26
NG	7.9	4.1	27
Wind	15	-	15
CAES	7.5	4	17.9/12.5

The Role of Demand Response in Complementing Wind on a Grid

PETER MCHALE
Wind Energy Science Engineering and Policy REU, Iowa State University, Ames, Iowa
Mentors: J. McCalley, V. Krishnan, N. A. Brown

Abstract

The objective of this study was to examine demand response as a grid service for decreasing total cost for providing generation on a grid with different degrees of wind penetration and with and without storage capabilities. Existing work in this area includes simulations of demand response on a grid without wind penetration and tracking the results of current implementations of demand response programs offered by ISO's and third party companies. My aim was to understand if demand response should be used to compliment wind penetration variability on a grid, which was tested by simulating the results of an IEEE 24-bus system with modified load curves. The result of these simulations was a substantial decrease in overall generation costs, though to lesser degrees with larger wind penetration levels, and without much change in impact of demand response between runs with and without storage capabilities. With the goal of twenty percent wind-penetration levels by 2030 set by the DOE, it is important that we have a smart enough grid to accept large amounts of wind penetration while maintaining stability and keeping costs down. Demand response may have a place in creating that smart grid, so it is important that we understand the impact of demand response on the electricity market in different contexts.

1. Introduction

With our need for reduced carbon-dioxide emissions, increased energy security as a nation, and decreased dependence on limited resources, renewable energy resources are becoming more prominent, and wind is no small player. In 2008, wind turbines produced about one percent of the United States energy supply while the Department of Energy has made a scenario for a penetration level of twenty percent by 2030 (U.S. DOE, 2008). Because of its major role in our future energy portfolio, it is important to address the problems that come with greater wind penetration levels and to invest in their solution.

With greater amounts of wind energy going into the grid it is important that we adjust the current grid to accommodate for the added wind generation. Currently, we treat our small amount of wind-energy input to the grid as a negative load. First we subtract from the total load the wind-energy supply, and then we address what is left with traditional generators and ancillary services (Eriksen, 2005). Wind varies throughout the day, and so this total load with wind subtracted has greater variation. Usually we handle the different degrees of variability with ancillary services, however as greater amounts of wind are added to the grid the cost of the necessary ancillary services increases. If we can decrease the variation in generation and load, then we can reduce the amount of ancillary services that are needed and increase the stability of the grid.

There are three methods of decreasing variation that are currently being considered. One is to add storage capabilities to the grid, another is to apply controls to the variable wind generation, and the last is to have some control over demand through methods of demand response. The optimal solution likely makes an appropriate use of all three methods, though this paper will focus on the possibilities of demand response.

This paper begins by considering what differences demand response might make on the load curve throughout the day and at what cost. Then a mixed-integer linear-program solver is used with the program created by Trishna Das (2013) to find the effects of different implementations of demand response on costs and the local marginal cost (LMP). After appropriate attention is given to demand response, its place in an optimal solution with storage and control methods is considered.

2. Literature review

Here I will give a brief review of storage and controls for context, since the solution that demand response is a part of will likely require some degree of these other methods for stability. Then I will go into depth on demand response, its past implementations, and its results, which will provide context and justification for my decisions when simulating demand response in the IEEE 24-bus RTS system.

Different means of storage could be used to solve different problems in the shorter and longer time frame.

Short term storage (such as flywheels or smaller batteries) could be used as a form of regulation, quickly charging when energy demand momentarily decreases and then quickly discharging when energy demand temporarily increases. Long term storage (such as compressed air energy storage (CAES) or pumped hydro) could be used to charge before peak load and then discharge during peak load in order to flatten the load curve to some degree. Different storage devices could further be characterized by their ability provide regulation up and regulation down while charging and discharging (Das, 2013). In simulations used in this research, all storage is modeled as CAES due to its convenient ability to operate in all four quadrants.

Controls could be used to cap wind at certain amounts of generation in order to provide a consistent energy source (adding a constant amount of MW to the grid) from wind turbines. This decreases the variation in generation added to the grid and thus decreases regulation and ancillary services required and increases grid stability. Different methods of controlling wind generation are used, each with their benefits and costs, but each requires wind to generate below its maximum potential. A control method currently being researched is delta control, which cuts the wind energy provided to the grid at some fraction of the forecast and then sells some remaining potential energy as capacity in ancillary services.

Demand response can be implemented in many different ways, each making the electrical grid more stable. The different methods vary in the consumers they work with (industrial or individual households) and grid costs they intend on dissolving (some focus on peak-load shedding and others on directly complementing wind generation levels with demand). Despite these differences, all means of demand response are potential solutions to the same real-world problem, and so must be effective and economically attractive in order to be practical. The energy consumer must have reasonable incentive to give up some comfort and the service provider must be able to make sizeable profits. By simulating a demand response solution under real-world conditions and by observing current implementations already in effect, we can consider which methods of demand response are practical.

Demand response at the household level for peak load shedding is the topic of a great amount of research, and could be a means of decreasing the market clearing price (and thus the electricity bill of every consumer) and costs for the utilities to run the generators. In a simulation done by Chua-Liang Su and Daniel Kirschen (Su, 2009), household consumers are allowed to bid their demand in a similar way that utilities bid their generation. The effect of bidding was to shift some energy consumption at peak demand to periods of less demand (peak shifting). As a result of this shift, the market clearing price increases during off-peak periods and decreases during peak periods. Both of these effects can be seen in the figures below (taken from Su, 2009), with LPF representing the ratio of price responsive demand to total demand. In the first figure (Fig. 1), the system demand is measured in MW and the period is measured in hours through a day. In the second figure (Fig. 2), the change in market clearing price is measured in dollars per MWH, and the period is again measured in hours over the course of one day. In this study it was observed that overall market-clearing prices tend to decrease with increasing levels of demand response.

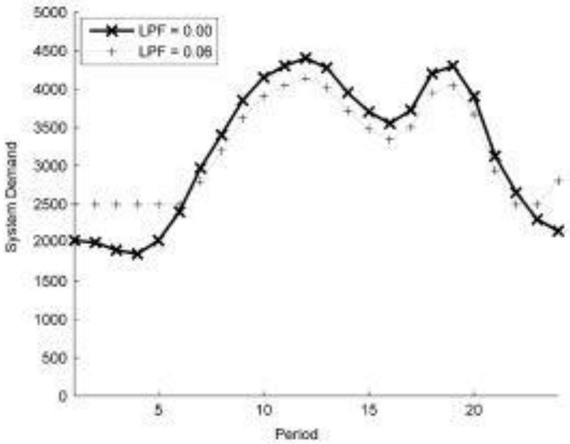

Figure 1 Electricity Demand Curve Comparison LPF=0 to LPF=.06

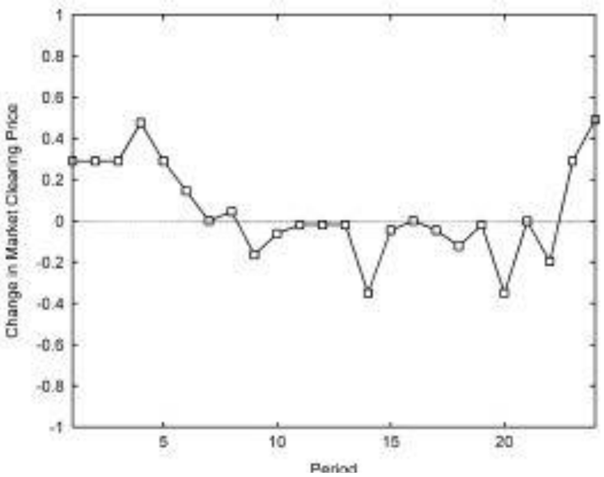

Figure 2 Change in MCP from a Demand with LPF=0 to LPF=.06

Demand response is beginning to be implemented in the real world with real, observed benefits by not just the ISO's themselves, but also by third party companies. There is a great advantage to having third party companies offering demand response programs, as large companies often do not take the initiative to participate in the demand response programs offered by the ISO's when it requires learning technical details or installing hardware with considerable up-front cost. These companies offer their services to medium and large sized companies, help install the required hardware for the company to participate in demand response, provide software with which the company can make decisions, and then provide technical help services and keep in communication with the company. In the case of EnerNOC, the companies which participate in their demand response program are paid a flat fee for participating in the program (which is called DemandSMART) and for every bit of energy they decide to save (based on the wholesale price of energy at the time of reduced use). The company can decide to have some of these decisions automated under parameters that they set in the software or can make the decisions themselves in real-time. These companies have helped decrease costs in the grid, as decreasing peak load allows the ISO to not utilize the more expensive generator bids, as well as save the energy customers a good amount on their electricity bill. EnerNOC claims that their customers can save up to thirty percent of their electricity bill while one of their customers reports savings around $30,000 a year from DemandSMART services (EnerNOC, 2013).

Demand response can also be used to complement wind energy supply directly. In a report on integrating renewable generation resources into the electrical grid, Shie-Jie Deng et al. (Shie-Jie, 2012) simulate a market in which customers (individual household consumers) can choose to participate in one of two programs of demand response, or choose to not participate at all. The services directly control thermostatically controlled loads (TCL's) to have demand complement wind directly. TCL's include air cooling, air conditioning, and refrigeration and were shown in 2007 by the Department of Energy to account for sixty to seventy percent of household energy consumption. The simulations ran with offering programs of different degrees of control allowed and different rebates given to customers per KWH saved. The result of some of these simulations was a net cost increase, while some resulted in a net cost decrease. This shows that demand response programs must be fine-tuned to the specifics of the customer base and generation resources in each market in order to prove beneficial. This is great reason to simulate possible implementations of demand response and to note their probable impacts before implementing them.

In order to simulate demand response in a market, it is important to work with realistic values. We must find out what amount of participation in demand response programs might be expected, along with what amount of controllable load might be offered from that participation. For example, even if 5% of the household energy load is involved in a TCL demand response program, they will not offer up the entirety of the 60-70% of their load to be controlled. As the Su paper points out, instead of offering their entire heating or cooling load, energy consumers may allow the temperature of their house to deviate by a few degrees Celsius, given fair compensation (Shie-Jie, 2012).

Big business loads, making up more than 86% of the demand response activity in PJM's energy market (PJM, 2013), is equally, if not more, important to consider when it comes to amount of controllable load. Some industries, such as restaurants and hospitals, do not have much control over when they use their electricity, and this creates a considerable amount of unmovable load. Industrial and Manufacturing load can be much more flexible, as some energy-expensive processes can be moved to earlier or later parts of the day and out of peak load times. As you can see from the illustration in Fig 3, in the PJM market, food services composed close to zero percent of the energy moved by a demand response program and hospitals contributed about 2% while industrial and manufacturing processes contributed to 67% of the energy (PJM, 2013). With this amount of variation in elasticity among customers, it is important to take note of past simulations and implementations when considering who might be the ideal customers for a demand response program and what the controllable load percentage might be. By considering the results of simulations and past implementations, it is possible for us to understand what place demand response should have in our future electricity markets.

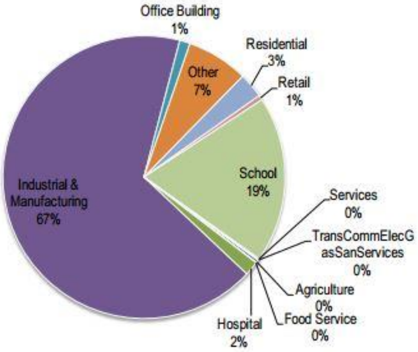

Figure 3 Distribution of Controllable Load for PJM Area

3. **Experimental methods**

My simulations show the impact that demand response might have on the costs of generation and the market LMP. By noting the results of demand response, we can consider if it is worth implementing when performing cost-benefit analysis, which will be done in the analysis section of this paper. These demand-response simulations use the program written by Trishna Das.

Trishna Das' program uses a mixed-integer linear solver to optimize economic costs for energy generation. Using the IEEE 24-bus RTS system, along with a 48-h load and weather forecast taken from California Independent System Operator (CAISO) public data, she organized a graph of arcs representing different generators (including wing turbines), compressed air energy (CAE) storage units, and loads. This graph of arcs contained information on all relevant values associated with these units, including energy bids for the generators' three regions of operation, their bids for ancillary services, the ramp rate of the storage and generators, and minimum and maximum operating constraints. The total two-day load is distributed to multiple load arcs and the weather forecast is used to consider what the generation from wind turbines should be.

Once this graph of arcs is established, the program calculates values for every 5-munite time step of the total 48 hours, and then repeats this process, using the monte carlo method to gather information from different situations of possible changes. This means the program's output is ran through a mixed-integer linear solver many times over with minor variations in generator outages and fuel prices. For the sake of having deterministic results to easily compare the results of different changes and to decrease the run time of the program, this monte carlo aspect of the program and the variations were taken out.

The objective function that the linear solver minimizes is a summation calculating the total production cost of energy generation. This objective function is shown below as equation 1.

$$\begin{aligned}&\sum_{t\in T_k}\sum_{(i,j)\in G,T} C_{(i,j)}(t).\,e_{(i,j)}(t)\\
&\quad+\sum_{t\in T_k}\sum_{(i,j)\in G} C^{sr}_{(i,j)}(t).\,e^{sr}_{(i,j)}(t)\\
&\quad+\sum_{t\in T_k}\sum_{(i,j)\in G} C^{nsr}_{(i,j)b}(t).\,e^{nsr}_{(i,j)}(t)\\
&\quad+\sum_{t\in T_k}\sum_{(i,j)\in G} C^{reg+}_{(i,j)}(t).\,e^{reg+}_{(i,j)}(t)\\
&\quad+\sum_{t\in T_k}\sum_{(i,j)\in G} C^{reg-}_{(i,j)}(t).\,e^{reg-}_{(i,j)}(t)\\
&\quad+\sum_{t\in T_k}\sum_{(i,j)\in G} [S^{x}_{(i,j)}(t).\,(X_{(i,j)}(t)\\
&\quad+X^{0}_{(i,j)}(t))]\\
&\quad+\sum_{t\in T_k}\sum_{(i,j)\in G} [S^{y}_{(i,j)}(t).\,(Y_{(i,j)}(t)\\
&\quad+Y^{0}_{(i,j)}(t))]+\sum_{t\in T_k}\sum_{(i,j)\in G} Pen_j(t).\,L_j(t)\end{aligned}$$

(1)

- $e_{(i,j)}(t)$ is per unit energy flow and $C_{(i,j)}(t)$ its cost at hour t across all system arcs (i,j);
- $e^{sr}_{(i,j)}(t)$ is per unit spinning reserve capacity and $C^{sr}_{(i,j)}(t)$ its cost at hour t, where $(i,j)\in G$;
- $e^{nsr}_{(i,j)}(t)$ is per unit non-spinning reserve capacity and $C^{nsr}_{(i,j)b}(t)$its cost at hour t, where $(i,j)\in G$;
- $e^{reg+}_{(i,j)}(t)$ is per unit up-regulation capacity and $C^{reg+}_{(i,j)}(t)$ its cost at hour t, where $(i,j)\in G$;
- $e^{reg-}_{(i,j)}(t)$ is per unit down-regulation capacity and $C^{reg-}_{(i,j)}(t)$ its cost at hour t, where $(i,j)\in G$;
- $S^{x}_{(i,j)}(t)$ is start-up and $S^{y}_{(i,j)}(t)$ is shut-down costs, where $(i,j)\in G$;
- $X_{(i,j)}(t)$ is start-up and $Y_{(i,j)}(t)$ is shut-down indicators, where $(i,j)\in G$;
- $X^{0}_{(i,j)}(t)$ is start-up and $Y^{0}_{(i,j)}(t)$ is shut-down indicators for non-spinning reserves, where $(i,j)\in G$;

In order to consider how demand response may affect the market, I wrote a program that would modify the original load curve that came from the CAISO demand data. My modified load curve would then be fed as input to Das' program as the new load curve, and the linear optimization would run to minimize costs for meeting the new load curve with generation. The goal of my modification was to use the input percentage of controllable load to shift the energy consumed in the peak load time to be used in the low-demand times instead, while maintaining the characteristic load profile shape. This would, in effect, carry out the impact that peak-load shifting might have and level out the load curve to the degree possible with the amount of flexible load given. Since this method of peak-load shifting is not focused on finer-scale energy balancing (to decrease regulation costs), my program had to conserve the fine-scale variation of the load curve (in a discussion with a MISO employee, I learned that the quick variations in wind average out as the wind takes time to go from wind farm to wind farm, and so regulation-level demand response does not seem the appropriate choice in complementing wind energy on the grid). Also, since only a fraction of the energy not consumed during peak time would not have to be made up for in non-peak times, the amount of total energy consumed (the area under the load curve) would have to be very close to the original. In order to meet these conditions and apply an appropriate modification to the load curve, I used the below equation (eq. 2), which was applied to all points on the load curve.

$$
\begin{aligned}
&Load_{new}(i) \\
&= Load_{old}(i) \\
&+ \left(Load_{old}(i) * \left(\frac{percent}{100}\right) \right. \\
&* sqrt\left(\frac{abs\left(Load_{mean} - Load_{old}(i)\right)}{window}\right) \\
&\left. * \left(\frac{\left(Load_{mean} - Load_{old}(i)\right)}{abs\left(Load_{mean} - Load_{old}(i)\right)}\right) \right)
\end{aligned}
\tag{2}
$$

This equation is effectively determining the new value at each minute on the load curve by taking the old, original value at that time and adding another value to that original value. To find the value to be added, I used a quadratic function that would output a greater value the further the value is from the mean of the load and a lesser value the further it is from the mean. Also, this added value would be negative if the original value was above the mean and positive if it was below. This results in a "collapsing" of the load curve, causing it to be closer to the mean at all points and thus modify the load curve in a way a load-shifting program might. The overall result with two percent and five percent control over load can be seen in the figure below (Fig. 4).

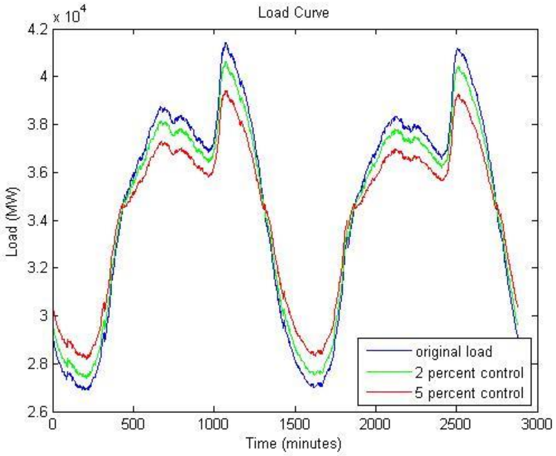

Figure 4 Comparison of Loads with 0%, 2%, and 5% control of Load for Load Shifting

This program effectively modifies the load curve in a fashion that we might expect from a peak-load shifting demand response program, though the percentage of the load that we have control over (the input to this load-modifying program) must be grounded in what is currently being done. By grounding this percentage value, we can understand what degree of control might be conservative, realistic, or ambitious. PJM (PJM, 2013) has offered demand response programs and has tracked the results of the load reduction, and so we use the information they have released to base our percentage of controllable load on. In July of 2012, the total economic demand response capability was 2,300 MW, while only 70 MW of the load were reduced. The average peak load in 2012 for the same area was 96,194 MW (State, 2012), which means 2.39 percent of the load was controllable, while only 0.07 percent was controlled. The PJM report further states that around 42,000 MWH were affected in July by this demand response program. It is unclear whether this energy was shifted from peak hours to non-peak hours or simply reduced, but it is assumed to have been shifted, since this seems more reasonable for significant classes of loads. At an average of 70 MW, this means that demand response program was in effect for 600 out of the 744 hours in July, roughly four-fifths of the time. The fact that demand response is implemented for such a large fraction of the time is promising, along with the 2.39 percentage of controllable load. As we offer more demand response programs, we will be able to make use of more of that controllable load, as well as increase the amount of controllable load involved in the demand response programs. Though it is likely for the numbers to increase as we get more experienced with demand response programs, it is unlikely that the percentage of controllable load will jump an order of magnitude in the near future. For these reasons, I use two percentage as a realistic amount of controllable load and five percentage as my upper bound of optimistic controllable load percentage. These expected percentages of controllable load would be the product of not only the percentage of participation of the load in the demand response program, but also the amount of elasticity of the participating load.

By running this simulation many times, each with a different combination of wind penetration levels (0%, 20%, 40% or 60%), percentage of controllable load (0%, 2%, or 5%), and amount of storage (0MW or 200MW), I was able to see how demand response might change the total costs of a grid system with varying degrees of wind penetration and with and without storage capability.

4. Results

Below are the results of my multiple simulations. In the first table are the total cost of each simulation without storage, with every combination of zero, two, and five percent control of load and of zero, twenty, forty, and sixty percent wind penetration and no storage. The second table is similar to the first table, but on a grid with 200 MW of storage capability.

Table 1 Generation Costs without Storage

Total Cost of Generation with Varying Wind Penetration Levels and Varying Degrees of Load Control from Demand Response
[In millions of dollars
(Difference from Zero-Percent-Control Cost)
(Percent decrease from Zero-Percent-Control Cost)]

		Percent Wind Penetration			
		0%	**20%**	**40%**	**60%**
Percent Control of Load	**0%**	**3.5405**	**3.2266**	**3.0698**	**3.0645**
	2%	**3.4775** **(-.0630)** **(-1.78%)**	**3.1898** **(-.0368)** **(-1.14%)**	**3.0352** **(-.0346)** **(-1.13%)**	**3.0632** **(-.0013)** **(-.04%)**
	5%	**3.3936** **(-.1469)** **(-4.15%)**	**3.1290** **(-.0976)** **(-3.02%)**	**2.9824** **(-.0874)** **(-2.85%)**	**3.0330** **(-.0315)** **(-1.03%)**

Table 2 Generation Costs with Storage

Total Cost of Generation with Varying Wind Penetration Levels, Varying Degrees of Load Control from Demand Response, and 200 MW of Storage
[In millions of dollars
(Difference from Zero-Percent-Control Cost)
(Percent decrease from Zero-Percent-Control Cost)]

		Percent Wind Penetration			
		0%	**20%**	**40%**	**60%**
Percent Control of Load	**0%**	**3.5193**	**3.2023**	**3.0203**	**3.0638**
	2%	**3.4563** **(-.0630)** **(-1.79%)**	**3.1627** **(-.0396)** **(-1.24%)**	**2.9853** **(-.0350)** **(-1.16%)**	**3.0625** **(-.0013)** **(-.04%)**
	5%	**3.3727** **(-.1466)** **(-4.17%)**	**3.1041** **(-.0982)** **(-3.07%)**	**2.9382** **(-.0821)** **(-2.72%)**	**3.0324** **(-.0314)** **(-1.02%)**

5. Analysis and interpretation

Results of my simulations demonstrate that the greatest benefit of demand response is in a grid with lesser wind penetration levels in both the grid with and the grid without storage capability (decreasing the total costs by around four percent with zero wind penetration, but then decreasing the costs by only around one percent with sixty percent wind penetration). Since this is counter-intuitive, and the motivation was to complement wind with a demand response service, I do not believe this would be the results of a demand response service in practice, and so an assumption made in my methods may have introduced an error.

In my method, I applied demand response by decreasing the peak points of the load and increasing the trough points of the load. While this is peak shedding in the way it is typically described, it does not account for what the wind is doing. Not only are the wind and load not positively correlated, but they are often thought to be negatively correlated, with the greatest wind occurring during the smallest load time (during the hours of the night). Because of this, a demand response service behaving only in response to the load will often increase the load when it should decrease it, and vice versa, when the grid has a higher level of wind penetration. I believe this is the reason that my simulation of demand response resulted in less change when wind penetration levels were increased.

Another observation from these results is that for each simulation of a fixed amount of wind penetration and a fixed amount of load control, whether or not the grid had storage capability had an insignificant impact on the results of demand response. While storage capabilities dramatically decreased the costs of the grid, the percentage difference in costs obtained as a result of demand response was barely affected. I believe this to be because demand response services and storage services are competing services, attempting to perform the same objective instead of complementing each other. Both services would increase the total load during times when load is low and decrease the total load during peak-load times, and so storage capabilities do not help the impact of demand response services.

6. Conclusions

While there is inherent error in computer simulations in never being able to account for all complexity involved in the market, we are able to get closer to real-world results when modeling the market more accurately. I believe that the above unexpected results were attributable to an insufficiently accurate model of how demand response might be used in a market. In order to implement any grid service for optimal results, you must account for the nature of the grid. With increasing levels of sustainable generators, such as wind turbines, being added to the grid, the behavior of the grid becomes more influenced by the behavior of those generators. In the case of wind, the amount of cheap generation available becomes more correlated with the wind forecast, and so any successful implementation of demand response must account for the wind forecast when determining when to increase and when to decrease energy use. Furthermore, because grid services demand their own costs in order to be implemented, it is necessary to consider which services are appropriate for a specific energy portfolio and which services may complement each other nicely. With substantially more sustainable generators being added to the grid in the near future, it is important that we consider their behavior in choosing which grid services to offer and to what extent to offer them.

Acknowledgements

Support for this research was provided by a National Science Foundation Research Experience for Undergraduates site program in Wind Energy Science Engineering and Policy (WESEP) grant number EEC-1063048 at Iowa State University.

References

Su, Chua-Liang and Daniel Kirschen, 2009: Quantifying the effect of demand response on electricity markets. *IEEE Transactions on Power Systems*, **24** (3). doi: 10.1109/TPWRS.2009.2023259

Das, Trishna, "Performance and Economic Evaluation of Storage Technologies" (2013). *Graduate Theses and Dissertations*. Paper 13047. pp. 33, 35-48.

Department of Energy, 2008: 20% wind energy by 2030. Energy Efficiency and Renewable Energy Rep. DOE/GO-102008-2567, 1-2.

EnerNOC, 2013: Company website. [Available online at http://www.enernoc.com/.]

Eriksen, Peter Borre, Thomas Ackermann, Hans Abildgaard, Paul Smith, Wilhelm Winter, and JuanMa Rodriguez Garcia, 2005: System operation with high wind penetration. *Power and Energy Magazine*, **3** (6). 65-74. doi: 10.1109/MPAE.2005.1524622.

PJM Interconnection, 2013: 2012 Economic demand response performance report. Pp 2, 7, 12. [Available online at http://www.pjm.com/~/media/markets-ops/dsr/economic-dr-performance-report-analysis-of-activity-after-implementation-of-745.ashx]

Shie-Jie, Shmuel Oren, and George Gross, 2012: Design and valuation of demand response mechanisms and instruments for integrating renewable generation resources in a smart grid environment. [Available online at http://www.pserc.wisc.edu/documents/publications/reports/2012_reports/Deng_PSERC_Report_M-23_Oct_2012.pdf.]

State of the Market, 2012: State of the market report for PJM. Pp 380. [Available online at http://www.monitoringanalytics.com/reports/PJM_State_of_the_Market/2012/2012-som-pjm-volume2-appendix.pdf.]

Numerical Simulations of Flow Convergence Phenomenon in Wind Turbine Arrays

ANGELO JEREZ CHAVES
Wind Energy Science Engineering and Policy REU, Iowa State University, Ames, Iowa
Mentors: Dr. Anupam Sharma and Dr. Eugene S. Takle

Abstract

A generalized actuator disk model in OpenFOAM is used to simulate wind turbine and wind farm aerodynamics. This model significantly simplifies wind turbine (and farm) computations by removing the need to discretize and simulate the rotor geometry. Instead, the effect of the rotor is modeled using body forces in the momentum equation. The model is first validated against analytical results from the 1-D momentum theory. The numerical results with the model as present in the OpenFOAM solver suite showed a small discrepancy, which was removed by using a Gaussian distribution of forces over the volume. Results from the improved model compare very well with the 1-D theory.

The phenomenon of flow convergence in wind farms is numerically investigated using the actuator disk model. Two wind farm configurations, one with finite turbines and another with infinite turbine (in one direction simulated with periodic boundary conditions) are considered. A slip wall approximation is first made to check if the hypothesis of pressure gradients setup by the turbines is responsible for flow convergence. The simulation results show flow deviation of the order of 2 degrees, which is qualitatively in the right direction by quantitatively far short of the 8-10 degree flow deviation observed in experiments. Viscous simulations are attempted which show larger deviation in flow angle however the results are preliminary and need more investigation before we can assert that the proposed numerical method is successful in capturing the flow convergence phenomenon.

1. Introduction

Finiteness of oil and gas reserves and increasing greenhouse gas emissions are driving the continuous growth of alternative and particularly renewable energy sources. Wind, solar, hydro, and geothermal are the top renewable energy sources that show promise to rid our dependence on oil and to slow down the accelerating pace of environmental pollution. Wind energy has been the fastest growing renewable energy source in the USA in the last decade. Government tax deduction policies support the development of this energy source. Currently, wind energy is harvested using wind turbines, which convert the kinetic energy in the wind to kinetic energy of rotor blades and subsequently into electrical energy using a generator. Most modern utility-scale wind turbines are horizontal axis wind turbines (HAWT) and are typically deployed in groups (arrays, clusters or farms) either on land or in water. Since the energy source is the flowing air, wind farm aerodynamics plays a critical role in determining the net power production from wind farms. Several interesting aerodynamic phenomena occur in wind farms and one such phenomenon is the subject of investigation of this study.

It has been observed experimentally that a wind turbine array tends to align the airflow (that may be coming at an angle) to the array orientation. This is referred to as “flow convergence”. The deviation in flow angle on the ground between upstream and downstream of an array has been observed to be as large as 10 degrees. While the consequences of this phenomenon are not well understood at this time, the implications in terms of turbine siting as well as farm operation are potentially significant.

The present study is an attempt to numerically analyze wind farm aerodynamics. The objective is to be able to predict the phenomenon of flow convergence using computational fluid dynamics (CFD) simulations. The software used for this study is OpenFOAM, which is a free, open source CFD software. OpenFOAM can be used to numerically simulate a variety of engineering and science problems. It has been particularly popular and successful in modeling complex fluid flows. The software also comes with a visualization tool called ParaView, which is very useful in post-processing and analyzing the results.

The rest of the report structure is as follows. A brief background and literature review is provided in the following section followed by a description of the numerical model used here. Some sample calculations with a single turbine are performed to verify the numerical model. A hypothetical wind farms is simulated to predict flow convergence.

2. Literature review

OpenFOAM is relative recent software available for users. The program is essentially a group of C++ libraries used to create solvers, known as applications. These applications are used to solve problems in continuous mechanics in a variety of problems in engineering and science applications. Some commonly used numerical solver for fluid flow simulations are provided in the software package. It includes several pre- and post-processing tools that ensure consistent data manipulation of a problem from start to finish. Figure 1 shows the software structure.

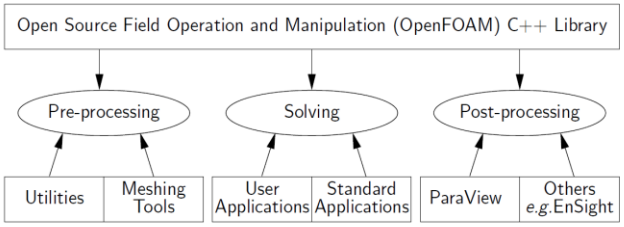

Figure 1. Overview of OpenFoam structure (adapted from OpenFoam user guide).

The interest here is in simulating aerodynamics of a wind *farm*. The length scales of interest are of the order of rotor diameter, therefore resolving blade boundary layers, and even individual blades is overkill. The simulations are therefore simplified by replacing the turbine blades by an actuator disk. Momentum sources equivalent to the aerodynamic forces experienced by the rotor blades (equal and opposite forces are exerted on the fluid by the rotor by Newton's third law) are applied on this actuator disk to mimic the effect of the rotor on the fluid. An incompressible formulation is considered here, hence only momentum sources are needed to completely specify the effect of the rotor; in a compressible formulation the energy equation would have to be solved with a corresponding energy source (sink). A simplified 1-D momentum theory is used to calculate the aerodynamic force. The 1-D momentum theory ignores the effect of swirl and hence only the thrust force needs to be applied in the simulations.

Mikkelsen (2003) studied this case and established two non-dimension parameters. It is convenient to work with non-dimensional force and power coefficients. In a wind turbine, thrust and drag coefficient, $C_{T,}$ C_P, are defined as

$$C_T = \frac{T}{\frac{1}{2}\rho_0 V_0^2 A} \text{ ,and } \quad C_P = \frac{P}{\frac{1}{2}\rho_0 V_0^3 A}.$$

Using the 1-D momentum theory these coefficients can be expressed as functions of another non-dimensional parameter called the axial induction factor, $a=1-(u/V_0)$, where u is the flow velocity at the rotor disk and V_0 the wind velocity before the rotor disk.

$$\begin{aligned} C_T &= 4a(1-a) \\ C_P &= 4a(1-a)^2. \end{aligned}$$

With both parameters known, simulation of turbine blades geometry is no longer necessary. The resulting forces can be applied to a selected simple geometry volume of control without loss of information.

When these parameters are derivate the maximum or minimum values of thrust of power are obtained. For wind turbines, when higher the thrust force, more energy can be extracted from the wind. For maximum power extraction, a = 1/3, C_T=8/9 and C_P=16/27. These values are known as *Betz limit*.

Glauert (1930) proposed an extension to the 1-D momentum theory that incorporates the effects of finite blades (as opposed to using an actuator disk). In this theory, the rotor is discretized into several annuli. For each annulus, momentum balance and energy conservation principles are combined with airfoil theory to obtain C_T and C_P. This theory is now famously known as the blade element momentum (BEM) theory and is one of the commonly used wind turbine blade aerodynamic design and analysis code. This method is simple and fast to run on a computer, which is why it gained popularity. Figure 2 shows a sample control volume and the rotor representation.

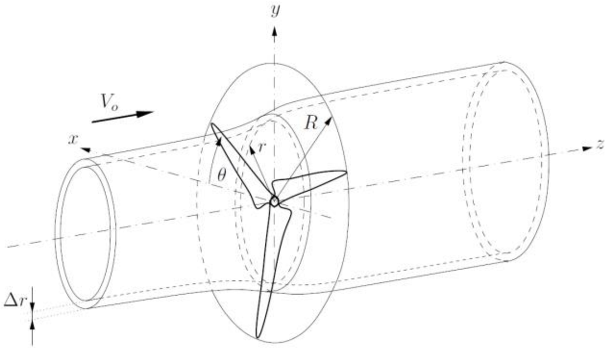

Figure 2. Streamtube through a three bladed rotor. (adapted from Mikkelsen [2003])

Although the BEM theory allows for semi-analytical computation of aerodynamic forces on the rotor, according to Sorensen (2002) it does not consider realistic situations as dynamic inflow, yaw misalignment, tip loss and heavily loaded rotor. Further still, it provides no means to study aerodynamic interaction between multiple turbines that occurs in a wind farm. The "generalized actuator disk" approach proposed by Mikkelsen (2003) uses CFD and it does not have the limitations of the BEM methods. CFD simulations are generally an order of magnitude more complex and time consuming than a semi-analytical method such as the BEM. The actuator disk model however simplifies the CFD quite substantially by replacing the rotors with body forces. Generation of grid thus becomes much more straightforward and also the computation time is significantly reduced.

The actuator disk model (when applied to a single turbine) can be considered an extension of the BEM where the main difference is that the annular independence of the BEM model is replaced by solution of a full set of Navier-Stokes equation. Breakdown of the assumptions made in the generalized actuator disk theory is provided by Mikkelsen (2003).

The particular implementation of the actuator disk model used in the present work uses the 1-D momentum theory to calculate the blade forces with a Gaussian force distribution applied throughout the disk.

3. **Experimental methods**

3.1 Flow Model

Wind turbines are designed to run in essentially incompressible flow regime (maximum Mach number is at the tip which is typically < 0.25). Also, our interest is in overall, average performance of turbines and wind farms, therefore we are not interested in modeling time transients. The suitable governing fluid flow equations therefore are the steady, incompressible continuity (1) and Navier-Stokes (2) equations. An explicit equation for pressure is obtained by taking a divergence of (2) to get a pressure Poisson equation.

$$\nabla \cdot \mathbf{u} = 0, \tag{1}$$

$$\nabla \cdot (\mathbf{u}\mathbf{u}) = -\frac{1}{\rho}\nabla \cdot p + \nabla \cdot (\nu \nabla \cdot \mathbf{u}) \tag{2}$$

In the above, ρ is the fluid density, p is pressure, and $\mathbf{u}$ is velocity. Reynolds's averaging of these equations gives additional unknowns (turbulence closure problem), which are obtained using a turbulence model. A k-e turbulence model is used here. A solver for these equations is available in OpenFOAM and is called *simpleFOAM*.

3.2 Tutorial Case

The project was initiated by first learning the implementation of the actuator disk model in *simpleFOAM* through one of the tutorials provided. The tutorial is called "turbineSiting". In this tutorial, the flow over a terrain with one turbine (represented using the actuator disk model) is solved. The case was successfully simulated. The initial grid is shown in Figure 3. Figure 4 shows results from a sample calculation performed for this example case. Tecplot360 and Paraview software were used for visualization of results.

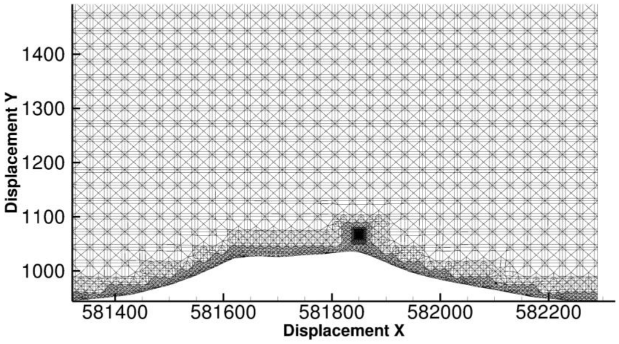

Figure 3. Cross-sectional view of the grid used for the "turbineSiting" example simulation.

In the tutorial, the freestream velocity is along the x direction and is set to 10 m/s at the inlet boundary. The bottom of the domain is a random topography with no-slip condition, while the top and sides are set as slip walls. The pressure, P is relative pressure and is normalized with the fluid density as

$$\mathrm{P} = \frac{P^*}{\rho},$$

where P is normalized pressure, P^* is relative pressure, and ρ is fluid density.

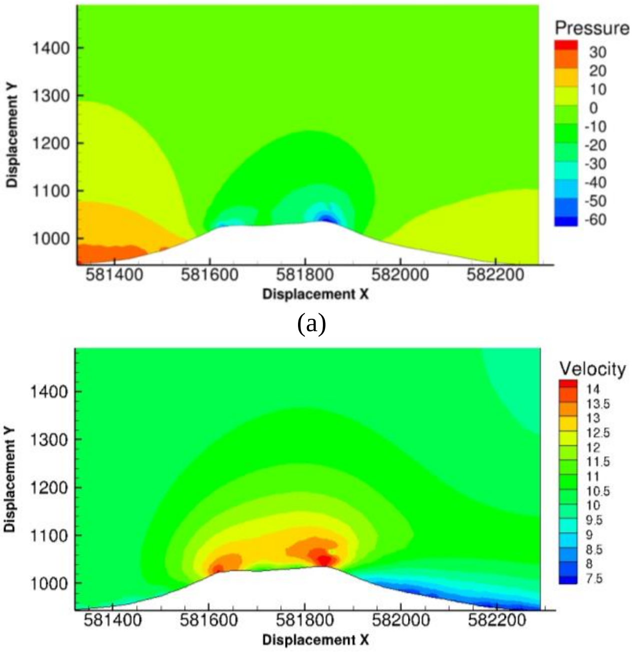

(a)

(b)

Figure 4. Contours from the solution of the example problem: (a) pressure, (b) velocity, U.

The "turbineSiting" tutorial proved to be a good learning exercise in how to setup simpleFOAM wind turbine simulations, modify number and placement of turbines, modify turbine force coefficients (mimic changing turbine operation), and to post-process and visualize results.

3.3 Comparisons against 1-D Momentum Theory

Validation of the actuator disk model implementation in OpenFOAM was sought to gain more confidence in the simulation results. The canonical problem of uniform flow through a turbine is used for validation. Since the flow is axisymmetric, only a small sector (2-D) of the rotor is simulated using periodic boundary conditions (in cylindrical frame).

The problem is setup as follows (see Fig. 5). Z=0 is the axis of symmetry. The inlet plane is at X=-3.0 here and the rotor (actuator disk) is placed at X=0. The rotor tip radius is 1 unit. The inlet velocity is set to 1 along the X direction. All the simulations used in this report are performed in non-dimensional variables: length is scaled by tip radius, and velocity is scaled by inlet flow velocity. The disk area is π and the blade (disk) tip speed is the tip speed ratio of the turbine; the tip speed ratio is not used in the 1-D model. Figures 5 and 6 plot the contours of velocity and pressure with streamlines. The simulation results look reasonable. Decrease of the wind speed in the wake region and expansion of streamtube as the flow goes through the turbine are as expected. It is also possible to notice an increase of pressure just upstream of the turbine followed by a sudden drop when the flow goes though the actuator disc. Figure 7 is a line plot of pressure and velocity along the X axis, drawn at Z=0.5 m. Quantitative validation with analytical solution is deferred to a later section.

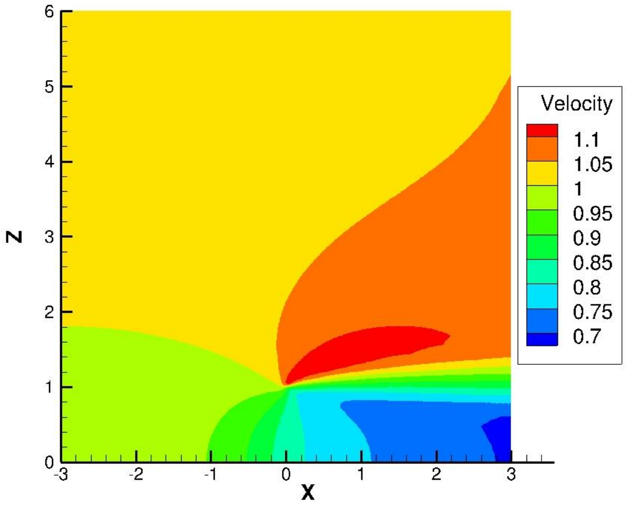

Figure 5. Velocity contours for the canonical validation problem.

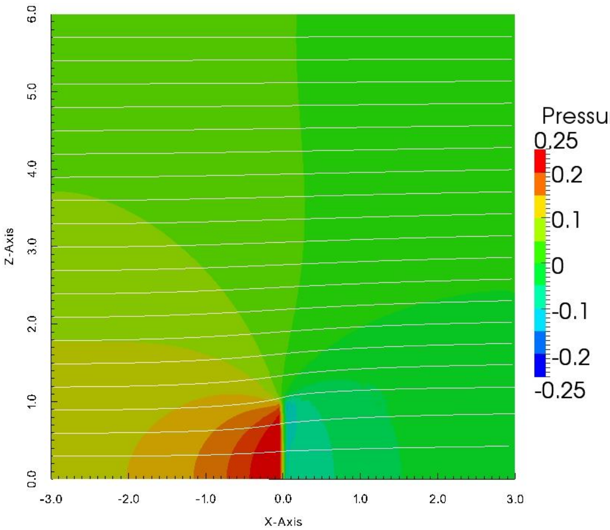

Figure 6. Streamlines and pressure contours for the canonical validation problem.

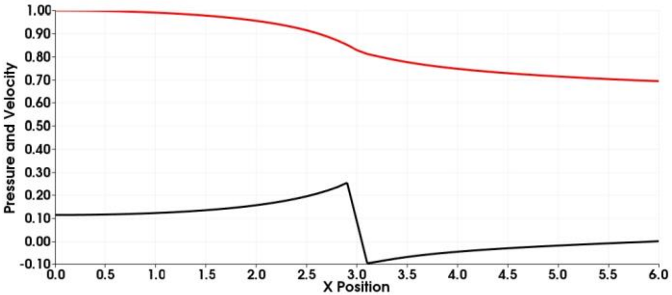

Figure 7. Velocity [m/s] and pressure [m^2/s^2] along X axis.

A 3D single-turbine simulation was then performed. Non-dimensional variables using a GE-1.5SLE turbine as reference was used, which has 77-meter diameter and its hub height is 80 m. The depth of the disk is taken to be 0.04 length units. Note that the source terms are applied as body forces on a finite *volume*, therefore the disk has a finite thickness. The domain was taken to be a square with edge length of 20 units and 10 unit height. The turbine is located in the center of the domain. The grid was built in order to have higher resolution on the wake area to be able to capture gradients expected there and it is gradually coarsened away from this region to save computation time. The *snappyHexMesh* pre-processing utility is used to create a highly refined mesh in the region where body forces are applied. Figure 8 shows the initial grid.

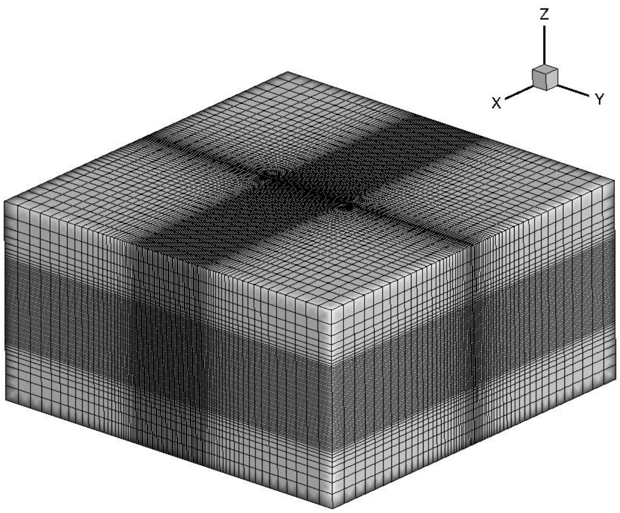

Figure 8. Initial grid.

The simulation was carried out for optimal operation (maximum power extraction) of the turbine, i.e., at the *Betz limit*. In this optimal condition, the axial induction “a” is set to 1/3, C_T=8/9 and C_P=16/27.

The faces on the plane YZ define the inlet and outlet faces of the domain. On the inlet face the initial velocity is prescribed while on the outlet the velocity is determined from the internal velocity. All other boundaries were set as *ZeroGradient*.

4. Results

4.1 Single-Turbine Simulations

The results from the single-turbine simulation described above are shown in Figs. 9 and 10, which plot the pressure and velocity contours along with the streamlines. Although the simulation is 3-dimensional, the figures show cross-sections in the Y=0 plane (that goes through the center of the turbine).

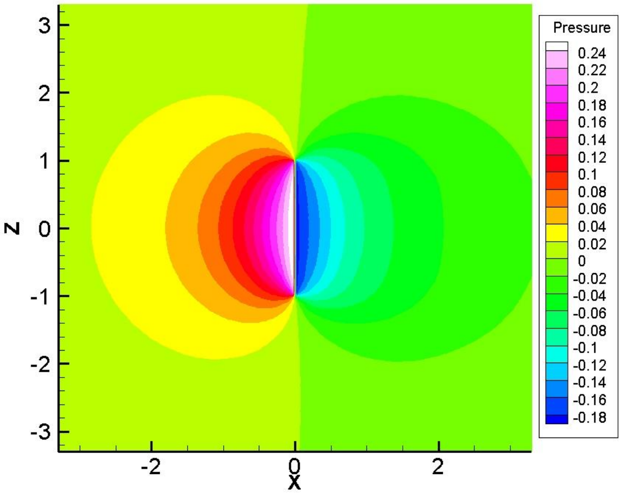

Figure 9. Pressure

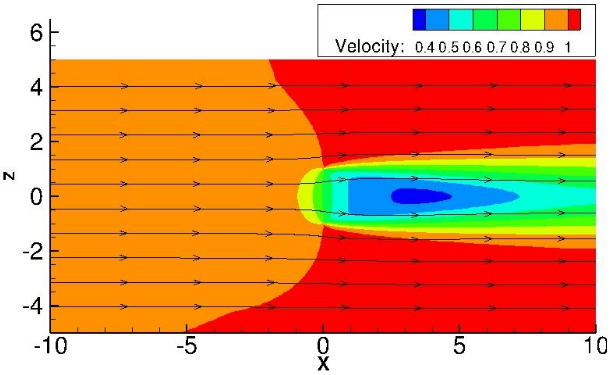

Figure 10. Streamlines and velocity

To verify the solver’s accuracy, a reverse calculation was applied. With the upstream and downstream pressure and velocity over the rotor it is possible to calculate the axial induction and the thrust coefficient.

Paraview has one utility that allows user to extract data from the cells over a line. Here these lines are plotted on upstream and downstream side of the disk and the data exported to an excel table. Those values were numerically integrated over the disk to determinate the thrust, power coefficient, and induction.

Five simulations were performed with different prescribed values of axial induction (thrust coefficient is analytic function of axial induction). Prescribed axial induction factor was varied from 0.1 to 0.5. Figure 11 shows a comparison of results from the simulation versus analytical solution. The calculated thrust coefficient was found to be lower value than expected for all simulations. Also, as the axial induction approaches 0.5, all values tend to deviate more. This part is expected as the 1-D theory breaks down at a=0.5.

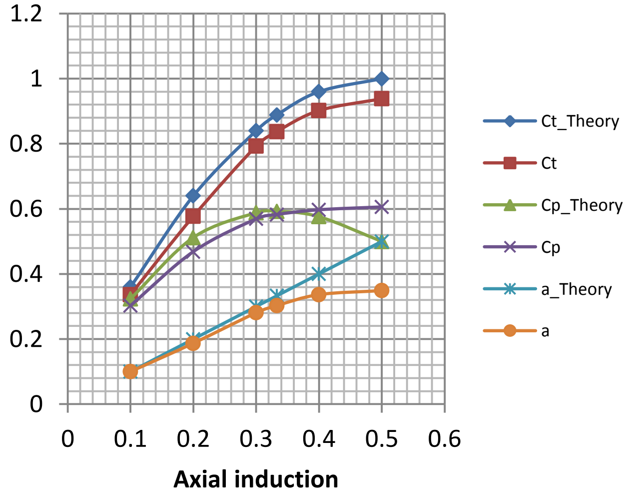

Figure 11. Expected and calculated C_T, C_P and “a” values.

The analytical thrust coefficient differs from the calculated one by a factor of 1.06. This problem with the model was investigated by other members of the research group and an improved model was developed. To compensate for this difference (in prescribed versus observed thrust force), the solver was modified and a "correction" factor was introduced in the prescribed force. Results from simulation with this arbitrary correction factor are shown in Figure 12. The calculated thrust force now matches the expected value, and the match in theoretical and calculated induction and power coefficient is good for a < 0.35. The deviation that still occurs when the axial induction approaches 0.5 is expected. Above these values the flow suffers a change on the regime towards an unsteady wake region. At such situation the 1-D momentum theory should be replaced by the Glauert empirical correlation.

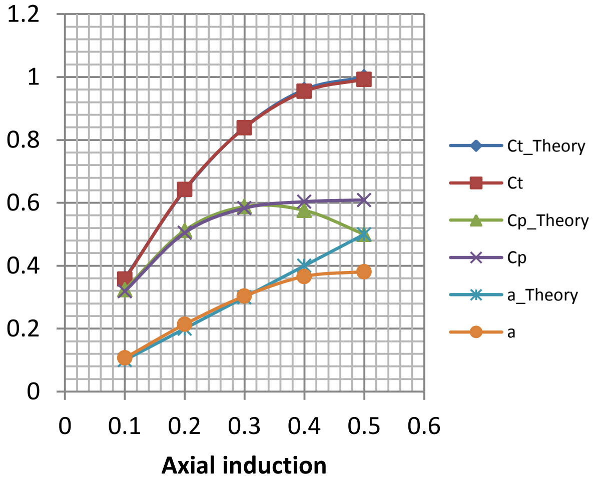

Figure 12. Expected and calculated C_T, C_P and "a" values after correction of the solver.

Investigation by other members of the research group showed that a Gaussian distribution along the flow direction for the applied force improved the accuracy of the solver and the arbitrary force multiplication factor was no longer needed. The solver was modified to incorporate this change.

Figure 13 adapted from Mikkelsen (2003) shows on the darker lines the expected values for thrust and power coefficient given the axial induction factor for the actuator disk model, while the thin lines represents Glauert's empirical correlation. Figure 14 shows a similar validation using the improved solver (without any correction factors). A very good agreement is now observed between predicted and analytical force and power coefficients. This completed the validation of the solver. Other members of the research group have performed further validation studies against BEM theory results for a realistic turbine using a higher fidelity actuator disk model. Those are not included here for brevity.

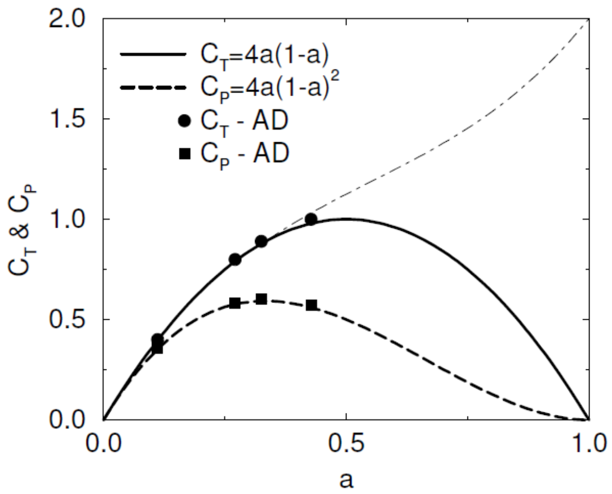

Figure 13.Thrust and power coefficients. (adapted from Mikkelsen [2003])

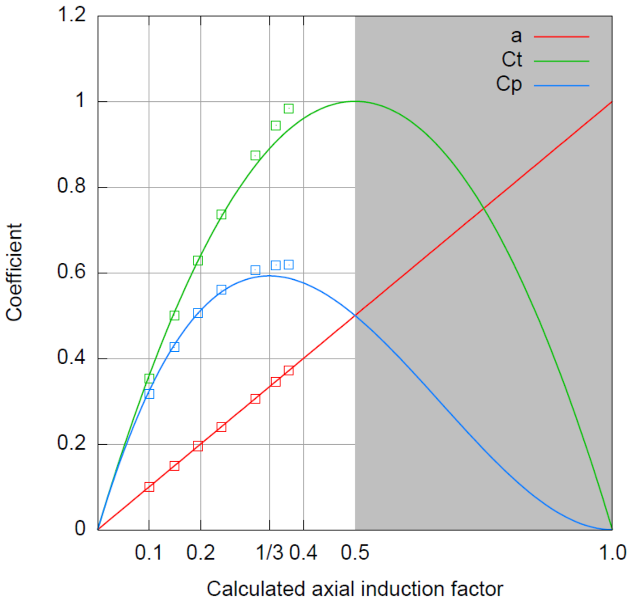

Figure 14. Thrust and power coefficients using Gaussian distribution of force over the actuator disk.

4.2 Effect of Planetary Boundary Layer

The validation cases considered until now are idealizations (of uniform inflow) that are removed from reality. In practice, the wind turbines operate in a planetary boundary layer (non-uniform spatial flow). This approximation is relaxed in the next simulation where a logarithmic wind profile is prescribed at the inlet to represent the planetary boundary layer. The flow is normalized so as to have a unit velocity at hub height. Time unsteadiness is still ignored.

The ground is treated as viscous wall with no-slip boundary conditions, while the sides and top of the domain were set as *ZeroGradient*. Figure 15 is a sketch of the wind profile and the location of the turbine.

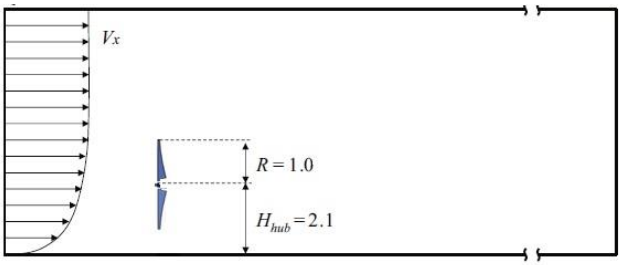

Figure 15. Inflow velocity profile. Profile is scaled to have unit velocity at hub height.

Figure 16 shows the velocity through a lateral cut of the actuator disk. Notice that the incident velocity is no longer the same along the Z axis. An analysis of the flow angle in relation to X was made. Incident velocity has a 0 degree angle, positive values means a clockwise convergence and negative values counterclockwise. Results are shown on Figure 17 and 18 at hub height and closet to the ground. Here the lower plane is not exactly on the ground because since the non-slip condition, the velocity at this surface would be zero and no conclusion could be drawn from it.

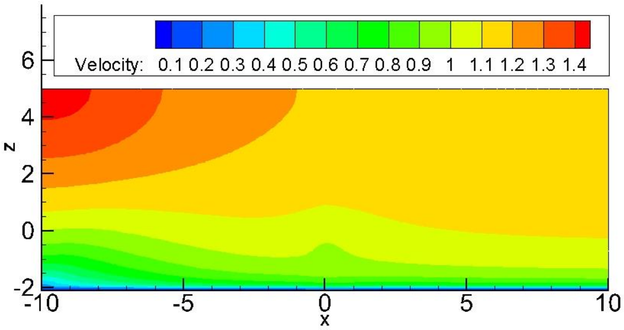

Figure 16. Velocity variation with height.

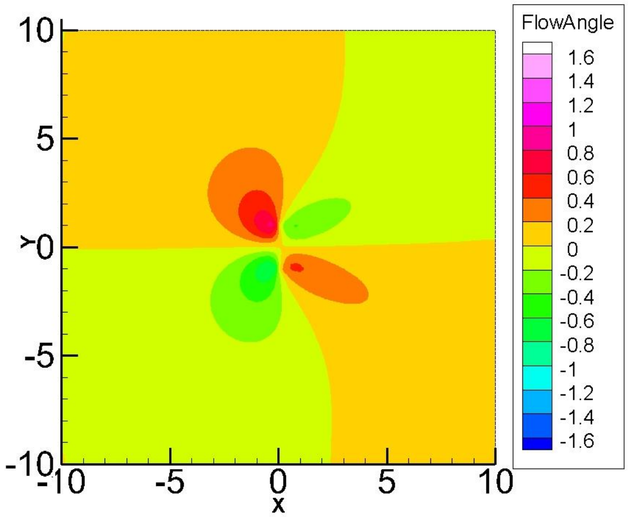

Figure 17. Angle change at hub high.

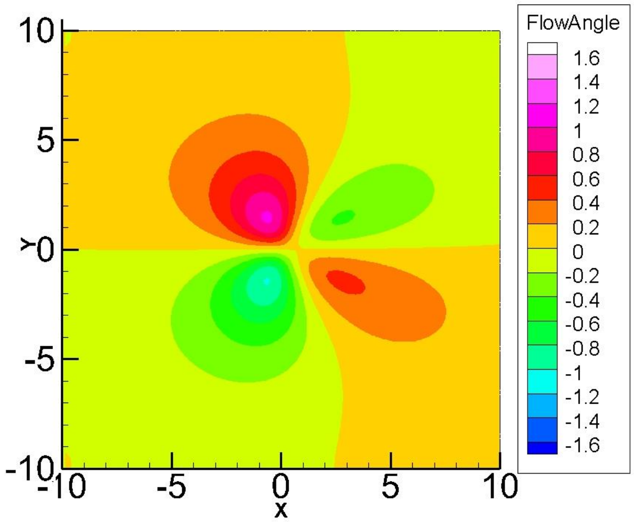

Figure 18. Angle change near the ground.

4.3 Wind Farm Simulations

The single-turbine simulations with and without planetary boundary layer provided sufficient confidence to undertake wind farm simulations. The phenomenon of interest that we want to be able to predict is referred to as “flow convergence” in wind farms. Flow coming an angle to a turbine array has been observed in experiments (by Prof. Eugene Takle’s group) to align itself to the direction of the array. Figure A.1 in the appendix shows sample measurement results. It is a graph with collected data from field measurements taken from CROP/Wind-energy experiment conducted at the Iowa State University. Those measurements *show flow deviation of around ten degrees* in neutral atmospheric stability condition. It is hypothesized that the reason for this flow convergence is the pressure gradient along the direction of turbine array that is set up by the turbines (see Fig. 19).

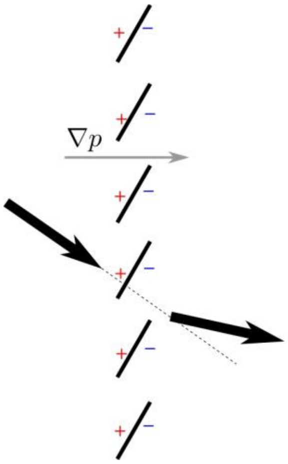

Figure 19. A schematic of a row of turbines showing the pressure gradient and consequent change in flow direction.

If the pressure gradient is in fact responsible for the phenomenon of flow convergence, then we expect to at least qualitatively see this behavior in inviscid (idealized) simulations. In these simulations, the planetary boundary layer effect is ignored and the ground is modeled as a smooth, slip wall. We do not expect to match the magnitude of flow turning with the inviscid simulation since the dynamic pressure (ρu^2) will be very different between the viscous and inviscid simulations.

Two different wind farm layouts were simulated. In the first configuration, the nearest turbines are separated by 10 rotor radius in each direction, and are located 2.1 units above the ground. The turbines are set to operate at the *Betz* limit (axial induction for the actuator disks set at 1/3). The grid was designed to avoid very large jumps in grid density, which is known to cause numerical errors.

Ground Modeled as a Slip Wall

The first case consists of three rows of turbines, five in the first and last rows and four in the middle row. The domain is 50x70x7 and the inlet flow velocity is at 45 degree angle from the X and Y axes. The bottom boundary of the domain is treated as a slip wall here while inlet flow boundary condition is imposed at the top boundary.

Figure 20 visualizes the grid and the domain boundaries. Velocity contours are plotted in Fig. 21. To measure the average change of flow direction, integration over lines of the velocity on the boundary planes and closer to the turbines were made. For each case the contours are plotted on the same two planes: (1) at the hub height, and (2) on the ground. On both cases the angle change is observed to be higher at the hub height. When analyzing 3 units upstream of the first array and 3 units downstream of last one, the angle deviation showed to be 0.95 degrees on hub height and 0.81 on the ground. More detailed data can be seen in Table A.2 on the appendix.

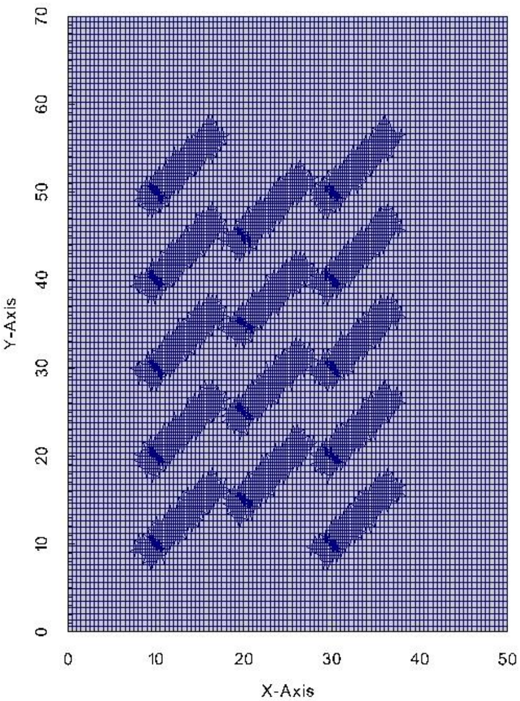

Figure 20. Cross-sectional view of the grid used for simulating wind farm configuration 1.

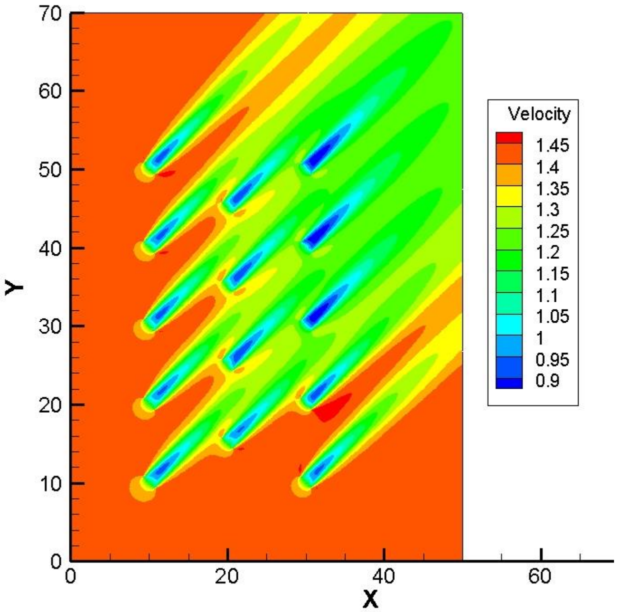

Figure 21. Velocity contours on the plane at hub height.

Since the variation of velocity in the Z direction is relatively small, it was neglected and the angles calculated only over the plane. Better visualization of the wind direction can be seen in Figs. 22 and 23 where contours of velocity angle (relative to the X axis) are plotted, at hub height and on the ground respectively. Notice that largest angle deviation occurs closer to the turbines.

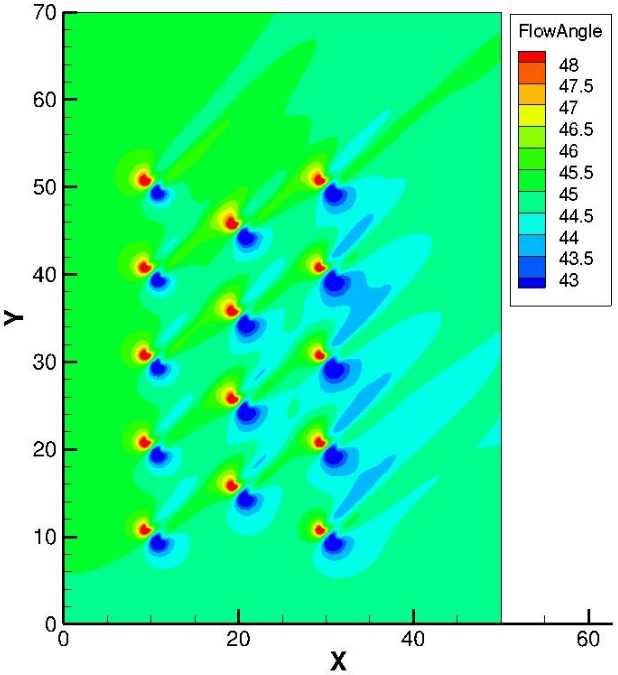

Figure 22. Hub high velocity angle in relation to X axis

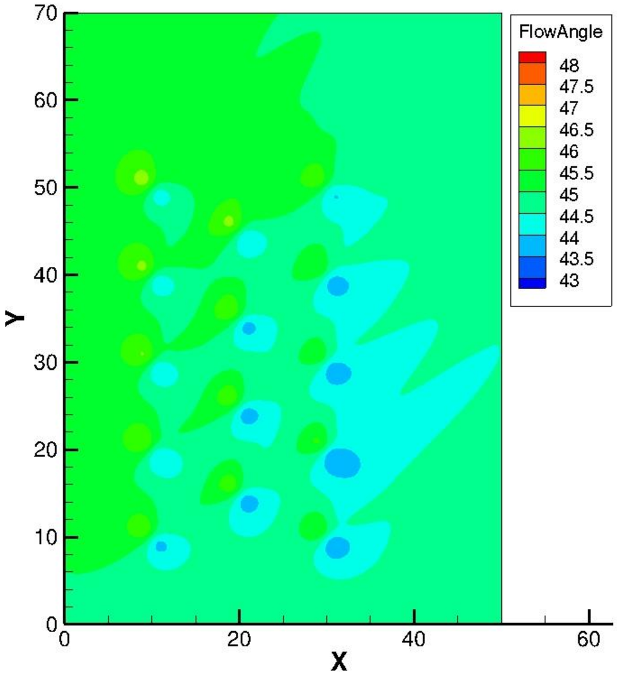

Figure 23. Ground velocity angle in relation to X axis

In the second configuration, an infinite array of turbines was simulated by using periodic (cyclic) boundary condition on the domain boundaries in the Y direction. Velocity and other parameters were kept the same as for the first configuration. Since the domain is treated as a repeated geometry, only three turbines were set on strategic position ensuring the distance between arrays and turbines was the same as in the first configuration. The *cyclic* boundary condition significantly reduces the simulation and the post-processing time. Figures 24, 25 and 26 show the velocity, flow angle at the hub height and on the ground respectively. Angle deviation (flow convergence) of about 2 degrees can be seen in these inviscid simulations.

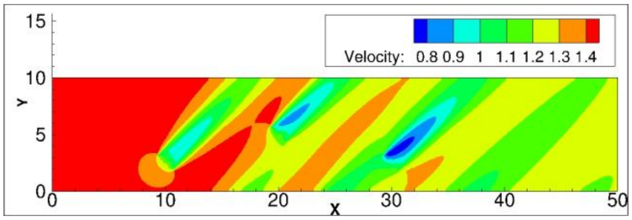

Figure 24. Velocity magnitude contours at hub height.

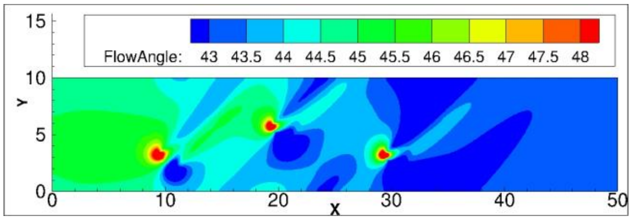

Figure 25. Flow angle (relative to X axis) at hub height.

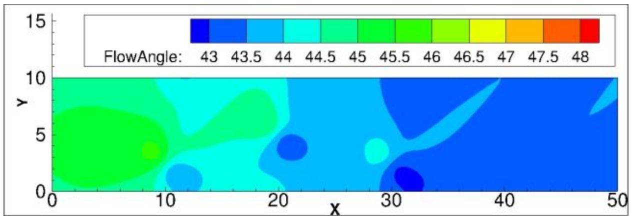

Figure 26. Flow angle (relative to X axis) on the ground.

Ground Modeled as Viscous Wall

The second wind farm configuration with periodic boundaries was used to then include the effect of planetary boundary layer. The results from this simulation are very preliminary and need more investigation.

The flow angle at the hub height and close to the ground can be seen on Figure 27 and 28. Much larger variation in flow angle is seen with the viscous simulations (in agreement with our expectations) however there are some open questions with these simulations that need more investigation. For example the sharp change in flow angle close to the inlet boundary does not appear physical.

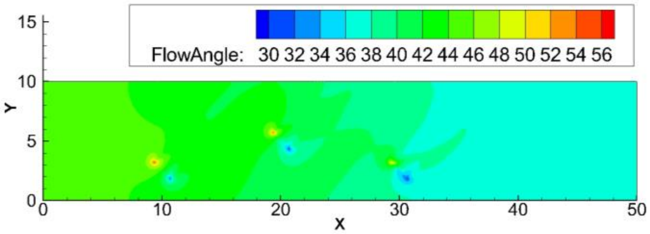

Figure 27. Contours of flow angle at hub height (viscous wall simulation).

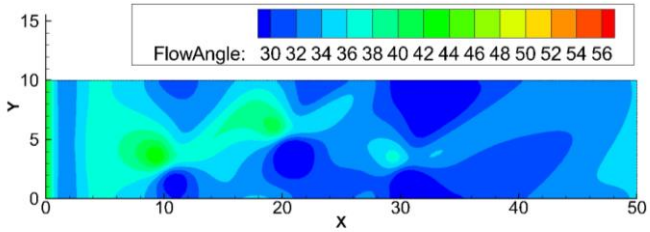

Figure 28. Contours of flow angle near the ground (viscous wall simulation).

5. Analysis and interpretation

Post processing software made it possible to visualize the flow convergence phenomenon in wind farms over the entire domain simulated. It is possible to conclude that an increase on the number of arrays increases the change on wind direction. On the first wind farm simulation the turbine located at X=10, Y=50 is not affected by any other one and the change on flow direction is limited to a closer area around and downstream of it. On the other hand, the second simulation using a *cyclic* domain shows that the flow direction downstream the turbines are in a different direction than the incident one, confirming the idea that the convergence phenomenon is directed related to the number of arrays.

For both cases the planes though the turbine hub show a bigger change of the flow direction near them. This phenomenon is easily explained by the streamtube expansion. On the ground plane the angle changes are smoother and more equally distributed. Once the viscous effects caused by change of velocity profile are not considered on these simulations, it is possible to affirm that the pressure gradient which drives the convergence phenomenon is caused by the turbines.

The last two cases where the atmospheric boundary layer is considered on the simulations, the convergence phenomenon is more significant. Reduced velocity near the ground due to the boundary layer implies reduced dynamic pressure. The static pressure difference due to turbine arrays therefore causes a much larger change in velocity direction when the mean velocity is reduced near the ground. The numerical results show an average change of eight degrees in the flow direction after the third turbine array. While there is no attempt made here to do a one-to-one validation against measured experimental data. However as a sanity check the magnitude of flow angle deviation measured in experiments is reported here.
In neutral atmospheric stability condition, flow deviation of 10 degrees has been observed by Prof. Takle's group (see Fig. A.1).

6. Conclusions

A generalized actuator disk model in OpenFOAM to simulate wind turbine aerodynamics was exercised, improved and validated. The validation was performed with analytical solutions for the 1-D momentum theory method. Slight inaccuracy in the model was removed by incorporated a Gaussian distribution of forces in the actuator disk volume.

Two wind farm configurations were simulated using the actuator disk model to investigate the phenomenon of flow convergence. Uniform inflow (at 45 degree angle to turbine array alignment) was first considered with a slip wall approximation made for the ground. The results qualitatively showed the flow turning but the magnitude of angle deviation was much smaller (2 degrees compared to 10 degrees observed in measurements).

Viscous simulations with prescribed inlet velocity profile (logarithmic law) were then conducted. The simulations currently exhibit some behavior that needs further investigation but the results look very promising. The simulations predict flow angle change of around 8 degrees near the ground. The "agreement" with data appears quite fortuitous since no attempt was made to simulate the same wind farm configuration as in the experiments. Also the simulations completely neglect the effects of buoyancy effects and atmospheric stability conditions.

Acknowledgements

Support for this research was provided by the Brazil Science Without Borders undergraduate program. CAPES Foundation, Ministry of Education of Brazil, Brasilia -DF. Partial support also was provided by the National Science Foundation under the State of Iowa EPSCoR Grant 1101284.

References

OpenFOAM Foundation, 2013: OpenFOAM User Guide, version 2.2.0. Accessed February 2013 [Available online at http://www.openfoam.org/docs/]

Mikkelsen, R, 2003: "Actuator disk methods applied to wind turbines," Ph.D. dissertation. Department of mechanical engineering, Technical University of Denmark

Churchfield, M. J., P.J. Moriarty, G. Vijayakumar and J.G. Brasseur, 2010: "Wind energy-related atmospheric boundary layer large-eddy simulation using OpenFOAM," Conference Paper NREL/CP-500-48905, *19th Symposium on Boundary Layers and Turbulence.* Amer. Meteor. Soc. Keystone, CO.

Sorensen, J. N., and W. Z. Shen, 2002: "Numerical modeling of wind turbine wakes," *Journal of Fluids Engineering*, Vol.124 pages393-399.

B. Sanderse, "Aerodynamics of wind tubines wakes," Energy research center of the netherland.

Appendices

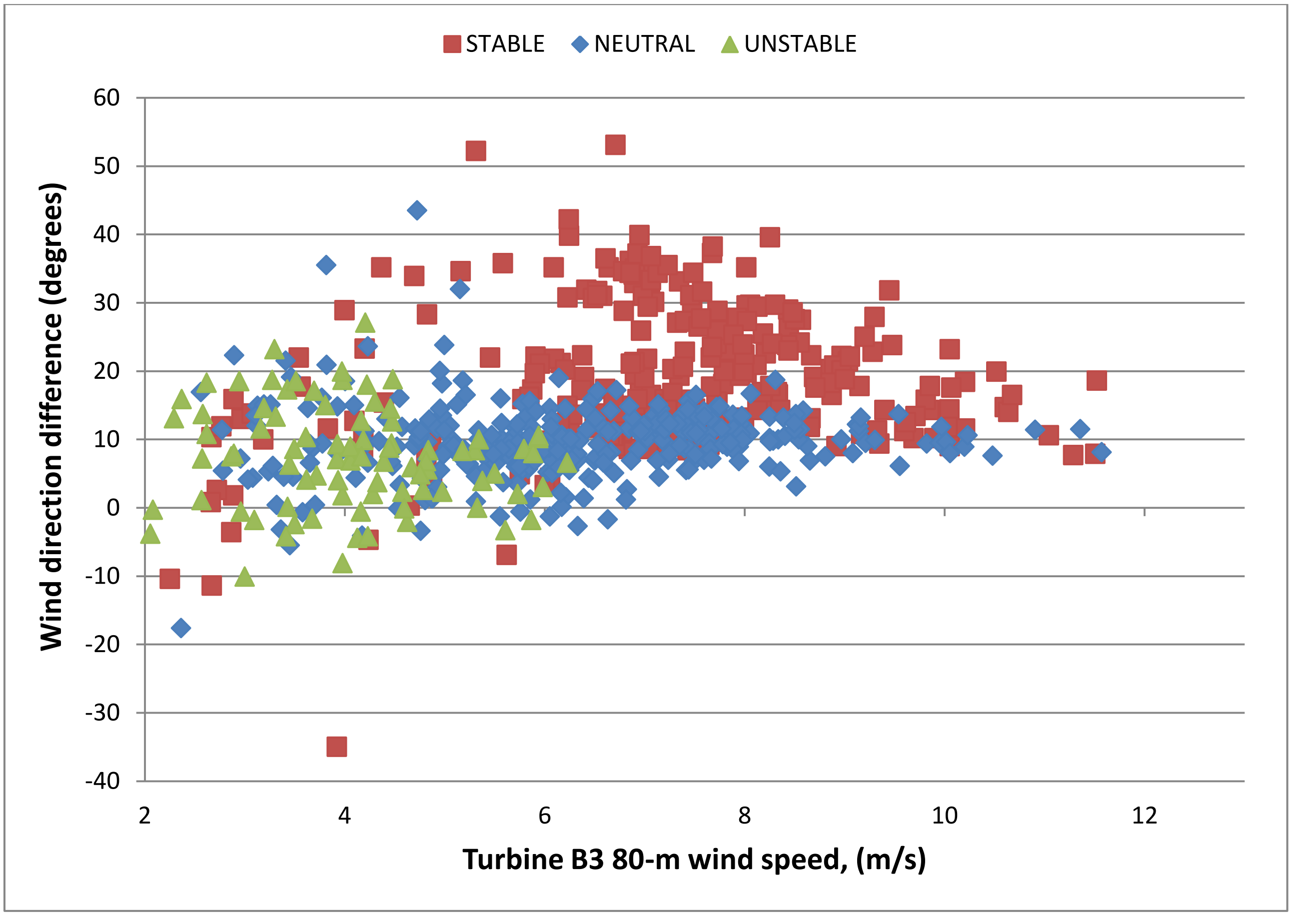

Figure. A.1

	Velocity X	Velocity Y	Velocity X	Velocity Y
	inlet and outlet planes.		3 units away from the turbine.	
Hub High			Hub High	
Inlet Velocity	0.999978	1.00125	0.99785	1.00772
Outlet Velocity	0.938115	0.929208	0.884431	0.863943
Angle[Degrees]	0.309712535		0.953346463	
Ground			Ground	
Inlet Velocity	0.999967	1.00125	0.997995	1.00772
Outlet Velocity	1.02641	1.01546	1.0409	1.02171
Angle[Degrees]	0.343991806		0.81085473	

Figure A.2

Meteorological Phenomena Impacting Spatial Consistency of Ramp Events in Wind Farms

IAN JAMES CAMERLIN
Wind Energy Science Engineering and Policy REU, Iowa State University, Ames, Iowa
Mentors: William Gallus, Jr., Dan Rajewski and Renee A. Walton

Abstract

Previous research has shown the importance of improving overall wind resource predictions and predictions for what are known as wind ramp events. Wind ramp events are sudden increases or decreases in power output from a wind turbine. In this research they are more precisely defined as a minimum change of ±3 m/s between 6 m/s and 12 m/s in wind speed over a 4-h period. Earlier investigations could not identify some of the causes of wind ramp events and found that in the wind farm not all turbines have ramps of the same type as other turbines currently ramping. Nacelle data from 13 wind turbines in central Iowa, along with archived meteorological data (including surface pressure, 850-mb height wind speeds and directions, and thermal stability, etc.) were used in the present study to identify and classify ramp events and attribute meteorological causes to the ramps. Statistical analysis was used determine the conditions most likely for these ramp events to occur. It was found that ramps only occurred 0.17% of the time in unstable atmospheric conditions. We also that some conditions lead to uniformity of wind ramps (all turbines ramping in the wind farm) or the variability of the wind ramps (some turbines ramping while others are not or having opposite ramps within the same wind farm). Lower pressure, higher wind speeds at 850mb, and neutral atmospheric stability suggest more uniformity in ramps. Night time conditions for net heat radiation and more stable atmospheres seemed to correlate with more variability in wind ramping. Future research should refine some classifications made in this research and ultimately improve wind forecasting models.

1. Introduction

Wind energy is one of the fastest growing forms of energy generation in the United States and around the world. A Department of Energy report states that from 2004 to 2009 wind was the second largest resource added to the electric grid in the U.S. behind natural gas. It also projects, going at that pace, about 35% of the increase in electric generation in the U.S. will be met by wind energy by 2035 (Wiser & Bolinger, 2011). Even with this boom in the industry, wind energy is a technology still considered in its infancy and is not without its problems.

One problem with this energy source is its inherent variability. This variability puts wind energy in the category of variable renewable resources (VRE's) (Marquis et al., 2011). This variability can lead to unexpected rapid increases and decreases in power output, which are known as wind ramp events. These ramp events can cause power curtailment for wind farms, where the wind farms are producing electricity but are not allowed to put it on the grid due to transmission overloads. This is very costly to utilities (Marquis et al., 2011). Formally a ramp event is defined as a minimum change of ±3 m/s between 6 m/s and 12 m/s in wind speed over a 4 hour period (Gallus & Deppe, 2012). A positive change is labeled a "ramp up" and a negative change a "ramp down." The range between 6 m/s and 12 m/s is usually when a wind turbine has its most variable power output. Quick changes in this range can cause problems in the power grid (Ferrier et al., 2010). Better predictions on when wind ramps may occur will be beneficial to utilities. A Department of Energy report (Schreck et al., 2008), states that a 1% error in wind estimation could lead to about $12,000,000 loss over the lifetime of a 100-MW wind plant.

Previous research focused on when these ramp events occurred and different methods of predicting their characteristics. An unresolved outcome of previous research was that in the same wind farm some turbines ramp up while some turbines do not or even ramp down (Showers Walton 2012). The purpose of this research was to search for a meteorological explanation for these important events.

2. Literature review

The prospects for future development in wind energy were made realistic in the Department of Energy's 2008 report "20% Wind by 2030." To make wind a more reliable resource, DOE stated that improved short-term wind forecasting would be needed. Improvements will allow operators to make better unit commitment decisions and warn operators of possible extreme weather (DOE, 2008).

Marquis et al. (2011) discuss the economic impact of errors in forecasting wind. Using current forecasting there has been over estimations as great as 11,000 MW in one hour. Studies show that with 20% wind power generation, a perfect wind forecasting system could save, nationally, $2.1 billion every year (Marquis et al., 2011).

Marquis et al. also mentions difficulty of predicting wind ramp events. Wind ramps can be caused by many different meteorological phenomena at all levels of the atmosphere (Marquis et al., 2011). Francis (2008) also writes about the difficulty for wind ramp forecasting. Pressure gradients, thunderstorm cells, and boundary layer processes are all possible causes for these ramp events. The article concludes that further research needs to be done to fully understand ramps events (Francis, 2008).

Deppe et al. (2012) used different weather models to forecast wind speeds at turbine height (80m). They used planetary boundary layer (PBL) schemes, and found there was a significant underestimation by each scheme. However, by using an ensemble of schemes, predictions could be improved. This research group also examined predictions of ramp events which they described as a “change in wind power of 50% or more in total capacity in either four or two hours or less. This was approximated using a typical wind turbine power curve such that any wind speed increase or decrease of more than 3m/s within the 6-12m/s (where power varies greatly) in 4 h or less would be considered a ramp” (Deppe et al., 2012). The group found that most planetary boundary layer schemes in the prediction models did not lead to well-predicted predict ramp events. The most successful scheme, the MYNN 2.5, only predicted ramp up events 50% of the time. For most schemes the mean average error (MAE) was larger than the calculated biases, meaning that the schemes predicted times for the ramps were off from the times the ramps actually happened (Deppe et al., 2012).

Deppe et al. (2012) found only 17% of ramp events could be accounted for by the passage of frontal system. 32% occurred during the presence of a low level jet (LLJ) and 10% were likely related to the growth of the planetary boundary layer (PBL). 24% of ramps could not be explained by obvious causes (Deppe et al., 2012).

Similar research was done by Showers Walton et al. (2012) with similar difficulties in predicting ramp events. Using a persistence forecast model, it was found that the hit rate (HR) was never over 45%, and the false alarm rate (FAR) was between 50% and 70%. The HR was defined as the total number of correct forecasts divided by the total number of events observed, while the FAR was defined as total number of false alarms divided by the total number of events forecast. She also observed that in one wind farm not all turbines were ramping at the same time or having the same type of ramp (Showers Walton et al., 2012).

Solving the lingering questions is the point of this research. I am seeking physical explanations for the 24% of ramps the Deppe et al. research failed to explain, and I am also exploring why turbines in the same wind farm can be ramping in opposite directions.

3. Experimental methods

Data were taken from the nacelles of thirteen wind turbines in a wind farm close to central Iowa. The thirteen turbines included two lines of turbines, eight from the “B” line, which was at the south edge of the wind farm and five from the “A” line which was one line north of the “B” line (see Figure 1). Data were taken every ten minutes between 29 June, and 16 August, 2011. The nacelle data included, for each individual turbine, the wind speed (in m/s) at turbine height, yaw angle of the turbine (in degrees), ambient temperature (in ºC), and active power (in KW).

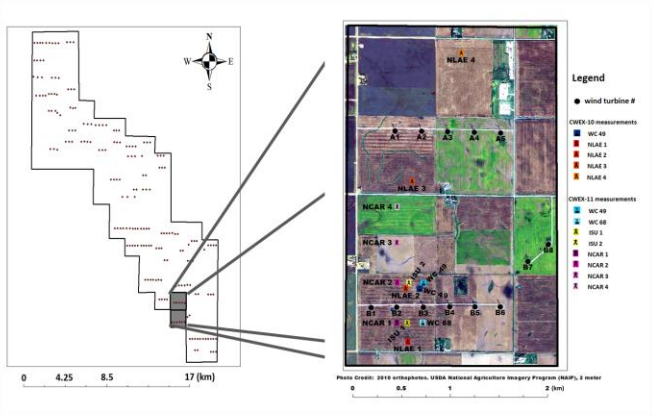

Figure 1. Turbine Locations (photo from Rajewski et al., 2013)

The nacelle data were first searched to identify wind ramp events. The definition of a wind ramp has been debated, and different studies have used different definitions of a wind ramp event (Ferrier et al., 2010). For this study the definition of a ±3 m/s change in wind speed between 6m/s and 12 m/s over a 4-h period was used. This is the same as Deppe et al. (2012), Gallus and Deppe (2012), and Showers Walton (2012). Wind ramps identified by Showers Walton et al. (2012) were used as examples for identifying ramps in this research.

Ramp events were divided into 5 categories: all the turbines simultaneously ramping up (“All up”), all the turbines ramping down (“All down”), a mix of up ramps and no ramps (“Some-up”), a mix of down ramps and no ramps (“Some-Down”), or a mix of up, down and no ramps (“Mixed”).

Meteorological data were collected for the start times of these group ramp events from the Iowa State University's Mtarchive data server [Available online at http://mtarchive.geol.iastate.edu/]. Measurements examined included: surface pressure (mb), 850-mb height wind speed (knots) and wind direction (degrees). Looking at archive maps the ramps were also classified by the turbines' relative position to synoptic features: east of high or low pressure ("Ahead"), west of high or low ("Behind"), or in the middle of high or low ("Mid"). Ramps were classified by the curvature of the isobars near the turbines, cyclonic, anti-cyclonic, or straight which implies the likelihood of ascent and descent. For some dates where group ramps occurred, not all of the meteorological data could be obtained due to missing information in the archive.

Atmospheric stability and net radiation readings were acquired from research done by Rajewski et al. (2013). Net radiation data were taken from a net radiometer placed 4.5 m above the ground on a tower just south of the "B" line (labeled ISU-1 on fig. 1). Stability was measured using the z/L_0 calculation, where z is the height of the sonic anemometer (also located 4.5m above the ground at the ISU-1 site) and L_0 is the Obukhov length:

$$L_0 = \frac{-\theta_v u_*^3}{kg(w'\theta'_v)_s}$$

Where θ_v is the virtual potential temperature, u_* is the friction velocity, k is von Karman's constant (0.4), and $(w'\theta'_v)_s$ represents the surface moist sensible heat flux (Rajewski et al., 2013).

Group ramp events were classified in ranges of stability following the convention laid out in Rajewski et al. (2013), and ranges in net radiation by guidelines laid out upon personal conversation with Dan Rajewski. Atmospheric stability was separated into 3 categories: stable atmosphere ($z/L_0 > 0.05$), neutral atmosphere ($-0.05 < z/L_0 < 0.05$), and unstable atmosphere ($z/L_0 < -0.05$). Net radiation, R, was divided into three categories: day time conditions ($R > 300$ W/m^2), transition period ($0 < R < 300$ W/m^2), and night time conditions ($R < 0$ W/m^2).

4. Results

Table 1 shows the number of ramps identified in the different group ramp classifications. There were 127 groups identified overall. Figure two shows the percentages of each classification. "Some-up" is the largest class, with 40%.

Table 1: Breakdown of group ramp events into five different classifications

	Totals:
All_Up	12
All_Dwn	15
Some_Up	51
Some_Down	42
Mixed	7
Overall	127

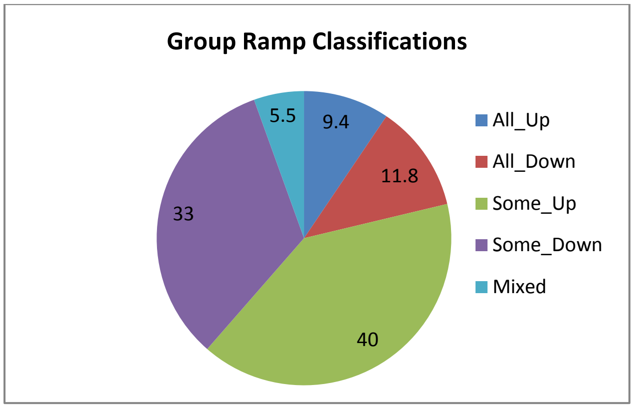

Figure 2: Pie-chart showing percentages of group ramps events in the different five classifications

For each ramp classification an average pressure (mb), average wind speed (knots), average wind direction (degrees), and average stability were identified. Table 2 shows each of the group ramp classifications along with the respective averages. Figures 3-6 show a comparison between the classifications and respective averages. The error bars represent the standard deviation from the average. It should be noted that out of the 127 group ramp events, 1 was missing meteorological data and was not included in the averages or following sections.

Table 2: Measurement averages for each group ramp classification

	Avg. Pressure	Avg. Wind Speed	Avg. Wind Dir.	Avg. Stability
All_Up	1009.8	23.8	232.1	0.1
All_Dwn	1008.6	25	242.5	0.03
Some_Up	1011.4	14.7	219.4	0.4
Some_Down	1011.6	16.3	221.6	0.1
Mixed	1011	20	226.4	0.02

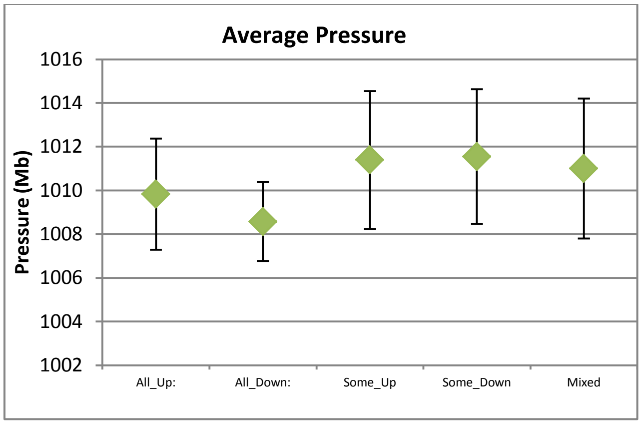

Figure 3: Comparison of average pressures for each of the different group ramp classifications

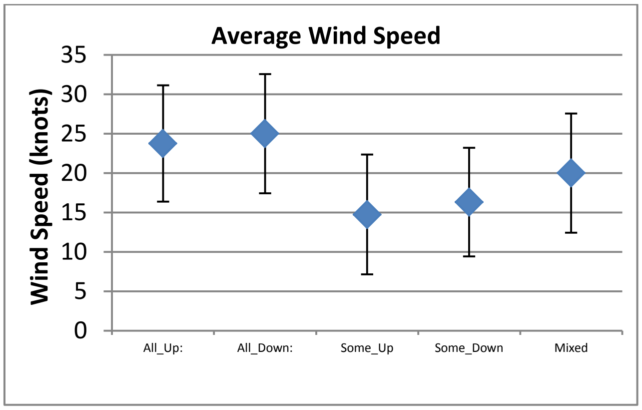

Figure 4: Comparison of average wind speed for each of the different group ramp classifications

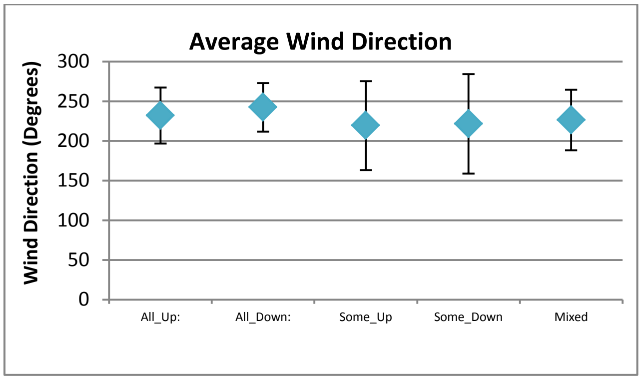

Figure 5: Comparison of average wind direction for each of the different group ramp classifications

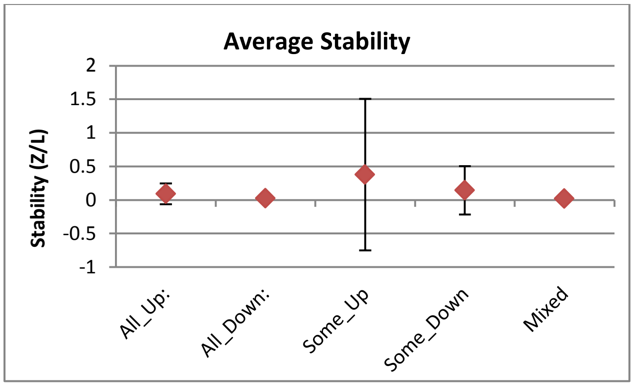

Figure 6: Comparison of average stability for each of the different group ramp classifications

Table 3 shows the number of times group ramps were classified in their position in respect to major synoptic features. As some occurrences could be put in two different categories, weighting was used such that if a turbine was said to be Ahead of a Low and Behind a High, 0.5 was put into each category. Table 4 shows the percentages of each occurrence. Figure 7 is a pie chart pictorially showing these percentages.

Table 3: Group ramp events classified by their position to synoptic features

	Ahead Low	Behind Low	Mid Low	Ahead High	Behind High	Mid High
All_Up	4.5	1	1	0.5	4	1
All_Dwn	4.5	1	2	1	3.5	2
Some_Up	23.5	2	3	2.5	14	6
Some_Down	17	3	4	2.5	10.5	5
Mixed	2.5	0	1	0	2.5	1
Total	52	7	11	6.5	34.5	15

Table 4: Percentages of group ramp events by their position to synoptic features

	% Ahead Low	% Behind Low	% Mid Low	% Ahead High	% Behind High	% Mid High
All_Up	37.5	8.3	8.3	4.2	33.3	8.3
All_Dwn	32.1	7.1	14.3	7.1	25	14.3
Some_Up	46.1	3.9	5.9	4.9	27.5	11.8
Some_Down	40.5	7.1	9.5	6	25	11.9
Mixed	35.7	0	14.3	0	35.7	14.3
Total	41.2	5.6	8.7	5.2	27.4	11.9

Curvature of isobars fluctuated more substantially with group ramp classification than with synoptic feature position. Table 5 shows the number of occurrences of each of the different curvature classifications. Table 6 shows the respective percentages for each category.

Table 5: Group ramp events organized by curvature of isobars

	Cyclonic	Anticy	Straight
All_Up	4	5	3
All_Dwn	6	3	5
Some_Up	11	27	13
Some_Down	10	16	16
Mixed	5	2	0

Table 6: Percentages of ramps occurring with certain curvature of isobars

	% Cyclonic	% Anticy	% Straight
All_Up	33.3	41.7	25
All_Dwn	42.9	21.4	35.7
Some_Up	21.6	52.9	25.5
Some_Down	23.8	38.1	38.1
Mixed	71.4	28.6	0
Total	28.57	42.06	29.37

Stability measurements were not available for every time of nacelle data, so some group ramps were not included when being analyzed with stability. One hundred thirteen group ramps were examined with stability. When divided into categories of stability it was found that 41 were classified as ramps occurring in "stable" atmosphere, 72 classified as being in a "neutral" atmosphere, which means 0 group ramps started in an "unstable" atmosphere. Since 0 ramps started in unstable atmospheric conditions, we examined if any part of any ramp occurred at all in unstable conditions. The stability data were on the same time step as the nacelle data. It was found that periods said to be part of a ramp occurred 38.6% of the time in stable atmospheric conditions, 61% of the time in neutral atmospheric conditions, and only 0.17% of the time in unstable conditions.

This same type of analysis was done for the different ramp group classes. Table 8 shows the percentages of stability for each of the group ramp classifications.

Table 7: Percentages of ramps occurring in different stability classifications

	% Unstable	% Neutral	% Stable
All_Up	0.29	73.1	26.6
All_Dwn	0.0	79.7	20.3
Some_Up	0.4	49	50.6
Some_Down	0.0	54	46
Mixed	0.0	100	0.0

Net Radiation was looked at in the same way as atmospheric stability, since it was also ten minute data. Without considering group ramp classification it was found that 58% of the time ramps were occurring during night time conditions, 23% were occurring during transitions period conditions, 19% of ramps occurred during day time conditions.

Each group ramp classification was also analyzed. Table 9 depicts the percentages of each net radiation classification for each group ramp class.

Table 8: Percentages of ramps occurring in different net radiation ranges

	% Night	% Trasition	% Day
All_Up	37.4	33.7	28.8
All_Dwn	44.5	28.4	27.1
Some_Up	74.6	13.8	11.6
Some_Down	61.1	24.4	14.5
Mixed	67.9	32.1	0.0

5. Analysis and interpretation

When wind turbines were ramping, most of the time, several but not all wind turbines were ramping up. This is seen as our biggest ramp class, the "Some-up" classification, which makes up 40% of all ramp groups. This is followed by 33% being identified as "Some-Down" (see Figure 2). This suggests that when ramps happen in a wind farm there is usually variability and not all turbines will ramp.

It is useful to notice the smallest classification is when turbines are simultaneously ramping up, down and not ramping. These events suggest that while there could very be small scale phenomena affecting wind ramps in a wind farm, most of the ramps (about 94.5%) occur over a large enough scale that opposing ramps within the same farm will not happen.

Turbine position relative to large scale weather systems does not seem to provide much insight into the differences between the "All" ramps and the "Some" classifications. All classifications seem to have roughly the same probability of being in one of the synoptic classifications ("Ahead of Low" etc.). For example the difference between the spread of the data without regard for classification (“Total Ramp”) and the spread for the “Some-down” classification is never more than ±3% in any of the sections. For most classifications there is not a ±10% difference from looking at the data as a whole. The only chart that appears to look different is “Mixed” classification where 0% occurred “Ahead of a High” and “Behind a Low.” It is difficult to tell whether the 0% in both classifications is just caused by the small data set in the “Mixed” category. Moreover, the position of the farm to synoptic systems seems to give no real clue as to the reason there is this variability in turbine ramping. However, in the broad picture, ramp events seem to occur when turbines lay ahead of low pressure systems and behind high pressure systems. Both of these scenarios typically support warm air advection which by itself usually favors upward motion and reduced mixing near the surface. This could be significant if it is not simply reflecting a tendency for turbines to lay in that position relative to those pressure systems more often.

Data on isobar curvature does not clarify the picture. The “Total Ramp” data (group ramps as a whole) looks almost identical to the probability in the “All Up” classification, with a maximum variation of about ±4% of each classification of curvature (See in Appendix A Figures A7 & A8). The picture does get a bit more clear for other categories, but not in any really discernible pattern. “All Down” sees more cyclonic curvature (42%), and when comparing it to the “Some-down” classification they do not seem to compare (23.8%), so it cannot be confidently said that cyclonic curvature would be more related to down ramps. Reasons for variability of ramps are equally as muddled. The even 38.1% split between Anti-cyclonic and Straight curvature in the “Some-down” classification does not mesh with the “Some-up” classification, which is more dominated by Cyclonic curvature (42.9%). The fact that this classification can be such a subjective measurement and that there appears no concise pattern in the data makes any conclusion difficult.

Analysis of the averages of the group ramp classifications does provide a better picture. However, no clear signals are seen comparing average stability and average wind direction does not seem to provide too much information. The average stability seems fairly clustered. The “Some-up” class seems to have the highest stability, looking at the standard deviation; it seems to be affected by some outliers. The argument could be made that the higher stability leads to more variance in which turbines ramp, because the “Some-up” and “Some-down” classifications’ average stability is higher than either “All” classes. However this is contradicted by the “Mixed” average which is lower than the “All” classes (See Figure 6).

The average wind speed does shed some light on what might cause the variability. Higher wind speed at the 850-mb height does seem to suggest more uniform ramping (see Figure 4). The “All” classifications have higher average wind speeds then the variable ramp classifications. This could be explained by the idea that with strong winds at higher levels there is more uniformity through the atmosphere and at turbine height the effects of the higher winds can be seen. However, lower wind speeds higher up in the atmosphere might suggest less potential for higher speeds to affect turbines, and maybe small scale phenomena would play a bigger role in getting ramps.

Average pressure also shows a reasonable distinction between the “All” classes and the “Some” and “Mixed” classes. The “All” classes have a lower average pressure than the variable classifications (see Figure 3). This suggests that more uniform ramping occurs during lower pressures and more variable ramping in a wind farm would happen at higher pressures. This result suggest more organized weather systems, accompanied by lower pressure, result in more uniform ramping.

Net radiation provides another key to the difference between uniform ramps and variable ramps in a wind farm. When looking at Table 4, for the “All” categories we see a fairly close three way split between the net radiation classifications. This is clearly not true when analyzing the “Some” and “Mixed” categories. “Some-up” classification had over 70% of its ramps happening at night and the both “Some-down” and “Mixed” classifications had over 60% of their ramps at night. “Mixed” had 0% happen during day-time. These data suggest that more variable ramping occurs during night.

Stability seems to play an important factor for wind ramping, both in just the existence of ramps and also the variability. Before considering the results of the stability data it is important to know what the climatology of stability looks like (was that atmosphere mostly neutral? etc.). It was found that for the time period over which the nacelle data were taken the atmosphere was 43% neutral, 18% unstable and 39% stable. It would follow that if ramps had no real correlation to stability that overall we would see ramps occurring at around those percentages. This is not what the data show. It is seen that only 0.17% of ramps happened in an unstable atmosphere. We also considered what happened as neutral reading tended toward unstable ($-0.05 < z/L_0 < 0$). It was found that only about 25% of ramps that occurred with values in the negative neutral range occurred with reading less -0.025, suggesting strongly that as neutral readings tend toward unstable there is a considerable drop off. Unstable atmospheres are not conducive to ramp events.

Stability was also considered in relation to look into variability of the ramp events. In Table 3, the “All” classes are dominated (over 70%) by a neutral atmosphere, while in the “Some” classifications there is a more even 50-50 split, between neutral and stable. Here it suggests that neutral atmospheres might be better for uniform ramping and that more stable atmospheres lead to more variability.

6. Conclusions

Improved wind forecasting and wind ramp forecasting would improve the economics of wind energy (Marquis et al., 2011). Understanding and predicating wind ramp events is very complex and difficult (Francis 2008). Wind ramp events can have unknown causes (Deppe et al., 2012) and are variable around the wind farm (Showers Walton et al., 2012). Patterns in meteorological data were used to attempt to solve these questions. As a result the following conclusions were made: Location to different weather systems and isobar curvature do not affect ramp variability. On average lower pressures are related to uniform ramping along with higher wind speeds at the 850mb heights. Night time conditions from net radiation usually correlate to higher variability in ramps. Unstable atmospheric conditions produce barely any ramp events, and even as the atmosphere tends toward being unstable (negatively neutral) the occurrence of ramp events drop off. When looking at variability it appears that neutral conditions relate more directly to uniform ramping across a wind farm. Stable conditions are seen more frequently in the variable cases.

Opportunity for future research is apparent, both in terms of looking deeper into the data acquired in this research and utilizing the conclusions made in this research. The classifications of "Some-up" and "Some-Down" could be further broken down into subcategories relating to how many turbines were actually ramping up or down. For example, in this research if all but one turbine was ramping it was still considered a "Some" ramp. If the "Some" classifications was better defined one could compare the cases where all turbines were ramping to cases where "most" turbines were ramping. Organizing the data in wind direction may reveal further difference between the uniform and variable categories. Wind direction was skimmed over in this research and when sifting through the data looked like a dead end but quantifying this "dead end" could be beneficial. In all areas, looking at more data would be beneficial. More data would hopefully give a better look into the "Mixed" category. It would help confirm that unstable conditions did not allow for ramps.

The future research of most importance is trying to utilize these results into wind forecasting models. Hopefully, these results will improve wind prediction accuracy.

Acknowledgements

Support for this research was provided by a National Science Foundation Research Experience for Undergraduates site program in Wind Energy Science Engineering and Policy (WESEP) grant number EEC-1063048 at Iowa State University.

References

Department of Energy, 2008: 20% wind energy by 2030. Energy Efficiency and Renewable Energy Rep. DOE/GO-102008-2567, 1-2.

Deppe, Adam J., William A. Gallus, Eugene S. Takle, 2013: A WRF Ensemble for Improved Wind Speed Forecasts at Turbine Height. *Wea. Forecasting*, **28**, 212–228. [Available online at http://journals.ametsoc.org/doi/abs/10.1175/WAF-D-11-00112.1]

Ferreira, C., J. Gama, L. Matias, A. Botterud, and J. Wang, 2010: A survey on wind power ramp forecasting. *Argonne National Laboratory. ANL/DIS*

Francis, N., 2008: Predicting sudden changes in wind power generation. *North American Windpower*. **5**, 58-60.

Gallus, W. A. Jr., and A. J. Deppe, 2012: Wind ramp events at an Iowa wind farm: A climatology and evaluation of WRF ensemble forecast skill. *Unpublished manuscript*, Department of Geological and Atmospheric Sciences, Iowa State University , Ames, IA.

Iowa State University, cited 2012: Mtarchive data server. [Available online at http://mtarchive.geol.iastate.edu/.]

Marquis, M., J. Wilczak, M. Alhstrom , J. Sharp, A. Stern, J. C. Smith, and S. Calvert, 2011: Forecasting the wind to reach significant penetration levels of wind energy. *Bull. Amer. Meteor. Soc.*, **92**(9), 1159–1171. [Available online at http://journals.ametsoc.org/doi/pdf/10.1175/2011BAMS3033.1]

Rajewski, D., E. Takle, J. Lundquist, S. Oncley, J. Prueger, T. Horst, M. Rhodes, R. Pfeiffer, J. Hatfield, K. Spoth, & R. Doorenbos, 2013: Crop wind energy experiment (CWEX): Observations of surface-layer, boundary layer, and mesoscale interactions with a wind farm. *Bull. Amer. Meteor. Soc.*, **94**(5), 655-672. [Available online at http://journals.ametsoc.org/doi/abs/10.1175/BAMS-D-11-00240.1]

Schreck, S, J. Lundquist, and W. Shaw, 2008: U.S. Department of Energy Workshop Report - Research needs for wind resource characterization. NREL Rep. TP-500-43521, 81-82.

Showers Walton, R., W. Gallus Jr., and E. S. Takle, 2012: Analysis of ramp events and two-day WRF wind forecast accuracy at 80 m. *Proc. Wind Energy Science, Engineering, and Policy National Science Foundation Research Experiences for Undergraduates Symposium*, Ames, IA, NSF and Iowa State University, 3/1-3/11. [Available online at http://www.meteor.iastate.edu/windresearch/resources/Binder1.pdf].

Wiser, R., and M. Bolinger, 2011: 2010 wind technologies market report. , *U.S. Department of Energy, Energy Efficency & Renewable Energy*. [Available online at http://www.windpoweringamerica.gov/pdfs/2010_annual_wind_market_report.pdf]

Appendix A

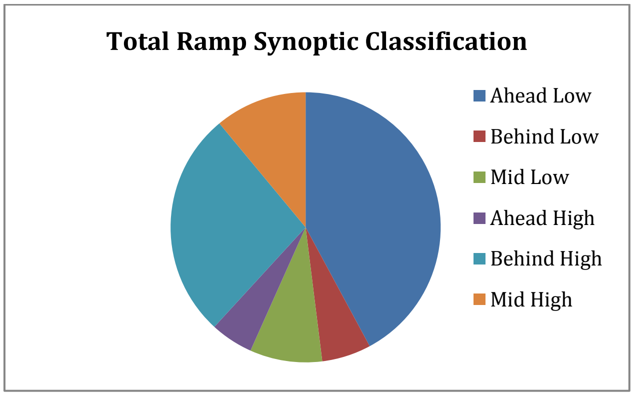

Figure A1: Pie-chart depicting the percentages of all ramp groups in their position to synoptic features.

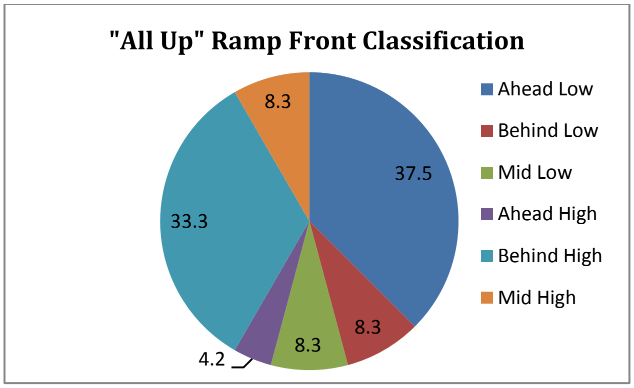

Figure A2: Chart showing percentages of group ramps in the "All Up" classification with their relative position to synoptic features

Figure 7

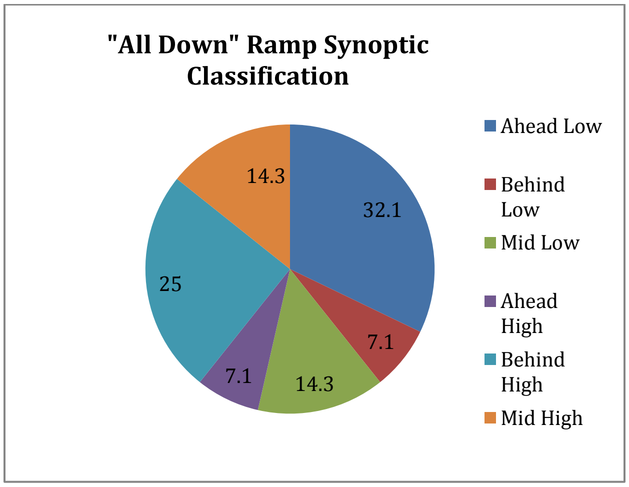

Figure A3: Chart showing percentages of group ramps in the "All Down" classification with their relative position to synoptic features

Figure 8

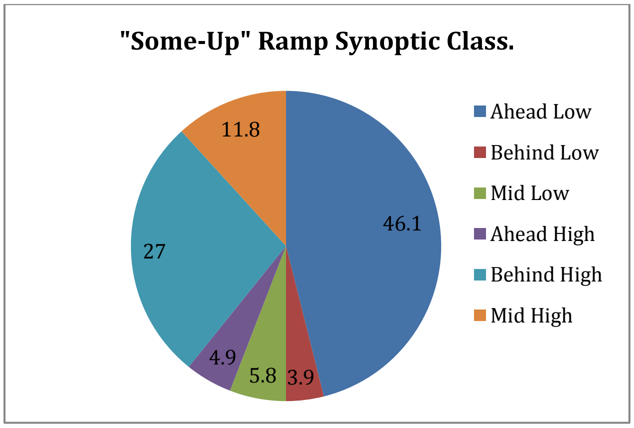

Figure A4: Chart showing percentages of group ramps in the "Some-Up" classification with their relative position to synoptic features

Figure 9

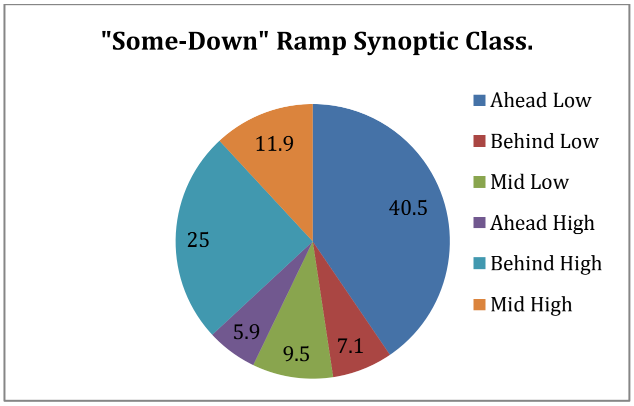

Figure A5: Chart showing percentages of group ramps in the "Some-Down" classification with their relative position to synoptic features

Figure 10

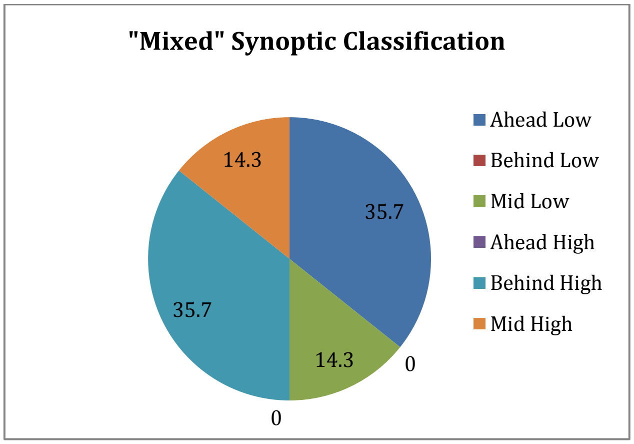

Figure A6: Chart showing percentages of group ramps in the "Mixed" classification with their relative position to synoptic features

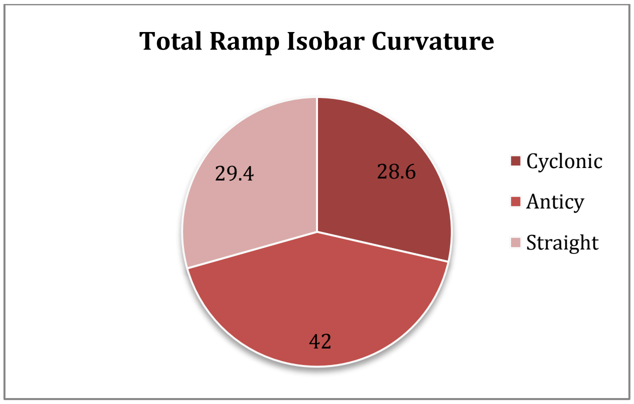

Figure A7: Chart showing percentages of all ramps for each isobar curvature classification

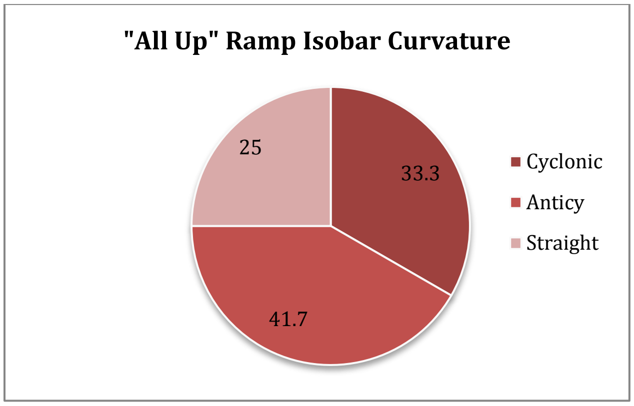

Figure A8: Chart showing percentages of ramps in the "All Up" classification for each isobar curvature classification

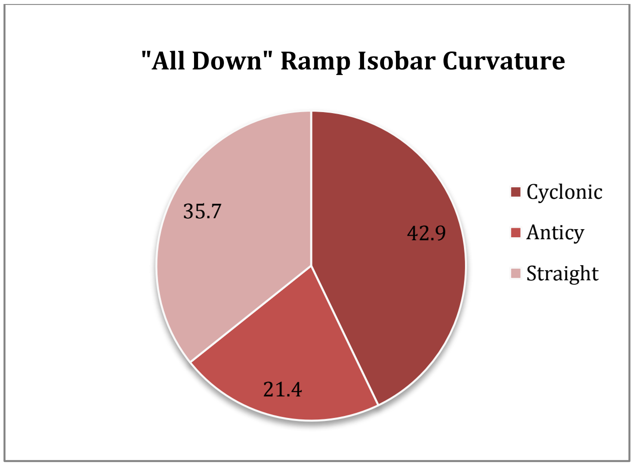

Figure A9: Chart showing percentages of ramps in the "All Down" classification for each isobar curvature classification

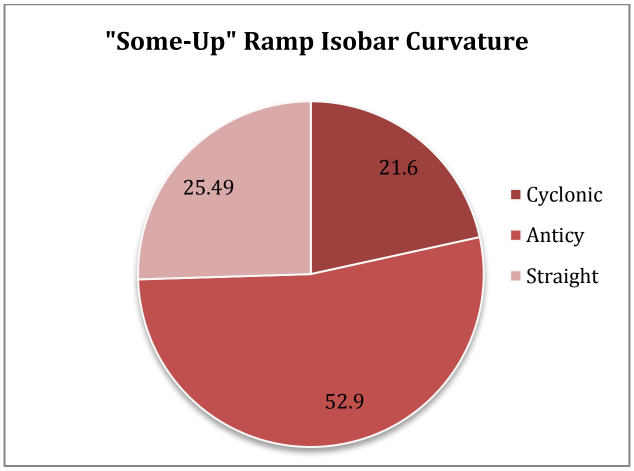

Figure A10: Chart showing percentages of ramps in the "Some-Up" classification for each isobar curvature classification

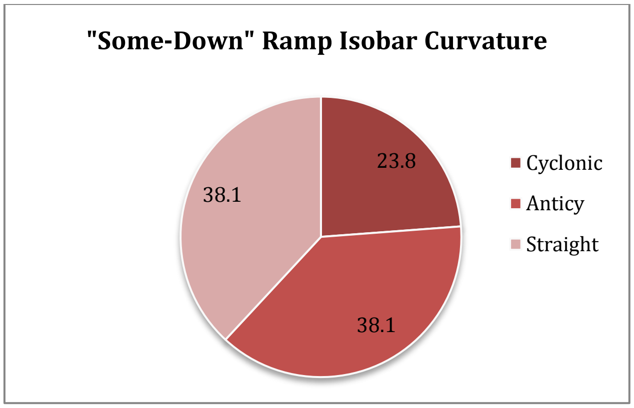

Figure A11: Chart showing percentages of ramps in the "Some-Down" classification for each isobar curvature classification

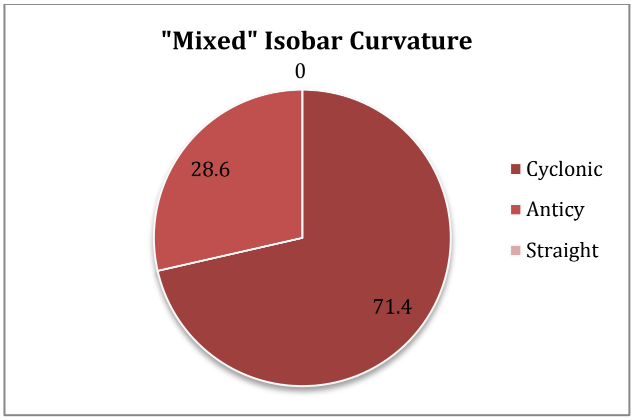

Figure A12: Chart showing percentages of ramps in the "Mixed" classification for each isobar curvature classification

Modeling Absolute Power Rate Limitation based Wind Control Strategy in Production Costing Program

MICHAEL F. HOWLAND
Wind Energy Science Engineering and Policy REU, Iowa State University, Ames, Iowa
Mentors: Dr. V. Krishnan, N. A. Brown and Dr. J. D. McCalley

Abstract

The electricity market is the system by which most Americans obtain power to their homes, industries, and any other locations. To ensure reliability of the system, energy markets are required by FERC to supply ancillary services to the grid, which for the purposes of this study, mostly include regulation, spinning, and non-spinning reserve requirements. With the DOE 20% by 2030 scenario for wind capacity, wind penetration is on the rise, and intermittency of this energy resource must be addressed since it hurts grid reliability and increases ancillary service needs. To cope with the rising variability, this study analyzed the effects of wind control, specifically absolute power rate limitation (ramping control). A ramping up constraint was modeled to cap the increase in energy output of a wind generation unit for a minute interval, simulated using the IEEE 24 bus system. Results of this study include a decrease in variability of the wind output a decrease in the ancillary service regulation requirement, a decrease in the production cost of the system, a decrease in decommitments of coal-fired power plants, and a decrease in cycling cost of the system. CAES storage was also considered in the model as a method to decrease the costs due to variability in wind generation. Storage reduced regulation requirements that were served by conventional generation units, and combined with the wing generation ramp rate constraint, vastly reduced the cost of regulation requirements and cycling costs of the system; dropping up to 22%.

1. Introduction

The electricity market is the system by which most Americans obtain power to their homes, industries and any other locations. At all times in the market there must be a balance between load demanded and output from the electricity generation units. Electricity demand is constantly varying, on large seasonal timescales and minute to minute as well. To handle this fluctuation, the Federal Energy Regulatory Commission (FERC) mandates a certain percentage of unused energy potential be dedicated to ancillary services.

Ancillary services, consisting of: regulation, load following, spinning reserve, non-spinning reserve, replacement, and supplemental reserve, are structured by Independent Systems Operators (ISO). Frequency regulation is the smallest unit of ancillary services and must respond and be available in 5-min time frame. The United States power grid has a base frequency of 60 Hz and the regulation requirements constantly change to account for possible load fluctuations. Reserves (spinning or non-spinning) are potential of direct energy production that is purchased in advance, day-ahead, by the ISO, in general, at a price roughly equal to the opportunity cost, which is roughly based on the locational marginal pricing (LMP) of the power demand, and can be activated in under 10-min time scales to be placed onto the grid to satisfy unexpected load variances. Aside from small scale increases or decreases in MW power output, ancillary services also must have on standby larger amounts of generation potential to handle any feasible blackout or brownout due to electrical, mechanical, or other failure. Ancillary services are the mechanism with which the governing body of the electricity market ensures efficiency and reliability (Ackerman, 2005)

On the supply side, variable wind creates uncertain generation profiles that affect the overall electricity market. Since wind has very low marginal cost compared to conventional generation units, wind turbines will generate electricity for the grid whenever wind availability and system conditions allow them to do so. Therefore, the conventional generators that have marginal costs for their electricity generation will only produce electricity for the grid when there is leftover demand exceeding that of the wind generation capabilities or is impossible to meet given system constraints. This creates the concept of Net Load (NL), which mathematically is the wind output subtracted from the demanded gross load of the electricity market (Ackerman, 2005). NL is subject to considerably more strong fluctuations than traditional load (load decreases but wind increase, high NL variability). Wind is one of the fastest growing energy resources, with about half of the total 5.1 GW of installed capacity being installed in 2009. President Obama announced an ambitious plan to have 80% of electricity demand satisfied by renewable energy sources by 2035 (MISO, 2012).

Power generation due to wind variability creates variable supply profiles, and the fluctuating demand profile requires peaking units to satisfy the rest of the net load demanded. These units also supply regulation services for the grid, as they can be dispatched on small timescales. This demand calls for traditional base and intermediate load units to supply the peak load at high cycle and ramping rates. Cycling consists of a larger variation in generational output, including on and off, load following, minimum run operation, and maximum run operation. The inevitable temperature and pressure fluctuations that accompany cycling cause damage to base and intermediate load power plants that have considerable startup times and considerably slower ramping rates than newer combustion turbine plants built for peaking. Older plants were not efficiently designed to handle accelerated ramping rates associated with rapid energy fluctuations throughout a 24-h cycle and operate at higher generation costs and higher GHG emission rates. Higher operation and maintenance costs will be incurred by these units, as well as increased rate of component failure, further straining the grid and the operational cost of the unit. Further, cycling has decreased the life span of these plants.

Midcontinent Independent Transmission System Operator (MISO) has led the way in the integration of wind energy resources. Dispatchable Intermittent Resources (DIR) was pioneered by MISO and allows for wind to be an active participant in the electricity market rather than acting as a price taker and pricing out the most expensive generation unit (MISO, 2012). It is possible, however, that DIR may increase generation variability, since before DIR, wind energy was taken after other units were dispatched and curtailed as necessary. Now wind is used by MISO based on an 8% error (schedule band) of the wind prediction models, which have a tendency to be inaccurate. Thus, wind energy variability has been furthered by its active role in the energy market. Beneficially, DIR opens the possibility for wind to be sold in the ancillary services market in the future.

This paper will use production-costing modeling to assess the possibility of controlling wind generation to decrease AS requirements and positively impact grid reliability and cost in an optimal solution.

2. Literature review

Optimal production costing models, which have incorporated unit commitment (UC) models in their programming, must take into account the thermal systems with uncertain demand. Demand not being met by the committed energy services is to be satisfied with ancillary services (Hobbs et al, 2001). Increasing generation from wind turbines will increase strain on traditional thermal combustion plants and will alter their feasible solutions and possibly make them suboptimal (Das, 2013).

2.1 Previous Models

Hargreaves and Hobbs proposed Stochastic Dynamic Programming based model (Hargreaves et al, 2012) that used small time steps to determine a least-cost solution to allocate which units were operating and at what level using a stochastic mixed-integer unit commitment model. This model considered variable wind penetration (WP), demand, commitment, and storage. This model allocated resources in a least-cost method which aimed to minimize operating costs of the energy market by deciding which units to turn on and off using decisions at time steps of 15 min, aiming to consider the ramping constraints of traditional thermal combustion power plants. The model did not consider the possibility to control wind power generation using specific techniques that will be discussed in this paper (Das, 2013).

Further, energy storage situations have been modeled with co-optimization techniques. Specifically, in the assessment of the UK energy Strbac et al. (2012) assess the ability of energy storage to provide ancillary services as well as energy. This model however did not properly account for energy storage as an interacting provider of reserves in the market. Energy storage as a price taker does not sufficiently model real applications of energy storage, which will intricately and intimately involve itself in the LMPs of the energy grid. This model, and others, use storage purchased day-ahead as based on planning models of the ISOs which will determine a price at which energy from storage will take rather than the energy storage being directly involved in real-time transactions of the grid and variable LMPs. The full potential of the energy storage cannot be met without its dynamic involvement in real-time market trading (Das, 2013).

Energy storage is modeled in Das's dissertation (Das, 2013) as a dynamic influence on the power grid. Modeled in a co-optimization to minimize the overall cost across both electricity and ancillary service components of the power system market, energy storage was used dynamically, influencing the LMPs, rather than just being a price taker as it was modeled previously (Strbac et al., 2012). The production costing model contained a Mixed Integer Linear Program (MILP) as the UC and also contained an economic dispatch model (ED), both of which were used to analyze the effectiveness of compressed air energy storage (CAES), flywheels, and batteries as potential energy and ancillary service providers. The Das dissertation reveals energy storage worked effectively to reduce production cost in the co-optimization between the two services and also reduced the overall LMPs of the system on a 48-h cycle due to its usefulness to charge with energy during low LMP time periods and discharge energy at time periods of higher LMPs.

From the model, it is shown that as CAES increases, production costs decrease. Additionally, when increased wind penetration (the percentage of total capacity from wind units) decreases production costs, the combination increased WP and increased CAES, the production cost drops moderately, by about $20,000 from an original production cost of $2.31M. Furthermore, CAES reduces GHG emissions of the system upon implementation. However, with higher wind penetration comes a higher need for regulation reserves due to increased variability in system generation, unless the wind is controlled to provide the regulation itself (Das, 2013). Storage has the potential to fill a large amount of that regulation, but wind control may be seen as a method to reduce the amount of regulation required by controlling the variability of wind energy resource. CAES was seen as ideal as a result of the four quadrant study (Das, 2013), which found that storage may provide up regulation with increasing discharging or decreasing charging and may provide down regulation by increasing charging or decreasing discharging. These quadrants allow for more control for the ISO to regulate the electricity market.

Cycling costs were modeled as a function of short-term operational heat rate impacts on conventional base load plants, which will increase their cost of cycling and therefore increase their cost of providing regulation services. While CAES was shown to decrease the cycling costs for conventional generation units and therefore overall system cycling costs, wind control may prove to reduce the need for regulation services and will thus, in tandem with power storage, reduce overall system production costs by reducing the needs for ancillary services.

The potential for CAES to make money on regulation services strongly depends upon wind penetration of the system. Investments will have to be carefully considered before being put in place as a result of this dependence on wind levels.

An issue raised by the Das dissertation is that under situations of lower wind penetration, CAES may charge its reserves with low cost fossil fuel conventional generation units. In this case, emissions for this energy will be double counted as low cost and dirtier (NO_x, SO_2, CO_2) fuel will be used to charge the CAES, and the CAES system has its own emissions associated with it. This situation, although economically optimal, is not optimal from an environmental or social standpoint (Das, 2012).

2.2 Wind Control

The various methods of wind energy control are absolute power limitation, delta control, balance control, and power rate limitation (see Figure 1). These different methods use a variety of individual turbine power reducers and automated shut offs as well as large-scale power downs of multiple wind turbines on a wind farm. All of the referenced methods are currently being employed at the Horns Rev Wind Farm (Kristofferson, 2005).

Absolute power limitation sets a maximum output for a particular turbine or farm based on the predicted demand and wind predictions for a given discrete time interval. Delta control uses the wind farm as frequency regulation and spinning reserves, in which the turbine or farm will operate below its rated maximum output at a given wind level at a given time but will have the ability to increase output, or ramp up, on a 5 to 10 min notice. Balance (power) control allows the turbine or farm to be specifically controlled at a given optimal power output. Power rate limitation serves as a ramp control method by limiting the rate at which a wind turbine or farm can ramp up or down at given time periods, a decision that will be based on anticipated demand and anticipated ramps in wind levels (Kristofferson, 2005).

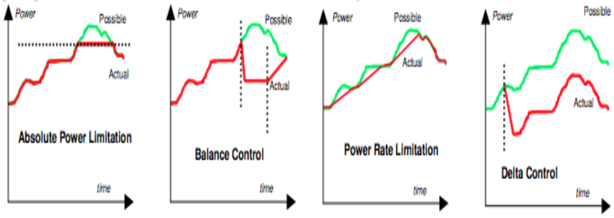

Figure 1. Figures depicting the four methods of wind control that the Horns Rev Wind Farm uses (adapted from Kristofferson, 2005)

The German energy transmission system limits wind energy ramp rates to 10% of the rated output of the wind farm per minute. Denmark uses 8% per minute as the absolute power rate limitation (Rose, 2010).

Mechanically, there are two different ways to control the output of an individual turbine or of a wind farm. The two main methods, torque control and pitch control, have been studied in an effort to determine the preferred method. The Jeong study found that torque control is ideal in terms of following a rated power, yet it has a tendency to speed up at higher wind through-flow. Pitch control tends to have more oscillations but overall preformed more aptly in terms of tracking and turbine loads. Either method can be used for the four methods listed previously, yet they vary in their efficiency in completing the desired wind control. Pitch control is in place in most commercial wind turbines, while torque control has a greater startup cost since it is not currently implemented on a large scale (Jeong et al., 2013).

One benefit of torque control for variable speed wind turbines is that they will be able to operate above their maximum output at a given wind speed (based on the wind power curve) for small timescales. The turbine can, in essence, save torque for brief periods of time as the wind decreases, and it can operate above what the wind would allow until frictional laws reduce the output (Jeong et al., 2013). This can be ideal in terms of a ramp down constraint as will be discussed in the experimentation component of the paper.

3. **Experimental methods**

3.1 Objective Function

This study builds on the work in Trisha Das's dissertation (Das, 2013), which effectively modeled a Monte Carlo simulation of a production costing model to analyze the benefits of storage on the IEEE 24-bus system. To simplify, preliminary studies will use deterministic modeling with control variables and base studies. Monte Carlo simulation will be added after preliminary studies find results. The Das dissertation contains a day ahead mixed integer linear unit commitment program and a real time economic dispatch model to allocate optimal decisions on the grid in a production cost minimization problem with increasing WP on the grid. Electric demand and ancillary services are considered. The objective function is as follows:

MINIMIZE:

$$\begin{aligned}
&\sum_{t\epsilon T_h}\sum_{(i,j)\epsilon G,T} C_{(i,j)}(t)\cdot e_{(i,j)}(t) + \\
&\sum_{t\epsilon T_h}\sum_{(i,j)\epsilon G} C^{sr}_{(i,j)}(t)\cdot e^{sr}_{(i,j)}(t) + \\
&\sum_{t\epsilon T_h}\sum_{(i,j)\epsilon G} C^{nsr}_{(i,j)}(t)\cdot e^{nsr}_{(i,j)}(t) + \\
&\sum_{t\epsilon T_h}\sum_{(i,j)\epsilon G} C^{reg+}_{(i,j)}(t)\cdot e^{reg+}_{(i,j)}(t) + \\
&\sum_{t\epsilon T_h}\sum_{(i,j)\epsilon G} C^{reg-}_{(i,j)}(t)\cdot e^{reg-}_{(i,j)}(t) + \\
&\sum_{t\epsilon T_h}\sum_{(i,j)\epsilon G} S^{x}_{(i,j)}(t)\cdot\left(X_{(i,j)}(t) + X^{0}_{(i,j)}(t)\right) + \\
&\sum_{t\epsilon T_h}\sum_{(i,j)\epsilon G} S^{y}_{(i,j)}(t)\cdot\left(Y_{(i,j)}(t) + Y^{0}_{(i,j)}(t)\right) + \\
&\sum_{t\epsilon T_h}\sum_{j\epsilon D} Pen_j(t)\cdot L_j(t)
\end{aligned}$$

where:

$e_{(i,j)}(t)$ is per unit (p.u.) energy flow and $C_{(i,j)}(t)$ its cost at hour t across all system arcs (i,j)

$e^{sr}_{(i,j)}(t)$ is p.u. spinning reserve capacity and $C^{sr}_{(i,j)}(t)$ its cost at hour t, where $(i,j) \in G$;

$e^{nsr}_{(i,j)}(t)$ is p.u. non-spinning reserve capacity and $C^{nsr}_{(i,j)}(t)$ its cost at hour t, where $(i,j) \in G$;

$e^{reg+}_{(i,j)}(t)$ is p.u. up-regulation capacity and $C^{reg+}_{(i,j)}(t)$ its cost at hour t, where $(i,j) \in G$;

$e^{reg-}_{(i,j)}(t)$ is p.u. down-regulation capacity and $C^{reg-}_{(i,j)}(t)$ its cost at hour t, where $(i,j) \in G$;

$S^{x}_{(i,j)}(t)$ is start-up and $S^{y}_{(i,j)}(t)$ is shut-down costs, $(i,j) \in G$;

$X_{(i,j)}(t)$ is start-up and $Y_{(i,j)}(t)$ is shut-down indicators;

$X^{0}_{(i,j)}(t)$ is start-up and $Y^{0}_{(i,j)}(t)$ is shut-down indicators for non-spinning reserves, where $(i,j) \in G$;

$L_j(t)$ is p.u. energy demand not served at hour t, where $j \in D$

$Pen_j(t)$ is the cost penalty for $L_j(t)$

(Das, 2013)

Storage may do well for the system (and for its own profit) to provide regulation services yet the services come at an economic cost, which is accounted for in the minimization objective function of production cost.

Through pitch changes, wind turbines already have the infrastructure to control their output, and they often do, in cases of extreme weather ramping to protect the hardware of the turbine. This pitch control can be used either as wind control in terms of ramp control or delta control with the wind contributing to the frequency regulation market.

The IEEE 24 bus system is depicted in the Appendix as Figure A1. The wind generation units are located at busses 17, 21, and 22, and the storage devices of two 100 MW capacity systems are located at busses 2 and 21.

The base case uncontrolled wind results are represented in Table A2.

3.2 Power Rate Limitation

The wind ramp rate control is modeled as follows:

$$ew_{(i,j)}(t) - ew_{(i,j)}(t-1) \le wrr_{(i,j)}(t),\ \forall (i,j) \in WG$$
$$ew_{(i,j)}(t-1) - ew_{(i,j)}(t) \le wrr_{(i,j)}(t),\ \forall (i,j) \in WG$$

$$mean(WGR) = mean(WG)$$

(For ramping up and down constrained wind generation)

where:

$ew_{(i,j)}(t)$ is the output of wind generation in MW

$wrr_{(i,j)}(t)$ is the p.u. per minute wind ramp rate

WG is the wind generation

WGR is the wind generation with the ramping constraint

German law has a ramping constraint of 10% the rated capacity for a wind farm per minute. However, this law is not constructed to help grid impacts of variability but to protect the wind turbine generators. The ramping rates considered for this study will be 1%, 0.5%, and 0.25% of the rated capacity of the wind farms per minute. For example, with 1% ramping constraint, it would take the wind turbine 100 min to ramp from zero MW output to maximum output (with wind through-flow being as necessary for the ramping). This constraint may seem heavy, but it is extremely uncommon for wind to ramp from zero output to maximum output even in a time frame of 100 min. Additionally, these ramping constraints are mainly built to handle the short-term regulation time scale variability within 5-10 min intervals. Large ramping events that generally result from storms or frontal passage that will drastically increase wind speed in a short time scale are generally bad for the life cycles of a wind turbine and must be assessed in other experimentation.

The metrics, which will be analyzed to assess the impact of power rate limitation, will be production cost of the system, regulation requirements, LMP, and total wind output (in MWh and money earned from the output). The impact of power rate limitation is expected to decrease the regulation requirements of the system due to a decrease in variability of the energy generation portfolio through a reduction in rate and number of ramping events. The overall reduction in regulation requirements and wind variability should serve to reduce cycling costs for conventional generation units and should increase these base load unit's longevity by reducing maintenance needs.

Regulation Requirement Calculation:

$$R^{+}(t) = \alpha^{+}\max(\sigma_{5\ min.})$$
$$R^{-}(t) = \alpha^{-}\max(\sigma_{5\ min.})$$

where:

$\max(\sigma_{5\ min.})$ is the maximum of standard deviations of 1-min net load deviations over a 5-min interval.
α^{+} and α^{-} are so that up to the 99th percentile of deviations are accounted for to comply with CPS-2 standards. (Das, 2013)

The system operates on a production cost minimization, and the power rate limitation constraint shown above will provide the desired ramping limitation. This constraint will not be broken on an economic basis, as there is a significantly large penalty upon the system for infringement on the absolute ramping rate limit.

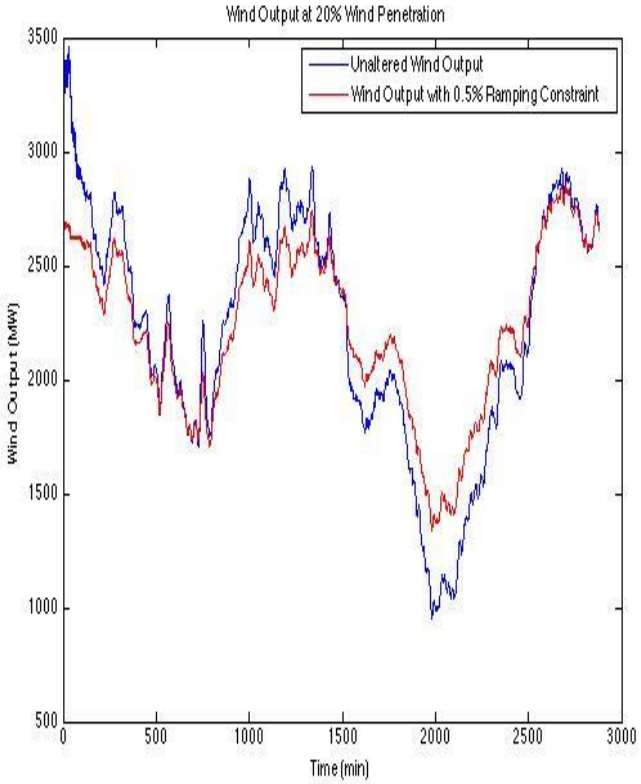

Figure 2. Unaltered wind output vs. 0.5% ramping up and down constrained at 20% penetration.

Figure 2 shows the effect of a 0.5% absolute power ramping constraint on total wind output of a 20% wind penetration system. The mean energy output of the system remains constant with the constraint, meaning that this remains a controlled experiment and all changes to the output data from the linear program can be seen as a direct change of only the wind ramping data and not the total wind output in MWh for the 48 hr simulation. As seen in the plot, with the ramping constraint, the variability of the wind generation is considerably decreased. The data for a different level of WP would be the same curvature, just scaled at a different rate since the assumed to be the same for all the WP. All of the same ramps will be controlled in the same way at a higher WP, as the ramp will be greater due to larger numbers, but also the rated capacity will be greater due to the higher WP level.

Ramping up and down constraints represent an idealized situation, as it is not always possible for a wind generation unit to control its ramping down, for at some points it would require them to produce more wind than is physically available. Wind farms are able to do this through torque control for shorter periods of time but on longer time scales (hours), this might not be as feasible. Storage on location of the wind farm is seen as an option for producing more energy than is possible with a given wind through flow but this comes at an economic cost to the wind resource, which is not modeled. Therefore, in addition to this idealized case being considered, a situation in which there are only ramping up constraints will also be considered; this constraint has no physical limitation but will not affect the variability as much as both ramping up and down constraints. Beneficially, the lack of a ramping down constraint will result in less economic drawbacks, as the ramping down constraint requires on site storage which come at a high capital cost.

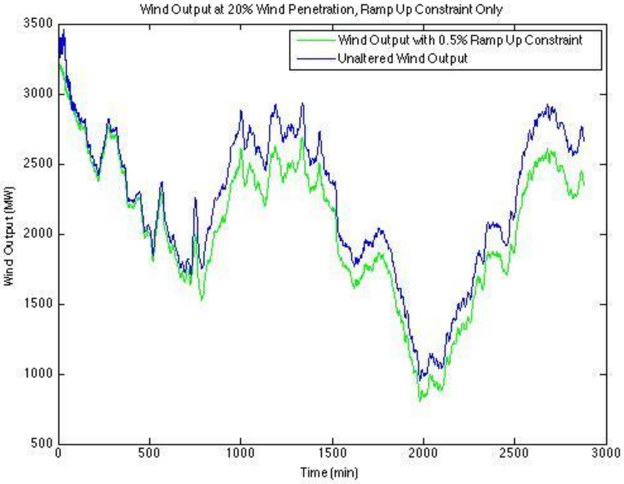

Figure 3. Unaltered wind output vs. 0.5% ramping up constrained at 20% penetration

Thus, there is no situation in which a wind farm is required to output more than that wind physically allows. More variability in the wind generation profile is incurred as a result since there is no ramping down constraint, yet there is no capital investment cost of storage. There is moderate to significant economic cost for the ramping constraint being in place for wind generation units, represented as the difference between the green curve actual output and the blue curve actual wind (Figure 3). Any situation in which the blue curve is significantly above the green curve, the wind generation unit is losing potential income, which must be balanced by an economic incentive. The ramping rates are hypothesized to provide grid incentives in the form of decreased cycling costs and decreased regulation requirements. As the wind ramp rate control limits the ramping capability of the wind generation units per minute, there must be a certain amount of wind generation potential that is lost due to this constraint. For 1% ramping up constraint, the loss is 1.62% of the total wind generation capability. For 0.5% and 0.25% ramping up constraints, the losses are 8.10% and 14.33% respectively (these numbers are for the considered wind data, subject to change based on different wind profiles). The loss in wind farm generation potential does not necessarily mean a loss in the wind farm energy output or the economic revenue of the wind farm, for transmission constraints and decrease in wind spillage may cover for the loss in wind potential. The economic losses for the wind units will be considered after the simulation. Figures 4 and 5 show the other considered ramping constraints.

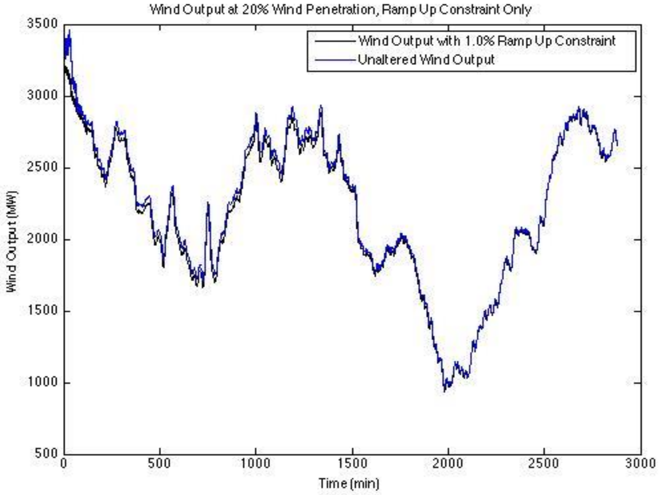

Figure 4. Unaltered wind output vs. 1.0% ramping up constrained at 20% penetration

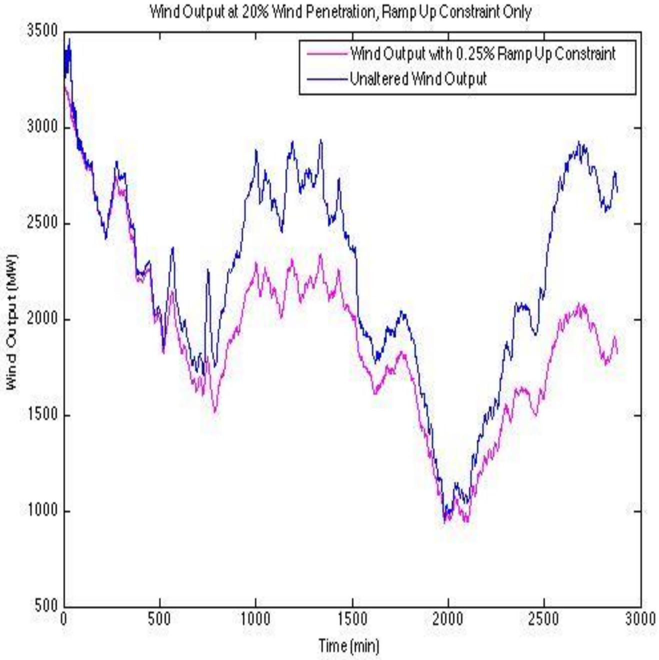

Figure 5. Unaltered wind output vs. 0.25% ramping up constrained at 20% penetration

Ramping constraints on wind generation also influence NL, as shown in Figures 6 and 7. With higher ramping up constraints, there will be less wind generation potential, and therefore, NL will be larger, as less wind is subtracted from the gross load. ED will satisfy the newly constrained NL through commitments to conventional generation units.

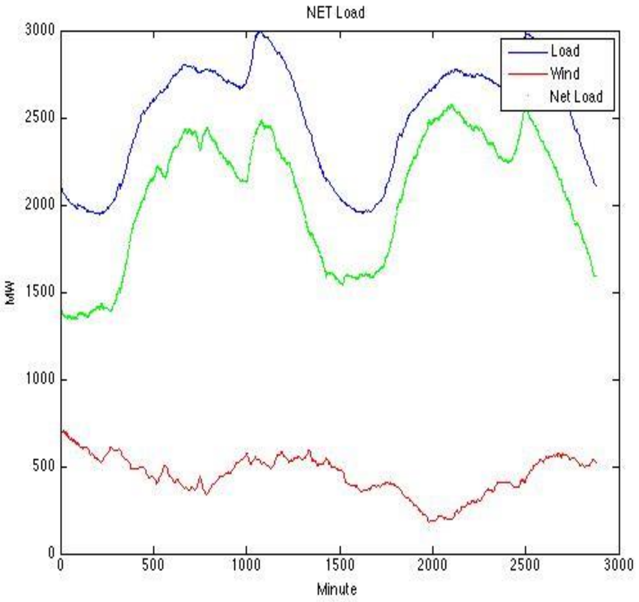

Figure 6. Wind generation, gross load, and net load for 20% WP and 0.5% ramping up constraint

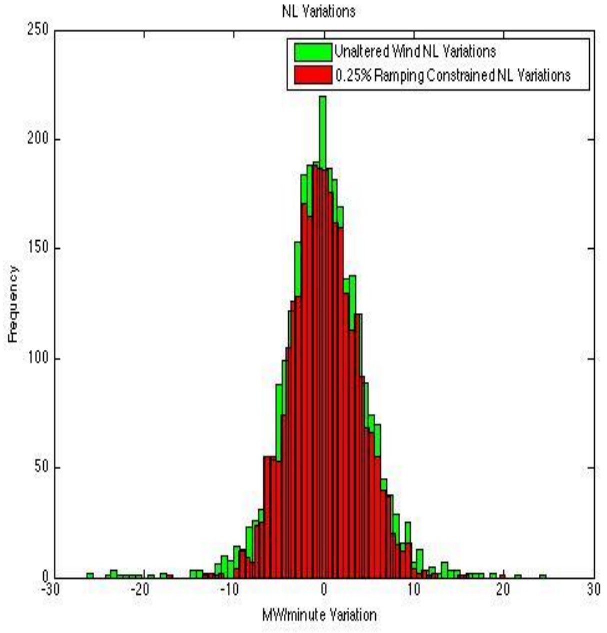

Figure 7. Histogram of NL variations with unaltered wind generation and 0.25% ramping constrained at 20% WP

3.3 Cycling Cost

Cycling costs in the Das model were modeled as influencing the bids for regulation and spinning reserve by adding the costs to original bids. When cycling costs were included, generation units bid higher according to Table A1 of cycling costs.

Cycling cost calculation:

$$Cy\$ = \sum_t \sum_i Starts_i(t)\Delta HS_i + (RU_i(t) + RD_i(t))(2 \cdot \Delta HRD_i + \Delta VOM_i + \Delta MA_i) + SR_i(t) \cdot \Delta HRD_i$$

where:
Starts: Start-ups for conventional generators
i: Conventional Generation Units
t: Time points
HS: Hot Start
RU: Regulation-Up served (MWh)
RD: Regulation-Down served (MWh)
HRD: Heat Rate Degradation
VOM: Variable Operation and Maintenance
MA: Margin Adder
SR: Spinning Reserve served (MWh)

4. Results

4.1 Ramp Rate Control Effect on Regulation

Results from the controlled variable deterministic simulations show that, in general, an increase in wind control decreases the regulation requirements for the grid. Since regulation requirements are paid for day ahead and real time to account for system energy output variability, WP increase will increase the need for regulation requirements. With studies of 0%, 20%, 40%, and 60% WP, it is shown that a use of wind ramp rate control decreases the need for regulation for the grid. The deduction in regulation requirements is amplified with an increasing WP, which was expected due to the variability increase that comes with increasing WP. As shown in Figure 7, at 60% WP, a 0.25% ramping up only constraint, the reduction in mean regulation requirements drops for both down regulation and up regulation from 2146 MWh energy to 1683 MWh energy, a drop of 21.51%. With a price of $27/MWh for natural gas (NG) generators to supply this regulation, the decrease creates a 48 hr savings of $12460 in regulation reduction. At a more realistic scenario of 20% WP, the drop is 10.21% of regulation requirements that now do not need to be purchased by the grid (see Tables 1 and 2).

Further, a more moderate wind ramp up rate control of 0.5% max capacity/minute would allow a wind ramp to ramp from zero output to full capacity in 200 minutes. The reduction in the regulation requirements for the 20% WP situation was modeled as 2.99%.

The variability of wind generation appropriately decreased with the ramping constraints and the regulation requirements for the system was decreased, shown in Figure 8.

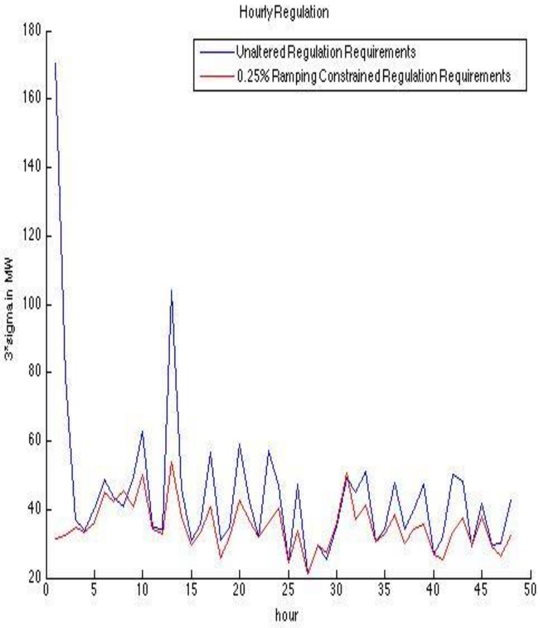

Figure 8. Unaltered wind output regulation requirements vs. regulation requirements for 0.25% ramping up constrained output

Additionally, with more stringent constraints on ramping rate, moving from 1% to 0.5% to 0.25%, the drop in regulation requirements was more significant. It was also found that placing the ramp rate control on the wind generation units also decreased the production cost for the system since the variability of the wind resource was decreased and the need to purchase regulation also dropped.

As shown in Table 1, non-constant nonlinearity of the reduction in regulation requirements as WP increases for a given ramping constraint percentage is most likely the result of the variable demand profile. Since different ramp rate constraints alter the wind generation potential to create new generation possibilities, there is the possibility of stacking constraints. For example, if the ramping constraint is 10 MW/min and the unconstrained wind generation ramps up from 100 MW to 115 MW to 130 MW, the real output for the constrained wind farm will be 120 MW. This stacking constraint as well as a variable demand profile will lead to nonlinearity in the regulation reduction.

Ramp Rate Constraint (%)	WP (%)	Percent Reduction in Reg (%) with Ramping Up
1	20	0.34
1	40	3.47
0.5	20	2.99
0.5	40	2.46
0.5	60	1.84
0.25	20	10.21
0.25	40	18.38
0.25	60	21.51

Table 1. Reduction in regulation requirements due to ramping up constraints

Ramp Rate Constraint (%)	WP (%)	Total Money Saved for System from Regulation ($) Up only
1	20	58.06
1	40	1059.61
0.5	20	518.4
0.5	40	725.76
0.5	60	1076.90
0.25	20	1768.78
0.25	40	5412.10
0.25	60	12460.26

Table 2. Reduction in cost due to the reduction in regulation requirements for ramping up constraints

4.2 Effect on Commitment

The most significant cycling cost and decay of the conventional generation units are associated with coal-fired power plants. In this model, coal plants serve as the base load power plants with significant MWh output. As in the real electricity grid, coal plants have significant startup constraints, and HS and downtimes are considered. Increased WP influences the number of start-ups and shut downs that the coal power plant experiences. With no ramping constraints modeled and 20% WP, the three coal power plants in the system experience a total of 35 time steps in which they are decommited. At 60% WP, coal plants experience 42 decommitments. However, with a 0.25% ramping constraint, decommitments for 20% and 60% WP are 32 and 37 respectively.

These reductions in start ups and shut downs for coal-fired power plants can be beneficial to the longevity of the units in terms of cycling decay. This can reduce maintenance required as well as operational hazards that come with turning off large coal units.

4.3 Wind Farm Economic Loss

The model also, importantly, found that absolute ramp rate control decreased the wind spillage, which in most cases, occurred as a result of transmission constraints upon the grid. Therefore, some of the economic loss for the wind farms will be counter balanced by the decreasing wind spillage. In fact, as seen in Table 3, in the modeling of some cases of wind control (0.5% and 0.25% ramping constraints) actually increased the profitability of the wind generation units at a lower WP (20%). This is the result of a small increase in wind output from the wind turbines with the ramping constraint considered, even though the overall potential for wind generation was less due to the constraint.

In general, at higher WP, the economic loss for the wind generation units was moderate, with the loss being greatest at 40%. At 40% WP and 0.25% ramping up constraint, the wind generation units lost 0.55% of revenue, which is interesting since the 0.25% ramping up constraint eliminated 16.72% of the wind generation capabilities. The loss was greatest at 40% as a combination of the higher WP than 20% and the higher LMP than 60% WP shown in Table 3. The total loss for the wind generation units in this case came to be $8980 (calculated using real-time LMP and actual wind output) out of total revenue with no ramping constraint of $1642500. However, the drop in production cost for the system between these two cases came to be $22500, which is significantly larger than the economic losses for the wind generation units.

Ramp Rate Constraint (%)	WP (%)	Economic Loss for Wind Units ($)
1	20	-2.09E+02
1	40	-3.53E+02
0.5	20	-2.74E+02
0.5	40	2.32E+02
0.5	60	-2.48E+04
0.25	20	-5.84E+02
0.25	40	8.98E+03
0.25	60	-1.74E+04

Table 3. Economic loss for the wind generation units (negative loss means economic gain)

4.4 Ramping Control and Storage

When two 100 MW storage units are modeled into the system with the ramping up constraint, there is a significant reduction in the MWh of regulation services provided by the conventional generation units. There is the aforementioned reduction in regulation requirements as a result of the ramping up constraint as well as the CAES supplying a significant amount of regulation services. Together, they decrease the AS requirement for conventional generation units.

The storage units come with a significant production cost reduction that, in tandem with ramping constraints, is furthered. Table 4 compares control cases with constrained cases.

Ramp Rate Constraint (%)	WP (%)	Production Cost ($ E+06)	Regulation Requirements (MWh)
0	20	3.0795	188.47
0	40	2.9301	501.35
0	60	2.9787	2145.64
1	20	3.0799	203.67
1	40	2.9272	468.86
0.5	20	3.0791	193.99
0.5	40	2.9239	425.09
0.5	60	2.9526	2106.09
0.25	20	3.0774	576.38
0.25	40	2.9142	890.27
0.25	60	2.9117	1684.15

Table 4. Production cost and regulation requirements with ramping up constraint and two 100 MW CAES storage units

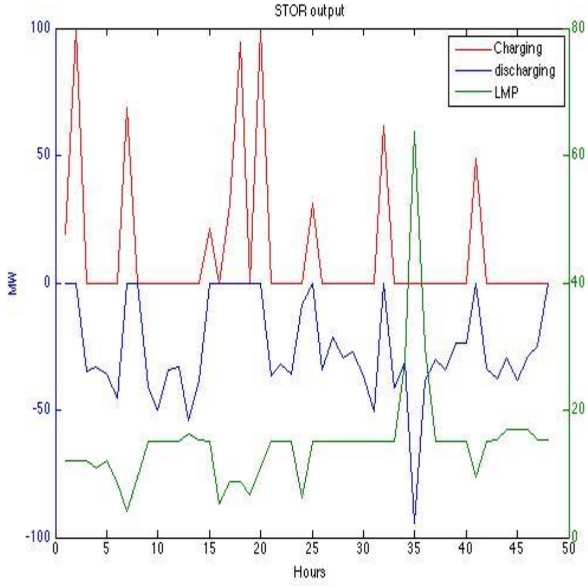

Figure 9. LMP and charging and discharging for a 100 MW storage unit for 48 hr simulation for 60% WP and 0.25% ramping constraint

4.5 Cycling Cost

With cycling cost modeled as shown in the experimental method and using data from the Cycling Costs Table (Table 6) in the Appendix, the production cost significantly increases for the system. As hypothesized, cycling cost further negatively impact the energy system with increasing WP. Additionally, more money is saved by the system with the ramping up constraints modeled in the cycling cost situations. With the more realistic situation of cycling costs included for the conventional generation units, the ramping rate constraints are more beneficial for the grid.

Cycling costs considered added an economic penalty to the production cost of $45500 in the 20% WP 48 hr simulation. This cost increased with the rising WP, jumped to $52200 for 40% WP, and $70400 in the 60% WP system. The increased cost is due to increased variability for higher intermittent resource penetration.

The reduction of regulation requirements is more beneficial for the grid with cycling costs modeled. The regulation market-clearing price is changed from $27/MWh as provided by NG generation units to $34.75/MWh. Therefore, the reduction in regulation requirements as modeled above is amplified in the cost savings for the energy system. Further, the reduction in commitments and decommitments is beneficial with an increased startup and shutdown cost that is the result of cycling cost.

In comparison with the no cycling cost runs, the money saved by the energy grid in terms of regulation requirements increased. For example, at 60% WP and 0.25% ramping up constraint, the no cycling cost run showed a savings of $12460, as shown in Table 2, while modeling with cycling costs showed a savings of $16038, as shown in Table 5.

Ramp Rate Constraint (%)	WP (%)	Production Cost ($ E+06)	Production Cost Saved With Constraint ($)	Money Saved on Reg ($)
0	20	3.2721	0	N/A
0	40	3.122	0	N/A
0	60	3.1349	0	N/A
1	20	3.2723	-200	74.73
1	40	3.1253	-3300	1363.87
0.5	20	3.2699	2200	667.26
0.5	40	3.1182	3800	934.16
0.5	60	3.1199	15000	1374.55
0.25	20	3.2648	7300	2276.68
0.25	40	3.0962	25800	6966.15
0.25	60	3.0777	57200	16038.16

Table 5. Reduction in production cost and regulation requirements with cycling costs modeled (negative cost saved means money lost)

4.6 Ideal Ramping Up and Down Constraints

The ideal power rate limitation constraint would consist of both a ramping up and a ramping down constraint, meaning that the wind generation unit would not be able to increase output past a certain speed as modeled previously but also that the generation unit may not decrease output past a certain speed. With these constraints modeled, the decrease in variability was significant.

Inclusion of the ramping down constraint further decreased variability that was modeled as a result of the ramping-up-only constraint. At various WP levels, total ramping constraints of 1%, 0.5%, and 0.25% of the rated capacity/min were modeled. With a 0.25% total ramping constraint on a 60% WP system, the change in regulation requirements amounted to a substantial 33.7% reduction in both up and down regulation. This is an economic impact of $30884 regulation requirements that do not need to be purchased by the grid.

Further, the ramping constraint on the wind decreased production cost of the system for all cases of WP and percentage wind control modeled. In a realistic run of 20% WP and a 0.25% ramping constraint; the production cost of the 48-hr system was reduced by $7400. However, at a higher wind penetration of 60%, reduction in production cost from the unconstrained wind data to the constrained wind data was a significant $70,700, of which $30,884 was the result of regulation reduction (the rest being less commitments and de-commitments and other ancillary reserves).

Ramp Rate Constraint (%)	WP (%)	Percent Reduction in Reg (%) Ramp Up and Down
1	20	0.05
1	40	2.59
0.5	20	5.77
0.5	40	9.32
0.5	60	10.51
0.25	20	13.58

0.25	40	27.63
0.25	60	33.74

Table 6. Reduction in regulation requirements due to ramping up and down constraints

Ramp Rate Constraint (%)	WP (%)	Total Money Saved for System from Regulation ($) Up and Down
1	20	8.29
1	40	783.82
0.5	20	999.48
0.5	40	2743.37
0.5	60	6090.16
0.25	20	2353.54
0.25	40	8136.81
0.25	60	19545.75

Table 7. Reduction in cost due to the reduction in regulation requirements for ramping up constraints

4.7 Monte Carlo Simulation

Monte Carlo simulation was necessitated as a result of the unexpected outcome in the wind revenue in the deterministic controlled variable experimentation. The Monte Carlo simulation (n=100) will yield more accurate results in terms of variable energy pricing and random outages to cause more realistic LMP.

The unexpected result of wind revenue being higher in the ramping constrained data with less wind being produced remained consistent with the n=100 iteration Monte Carlo simulation, as it was in the controlled, deterministic experimentation, as can be seen in Table 7. In the Monte Carlo simulation, there was a regulation reduction of 10.2% and a decrease in production cost of the system by $61600, or a decrease of 2.5% of the overall system production cost.

Ramping Constraint (%)	WP (%)	Production Cost ($ E+06)	Reg (MWh)	LMP ($)	Wind Revenue ($)
0	20	2.4943	641.89	54.11	808240
0.25	20	2.4326	576.34	57.49	902020

Table 8. Data for the base case and 0.25% ramping constrained Monte Carlo simulation at 20% WP

5. Analysis and interpretation

The wind control was implemented, and in terms of reduction in regulation requirements, absolute power rate limitation preformed as hypothesized (Tables 1, 2, 4, and 5). As WP increases, the need for regulation increases. As modeled in the base case, moving from 0%, 20%, 40%, to 60% results in regulation requirements of 494.05 MWh, 641.89 MWh, 1090.71 MWh, and 2145.64 MWh respectively. Additionally, as more stringent ramping regulations are enforced on wind generation units, the need for regulation decreases for a given WP level. As WP levels increase, ramping constraints have a larger impact upon the system as well, reducing more percentage of regulation requirements and saving larger amounts of money.

The effect of the wind control strategy on the energy output to the system was not as extreme as the effect upon the generation availability of the wind farms. This is due to transmission constraint, which create the phenomena of wind spillage, or energy from wind farms that cannot be sent to the grid as a result of congestion, or other transmission constraints. At higher WP levels, the grid cannot take the excess of wind being forced on as a result of transmission constraints and will cap the wind at some value below its generation potential. At these time points, the ramping constraint will become null since the unconstrained wind generation in terms of ramping will then be constrained by the transmission capacity of the power lines. To illustrate this example, at 60% WP and 0.25% ramping up constraint, the loss of wind generation potential is 14.33%, yet the difference in MWh output from the wind farms to the grid comes out to be 10.23%. There is a “loss” of 4% of the ramping constraint as a result of transmission constraints, yet the 60% WP and 0.25% ramping up constraint is the most prevalent case of this phenomena. Therefore, the ramping constraint still impacted the overall grid, just 4% less than would be anticipated without the transmission constraints.

Positive outcomes were also seen in terms of the decommitments of conventional generation units. Decommitments of these units are an issue with increased pressure and heat fluctuations that causes damage for them. At 20% WP, the 0.25% ramping constraint decreased the number of decommitments from 35 to 32 and at 60% from 42 to 37. The reduction in decommitments for coal-fired power plants most likely had a positive impact on production cost for the system.

There was an unexpected effect on income of the wind generators with ramping constraints. Ramping constraints of 1%, 0.5%, and 0.25% of rated capacity per minute have a wind generation potential loss of 1.62%, 8.10% and 14.33% respectively, leading to the hypothesis that ramping constraints would reduce economic income for wind generation units. This, however, was not uniformly the case, as can be seen in Table 3. The ramping constraints, with the exception of the 40% WP case, increased LMP at their respective busses, thus increasing their total income. Therefore, there is potential for wind generation units to not require monetary compensation for their subjectivity to ramping constraints. In the 40% WP case, the wind generation units lost money with 0.5% and 0.25% ramping constraints. Their losses were $232 and $8980 respectively. In the 0.5% case, money saved for the system from reduction in regulation requirements was $726, which more than accounts for the wind farm's loss and could thus be accounted for. In the 0.25% case, savings from regulation reduction only came to $5,412, which cannot account for the economic loss for the wind farms, and the ramping constraint for this specific case is not optimal only considering regulation reduction.

The analysis of cost above only considers savings from regulation, but other ancillary services are affected as well, and for the 40% WP 0.5% ramping constrained case, the decrease in production cost with the ramping constraint considered was $3,700, which is significantly more than the economic loss for the wind units and also significantly more than the savings from just regulation reduction, meaning the energy system has benefitted in multiple ways that are most likely accounted for by less commitments and decommitments of units and a decrease in requirements for other expensive ancillary services. In fact, the reduction in production cost for the 40% WP and 0.25% ramping constraint comes to $22,500 which more than accounts for the economic losses for the wind units in that case and the 0.25% ramping constraint is therefore optimal.

The 1% ramping up constraint had a negative effect on production cost of the system, increasing the cost for all WP cases. Therefore, a 1% ramping constraint is not stringent enough to reduce regulation requirements significantly and is therefore not optimal.

When cycling costs were considered, the overall production cost the system was drastically increased; increases as high as $70,400 were recorded. However, the ramping up constraint on the wind generation units had a positive impact by decreasing the cycling cost for the grid. The cycling cost being considered is the most realistic modeling situation, as cycling cost is a very real penalty generators will need to pay for their variable output in terms of heat rate degradation in start up and shut down. For the most realistic case to United States energy markets, WP 20% and cycling costs considered, the energy market production cost can save $2,200 and $7,300 with 0.5% and 0.25% ramping constraints respectively for the 48 hr cycle. As WP increases and cycling becomes more of an issue, the ramping rate control can be a very viable solution.

On the subject of energy storage, the Das dissertation (Das, 2013) appropriately addresses the payback time scale and other logistical constraints. This study was to model how ramp rate control interacts with the energy storage, and the results indicate that they can work together to help solve the issue of wind intermittency. Together, they decreased regulation requirements heftily, decreasing the cost of regulation by $2,277 for the 48 hr model at 20% WP with a 0.25% ramping constraint. Additionally, since this type of wind control does not include wind bids into the AS market, wind control and energy storage do not hinder each other's profitability and only work together to decrease AS requirements.

Ramping down constraint, when considered, extended the reduction in regulation requirements as compared to the ramping up only constraint. However, there would be an economic capital cost for the wind farms associated with the ramping down constraint, in the form of a purchase of on-site storage, which is not modeled in this paper.

Finally, with the inclusion of Monte Carlo simulations of 100 iterations, the regulation requirements were appropriately decreased and the production cost of the system experienced a 2.5% decrease. The wind farms again made more money with the lower output, constrained generation profile due to an increase of LMP by $3.38/MWh.

6. Conclusions

In the coming years, with the DOE 20% by 2030 scenario for wind generation, variability of energy generation will rise sharply due to the intermittency of the wind resource. Variable and difficult to predict in nature, wind will cause a huge issue at higher WP levels for the energy grid's ability to meet supply and demand in a low cost method with reliability. To account for that variability, energy markets will use an increased level of AS, especially on small timescales, such as regulation, spinning, and nonspinning reserves. However, AS are expensive for the market and for the consumers, so there must be efforts to find an optimal solution to the energy intermittency issue. Wind control is one of those methods. Ramp rate limitation is a wind control that takes virtually no effort on behalf of the energy system other than a policy change. The wind turbines already have the capability to control their ramping rate through pitch control, which is standard in all units (Jeong, 2013).

The overall impact of the ramping rate limitation was a reduction in regulation requirements, a reduction in the production cost for the system, and an increase in economic revenue for the wind generation units. With cycling costs considered, the ramp rate limitation saved considerable amounts of money for the production cost of the system. Initially, goals of this study included allocating the monetary savings for the energy and AS market to the wind farm to compensate them for their participation in wind control to decrease variability, however, as seen in the modeling, the wind farms had no economic cost with the ramping rate limitations considered, and would therefore, not necessarily need to be compensated.

Finally, the ramp rate control does not interfere with future profitability in the energy storage field, as wind capacity is not offered into the AS market. In fact, in the simulation, ramping control and storage worked well to decrease the regulation that needed to be supplied by the conventional generation units, and thus worked to decrease cycling costs for the energy grid.

Future work must include more rigorous studies into the economic feasibility of on site storage to satisfy ramping up and down constraints. Energy markets would benefit from decreased intermittency of a ramping down constraint; yet, this would come at a significant economic cost to wind farm operators.

Future work must also include specific case studies of real energy grids and how the ramping rate affects the economics of the wind farms. With deterministic and Monte Carlo simulations, the wind farms had higher revenue with the ramping constraint than with no ramping constraint. This must be studied using models representative of a real energy grid to assess the result's validity.

Acknowledgements

Support for this research was provided by a National Science Foundation Research Experience for Undergraduates site program in Wind Energy Science Engineering and Policy (WESEP) grant number EEC-1063048 at Iowa State University.

References

Ackermann, Thomas, 2005: *Wind Power in Power Systems*. Chichester, West Sussex, England: John Wiley, Chichester, West Sussex, England. 2005. Print.

Hobbs B. F., M. H. Rothkopf, R. P. O'Neill, and H. Chao, 2001: *The Next Generation of Electric Power Unit Commitment Models*. Kluwer. Norwell, MA

Das, Trishna, 2013: Performance and Economic Evaluation of Storage Technologies. PhD Dissertation. Dept of Electrical Engineering. Iowa State University. PhD. Dissertation, 237 p.

Strbac G., Aunedi M., Pudjianto D., Djapic P., Teng F., Sturt A., Jackravut D., Sansom R., Yufit V., and Brandon N., 2012: Strategic Assessment of the Role and Value of Energy Storage Systems in the UK Low Carbon Energy Future. Report for Carbon Trust, prepared by Energy Futures Lab, Imperial College London.

Hargreaves, J. J., and B. F. Hobbs, 2012: Commitment and dispatch with uncertain wind generation by dynamic programming. *IEEE Transactions on Sustainable Energy*. 3-4. 724-734.

IEA, 2013: IEA Wind Energy Annual Report 2010. http://www.ieawind.org/annual_reports.html

Jeong Y., Johnson K., and P. Fleming, 2013: Comparison and Testing of Power Reserve Control Strategies for Grid-Connected Wind Turbines. *Wind Energy*. 16 (2) [http://onlinelibrary.wiley.com/doi/10.1002/we.1578/abstract]

Kirby, B., 2007: Ancillary services: Technical and commercial insights. *Report prepared for Wartsila*. Helsinki, Finland.

Kristofferson, Jesper R., 2005: The Horns Rev Wind Farm and the Operational Experience with the Wind Farm Main Controller. *Copenhagen Offshore Wind*. [Available online at http://wind.nrel.gov/public/SeaCon/Proceedings/Copenhagen.Offshore.Wind.2005/documents/papers/Wind_power_plant_control/J.R.Kristoffersen_TheHornsRevWindFarm.pdf]

Kumar, N., P. Besuner, S. Lefton, D. Agan, and D. Hilleman, 2012: Power plant cycling costs. *Contract*, *303*, 275-300.

Miso, 2012: Dispatchable intermittent resources. MISO Markets Committee PPT. [Available online at https://www.midwestiso.org/Library/Repository/Meeting%20Material/Stakeholder/BOD/Markets%20Committee/2012/20120620/20120620%20Markets%20Committee%20of%20the%20BOD%20Item%2007%20Dispatchable%20Intermittent%20Resources.pdf.]

Kumar N., M. Philip, Besuner S., Lefton D., Agan D., and Hilleman Douglas D., 2012: Power Plant Cycling Costs. *Prepared for NREL.* Golden, Colorado, U.S. [Available online at http://wind.nrel.gov/public/WWIS/APTECHfinalv2.pdf.]

Rose, S. and Apt, J, 2010: The Cost of Curtailing Wind Turbines for Frequency Regulation and Ramp-Rate Limitation. In *Proc. 29th USAEE/IAEE North American Conference on Energy and the Environment: Conventional and Unconventional Solutions*. 1-18. Cleveland, Ohio, U.S.

Ma Rui, Ju Hu Shu, Bo Fu Xun, Hua Xu Hong, Hong Li Niag, 2012: Torque control and pitch control strategy in VSCF wind turbine above rated wind speed. *Advanced Materials Research*, Switzerland.volume? pages?

Sorensen, Paul and Jesper R. Kristoffersen, 2006: Wind Farm Control. *ECPE Seminar-Renewable Energies*. Kassel, Germany.

Appendices

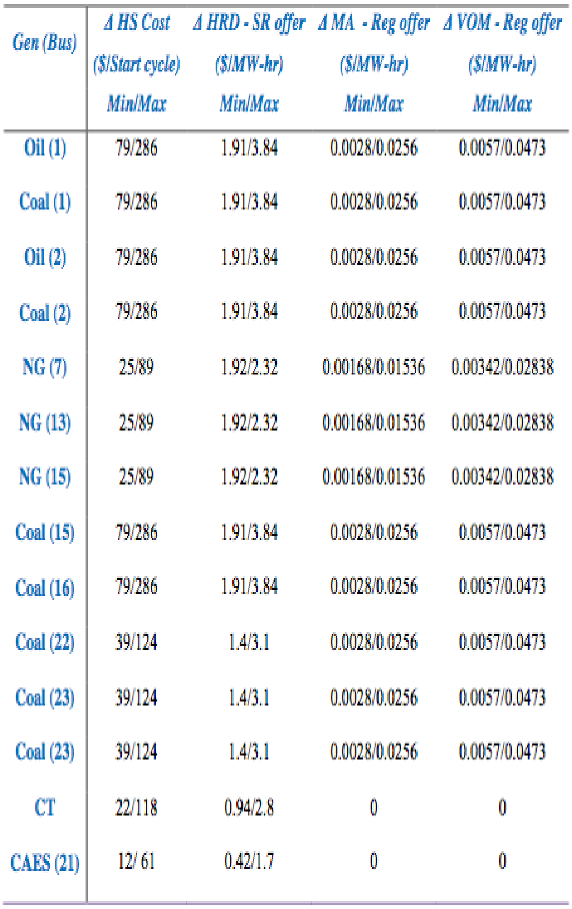

Gen (Bus)	Δ HS Cost ($/Start cycle) Min/Max	Δ HRD - SR offer ($/MW-hr) Min/Max	Δ MA - Reg offer ($/MW-hr) Min/Max	Δ VOM - Reg offer ($/MW-hr) Min/Max
Oil (1)	79/286	1.91/3.84	0.0028/0.0256	0.0057/0.0473
Coal (1)	79/286	1.91/3.84	0.0028/0.0256	0.0057/0.0473
Oil (2)	79/286	1.91/3.84	0.0028/0.0256	0.0057/0.0473
Coal (2)	79/286	1.91/3.84	0.0028/0.0256	0.0057/0.0473
NG (7)	25/89	1.92/2.32	0.00168/0.01536	0.00342/0.02838
NG (13)	25/89	1.92/2.32	0.00168/0.01536	0.00342/0.02838
NG (15)	25/89	1.92/2.32	0.00168/0.01536	0.00342/0.02838
Coal (15)	79/286	1.91/3.84	0.0028/0.0256	0.0057/0.0473
Coal (16)	79/286	1.91/3.84	0.0028/0.0256	0.0057/0.0473
Coal (22)	39/124	1.4/3.1	0.0028/0.0256	0.0057/0.0473
Coal (23)	39/124	1.4/3.1	0.0028/0.0256	0.0057/0.0473
Coal (23)	39/124	1.4/3.1	0.0028/0.0256	0.0057/0.0473
CT	22/118	0.94/2.8	0	0
CAES (21)	12/ 61	0.42/1.7	0	0

Table A1. Cycling Components for Generator Offers

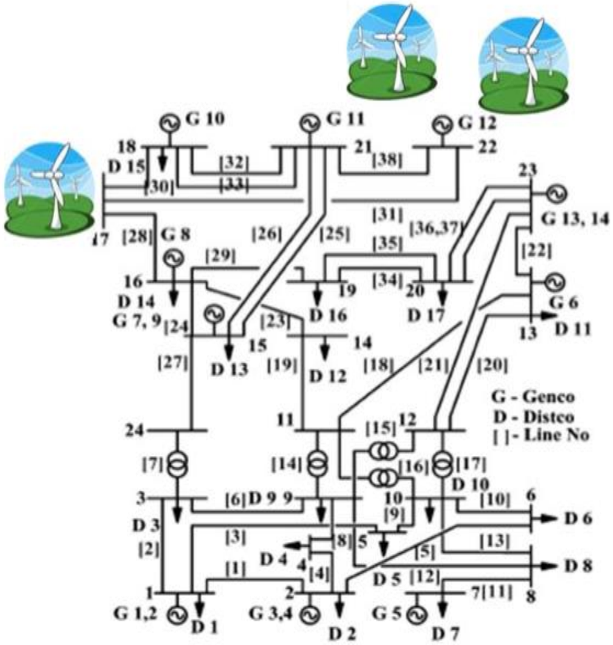

Figure A1. IEEE 24 Bus System with Wind Generation Units

WP (%)	Production Cost ($ E+06)	Reg (MWh)
0	3.5851	494.05
20	3.2721	641.89
40	3.122	1090.71
60	3.1349	2145.64

Table A2. Base case simulation results (no ramping constraint)

Effect of Out-of-Plane Waves on Fiber Volume Fraction in Wind Turbine Blade Composites

VICTOR AIELLO
Wind Energy Science Engineering and Policy REU, Iowa State University, Ames, Iowa
Mentors: Dr. Vinay Dayal and Sunil Kishore Chakrapani

Abstract

Wind turbine blade composites are vulnerable to several types of defects due to their manual manufacture. Out-of-plane waves are a relatively common defect that cause significant decrease in compressive strength and fatigue life of the blade. Ultrasound has proven to be a nondestructive evaluation technique that can be used in quality control to limit blades from leaving the factory with detrimental defects. This experiment explores the relationship between out-of-plane waves and localized increase in fiber volume fraction. Determining this relationship should aid in identification and characterization of out-of-plane waves using ultrasonic techniques. A sample was manufactured containing out-of-plane waviness by placing cured resin waves between ply layers before infusion. Micrographs (50X) were taken of the fiber and resin layers in the 1-3 plane of the laminate. Measurements of ply thickness in the regions with and without out-of-plane waviness were compared to determine change in fiber volume fraction. Multivariate first order error propagation was used to determine uncertainties in calculated values. The results showed that the change in fiber volume fraction of a ply from a region compacted by an out-of-plane wave to one unaffected was the same for all plies affected by the wave. Therefore, the fiber volume fraction of a ply in a region containing waviness is dependent on the fiber volume fraction in the unaffected region. This experiment also showed that resin layers between plies do not follow the same trend. Future research should explore the effect of resin flow during infusion and how it affects resin layer thickness in regions containing waviness. By combining relationships for an out-of-plane wave's effect on both ply thickness and resin layer thickness, there is significant potential for improved characterization of out-of-plane waves using ultrasonic nondestructive evaluation.

1. Introduction

The effects of carbon dioxide emissions on climate change have caused a push for low and no carbon sources of electric power generation. Wind energy shows potential to be a significant contributor to the portfolio of energy sources while reducing greenhouse gas emissions. In order for wind energy to reach this potential, it must become cost competitive with conventional sources of electric power generation, coal and natural gas.

The U.S. Energy Information Administration estimates that the levelized cost of energy in 2018 for wind, conventional coal, and conventional combined cycle natural gas will be $86.6, 100.1, and 67.1 per MWh (EIA, 2013), respectively. Although, since the primary cost of wind energy is capital investment, any reduction in lifetime of wind turbines causes a significant increase in levelized cost. Wind turbine blades make up about 18% of the cost of a wind turbine (Jamieson, 2011), and their ability to last the intended lifetime is crucial to the competitiveness of wind energy.

To insure that wind turbine blades meet reliability standards, quality control procedures must be performed by the manufacturer. Wind turbine blades are composed of commercial grade composite materials that are vulnerable to several types of defects in the manufacturing process. The manual manufacture of these large blades is one of the primary reasons for manufacturing defects. To demonstrate their usefulness, nondestructive evaluation techniques must be able to identify defects within manufactured blades and determined if they are acceptable for the performance and expected lifetime of the blade. These techniques must be able to scan large areas quickly and efficiently, they should be able to characterize the type or size of the defect, and they must have simple setup that allows for on-site inspection.

Typical defects in wind turbine blade composites, characterized by Riddle et. al (2011), include in-plane and out-of-plane waviness. In-plane waves exist within the plane of each ply, while out-of-plane waves occur through the thickness of the laminate. This paper examines the effect out-of-plane waviness has on fiber volume fraction.

2. Literature review

Considerable research has been performed to investigate fiber waviness in wind turbine blades. The size of waves are defined by two parameters, off-axis fiber angle, the maximum angle between fiber direction and slope of the wave, and aspect ratio, the wavelength divided by amplitude. Riddle et. al (2011) examined commercial scale wind turbine blades to determine the geometric nature of waves. It was found that out-of-plane wave amplitudes ranged from 0.02 to 0.85 cm, wavelengths varied from 1.58 to 21.49 cm, and off-axis fiber angles varied from 0.59 to 39.01 degrees. By quantifying the dimensions of out-of-plane waves in commercial blades, they can be replicated in samples for testing.

Fiber waviness has been analyzed for its effect on the strength of composite materials. It was shown by Nelson et. al (2011) that compressive and tensile ultimate strength for a laminate containing an out-of-plane wave with an aspect ratio of 7.7 decreased by 57% and 27%, respectively. Fatigue life is also significantly affected by out-of-plane waviness, as demonstrated by Galappaththi et. al (2013). For an axial fatigue loading 32-38% of maximum, the number of cycles to failure for specimens with out-of-plane waves of aspect ratio 12 and 24 were shown to decrease by as much as 70% compared to a flat specimen. These studies demonstrate the effects out-of-plane waves have on the strength of composite materials, and they exemplify the need for nondestructive evaluation techniques that reveal location and severity of out-of-plane waves.

Ultrasound has become an important contributor to nondestructive evaluation of wind turbine blades. Ultrasonic pulse-echo immersion testing for circular defects was demonstrated by Jasiuniene et. al (2008). Instead of immersing the entire blade sample in water, a small water bucket was attached to the transducer, creating contact among sample, water, and transducer. Two frequencies were used to analyze the defects, 2.2 MHz and 400 kHz. As expected, the higher frequency was more effective for detecting defects near the outer surface of the blade sample, and lower frequency allowed detection in deeper layers. Amenabar et. al (2011) used a pulse-echo transducer with a gel coupling agent to detect delaminations. A delamination occurs when two fiber-glass layers separate, leaving a void within the laminate. Using the pulse-echo technique, the size and depth of the delamination could be determined in thick composites. Both immersion and contact techniques use a single transducer to scan points across the entire test piece. They are effective in characterizing size and depth of defects to finer detail once they have been found, but the time required to scan the entire wind turbine blade point by point makes these ultrasonic techniques undesirable to manufacturers when searching for defects.

The ability to use air coupled ultrasonics to detect out-of-plane waves in wind turbine blades was demonstrated by Chakrapani et. al (2012). Rayleigh (near surface) waves were generated across one side of a laminate using a transmitter and receiver separated by 5 in. A C-scan was created by scanning down the fiber direction of the sample and indexing perpendicularly. As the scan passed over a wave, an increase in amplitude was noticed. This process detected out-of- plane waves with aspect ratios ranging from 4 to 20 at depths up to 12mm within the laminate. Scanning time decreased by 75% compared to pulse-echo. The speed and cleanliness of this testing technique make it plausible for industrial applications when scanning wind turbine blades for defects. This process is effective at identifying the location of out-of-plane waves; although, it is not as effective at characterizing their size.

Out-of-plane waves occur when a pocket of resin, known as a root defect, develops between plies. The plies near the root defect are forced to shift, yet the surfaces of the laminate are pressurized during vacuum assisted resin transfer molding (VARTM) and remain flat. This causes compaction of plies within the laminate. The compaction of fibrous materials has been studied extensively by the textile industry. The first person to attribute the compression of fiber bundles to a series of bending beams was van Wyk (1946). The research has been expanded to that of fiber composites, primarily to understand thickness changes in resin transfer molding processes. The theory developed for compaction of plies is primarily based on the work by Gutowski (1992). Also based on the concept that the fibers act as bending beams, a relationship was created between applied stress and fiber volume fraction of a fiber bundle, Eq. 1:

$$\sigma_b = \frac{3\pi E}{\beta^4} \frac{1 - \sqrt{\frac{V_f}{V_o}}}{\left(\sqrt{\frac{V_a}{V_f}} - 1\right)^4} \tag{1}$$

where σ_b is the bulk stress applied in the transverse plane, E is the bending stiffness modulus, V_f is the fiber volume fraction, V_o is the maximum fiber volume fraction when no stress is applied, V_a is the available or maximum fiber volume fraction under stress, and β is a constant defined empirically. It has been shown that by varying the constants V_o, V_a, and β, data sets can be fit very well. Although, these constants are based on the state of the fiber bundle, and there is no unique relationship for compaction of similar fiber bundles. This was demonstrated by experimental results for the fiber volume fraction of several similar fiber bundles, shown in Fig. 1:

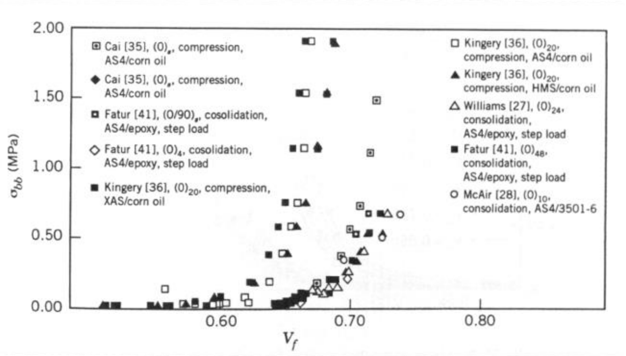

Figure 1: Stress and fiber volume fraction relationship for similar fiber bundles (Gutowski, 1992).

Although each curve seems to fit the same shape, they are spread along the x-axis. Each curve was shifted based on the difference of V_f and V_o, Fig. 2:

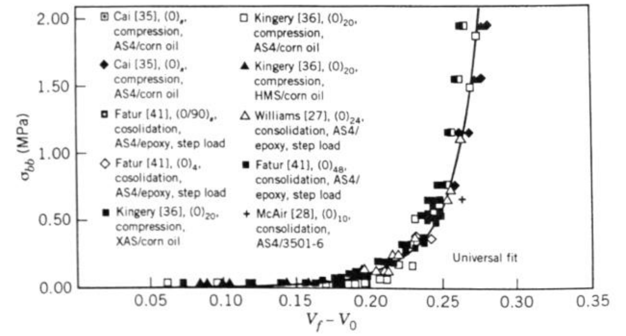

Figure 2: Curves shifted based on original fiber bundle state (Gutowski, 1992).

This figure shows that for similar bundles enduring the same stress, the change in fiber volume from their original state is the same.

As demonstrated by Eq. 1 and Figs. 1 and 2, increase in fiber volume fraction occurs rapidly at low stress, and as $V_f \rightarrow V_a$ the stress required to increase fiber volume fraction increases exponentially. Saunders et. al (1998) performed a microstructural study that described this phenomenon in three modes. Initially, the fibers nest closer by slipping under relatively low stress. Once the stress is great enough, the second mode occurs, in which natural waviness in the fibers is decreased in amplitude. The third mode involves load transfer from the resin to the fibers, and the fibers begin to compress and deform individually. Chen et. al (2001) performed dry compaction experiments with unidirectional laminates similar to those used in this experiment. Testing samples with 1, 10, and 25 plies, they found that the average ply thickness under the same pressure for the 1 ply laminate was greater than that for the 10 and 25 ply laminates. This was attributed to an increase in nesting between plies, yet the ply thickness-pressure relationship for the 10 and 25 ply laminates was nearly identical, showing that nesting reaches a maximum. The results of experiments by Saunders and Chen both match the trend of fiber volume fraction variation under increasing stress demonstrated by Gutowski.

Change in fiber volume fraction caused by compaction affects the localized density and elastic properties within the laminate. Ultrasonic wave propagation is highly dependent on the ratio of elastic modulus to density. Determining a relationship between out-of-plane wave size and the resulting localized change in density and elastic properties may allow for improved characterization of out-of-plane waves using ultrasonics.

3. **Experimental methods**

A unidirectional fiberglass laminate was manufactured containing an out-of-plane wave of aspect ratio 8. To do this, a cured resin wave was inserted between plies before they were infused. During the infusion process, a plate was placed on the top of the laminate so that the top surface wouldn't contain waviness. A sample is below in Fig. 3:

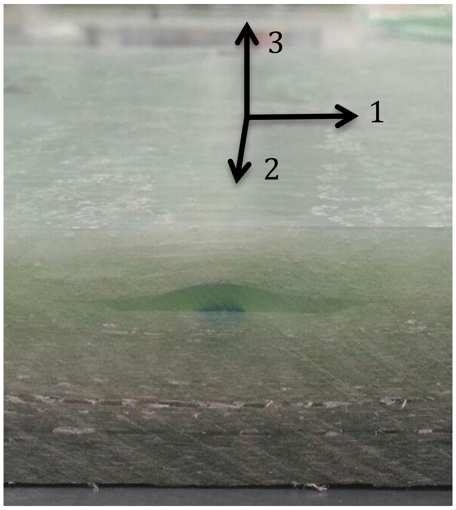

Figure 3: Fiber-glass laminate containing an out-of-plane wave of aspect ratio 8.

where 1 is the fiber direction, 2 is the direction perpendicular to 1 in the plane of each ply, and 3 is the thickness direction. A close up of the out-of-plane wave in the 1-3 plane is shown in Fig. 4 with labeling of the characteristic dimensions and regions within the laminate:

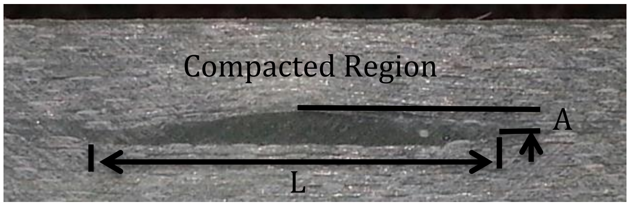

Figure 4: Characteristics of an out-of-plane wave in the 1-3 plane.

where L is the length and A is the amplitude. The compacted region consists of the plies above the root defect within the dimensions of the length of the wave. All other areas beyond the edges of the wave are referred to as the unaffected region. To determine change in fiber volume fraction, it was assumed that due to the relatively large width of each ply in the 2-direction as compared to the thickness in the 3-direction, compaction of fibers would only occur in the 3-direction and no spreading of fibers would occur in the 2-direction. With this assumption, increase in fiber volume fraction for a ply was represented with Eq. 2:

$$\frac{V_{f_c} - V_{f_o}}{V_{f_o}} = \frac{t_o}{t_c} - 1 \qquad (2)$$

where V_{f_c} and t_c are fiber volume fraction and ply thickness in the compacted region, and V_{f_o} and t_o are fiber volume fraction and ply thickness in the unaffected region. To measure the thicknesses of each ply, micrographs at 50X were taken in the 1-3 plane, both of the compacted and unaffected region.

Two techniques were used to make measurements in this experiment. The first thickness measurement was that of one ply layer plus its adjacent resin layer, which will be referred to as *measurement A*. The second thickness measurement was that only of the ply and is referred to as *measurement B*. The measurement techniques are shown in Fig. 5:

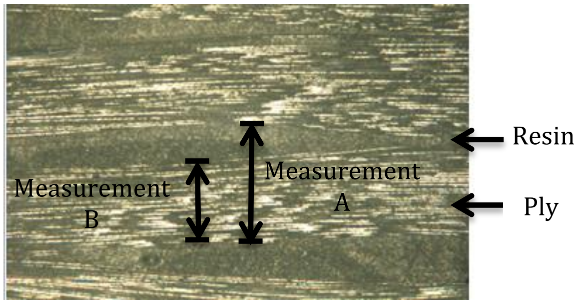

Figure 5: Micrograph (50X) displaying measurement techniques.

These measurements were made for each ply, both in the unaffected region and at the amplitude of the wave in compacted region, where the maximum compaction should occur. *Measurement A* is considered to be more representative of fiber volume fraction because it takes into account both resin and ply layer, yet including the resin layer measurement could mask a trend amongst ply thickness from the top of the laminate to the root defect. For this reason, ply thickness was measured as well.

Two techniques were also used for comparing measurements in the compacted region to that in the unaffected region and determining percent increase in fiber volume fraction. *Comparison A* used Eq. 2 as it is originally depicted, and compares each measurement in the unaffected region to that in the compacted region individually. *Comparison B* takes the average thickness of all the measurements in the unaffected region and compares that value to each measurement in the compacted region. For this situation, Eq. 2 will look as follows:

$$\frac{V_{f_c} - \overline{V_{f_o}}}{\overline{V_{f_o}}} = \frac{\overline{t_o}}{t_c} - 1 \qquad (2b)$$

where $\overline{V_{f_o}}$ and $\overline{t_o}$ are the average fiber volume fraction and thickness in the unaffected region, respectively. Data agreement with comparison A would show that increase in fiber volume fraction is dependent on the thickness in the unaffected region, while agreement with comparison B would show that a given thickness ply has a given fiber volume fraction.

Overall, four methods were used to attempt to cover any possible trends between percent change in fiber volume fraction and ply location within the laminate. The four methods are summarized in Table 1:

Method	Measurement	Comparison
1	A	A
2	B	A
3	A	B
4	B	B

Table 1: Summary of experimental methods by combining measurement and comparison techniques.

The method that was determined to be most effective in determining percent change in fiber volume fraction was used to calculate the density and longitudinal elastic modulus, Eq. 3a,b:

$$\rho = \rho_f V_f + \rho_m (1 - V_f) \qquad (3a)$$

$$E_1 = E_f V_f + E_m (1 - V_f) \qquad (3b)$$

where subscripts m and f represent the matrix and fiber, respectively. The unidirectional laminates used in this experiment were considered to be transversely isotropic. Micromechanical analysis determined the necessary properties to construct the compliance matrix, Eq. 4:

$$[S] = \begin{bmatrix} \frac{1}{E_1} & -\frac{\nu_{12}}{E_1} & -\frac{\nu_{13}}{E_1} & 0 & 0 & 0 \\ -\frac{\nu_{21}}{E_2} & \frac{1}{E_2} & -\frac{\nu_{23}}{E_1} & 0 & 0 & 0 \\ -\frac{\nu_{31}}{E_3} & -\frac{\nu_{23}}{E_3} & \frac{1}{E_3} & 0 & 0 & 0 \\ 0 & 0 & 0 & \frac{1}{G_{23}} & 0 & 0 \\ 0 & 0 & 0 & 0 & \frac{1}{G_{31}} & 0 \\ 0 & 0 & 0 & 0 & 0 & \frac{1}{G_{12}} \end{bmatrix} \tag{4}$$

Where ν is Poisson's ratio, G is the shear modulus, and E is Young's modulus. The inverse of the compliance matrix is known as the stiffness matrix, [C], which is critical to the determination of ultrasonic wave speed through a composite material.

4. Results

Measurements in the micrographs could not be made for actual size, so they were scaled to determine the percent increase in fiber volume fraction. For methods 1 and 2, several measurements were made of each ply in the unaffected region and uncertainty was reported as two standard deviations (95% CI). In the compacted region, uncertainty was based on the measuring tool precision. This information was used with multivariate first order error propagation to determine the uncertainty in the fiber volume fraction. The results for method 1 and 2 are shown below in Figs. 6 and 7:

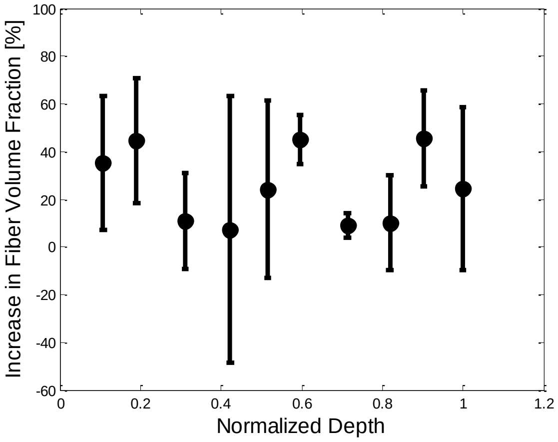

Figure 6: Method 1 - comparison of ply plus resin thickness from compacted region to unaffected region.

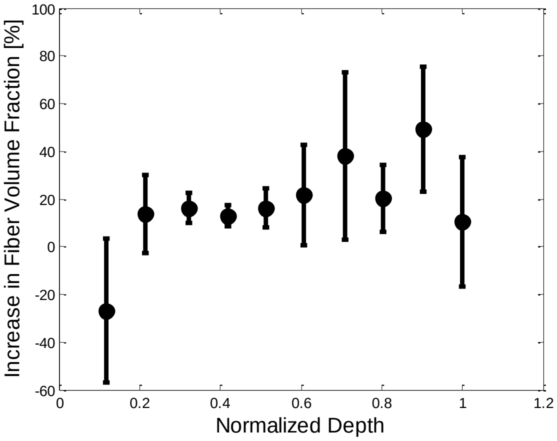

Figure 7: Method 2 - comparison of ply thickness from compacted region to unaffected region.

where depth is normalized by the distance from the laminate surface to the root defect. For methods 3 and 4, a measurement of each ply was made through the thickness of the unaffected region. An average was taken, and the uncertainty was again taken to be two standard deviations. Uncertainties for fiber volume fraction were then determined by the same means as in methods 1 and 2. The results for methods 3 and 4 are plotted in Fig. 8 and 9:

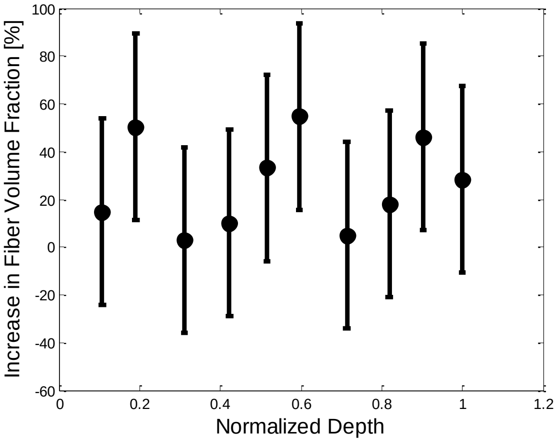

Figure 8: Method 3 – comparison of ply plus resin thickness in compacted region to the average in the unaffected region.

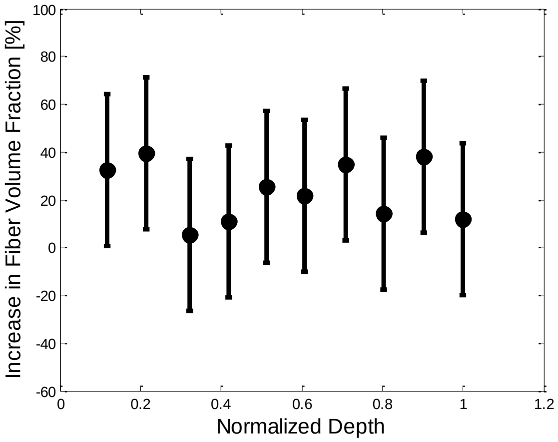

Figure 9: Method 4 – comparison of ply thickness in compacted region to the average in the unaffected region.

A summary of the average, standard deviation, and range of the percent increase in fiber volume fraction for each method is shown in Table 2:

	Increase in Fiber Volume Fraction [%]		
Method	*Average*	*Standard Deviation*	*Range*
1	24.6	16.6	38.1
2	22.0	13.0	38.9
3	26.4	19.1	51.9
4	23.3	12.5	34.2

Table 2: Comparison of Methods 1-4

The values above for method 2 do not include the results for the ply nearest the surface. This ply was visibly damaged in the micrograph, and it is unreasonable that the thickness in the unaffected region would be less than that of the compacted region. Table 2 shows that method 4 lead to the most consistent results. Assuming $\overline{V_{f_o}} = 0.6$, the percent increase in density and the values in the stiffness matrix were calculated for a percent increase in fiber volume fraction of 23.3%. The density of the laminate above the amplitude of the out-of-plane wave increased by 9.2% on average. The percent increase of each value in the stiffness matrix is shown below:

$$\frac{C_f}{C_o} = \begin{bmatrix} 22.3 & 40.9 & 40.9 & 0 & 0 & 0 \\ 40.9 & 52.7 & 53.5 & 0 & 0 & 0 \\ 40.9 & 53.5 & 52.7 & 0 & 0 & 0 \\ 0 & 0 & 0 & 52.2 & 0 & 0 \\ 0 & 0 & 0 & 0 & 57.5 & 0 \\ 0 & 0 & 0 & 0 & 0 & 57.5 \end{bmatrix} (\%)$$

5. Analysis and interpretation

The significant increase in density and the stiffness matrix display the potential for ultrasonic wave speed to be an important factor in identifying and characterizing out-of-plane waviness. A relationship between fiber volume fraction and wave size and depth would be useful in characterization. Figures 6 and 8, which display the results for measurements of the ply plus the adjacent resin layer, show no trend between ply depth and fiber volume fraction. Figure 6 shows that for some plies there is significant variation in individual measurements in the unaffected region, while for others there is little variation, and the uncertainty is minimal. The uncertainty in Fig. 8 represents the non-uniformity of measurements through the thickness in the unaffected region. This uncertainty is similar for all values since each measurement in the compacted region was compared to the same value, the average of the measurements in the unaffected region. Determining a correlation for fiber volume fraction and ply depth using measurement A would be ideal since it fully accounts for all the resin layers and plies within the laminate. Although, Fig. 6 and 8 seem to show that there is no correlation, and the effect of an out-of-plane wave on the ply and resin layer must be looked at separately.

The results in Figs. 7 and 9, which made measurements of ply thickness only, show a smaller range of results. Again, the first data point in Fig. 7 will not be considered since the ply was damaged in the unaffected region either during infusion or when polishing the sample to take the micrograph. Taking this into account, Fig. 7 seems to show the least error and the most consistent results. It can be seen that a horizontal line could be drawn to contain the vast majority of data point error bars. The horizontal nature of the data in Fig. 7 can be compared to the scatter of data in Fig. 9 to conclude that the percent increase in fiber volume fraction for each individual ply is more relevant than the increase from some known or averaged value. This matches well with the findings by Gutowski (1992) that there is no unique relationship for compaction of a fiber bundle. The fiber volume fraction of a ply under stress is dependent on the original state of the ply. This was shown experimentally in Fig. 1 on pg. 6-2 for similar fiber bundles. It was also shown, in Fig. 2 on pg. 6-3, that the stress verse fiber volume fraction curve could be shifted based on the original fiber bundle state such that all curves were coincident. Demonstrating that under a certain stress the change in fiber volume fraction is the same for similar fiber bundles with varying original fiber volume fractions. Assuming that above an out-of-plane wave the stress distribution in each ply is constant, the change in fiber volume fraction for each ply from the unaffected region to the compacted region should be the same.

Although there is not a significant difference, Fig. 7 compares percent difference in fiber volume fraction whereas Gutowski compares the actual difference. Using the same assumptions used to derive Eq. 2, it was determined that the difference in fiber volume fraction for a ply is proportional to the difference of the inverse ply thickness, Eq. 3:

$$V_{f_c} - V_{f_o} \propto \frac{1}{t_{f_c}} - \frac{1}{t_{f_o}} \tag{3}$$

where t_{f_c} and t_{f_o} are the thickness of the ply in the compacted and unaffected region, respectively. A weighted average of the change in fiber volume fraction for each ply was calculated based on the uncertainty in each value. The value of Eq. 3 for each ply is shown along with the weighted average in Fig. 10:

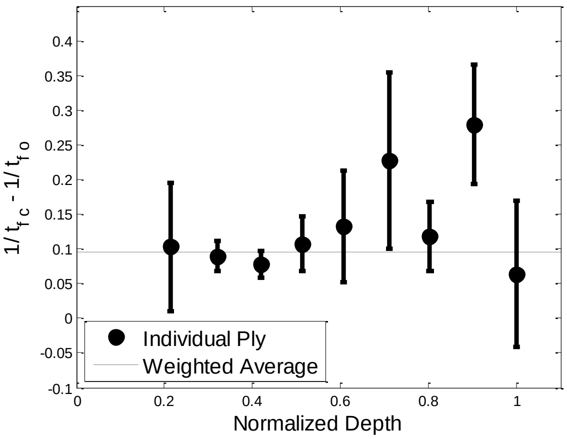

Figure 10: Comparison of experimental and predicted change in fiber volume fraction using method 2.

As can be seen above, the weighted average lies between the error bars of the majority of the data points, and it appears that the difference in fiber volume fraction from the compacted region to the unaffected region should be the same. In order to conclude this, future testing efforts must be made to reduce the uncertainty of ply thickness in the unaffected region. In this experiment, only one section of the unaffected region was analyzed. Several measurements were made for each ply, yet because of the limited size of the micrograph, they were made very close together. This could cause a localized variation in ply thickness to have a significant effect on the uncertainty. For future experiments, micrographs of the 1-3 plane should be taken at several locations in the unaffected region along the 1-direction. This will allow for more measurements over a broader span, decreasing the affect by localized variation in thickness. If uncertainties are successfully decreased and results don't show constant difference in fiber volume fraction, there are two primary possibilities for varying results. Either the stress in each ply is not constant through the thickness, or spreading of fibers is occurring in the 2-direction. The first cause is more difficult to determine, although, the second could be determined by taking a micrograph in the 2-3 plane of compacted and unaffected regions. Comparisons could be made between tow width and height between both regions to determine if spreading is occurring. If no spreading is occurring it can be assumed that the stress distribution changes with ply depth in the laminate. In this case, the change in fiber volume fraction will not be constant for plies above the root defect.

Confirming that the change in fiber volume fraction of each ply is constant would be an important contribution to the understanding of the effect out-of-plane waves, although understanding how resin layer thickness changes from the unaffected to compacted region is also imperative to creating a relationship between out-of-plane wave size and change in fiber volume fraction. By comparing Figs. 6 and 7, it can be seen that change in resin layer thickness is not the same through the thickness, and therefore another relationship must be developed.

6. Conclusions

Four methods were used to analyze the change in fiber volume fraction due to out-of-plane waviness. An out-of-plane wave of aspect ratio 8 that was 10 plies deep within the laminate caused an average increase in fiber volume fraction between 22 and 26 %. This resulted in an increase in density above the out-of-plane wave from 9 to 10% and even more significant increases in the values within the stiffness matrix. By comparing ply thickness in the compacted region to that in the unaffected region, it was shown that change in fiber volume fraction for each ply was approximately the same, no matter the depth of the ply within the laminate. This is attributed to the fact that there is no unique relationship between fiber volume fraction and stress applied for similar fiber bundles. Instead, the relationship between fiber volume fraction and applied stress is dependent on the original state of the fiber bundle. Although, as this experiment also found, under a certain stress the change in fiber volume fraction of similar fiber bundles is the same from an original state to some compacted state.

Understanding this phenomenon is an important piece to characterizing the change in fiber volume fraction due to an out-of-plane wave, yet, this experiment also showed that resin layer thickness does not follow the same trend that ply thickness does from the compacted region to the unaffected region. Determining the effects of out-of-plane waviness on resin layer thickness is also crucial to characterizing change in fiber volume fraction. Future research should focus on the effect out-of-plane waviness has on resin flow during infusion and explore how this affects the resin layers between plies. Pairing the understanding of ply thickness change found in this experiment to findings regarding the resin layers would allow for more accurate characterization of out-of-plane waves based on change in fiber volume fraction. Ideally, this will lead to effective identification of out-of-plane location and size based on ultrasonic wave speed.

Acknowledgements

Support for this research was provided by a National Science Foundation Research Experience for Undergraduates site program in Wind Energy Science Engineering and Policy (WESEP) grant number EEC-1063048 at Iowa State University.

References

Amenabar, I., A. Mendikute, A. Lopez-Arraiza, M. Lizaranzu, and J. Aurrekoetxea, 2011: Comparison and analysis of non-destructive testing techniques suitable for delamination inspection in wind turbine blades. *Composites: Part B*, **42**, 1298-1305, doi: 10.1016/j.compositesb.2011.01.025.

Chakrapani, S.K., V. Dayal, D. Barnard, A. Eldal, and R. Krafka, 2012: Ultrasonic Rayleigh wave inspection of waviness in wind turbine blades: Experimental and finite element method. *AIP Conf. Proc.*, **1430**, 1911-1917, doi: 10.1063/1.4716444.

Chen, B., E. J. Lang, and T. W. Chou, 2001: Experimental and theoretical studies of fabric compaction behavior in resin transfer molding. *Materials Science and Engineering: A*, **317(1)**, 188-196.

EIA, 2013:Levelized cost of new generation resources in the annual energy outlook 2013. *U.S. Energy Information Administration Annual Energy Outlook 2013*, DOE/EIA-0383.

Galappaththi, U.I.K., A. Picket, M. Draskovic, M. Capellaro, and A. De Silva, 2013: The Effect of Ply Waviness for the Fatigue Life of Composite Wind Turbine Blades. *Renewable Energy & Power Quality Journal*, **11.** ISSN 2172-038 X.

Gutowski, T. G. P. (Ed.), 1992: *Advanced composites manufacturing*. John Wiley & Sons.

Hsiao, H.M., and I.M. Daniel, 1996: Elastic properties of composites with fiber waviness. *Composites Part A: Applied Science and Manufacturing*, **27**, 931-941.

Jamieson, P., 2011: *Innovation in Wind Turbine Design*. John Wiley & Sons. ISBN: 1-119-97612-X.

Jasiuniene, E., R. Raisutis, A. Voleisis, and M. Jakas, 2008: Ultrasonic NDT of wind turbine blades using contact pulse-echo immersion testing with moving water container. *Ultrasound*, **63**, 28-32.

Nelson, J. W., D. S. Cairns, and T. R. Riddle, 2011: Manufacturing defects common to composite wind turbine blades: Effects of defects. *AIAA SDM Conference Denver*, doi: 10.2514/6.2011-1756.

Riddle, T. W., D. S. Cairns, and J. W. Nelson, 2011: Characterization of manufacturing defects common to composite wind turbine blades: Flaw characterization. *AIAA SDM Conference Denver*, doi: 10.2514/6.2011-1758.

Saunders, R. A., C. Lekakou, & M. G. Bader, 1998: Compression and microstructure of fibre plain woven cloths in the processing of polymer composites. *Composties Part A: Applied Science ad Manufacturing*, **29(4)**, 443-454.

Van Wyk, C. M., 1946: 20—Note on the compressibility of wool. *Journal of the Textile Institute Transactions*, **37(12)**, T285-T292.

A Comprehensive Approach to Health Monitoring and Management of Wind Energy Infrastructure Systems

LINDSEY J. WICKMAN
Wind Energy Science Engineering and Policy REU, Iowa State University, Ames, Iowa
Mentors: Dr. Halil Ceylan

Abstract

Advancements in micro-electro-mechanical systems (MEMS) sensors and wireless smart sensor networks provide opportunities for long-term, continuous, real-time health monitoring of wind energy infrastructure systems at low cost within the context of sustainable infrastructure systems. A number of recent studies have focused on the condition monitoring of wind energy converter's control system and turbine dynamics. There exists a need for the development of a detailed framework for systematic health monitoring of the entire wind energy infrastructure using wireless smart sensor technology. This is especially important for maintaining the increasing number of wind turbines to meet the U.S. goal of reaching 20 percent wind energy by 2030.

1. Introduction

According to the United States Department of Energy, wind energy has become the world's fastest growing renewable energy resource (Korkua, 2011). As the United States aims toward 20% of electricity generation from wind turbines there is an increasing need to develop a health monitoring system to improve the reliability and performance of the wind energy infrastructure. Through a multi-disciplinary approach this research attempts to identify advancements in micro-electro-mechanical systems (MEMS), nano-electro-mechanical systems (NEMS) technology, and wireless smart sensors networks that will provide opportunities for long-term, continuous, real time structural health monitoring. The goal is to understand the entire wind turbine system, including the responses of the structure and the interactions between the foundation and soil. Understanding the entire wind system could potentially lead to achieving optimal wind turbine designs. Within the wind turbine system several critical subsystems need to be monitored such as the rotor, drive train, generator, tower, blades, bearings, yaw joints, and shaft.

Several research studies and government funded projects are in the process of investigating cost effective monitoring and managing the health of wind turbines. For example, the UK Government Technology Strategy Board (TSB) funded 2 million UK-pound R&D project, "Advanced Health Management of Wind Turbine Transmissions (AHMWITT)" to demonstrate state-of-the-art wind turbine monitoring and health management techniques (Crowther, 2011).

A system-of-systems approach will be needed to effectively manage and monitor the health of wind farm. Wind farms are composed of individual wind turbines which include individual subsystems that contain critical components essential to the capture of the wind resource. Each individual subsystem needs to be monitored in order to obtain a comprehensive understanding of the wind farm. Thus, a network of wireless sensor can be deployed that can effectively communicate with each other the loading and health of individual wind turbines to gain knowledge of the health of the entire system that can immensely benefit wind farm owners and operators in terms of energy production and delivery, and manufacturers in terms of improved wind turbine designs, and quality control processes.

Recent studies show that predictive maintenance of wind turbines could provide a 50% reduction in overall maintenance cost compared to a reactive maintenance approach (Dana, 2011). In addition, a structural health monitoring system may reduce wind turbine life-cycle cost in turn making wind energy more affordable in the energy market. Information gathered could potentially be used in a condition based maintenance program that could minimize time needed for inspection of components, prevent unnecessary replacement of components, prevent failures, and allow utility companies to be confident of the power availability (Ciang et al., 2008). Current challenges facing the implementation of a system that would provide much needed monitoring is understanding turbine components and subsystems, determining maximum efficiency in monitoring which can include improved placement of sensors, methods of monitoring, communication techniques, and data acquisitions and storage.

Current wireless sensor networks (WSN) for structural health monitoring have several focused areas outside of wind energy infrastructures. Correlation can be made between specifics from other areas to improve the sensing system in wind turbines. Figure 1 shows the inclusion of several different fields within structural health monitoring that use wireless sensor networks. Incorporated into the infrastructure health monitoring sector is research on Intelligent Bridges in Germany. The German highway is suspect to challenges such as increasing traffic density and loads, climate change effects, and new quality requirements regarding sustainability. Similar challenges are seen for all highway systems. German federal road network includes 38,806 bridges which is valued at approximately 50 billion euros and constructed of approximately 90% concrete with a service life of 40 to 50 years with maintenance and repairs (Neumann and Haardt, 2012).

Structural Health Monitoring (SHM) has increasingly been implemented recently in both national and international applications in an attempt to support the maintenance management of engineering structures. For an Intelligent Bridge which parameters have to be measured to represent impacts or first indicators for deterioration is a leading defining task. Knowing the parameters, it is necessary to draw up an overview on the sensors available on the market, being able to provide the required measurements. Sensors on the market that are wireless and energy self-sufficient are being emphasized. Integrated or embedded sensors have the advantage of being protected by the structure itself. This may eliminate the risk of external damages and vandalism.

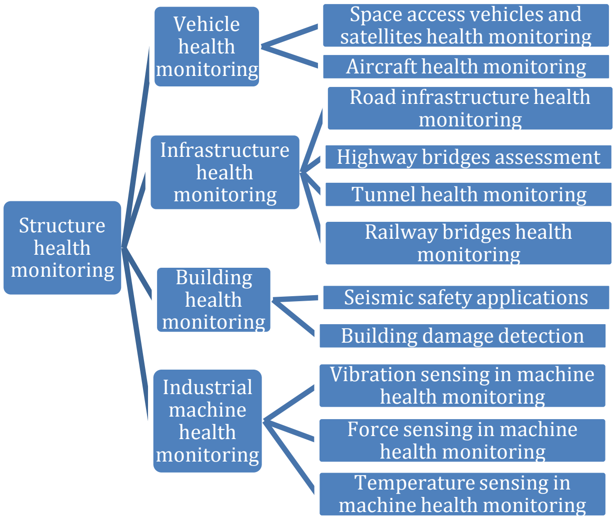

Figure 1. The classifications of WSNs for SHM applications (After Bengi et al., 2011).

The process being used for the Intelligent Bridges in Germany has the same methodology as the approach for WSNs for SHM of wind infrastructures. A relationship can assumed, since the foundation of a wind turbine infrastructure is under loads from the extreme amount of weight. In addition engineers are investigating how to increase the height of wind turbine towers to harvest a more reliable wind resource by constructing concrete towers.

Other multidisciplinary correlations are seen in monitoring soil moisture levels. Soil moisture and temperature are often of interest in the agricultural sector and soil moisture data has traditionally been collected using remote sensing techniques like radars and radiometers on-board satellites. Remote sensing covers reports data on the order of square kilometers. With recent advances in integrated wireless communication, sensing and processing technology has in-situ sensing become a feasible option. For gathering sufficient data for soil moisture sensing it is highly desirable to deploy moisture probes that are to deploy unmanned.

Similar information is desirable when developing a structural health monitoring system for a wind turbine as both weather and moisture can have effect on turbine performance. The planetary boundary layer (PBL), also known as the atmospheric boundary layer (ABL), is the lowest part of the atmosphere and its behavior is directly influenced by its contact with a planetary surface. Wind turbines can be influenced by the PBL.

1.1 Micro-Electro-Mechanical Systems

(MEMS) are miniature sensing devices that are able to interact with the environment to collect or change information. MEMS are often divided into three categories; sensors, actuators, and passive structures (Ceylan, 2013). With the implementation of MEMs into materials and structures condition and health monitoring can be performed along with integrity/damage detection, and structural control and repair. Sensors, more specifically, are transducers that often convert mechanical or thermal energy into electrical energy, whereas actuators perform the exact opposite function. With the third category, passive structures, no transducing occurs. MEMS are comprised of several components that give them there sensing ability such as piezoresistivity, piezoelectricity, and thermoelectricity.

MEMS can be thought of as involving both electronic and nonelectronic elements, and as performing functions that can include sensing, signal processing, actuation, display, and control. The design of MEMS devices must comprehend important system considerations including system partitioning, packaging, calibration, signal-to-noise ratio, stability, and reliability (Hilbert, 2008).

The potential benefits associated with the implementation of MEMS in a wind energy infrastructure include direct measurement of properties, readings closer to true in situ properties, high quantity and low cost, robust and improves ease of use, improves system reliability, and enhances overall system performance. Using MEMS in a wind energy infrastructure system could potentially provide crack monitoring, temperature monitoring, corrosion monitoring, and microcrack monitoring. Monitoring can be done remotely while gaining critical information from strain gauges and other sensors within the steel, concrete, and composite material structures.

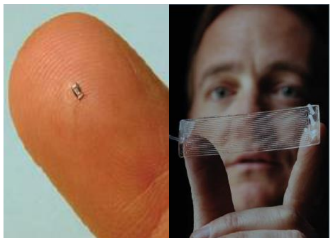

Figure 2. Left: Source: ADC USA, Inc.
Right: Source: Sandia National Labs

1.2 Turbine Components

The wind energy infrastructure system is composed of subsystems that play a critical role in the capture of the renewable resource wind. Failure in one subsystem can lead to detrimental outcomes for the entire wind turbine. Understanding components and interaction has been a focus of several research groups looking at health monitoring systems. A horizontal axis wind turbine is composed of four major components; the blades, the nacelle, the tower, and the foundation. The blades transfer a horizontal fluid flow into a rotational force that is then turned into electricity through a series of steps and are typically composed of a composite material. According to Meehan (2012), the basic composite material is formed by combining two or more distinct materials in attempt to achieve a higher stiffness to weight ratio. Due to this composition of non-isotopic material predicting mechanical properties becomes complex. The nacelle typically contains all components that transfer rotation of the blades into electricity. The tower must be able to support the weight of the nacelle and blades without failure and provides a path that connects the ground foundation to the nacelle (Meehan, 2012). The four components contain the essential subsystems including the rotor, rotor brakes, gear box, generator, drive train, speed shafts, yaw system, and electrical system. The configuration can be seen in figure 2 and the components inside the nacelle are shown in figure 3.

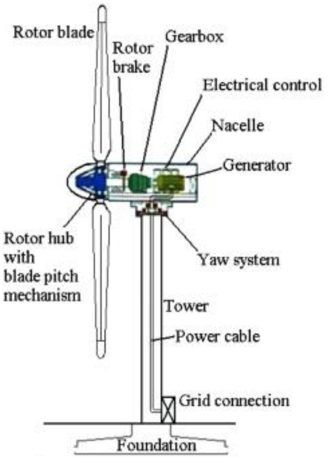

Figure 2. Typical configuration of horizontal wind turbine system (Ciang et al., 2008).

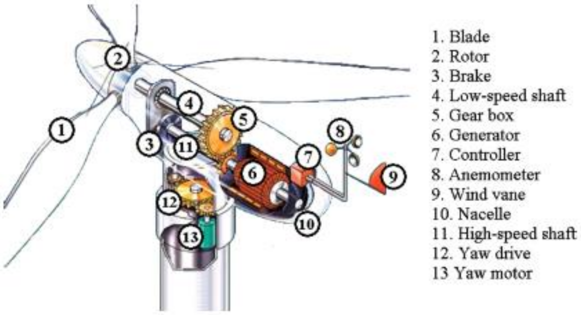

Figure 3. Components inside a wind turbine nacelle. Ciang et al. (2008).

In a health monitoring system, each aspect of the wind turbine that potentially could fail is examined and is of interest for researchers. A comprehensive health monitoring system is desired, but examining the frequency of specific damages to focus the structural health monitoring (SHM) system is of importance. A 15 year study in Germany shows that damage frequency to all the mechanical systems and to the structures is almost equal (Ciang et al., 2008). Figure 4 show the frequencies of certain failures, including failure of both mechanical and electrical components.

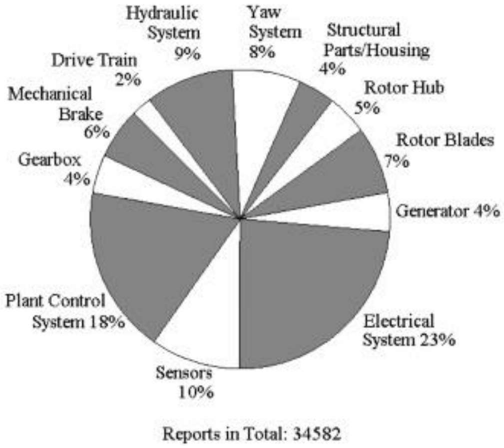

Figure 4. Unforeseen malfunction percentages for wind turbines in wind farm in Germany over 15 years. Ciang et al. (2008).

From Figure 4, the most often unforeseen malfunction occurs within the electrical system, the plant control system, and sensors, although this is true, measurable attention has been given to the structural health of the blades as they form the essential components of a wind power generation system and account for 15-20% of the total turbine cost. (Ciang et al., 2008). From this understanding, sensor placement becomes a critical component as to place both at common places of malfunctions but also implement in the location that costly damage could be detected.

2. Methods of Monitoring

An extensive number of devices are available for structural health monitoring. For a wind turbine infrastructure the devices used can be determined by what is desirable to detect. Detection is determined by typical damages seen throughout the wind turbine as outlines in Table 1 and Table 2. Table 2 is shown pictorially in figure 5. Specific measureable quantities that specific sensors can detect include strain, velocity, acceleration, temperature, vibration/frequency, and mass (unbalance).

Currently, wired SHM systems can be difficult to install and expensive to maintain. For a small-scale structure, installed sensor may cost $1000-$5000 per sensor and only increase as the structure becomes more complex. This motivates technologist to develop a low cost system that would collect data as accurately as a wired system to determine structural health. As a solution, wireless sensor networks (WSN) have emerged with the potential for low cost and easy installation. WSNs used for SHM needs to perform with no loss of data, data collection and transmission in real time and scalable to fit large structures such as a wind turbine (Krishnamurthy, 2008). Within the WSN several different network design parameters can be executed. As Krishnamurthy (2008) outlines, the key parameters are as follows:

- Fixed or Changing Topology
- Event Monitoring or Long Term Monitoring
- Local or Global Monitoring
- Baseline or Non-Baseline Damage Detection
- Input-output or Output-output Analysis

When considering these five design parameters the following must also be considered for hardware issues; sensor type, number of sensors, location of sensors, available bandwidth, sensor sensitivity, dynamic range, the acquisition/storage system, power/processor/memory requirements, sensor sampling interval, and cost (Krishnamurthy, 2008).

Table 1. Possible Wind Turbine Damage (Krishnamurthy, 2008).

Assembly	Possible defects
Rotor blade	Surface damage, cracks, structural discontinuities Damage to the lightning protection system
Drive train	Leakage, corrosion
Nacelle and force- and moment-transmitting components	Corrosion, cracks
Hydraulic system, pneumatic system	Leakage, corrosion
Tower and foundation	Corrosion, cracks
Safety devices, sensors and braking system	Damage, wear
Control system and electrics including transformer station and switchgear	Terminal, fastenings, functions, corrosion, dirt

Table 2. Typical Damage of wind turbine blades (Krishnamurthy, 2008).

Type	Description
Type 1	Damage formation and growth in the adhesive layer joining skin and main spar flanges (skin/adhesive debonding and/or main spar/adhesive layer debonding)
Type 2	Damage formation and growth in the adhesive layer joining the up- and downwind skins along leading and/or trailing edges (adhesive joint failure between skins)
Type 3	Damage formation and growth at the interface between face and core in sandwich panels in skins and main spar web (sandwich panel face/core debonding)
Type 4	Internal damage formation and growth in laminates in skin and/or main spar flanges under a tensile or compression load (delamination driven by a tensional or a buckling load)
Type 5	Splitting and fracture of separate fibres in laminates of the skin and main spar (fibre failure in tension; laminate failure in compression)
Type 6	Buckling of the skin due to damage formation and growth in the bond between skin and main spar under compressive load (skin/adhesive debonding induced by buckling, a specific type 1 case)
Type 7	Formation and growth of cracks in the gel-coat; debonding of the gel-coat from the skin (gel-oat cracking and gel-coat/skin debonding)

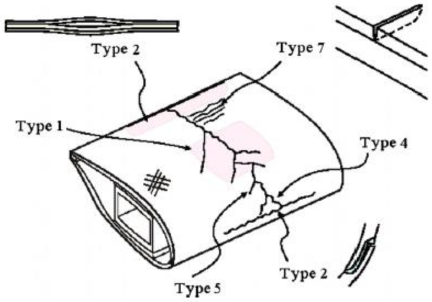

Figure 5. A pictorial representation of common damages found on a wind turbine blade as outline in Table 2. (Krishnamurthy, 2008).

To detect possible defects and the seven types of damage, several sensors are needed to sense parameters such as wind velocity, temperature, blade strain, moisture/humidity, angular position, torque, loading, blade acceleration, blade tip deflection, and blade imperfections (see Table A-1in the Appendix)

2.1 Strain Gauges

It appears that structural damage in the blade starts from inside and proceeds outward. In order to detect this, embedded MFSG may be a good option. However, there may be resistance from wind blade manufacturers to implement this due to potential lack of composite structural compliance. According to Meehan (2012), the MFSG shows the most promising for implementation (see figure 5). A 3-wire MFSG is required to accurately measure any thermal changes MFSGs work on the premise of a change in resistance of the wire is due to the change in length, cross-sectional area, and resistivity of the wire,

$$\frac{dR}{R} = \frac{d\rho}{\rho} + \frac{dL}{L} - \frac{dA}{A}$$

Where R, resistance, ρ, resistivity, L, length of wire, and A, cross sectional area of wire. (Meehan, 2012).

With collected stress data and understanding of the material properties, forecasting the possibility of the construction failures becomes feasible. For WSNs, typical low resistance strain gauges are not suitable as they have high power consumption which is not desirable for wireless application. An alternative to resistive strain gauges are sensors working on the capacitive principle. Working of the capacitive principle reduces the power consumption as well as increasing the resistance in the strain gauges (Berndt et al., 2012). In addition to power consumption, another challenge with strain gauges is the nature of the composite material of the blades. Strain gauges are typically designed for isotropic material as composite materials and orthotropic materials were few in development. The complication with strain gauges in orthotropic material is the difference in thermal expansion and the modulus of elasticity from the longitudinal to the transverse direction. Due to the orthotropic material having a thickness surface strains are no always indicative of what is occurring throughout the sampled material. (Meehan, 2012). With this complication emphasis is placed on the alignment and location of the gauge.

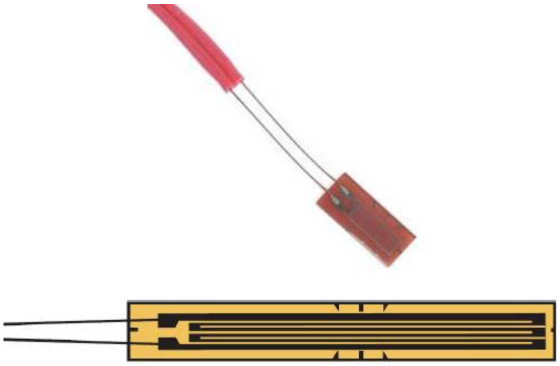

Figure 6. Metal Foil Strain Gauge (Meehan, 2012).

2.2 Fiber Optics

Advancement in telecommunication has led to precise fiber optic with multi-purposes including SHM. A reduction of cost as well as desirable size, fiber optics maybe implemented to monitor wind energy infrastructure. Fiber optics have proven to measure temperature accurately along with allowing multiple measurement location along a single fiber. The premise of fiber optics is such that cables allow light to pass through based on the internal refractive index of the fiber (see Figure 6).

A typical fiber optic implemented for SHM in composite is a Fiber Bragg Grating (FBG) which is attached to a test material to measure loads and to sense strain in the interested structure. FBG is classified as an intra-core grating because the cable causes scattered light to constructively add together with a specific wavelength. This wavelength is known as the Bragg wavelength. In addition to FBG, the Extrinsic Fabry-Perot Interferometer (EFPI) has promising characteristics. The EFPI uses two fiber optic fibers which allow the development of two signals to return to the receiver with a phases difference. As Meehan (2012) indicates, a combination of FBG and EFPI can accurately measure both strain and temperature in a structure.

Benefits associated with fiber optics as identified by Ciang et al. (2008) are that they are immune to drifts, have down-lead sensitivity, require no on-site calibration, and can be used to detect traverse crack evolution and impact damage. Discussion of the use of fiber optics for wind energy infrastructure estimate lifetime prediction and safeguarding of the stress level, especially for the blades. Current negatives include high cost.

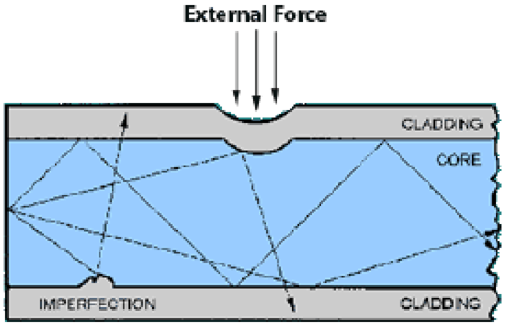

Figure 7. Basic fiber optic cable (Meehan, 2012)

2.3 Thermal Sensors

Thermal sensors maintain the ability to measure temperature, heat flow, or thermal conductivity. According to Gardner et al., temperature is the single most important device parameter due to the fact that almost every material has significant temperature dependence. Not only used to determine ambient temperature around the wind energy infrastructure, but MEMS operate more efficiently at a constant temperature. Therefore, thermal sensors are often packaged and embedded with a heating or cooling device regulated by a thermal sensor.

Several thermal sensor exist that can perform the necessary functions such as resistive temperature micro-sensors, micro-thermocouples, and thermotransistors (Gardner et al., 2001).

For implementation into the wind energy infrastructure thermocouples show benefit and promise in the WSN. Thermocouples are characterized by low cost, simplistic nature, and low profile, thermocouples provide dependent temperature devices. Thermocouples are controlled by the diameter of dissimilar metallic wires fused which make it a suitable device for implementation in composite turbine blades. Recognized issues with the use of thermocouples include the need for a current flow through the junction and often non-linear voltage response. (Figure 8)

Studies completed by Kim et al. (1992) investigated the use of thermocouples, Omega TT-J-36, in composite material to potential expose structural degradation. The composite material examined was developed with a symmetric nature of 18 plies thick with thermocouple gauges placed mid-plane. Kim et al. (1992) tested the material sample by performing compressive loading to failure and a three point bending to failure test. Results indicated that no significant changes in compressive or flexure strength of the composite material were found. Thus, implemented thermocouple sensors in composite material could be completed without degradation of the material. (Palmer, 2009).

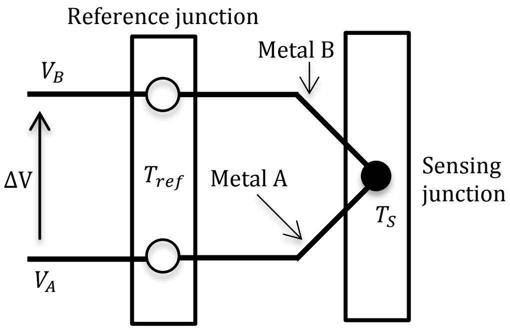

Figure 8. Basic Configuration of a thermocouple temperature sensor (Gardner et al., 2001).

2.4 Infrared Sensors

Infrared technology has been used in many different applications in military and civilian settings including night vision, environmental monitoring, biomedical diagnostics, and non-destructive testing. Infrared sensors work on the basis of detecting electromagnetic radiation with longer wavelengths than those of visible light (Liu, 2006).

Implementing infrared sensors on the blade would increase drag on blade as well as provided limited data collection due to small viewing window. This technology does provide internal flaw detection for blades. Infrared sensors have little application applied to MEMS and the knowledge would have to be improved before being applied in a WSN (Palmer, 2009).

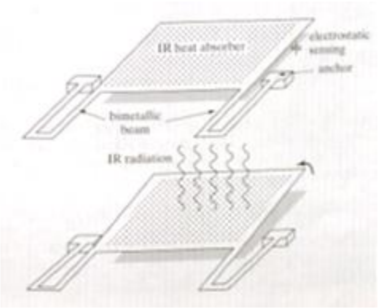

Figure 9. Infrared sensor based on the capacitive sensing (Liu, 2006).

2.5 Accelerometer

With the ability to accurately measure acceleration at a location on the wind energy infrastructure and several different types of accelerometer developed, accelerometers pose a specific interest for structural health monitoring. One specific type of accelerometer, piezoelectric accelerometer, use a mass to apply a force to the piezoelectric material. A change in the acceleration in the structure causes a force on the mass thus generating a charge in the piezo-material. Other accelerometers, such as a strain gage accelerometer work on a similar basis.

Accelerometers have shown a reliable way of monitoring forces applied to the surface of wind energy infrastructure blades but present challenges in embedding accelerometers sensors. The size of the sensors as well as the sensor accuracy during long steady acceleration may cause selection and implementation difficult (Palmer, 2009).

2.6 Humidity Sensors

As the authors of *Microsensors, Mems and Smart Devices* state there is a need for the development of a remote, wireless, and passive sensor system for humidity data collection that performs more accurately than conventional methods. The importance of measuring humidity is not only beneficial to the wind energy infrastructure but also to the proposed sensor network. Due to many electronics having humidity specification for optimal performance there implies a need to determined humidity throughout the structure (Gardner et al., 2001).

The effect of moisture produces a variety of outcomes. At high levels of humidity, the conductivity of permeable insulators increases ultimately leading to undesired malfunctions. On the other hand of the spectrum, very low humidity can cause different materials to become brittle or a build-up of static electricity, which may result in spontaneous shutdown of computers when discharges occur. Humidity in general is coupled with condensation which poses a danger to an electronic device. Condensation may coat circuit boards and other components potential causing short circuits inside sensing equipment. Short circuits may cause permanent damage if the equipment is powered on prior the condensation has evaporated (Gardner et al., 2001).

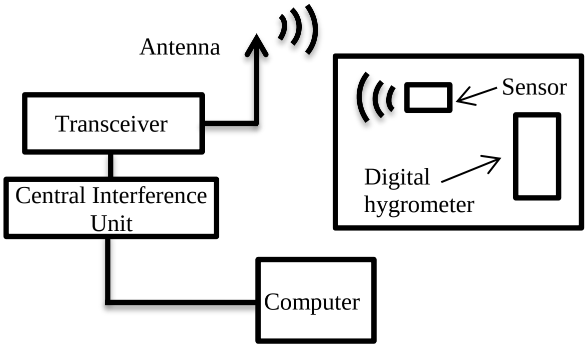

Figure 10. Setup for humidity measurement (Gardner et al., 2001).

2.7 Surface & Skin Sensors

There exist several applications of surface and skin sensors, but for the purpose of the report two specific sensors are explored and discussed.

The first is a skin sensor that can be embedded in concrete structures prior to casting. Performing as a resistor, the skin sensor consists of a carbon nanotube-cement based transducer. Abbreviated CNTCS for Carbon NanoTube Cement Sensor, is a self-sensing cement paste that can be applied over large linear segments or embedded as previously stated. CNTCSs have the potential to easily bind with the desired structure enabling the notion of an infinite set of potential sensor. With such notion, an increase in the sensitive volume is employed at maximum extent. The cementitious paste has the same durability as the monitored structure. The benefit of this is that the implemented sensor allow for long-term application with limited maintenance issues. The CNTCS work on the basis of local strain being transduced into a change in electrical resistance (Ubertini et al., 2013).

The second sensor proposed by Ubertini et al. consists of a Soft Elastomeric Capacitor (SEC) that can be deployed over large surfaces. The advantages of SEC are the relatively low cost and the possibility of meso-sensing. The SEC is fabricated from a poly-styrene-co-ethylene-butadiene-co-styrene (SEBS) matrix mixed with titanium dioxide (TiO2) sandwiched between electrode plates composed of SEBS mixed with carbon black (CB). The SEC works on the basis of monitoring local strain that is transduced in a change in capacitance. This sensor can be used to create an external sensing skin deployable in a network setup coving large structural surfaces.

Ubertini et al. performed two experiments, first an in-depth dynamic characterization of the sensors using a uniaxial test machine is conducted and second their performance at dynamic monitoring of a full-scale concrete beam was assessed and compared against o_-the-shelf accelerometers. The results of the experiment show that both the nanocomposite technologies compare well against mature sensors at vibration-based structural health monitoring, showing the promise of nanocomposite technologies at monitoring large-scale structural systems.

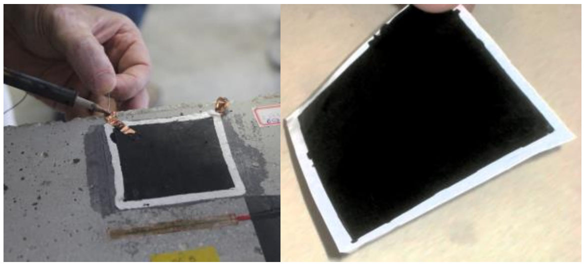

Figure 11. Visual of the Soft Elastomeric Capacitor (SEC) (Ubertini et al., 2013).

3. Sensor Placement

Location of sensors is critical to obtain desired data that provide information to perform health monitoring and proactive maintenance. According to findings presented by Ciang et al. (2008), sensors are placed in “Hot Spots” in the wind turbine infrastructure. These “Hot Spots” for both on-shore and off-shore wind turbines include the following:

a) 30-35% and 70% in chord length from the blade root
b) The root of the blade
c) Maximum chord
d) Upper spar cap/flange of the spar
e) Welded/bolted joints of tripod
f) Splash zone of towerThese “Hot Spots” represent areas more prone to damage and present increased fatigue in either simulation or experimental methods. E and F pertain specifically to off-shore wind turbines as the upper joint of the tripod is the most critical construction for fatigue design and the marine atmosphere presents a corrosive environment due to the humidity, temperature, airborne contaminants, and biological organisms (Ciang et al., 2008).

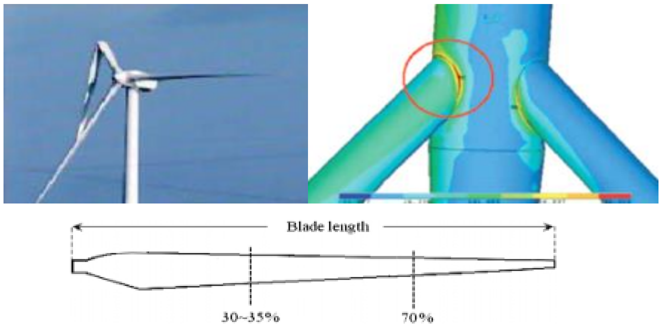

Figure 12. An example of a blade damage near 30% in length from the blade root, a). (upper left) Simulation result showing the stress hot spot of an off-shore wind turbine tower tripod, e). (upper right) The spanwise location of a blade that is likely to damage, a) (bottom) (Ciang et al., 2008).

4. Wireless Communication

From the basics, wireless communication is the transfer of information between two or more points that are not connected by any physical medium, Wireless communication can be in the form of multiple methods of data transferring such as radio waves, microwaves, RF, infrared. Focus over the last twenty years has been on computer and mobile phone networks, but a shift has begun in which the field of wireless sensor networks has exploded. Future networks will be dominated by small embedded sensors and devices. Current research is in the many areas including modulation schemes, design of power-efficient hardware, suitable medium access (MAC) protocol that are energy efficient, routing protocols (power efficient, data-centric, attribute-based addressing and location awareness), data aggregation, novel data dissemination algorithms, and application-layer query and dissemination protocols (Wong, 2012). According to K. Daniel Wong, some of the important characteristics of sensor networks are as follows:

- The number of nodes may be several orders of magnitude higher.
- Sensor networks might be more densely deployed.
- Individual sensors may not have global identification.
- Sensor networks may mainly broadcast, rather than unicast, data.
- Sensors tend to be limited in power, computational capabilities, memory, and so on.
- Individual sensors may have a high failure rate than a typical node in mobile ad hoc networks.

Communication for the wind energy infrastructure system happens at two different places due to the complexity of the sensor configuration. The first is the communication taking place among the sensor themselves. Typical sensor will communicate in a multihop path fashion which will be discussed further in 4.1 Ad Hoc Networks. The next place of communication occurs at the instrument or sensor level as it is communicating with the external devices such as computers or controllers that are part of the network. (Eren, 2006).

Radio Frequency (RF) which typically includes microwaves, allows users to influence existing infrastructure, utilize high-bandwidth flexibility in transmission schemes, and provide adequate networking over distances ranging up to tens of kilometers. Due to the layout of typical wind farms, RF communication could potentially provide an adequate methodology (Eren, 2006).

4.1 Ad Hoc Network

A collection of wireless mobile nodes that dynamically form a temporary network without the use of any existing network infrastructure or centralized communication is the simplistic definition of an ad hoc network. For the implementation in the wind energy infrastructure, ad hoc networks play a crucial role as the nodes or routers are able to freely move randomly, organize arbitrarily, and can be eventually connected to the internet. The connection to the internet can create an interface for easy display of data collected from the wireless sensors. Critical challenges facing the design of adequate routing protocol include multihop, mobility, network size, device heterogeneity, bandwidth, and battery power (Sarkar et al., 2013).

The concept of multihop is one in which a connection between a source and the destination is established over multi-hop path as the name implies (Murthy and Manoj, 2004). This is useful in the application of the wind energy infrastructure as the sensor can send information and data through sensors creating multiple hops before arriving to final destination potentially near foundation.

4.2 Noise

A common impairment with wireless communication occurs when noise enters the system. This is not the only difficulty that arises when information is being transferred through wireless means, as attenuation, delay, and data collision. Here a focus is placed on noise and the potential problems and solutions. To minimize the significance noise makes in the system the signal should be placed at higher power. (Note: very weak signals are typically on the order of 100dBm) The potential difference of minimizing the noise before it reaches the receiver is whether the receiver will be able to recover the transmitted signal or the receiver struggle with the noise fill signal hypothetically making it unusable. A critical question needed to be addressed is where the greatest concern for noise is (Wong, 2012).

According to K. Daniel Wong, the effect of the Signal-to-Noise Ratio (SNR) of noise added in the transmitter is much less than the effects on SNR of the same amount of noise added in the receiver. Therefore, there is an increased focus on the removal of noise from the receiving end to an extent as noise cannot be removed completely from the system. Noise will always exist in wireless communication. Classification of noise is important to identify potential noise entering the system and being able to minimize the source.

Several noteworthy types of noise include:

- Johnson-Nyquist noise
- Shot noise
- Flicker noise

As first outlined Johnson-Nyquist noise is also known as thermal noise and occurs when there exists an electrical conductor that is not at absolute zero. This then cause the charge carries to experience a “random” motion reflecting the energy associated with the nonzero temperature. Statistically, Johnson-Nyquist noise is characterized by additive white Gaussian. Shot noise is associated when there is a current carried by discrete charge carries resulting in random fluctuations of the current. Similar to Johnson-Nyquist noise, shot noise can be modeled as an additive white Gaussian. Lastly flicker noise transpires from trapping of charges and is often know as 1/f noise due to the noise having a probability density function that varies inversely with frequency (Wong, 2012).

5. Power Source

Research devoted to energy harvesting, the process of obtaining energy from the environment and transferring it to electrical energy, has been rapidly increasing. Used to prolong the lifespan of electrical devices, energy harvesting performs necessary functions that SHM and sensing network community. With a WSN it becomes critical for sensors to contain their own power such as conventional batteries. Currently wind turbines are estimated to be operational for 20 to 30 years. Since this is the case the conventional battery alone is not sufficient for wireless sensing. When the battery has consumed all of its power, the sensor must be retrieved and the battery replaced. Due to the remote placement of sensor the process of replacing can be expensive or even impossible. Research has recommended combining several energy harvesting strategies in order to capture energy in different situations and increase application capabilities (Park et al., 2008).

Typical ambient energies captured include sunlight, thermal gradient, vibrations, and ambient radio-frequency (RF) energy (Park et al., 2008).

5.1 Vibration

According to Park et al. (2008) one of the most effective methods of implementing an energy harvesting system is to use a mechanical vibration to apply strain energy to a piezoelectric material or to displace to an electromagnetic coil. Converting mechanical vibration to electrical energy has its challenges in generating significant energy to power electronics. In order to achieve a higher efficiency, it becomes necessary to match the resonance frequency of the transducer with the most distinct frequency of vibration source. However, the vibrations present in a structure, in this case the generator or another distinct subsystem in the wind infrastructure, is usually much lower than the resonance of a harvesting device and often fluctuates during operation. Therefore, this vibration does not always effectively couple energy to the harvester. Most research efforts are still in proof-of-concept demonstration in a laboratory setting such as Microstrain, Inc. (2007) development of a prototype of piezoelectric-based energy harvesters equipped with temperature and humidity sensors with wireless telemetry.

5.2 Thermal

A second method of obtaining energy from ambient sources is through the use of thermoelectric generators that capitalize on thermal gradients. Thermoelectric generators often use the Seebeck effect, which describes the effect of the current generated when the junction of two dissimilar metals experiences a temperature difference. Similar to the thermoelectric effect there is a direct conversion of temperature differences to electric voltage. A thermoelectric device creates voltage when there is a different temperature on each side. A mature technology and a reliable energy converter, the thermoelectric generator has no moving parts whereas vibration-based harvesters are built on the foundation of moving parts (Park et al., 2008).

Drawbacks of this technology are low efficiency when small temperature gradients present and the fabrication cost is high. In addition, the volume and weight are too large for microscale sensing systems needed for health monitoring systems. Therefore, recent advances made in nanotechnologies have focused on the creation of MEMS-scale thermoelectric generators (Park et al., 2008).

5.3 RF Wireless Transmission

Another way of supplying power to sensor networks within the turbine infrastructure is through the use of wireless energy transmission. In this case, power is generated elsewhere and transmitted to a sensor node by some form of electromagnetic wave or RF radiation.

Current efficiencies range between 50% and 80%. Research efforts in RF wireless energy transmission have been aimed at improving the conversion efficiency and maximizing the output power. Improved power output can be generated by designing efficient antennas among other research areas of interest. The application of a RF wireless energy transmission system for powering electronics typically used in distributed sensing networks has not been studied substantially in the past. Due to this, a new SHM sensing network was been proposed by integrating an energy transmission between the host and sensor node and uses this energy to both power the SHM sensing node and to transmit the signal back to the host (Park et al., 2008).

6. Knowledge Gaps and Research Priorities

Structural Health Monitoring for the wind energy infrastructure system is a multi-disciplinary obstacle that has considerable research potential and beneficial outcomes in the future. Taking a systems approach the infrastructure system contains several areas of interest, whether that be from the sensing perspective or communication viewpoint. Overall there exist pressing needs to establish a greater understanding of the systems that combine to generate the growing commodity of electricity.

From a civil engineering perspective, there exist similar holistic structural health monitoring of unique infrastructure systems such as roads and bridges. A similar approach for methodology could be followed to come to a means of in situ data collection and analysis. There are currently monitored roads with sensors collecting strain conditions with the interest of two specific categories of loading; mechanical loading and climatic loading. Both of the types of loading exist in the wind energy infrastructure system, with the main component of wind being of added interest due to the vertical nature of wind turbines compared to the horizontal characteristic of roads. Due to some overlap of infrastructure, future research needs to complete in depth examination of other working systems and make comparison to generate a working model for wind turbine.

As the sensing capabilities present challenges but also a crucial component to the overall WSN research needs to focus on producing a new generation of multi-functional systems. A sensor with multiple sensing parameters built into one package with a power source as well as communication ability that is all wireless, is highly desired. Research needs to be focused on increasing the survivability, power durability, and efficiency. Commercial off-the-shelf sensors need to be examined to have an understanding of baseline potential for new generation sensors. Researchers from here should improve current functions to output and create innovative sensor packaging.

Before reaching installation into manufactured wind energy infrastructure systems sensors must go through a series of testing to assess deficiencies and potential. Testing requires assessment of key components of research as mentioned; the survivability, power durability, ad efficiency. Such testing could include evaluating the survivability through freeze/thaw analysis. Further measurement could be analyzed by assessing real environment performance and functioning. Other aspects needing to consider is the direct environment in which the sensor is implemented. In the case of cement, there exist excessive amounts of acidity due to the alkali environment. This environment could potentially hinder the performance of the sensors.

Additional areas of interest to researcher could entail aspects of communication and data processing. Determination of the advantageous method of wireless communication whether via radio waves, micro waves, etc. With application of sensor there is no flawless method of communication but research aim at minimizing data loss, decreasing impairments such as noise, increasing reliability, and increasing resilience could maximize data transmission and therefor improving the wind energy infrastructure system. A balance of the requirements and trade-offs must be established.

From an alternative research approach, with continuous sensor collecting and sending data and increasing issue arises in the need to process and understand the critical failures and malfunction of the wind energy infrastructure system. Exploration of decision making controls and diagnostic algorithms should be at the forefront of interest to certain research groups. Such controls and algorithms should not only be established to maintain individual turbines output and performance but as well as assess an entire wind farm with a significantly larger number of turbines. Specific necessities of controls and algorithms should include notifying turbine owners of potential failures and malfunction before there occur in order to establish preventative maintenance. In addition to this feature, individual turbines should have the capability of shutting down to avoid damage without the need for human interference.

Research must determine the balance between the sensors, communication, and analysis in order to achieve an energy efficient wireless sensor network that enable structural health monitoring of the wind energy infrastructure system. The components of the balance are shown in Figure 13.

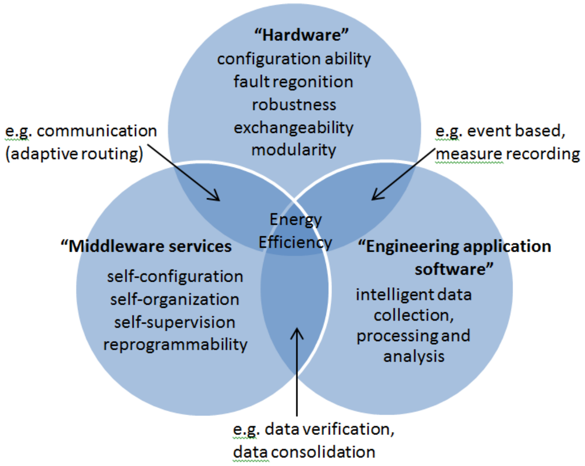

Figure13. Venn diagram of components necessary to achieve efficiency.

7. Summary and Recommendations

Following the literature review and synthesis, the research indicates that a systems approach is critical to provide a holistic system with the capabilities of providing both SHM as well as future management. Data collection will provide predictive maintenance along with management for individual turbine and entire wind farms. Management can take the form of cutting power for protective purposes, improving efficiencies, or even verifying theoretical models. Following the installment of research grade sensing systems additional research conclusions can be determined to support the future of wind energy.

From current research conclusions the following research grade wireless sensing network could advance the wind energy field (see Figure 14 a-c). From here there is potential to decrease the number of sensors after gaining a thorough understanding of the infrastructure system. Individual sensor are places at what researchers indicate to be critical points or “Hot Spots”. From there communication between sensors needs further research but end-to-end communication with acknowledgements could perform necessary functions. Lastly, the sensors may have multiple sensing capabilities packaged with energy harvesting devices.

Overall all technologies investigated must become wireless with power to transfer data to central location for significant data analysis.

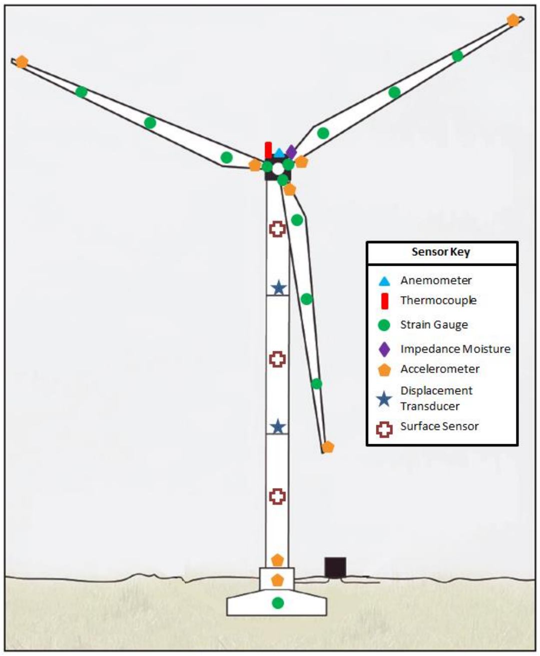

Figure 14 a) Suggested sensor type and placement for structural health monitoring and management of wind energy infrastructure system.

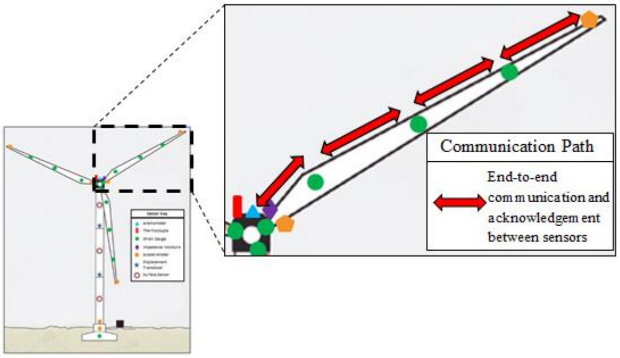

b) Suggested communication path with end-to-end communication and acknowledgment of data response between sensors.

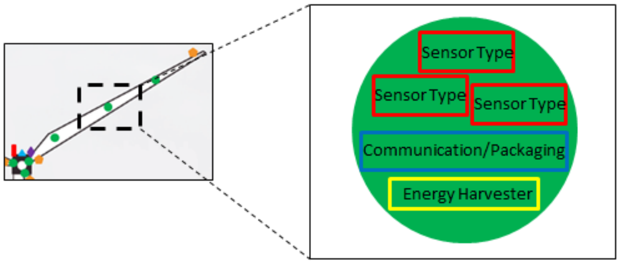

c) Suggested sensor arrangement with multiple sensor types, energy harvesting devices, and necessary packaging.

Acknowledgements

Support for this research was provided by a National Science Foundation Research Experience for Undergraduates site program in Wind Energy Science Engineering and Policy (WESEP) grant number EEC-1063048 at Iowa State University.

References

Dana, Scott Robert, 2011: Detection of blade damage and ice accretion for health monitoring of wind turbine using integrated blade sensors. MS Thesis, Mechanical Engineering Department, Purdue University. 129 pp.

Ubertini, F., S. Laflamme, H. Ceylan, A.L. Materazzi, G. Cerni, H. Saleen, A. D’Alessandro, A.Corradini, M. Fioriti, 2013: Novel Nanocomposite Technologies for Dynamic Monitoring of Structures: a Comparison between Embedded and Surface Sensors (Paper submitted for peer review to Structural Health Monitoring and Control, July 2013).

Ciang, C. C., J. Lee, and H. Bang, 2008: Structural health monitoring for a wind turbine system: A review of damage detection methods. *Meas. Sci. Technol*, **19,.** 1-21.

Ceylan, H., 2013: Use of Smart Sensor Systems for Health Monitoring of the Transportation Infrastructure System. *Presentation at the University of Perugia.*

Hilbert, Jeffrey L., 2008: RF-MEMS for Wireless Communications. IEEE Communications Magazine, 68-74.

Kim, Ki-Soo, Breslauer, Menachem and Springer, George**.** Stanford. The Effect of Embedded Sensors on the Strength of Composite Laminates. *Journal of Reinforced Plastics and Composites* , 1992, Vol. Vol. II. 0731-6844/92/08 0949-10.

Liu, Chang. *Foundations of MEMS*. Upper Saddle River, NJ: Pearson/Prentice Hall, 2006.

Crowther, A., 2011: Using Prognostics and Diagnostics for Wind Farm Health Monitoring. Romax Technology. NREL Presentation [available online at: http://www.nrel.gov/wind/pdfs/day1_sessioniii_04_crowther_romax.pdf]

Wong, Daniel K. *Fundamentals of Wireless Communication Engineering Technologies*. Hoboken: John Wiley & Sons, 2012.

Sarkar, S.K., T.G. Basavaraju, and C. Puttamadappa. *Ad Hoc Mobile Wireless Networks: Principles, Protocols, and Applications*. 2nd ed. Boca Raton: CRC: Taylor & Francis Group, 2013.

Eren, Halit. *Wireless Sensors and Instruments: Networks, Design, and Applications*. Boca Raton, FL: Taylor & Francis, 2006.

Murthy, C. Siva Ram., and B. S. Manoj. *Ad Hoc Wireless Networks: Architectures and Protocols*. Upper Saddle River, NJ: Prentice Hall/PTR, 2004.

Gardner, J. W., Varadan, V. K., & Awadelkarim, O. O. (2001). *Microsensors, MEMS, and Smart Devices*. Chichester: J. Wiley.

M. Berndt, T. Fellner, R. Zeiser, and J. Wilde, 2012: Energy-Efficient Strain Gauges for the Wireless Condition Monitoring Systems in Mechanical Engineering. *6th European Workshop on Structural Health Monitorin.*

T. Neumann, P. Haardt, 2012: Intelligent Bridges-Adaptive Systems for Information and Holistic Evaluation in Real Time. *6th European Workshop on Structural Health Monitorin.*

G. Park, T. Rosing, M. D. Todd, C. R. Farrar, W. Hadgkiss, 2008: Energy Harvesting for Structural Health Monitoring Sensor Networks. *Journal of Infrastructure Systems, ASCE,* **14,** 64-79.

Ghoshal, A., M. J. Dundaresan, M. J. Shulz, and P. F. Pai., 20xx?): Structural health monitoring techniques for wind turbine blades." *J. of Wind Engineering and Industrial Aerodynamics*, **85**, 1-16.

Meehan, Edward Charles, 2012: Development of embedded sensors for structural health monitoring of wind. MS Thesis, Department of Mechanical Engineering, Montana State University. 106 pp.

Korkua, Suratsavadee Koonlaboon, 2011: Wireless Health Monitoring and Improvement System for Wind Turbine. PhD Dissertation, The University of Texas at Arlington. 114 pp.

Krishnamurthy, Vidya, 2008: Wireless sensor network for structural health monitoring. PhD Dissertation, Department of Electrical and Computer Engineering, Clarkson University. 215 pp.

Palmer, Nathan Reed, 2009: Smart Composites; Evaluation of Embedded Sensors in Composite Material. MS Thesis, Mechanical Engineering Department, Montana State University. 237pp.

Appendices

Table A-1. Decision Matrix of what conditions on an industrial blade were deemed important. Palmer (2009)

What to sense	Why to sense	Comments	How	Where (location)	Final
Wind Velocity	Extreme wind velocities for monitoring limitations	May already be velocity sensors on turbines, but used to identify possible failure situations	Wind speed sensor, Anemometer	Top of tower or Nacelle	9
Temperature	Extreme variations to correspond with other data and corrections	May already be temperature sensors on turbines, but used to identify possible failure situations	Thermocouple, RTD, digital thermometers	Top of tower or Nacelle	6
Blade Strain	Check for extreme strain along blade length and leading/trailing edges	Check for delamination and strain at different positions along the blade	Metal Foil, Piezoelectric, Fiber Optics	At various locations along blade: base, max	1

				chord length, tip, leading and trailing edges	
Moisture/ Humidity	Moisture could affect material properties	Moisture accumulation along blade	Impedance moisture sensors	Atmosphere location, Top of tower or Nacelle	5
Angular Position	To correct with other acquired data for efficiency purposes	Used in conjunction with optimizing efficiency	In conjunction with other traim adjustment systems	Base of blades	8
Torque	Possible torsion at base of blades	Torque could lead to blade failure	Infrared (IR), FM transmitter, Strain Gages	Base of blade towards Nacelle	10
Loading	Excessive loads will lead to fatigue	Modeling of design or life purposes	Associated with Strain	Various locations along blade length	7
Blade Acceleration	Extreme changes in velocity could lead to failure	To model excessive changes in force	Piezoelectric, Accelerometers, Capacitive, Accelerometers, MEMS	Internally at tip where acceleration is greatest	4
Blade Tip Deflection	To avoid tower strikes	Keep overall blade tip deflection in check	Optical, Infrared (IR), Accelerometers	Attached to base at blade length to sense blade tip position	2
Blade Imperfections	To check for impurities within blade material	Non-destructive testing, cracks, voids	Ultrasonic, Acoustic	Ideally along entire blade length	3

Table A-2. Sensor groups considered in composites integration study. Palmer (2009).

Sensors	Impetus	Comments
Metal Foil Strain Gages	Reliable, well understood strain sensor with a relatively low profile. Relatively in expensive	Not well known as a reliable long term sensor in an environment where cyclical loading is present. Strain range is considerable less than that of fiberglass composites
Piezoelectric Films	Great dynamic strain sensor, also capable of monitoring temperature fluctuations, without a supply source	Not a reliable static load strain sensor. Also very susceptible to electromagnetic interference
Fiber Optic Cables	Innovative, strain sensor capable of monitoring strain in multiple locations using one fiber. Capable of also monitoring temperature changes	While not susceptible to electromagnetic interference. The sensor integration into manufacturing is formattable due to brittle nature of the fibers
Thermocouple	Simple, accurate sensor to monitor blade temperature	Due to the Seebeck effect a reference junction is needed
Ambient Humidity Sensor	Determine humidity levels which might be detrimental to blade longevity	Profile would make embedment problematic as well as potentially increasing drag if places on the exterior of the blade
Tri-axis Accelerometer	Reliable way of monitoring the forces applied to the surface of the blades	Size of sensor could inhibit embedment
Infrared emitter	Internal flaw detection	Increased drag on blade, as well as limited viewing window

Measurements of Wind Turbine Wake Conditions in a Utility-Scale Midwest Wind Farm

ERIN M. JACKSON
Wind Energy Science Engineering and Policy REU, Iowa State University, Ames, Iowa
Mentors: Eugene S. Takle and Daniel A. Rajewski

Abstract

The interaction of wakes between individual turbines has two known negative consequences: (1) loss of energy produced and (2) increased fatigue loading. By better understanding wake interactions and their effects on power losses, wind farm owners will be better able to predict their power losses and wind farms will be able to develop the most cost-efficient and effective design in order to maximize power outputs. There is a lack of research conducted in the area of wake interactions on onshore utility-scale wind farms. With the use of CWEX (Crop/Wind-Energy Experiment) 2010 and 2011 data, wake interactions on an onshore utility-scale wind farm were quantified and analyzed using statistical analysis in order to understand the interaction of turbine-created wakes down a single line of turbines and between multiple lines of turbines. In addition, one important variable in turbulence intensity, the thrust coefficient (C_T), was quantified and related to nacelle wind speed. Future research needs to be conducted on the far-wake interactions on turbines at opposite ends of a wind farm, along with the effects of turbulence on local atmospheric conditions.

1. Introduction

In 2008, the U.S. Department of Energy published a report titled 20% Wind Energy by 2030: Increasing Wind Energy's Contribution to U.S. Electric Supply, which outlined the major challenges associated with increasing wind energy from the current level of 3.5% to 20% of our nation's total energy supply DOE (2008). Although there are many challenges accompanying this goal, including improving the current U.S. transmission system, addressing local environmental and wildlife concerns, making enhancements to the current electric grid that will allow wind energy to be a competitive member of the energy market, perhaps the leading challenge will be to reduce wind capital costs. In order to decrease costs, wind turbine performance must be enhanced through design improvements, new monitoring systems and reliable turbine components that will increase the lifetime of the turbine DOE (2008).

Wind farms used for utility-scale applications are composed of tens or hundreds of individual horizontal-axis turbines, usually with a capacity of 1.5 MW or greater, that are installed over an area encompassing many square kilometers Wharton and Lundquist (2012). On modern wind farms, it is common to find two to four wind turbines installed per square kilometer. Each turbine on the wind farm produces electricity by rotating their blades and converting horizontal momentum in the airflow into rotation of a generator (Wharton and Lundquist (2012). The rotor disk is the term often used to refer to the area swept by the turbine blades. A region called a wake, characterized by reduced wind speeds and increased turbulence, exists downwind of each turbine as a direct result of the interaction between the flow and the rotor (Wharton et. al 2012). As a wake moves from one turbine to the next, it removes momentum from the flow, and therefore, less momentum is available for the downwind turbine to extract and use.

The interaction of wakes between individual turbines has two consequences: (1) loss of energy produced and (2) increased fatigue loading. In addition to decreasing the lifetime of turbines, previous studies have shown that the interference of wakes created by the rotating blades as the wind flows down a row of turbines changes the amount of power produced at each successive turbine Flowers (2012).

By better understanding wakes and their impact on turbine power losses, wind farm owners will be able to better predict their power losses. This research will also help wind farms develop the most cost-efficient and effective design in order to maximize power outputs. A combination of more accurate meteorological forecasts on wind farms and a change in wind farm design will ultimately lead to lower production costs and enriched turbine performance.

2. Literature review

Several recent studies have concluded that as wind flows down a row of turbines, the power produced at each successive turbine changes due to the interference of wakes.

The interaction of wakes has a profound impact on wind turbine power output. Studies have shown that maximum wake impact occurs at the lead turbine and then decays logarithmically with distance from the lead turbine. The power output decreases significantly after the first turbine, but then it increases to 60-70% of the initial value Flowers (2012). There have been studies conducted to analyze the effects of wakes on a single line of turbines, but there has been little research conducted on the interaction of wakes between multiple lines of turbines.

Until recently, research on the effects of wakes was scarce. Even today, a majority of the research on wakes has been conducted on offshore wind farms as opposed to onshore wind farms. Barthelmie (2005, 2007, 2009, 2010) has focused on studying offshore wind farms and, in particular, wake formation and modeling for large offshore wind farms. Barthelmie et al (2005) used six state-of-the-art wake models to observe wind speeds within a wake and free-stream conditions between 1.7D and 7.4D from an offshore wind turbine. According to this study, the large range of velocity deficits at hub height between the models suggests that there is not a direct connection between velocity deficits at hub height and distance from the turbine Barthelmie et al (2005).

One of the models analyzed in Barthelmie et al (2005) is the Risø WaSP (Wind Atlas Analysis and Application Program) model, which is used in the wind energy industry to estimate long-term energy production of wind turbines and wind farms. The WaSP contains a simple wake model that is based on the linear expansion of a wake downstream. The velocity deficit in WaSP is calculated using the following equation:

$$U_{wake} = U_{freestream}\left[1-\left(1-\sqrt{1-C_T}\right)\left(\frac{D}{D+2k_{wake}X}\right)^2\right] \quad (1)$$

In this equation, C_T represents the thrust coefficient (determined for a specific wind turbine at a specific free-stream speed), D is the rotor diameter of the turbine, X is the downstream distance from the turbine and k_{wake} is the wake decay constant (suggested as 0.05 for offshore wind farms and 0.075 for onshore wind farms). Because the near wake is not specified, the WAsP model is only valid for distances greater than 3D, or the far wake measurements. Although the WAsP model operates beyond its specifications, it has been shown to accurately capture wake losses.

Atmospheric turbulence is the set of seemingly random and continuously changing air motions that are superimposed on the wind's average motion Wharton (2012). This variation of motions can affect wind turbines in a variety of ways including: power performance, turbine loads, fatigue and wake effects and noise propagation. In the wind energy industry, turbulence is quantified using a metric called turbulence intensity – the standard deviation of the horizontal wind speed divided by the average wind speed over some time period (usually 10 minutes) Wharton (2012). Another equation used to analyze wake effects is the effective turbulence intensity equation, which determines fatigue loads for different cases considering different thrust coefficients Frohboese (2010). The equation for effective turbulence intensity is defined as follows:

$$I_{eff} = \frac{1}{V_{hub}}\left[(1-Np_w)\sigma^m + p_w \sum_{i=1}^{N} \sigma_T^m\,(d_i)\right]^{\frac{1}{m}} \quad (2)$$

In this equation, V_{hub} is defined as the average wind speed a hub height, N is the number of neighboring wind turbines, p_w is the probability density function of the wind direction, m is the Woehler exponent and σ is the ambient wind speed standard deviation. Equation 2 uses the generic thrust coefficient and individual turbine specific thrust coefficient values as input parameters to characterize the wake effect created by the specific turbine. Therefore, the added turbulence created by the wake effect will be a function of the thrust coefficient Frohboese (2010). The higher the value of C_T is, then the larger the wake expansion will be Kulunk (2011). The equation used to quantify the generic thrust coefficient value is defined as follows:

$$C_T = \frac{7c}{V_{hub}} \quad (3)$$

To use this equation, consider c to be a constant equal to 1. According to Frohboese (2010), the value of this approximation is about 8/9, or 0.88, and is supposed to fit for most modern turbines. The effective turbulence intensity calculated by using the generic turbine thrust coefficient values are conservative compared to results obtained by using turbine specific thrust coefficients Kulunk (2011).

Barthelemie et al. (2007) quantified wake effects offshore at a tightly spaced, 40 MW Middelgrunden wind farm. They used their result to evaluate the execution of state-of-the-art models in terms of predicted wake losses and wake-induced turbulence intensity under a variety of wind speed conditions. That study used two different methods to estimate turbulence intensity: one based on the mean and standard deviation of wind speed from the nacelle anemometer and another from the mean power output and its standard deviation. The power standard deviation method displayed a direct relationship between turbulence intensity and wind speed. In addition, results showed that turbulence intensity is about 9% higher when calculated using the data from the nacelle anemometer as opposed to the power standard deviation method. Therefore, the power standard deviation method gives a better representation of ambient turbulence in non-wake conditions in comparison to the nacelle anemometer method Barthelemie et al (2007).

According to Barthelemie et al (2007), the power losses due to turbine wakes experienced by large offshore wind farms is approximately 10-20% of the total potential power output of the wind farm. In addition to power losses, wake-generated turbulence also causes fatigue of parts and hence affects turbine lifetimes (expected to be about 20 years).

The interaction between wakes is complex and interconnected, which limits our ability to predict them accurately. An unanswered questions is whether the interactions that have been observed on the offshore wind farms Barthelemie (2007, 2009, 2010) can be applied to onshore operations.

3. Experimental methods

3.1 Site Layout

Data analyzed in this study comes from the Crop/Wind-energy Experiment (CWEX) (Rajewski et al., 2013) 2010 and 2011 data sets from an Iowa wind farm. CWEX is a multi-agency, multi-disciplinary research experiment whose goals are to understand the interaction between wind energy, meteorology and crop agriculture. CWEX research is conducted in a central Iowa utility-scale wind farm consisting of 200 turbines. These turbines have a hub height of 80 meters, rotor diameter of 74 m. Rated for winds of 12 m/s, these turbines cut-in at wind speeds of 3 m/s and cut-out at 25 m/s.

Figure 1 shows the layout of the wind farm observed. The turbines monitored form two lines, both oriented in the East-West direction. The A-line, composed of 5 turbines, is located 1.7 kilometers north of the B-line, which is comprised of 8 turbines. With the exception of turbines B7 and B8, both lines of turbines were equally spaced along their respective lines with a distance of 282 m, or approximately 3.8 rotor diameters, between each turbine. B7 sits 550 m to the northeast of B6 (300 m east and 460 m north). Turbine B8 is positioned in the same direction as B7 from B6, just 282 meters beyond B7.

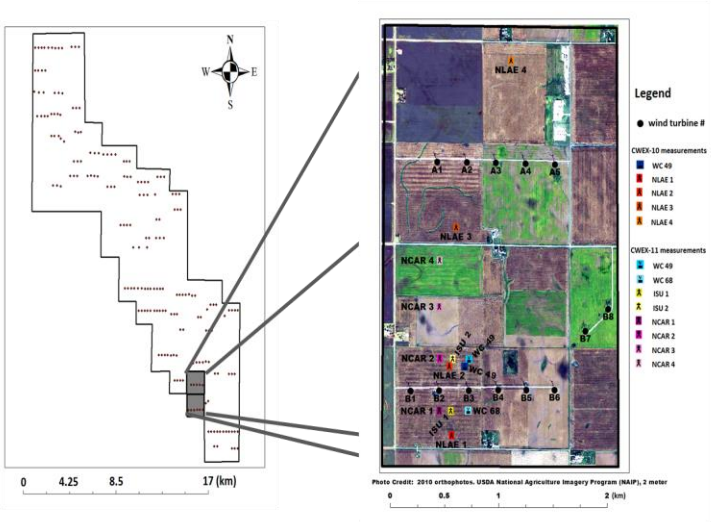

Figure 1: Overlay of the wind farm boundaries with a detailed view of the measurement locations for CWEX-10 and CWEX-11.

The turbine data archive consists of 10-min averages of higher frequency nacelle-based wind speed, yaw angle (direction), air temperature and power generated for each turbine. Wind speed is measured behind the blades of turbines as they face the wind, usually coming from the South. Thus, these wind speeds do not represent free stream airflow. Measurements were taken in the vicinity of the leading-line of turbines, designated as the B-line for the predominant wind direction (south to south-southeast) during mid-to late summer. Wind roses of the nearby Marshalltown, Iowa airport for the months of a) January and b) July are presented in Figure 2. Additional wind roses are provided by the Iowa Environmental Mesonet. (http://mesonet.agron.iastate.edu/sites/windrose.phtml?network=IA_ASOS).

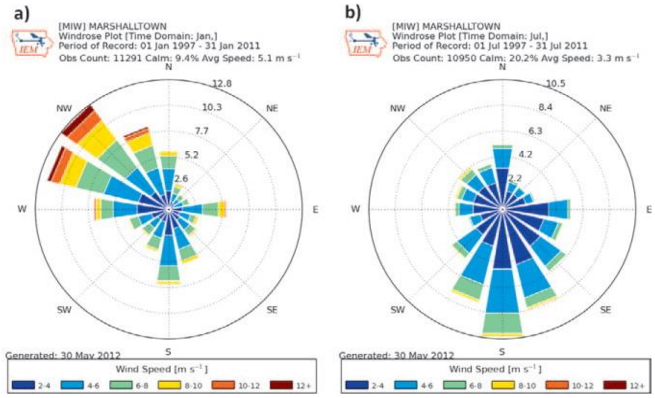

Figure 2: Climatological 10-m wind roses of the nearby Marshalltown airport for the months of a) Jan. and b) July.

3.2 Power Output

From previous studies, particularly Flowers (2012), we know that both the wind speed and power generated at each nacelle are influenced most when the wind direction aligns with the line of turbines (due East or due West). To better understand these wake interactions, the normalized (ratio of value at a downwind turbine in comparison to lead turbine) power and wind speed were analyzed. For this analysis, the normalized power ratio at the lead turbine is always 1, while the ratios for the following turbines usually have a value less than one.

3.3 Thrust Coefficient

Although individual turbulent motions are essentially unpredictable, some properties of turbulence can be analyzed in a statistical sense. Equation 1 was used to analyze the wake effect on a specific turbine in a line of turbines. $U_{freestream}$ represented the wind speed at the lead turbine and U_{wake} represented the wind speed at the second turbine in the line. Both values were found in our 10-min average data sets. Because the wind speed measured at the hub is only some fraction, a, of the real, undisturbed wind,

$$U_{turbine\ 1} = a * U_{freestream}$$

You can assume that the same is true for the second turbine in the line, so

$$U_{turbine\ 2} = a * U_{wake\ of\ turbine\ 1}$$

Therefore, $$\frac{U_{wake\ of\ turbine\ 1}}{U_{freestream}} = \frac{U_{turbine\ 2}}{U_{turbine\ 1}} \qquad (4)$$

By setting Equation 4 equal to the bracketed values in Equation 1, we were able to solve the equation for C_T. Our final equation for C_T was as follows:

$$C_T = \left(\frac{\frac{U_{turbine\ 2}}{U_{turbine\ 1}} - 1}{\left(\frac{D}{D + K_{wake} X}\right)^2} \right)^2 \qquad (5)$$

The values that were used in this equation included: wind speed at the second turbine in the line for $U_{turbine\ 2}$, wind speed at the lead turbine in the line for $U_{turbine\ 1}$, the rotor diameter of the turbine for D (in this case, this value was 77 meters), the downstream distance from the lead turbine as X (each turbine has a separation of 3.8D, or 282 meters, between them) and 0.075 for the onshore value of K_{wake}.

3.4 Wake Interactions

Due to the complexity of wakes, we decided to analyze the interaction of wakes at a particular wind direction of 190°. The goal of this analysis was to assess how many turbines are affected for each individual turbine wake and to analyze the variation on wind speed and direction.

We first evaluated single wake interactions. Using computer wake animations (Russ Doorenbos, private communication), nine different single wake interactions between turbines on both the A-line and B-line were identified. The yaw angle at which each single wake interaction was strongest was noted. Using this angle along with various distance measurements, the distance between the two turbines involved in each single wake interaction was calculated (in rotor diameters of 74 m). The SCADA (Supervisory Control and Data Acquisition) data for each turbine were then used to create a power ratio for every single wake interaction analyzed. The power ratio used was as follows:

$$Power\ ratio = \frac{P_{downwind}}{P_{upwind}}$$

In this equation, $P_{downwind}$ represents the power output (in kW) of the downwind turbine in the wake interaction and P_{upwind} represents the power output (in kW) of the upwind turbine in that particular wake interaction. Hypothetically speaking, this power ratio should be less than 1. This is due to the assumption that the interaction of wakes causes the power output at the downwind turbine to be less than the power generated by the upwind turbine.

Our multiple wake interaction analysis focused on the wake interactions around turbine A5. We found mutliple occassions when there were several wake overlaps involving turbine A5. Table 1 shows the individual interactions we analyzed.

Table 1. Turbines creating wake for A5 for various yaw.

Yaw Angle	Turbines Creating Wakes on A5
184°	B5 and B6
192°	B4 and B5
200°	B4 and B3
208°	B2 and B3

4. Results

4.1 Power Output

In Figure 2, winds defined as easterly were between 75° and 105° (90° ± 15°) and westerly winds were defined as having yaw angles from 255° to 285° (270° ± 15°). Complete sets of data (numbering about 280 for the east data and 195 for the west data) were included in the initial analysis. Figures 3 and 4 demonstrate the effect a smaller range of yaw angles has on the normalized power output. Winds defined as easterly in Figure 3 were between 80° and 100° (90° ± 10°) and westerly winds were those in the range of 260° to 280° (270° ± 10°). Data used in Figure 4 were even smaller, having easterly winds defined as those between 85° and 95° (90° ± 5°) and westerly winds between 265° and 275° (270° ± 5°). Data sets included in Figure 4 numbered about 85 for east winds and 91 for west winds. Each graph includes the mean normalized power output at each turbine in the line and error bars representing the standard deviation of data sets at that specific turbine.

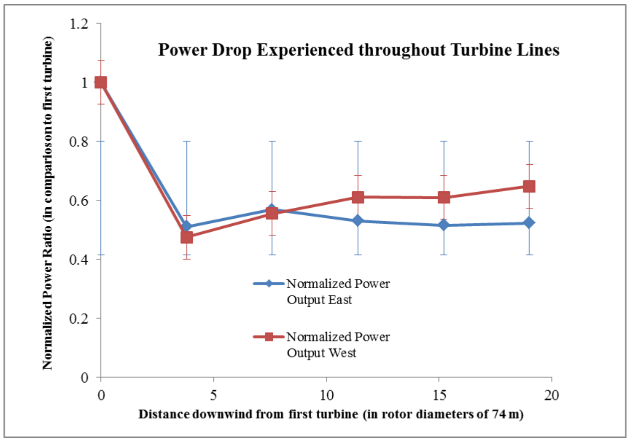

Figure 2: Power trends down a line of turbines. Data includes East and West wind events. Wind directions defined as easterly were between 75° and 105° (90° ± 15°), and westerly winds were defined as from 255° to 285° (270° ± 15°).

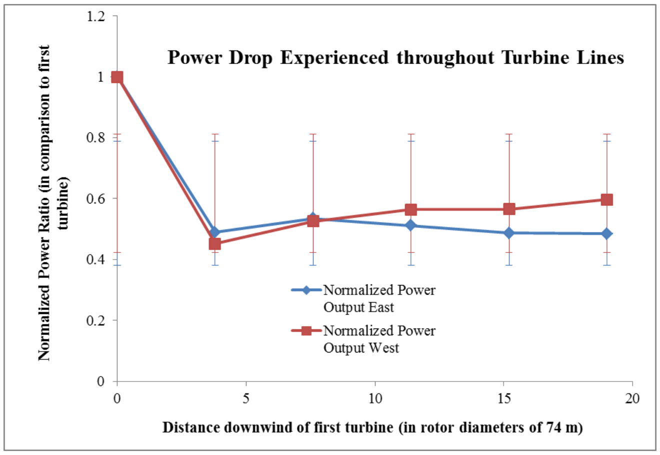

Figure 3: Power trends down a line of turbines. Data includes East and West wind events. Wind directions defined as easterly were between 80° and 100° (90° ± 10°), and westerly winds were defined as from 260° to 280° (270° ± 10°).

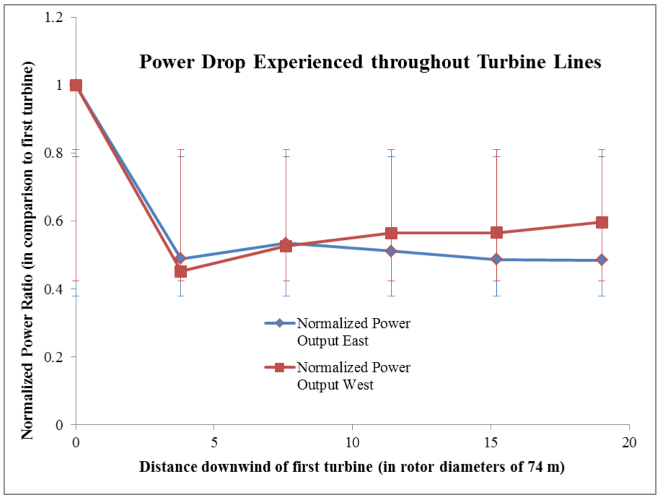

Figure 4: Power trends down a line of turbines. Data includes East and West wind events. Wind directions defined as easterly were between 85° and 95° (90° ± 5°), and westerly winds were defined as from 265° to 275° (270° ± 5°).

We divided the 10-min averages used in Figure 4 between day hours and night. Data points in the day category included 0800-1700 LST (14 UTC – 23 UTC), and the night hours were from 2000-0500 LST (02 UTC – 11 UTC). Trends from this analysis are shown in Figure 5 and Figure 6. Figure 5 shows most variation in normalized power output values at night when winds are easterly. Although the graph shows that there is still a 40% power drop between the lead turbine and second turbine during the day, there is a more significant (approximately 70%) power drop between those same turbines at night. The trends in both Figure 5 and Figure 6 display more variable power loss at night than during the day. This is most likely due to the highly variable low level jet and lower turbulence during the early morning hours.

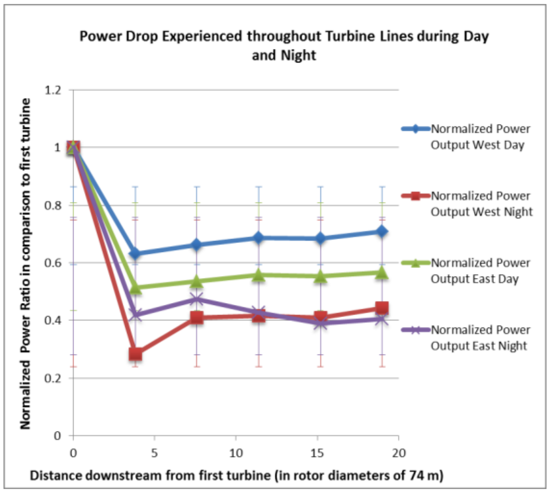

Figure 5: Power trends down a line of turbines. This graph compares the normalized power output at different directions and between specific times of the day.

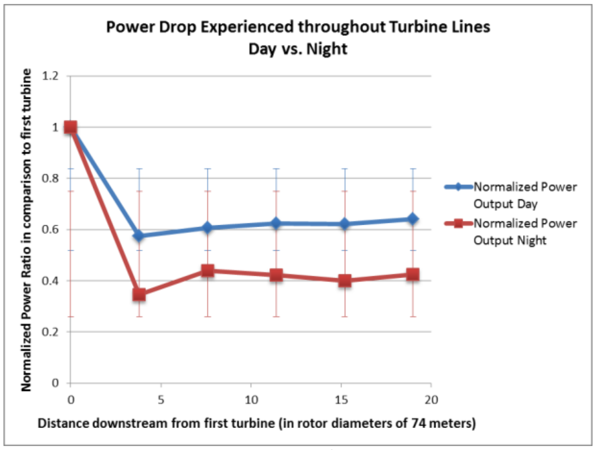

Figure 6: Power trends down a line of turbines. This graph compares the normalized power output between day and night hours, regardless of wind direction.

4.1 Thrust Coefficient

The thrust coefficient, C_T, is used to analyze the amount of added turbulence on wind turbines caused by wakes. Turbulence caused by wake effects will be a function of the thrust coefficient. Each individual turbine has a specific thrust coefficient value, but these numbers are primarily kept confidential by the wind turbine manufacturing companies. Therefore, researchers have developed a value for the generic thrust coefficient that is used in calculations (Equation 3), and whose value is approximately 8/9, or 0.88.

Mean values of C_T calculated between the lead turbine and second turbine in line are given in Table 1.

Table 2. Mean and standard deviation for C_T.

Year	Direction	C_T value	Standard Deviation
2010	East	0.813	0.164
2010	West	0.537	0.582
2011	East	0.609	0.403
2011	West	0.868	0.148

The calculated thrust coefficient values that are closest to the approximate value of 0.88 were from the East 2010 data and the West 2011 data. For reasons unknown, the values calculated with the West 2010 and East 2011 data span a wider range. A check for a correlation between thrust coefficient and wind speed (Figure 7 found in the Appendix), revealed no apparent relationship (the highest R^2 value was 0.0065).

From here, the 2010 data was further analyzed in search of a separate correlation between day and night or east and west and the nacelle wind speed. When testing the variables of night and day, day hours were considered those between 0800 – 1700 LST (14 UTC – 23 UTC) and those in the night category were between 2000 – 0500 LST (02 UTC – 11 UTC). Resulting mean values are given in Table 2.

Table 2. Mean and standard deviation for C_T calculated separately for day and night events.

Year	Variable tested	C_T value	Standard Deviation
2010	East	0.813	0.164
2010	West	0.616	0.268
2010	Day	0.530	0.269
2010	Night	0.826	0.212

The calculated thrust coefficient values that are closest to the approximate value of 0.88 were from the 2010 East and 2010 Night data. When the thrust coefficient, C_T, and the respective nacelle wind speed were plotted against one another (Figure 8), the best correlation was shown with the 2010 Night data. The R^2 value for this data was 0.2703. A check for correlation between the additional variables of day, east and west and the respective nacelle wind speeds were also conducted (Figures A1-A4 in the Appendix) and showed no apparent relationship.

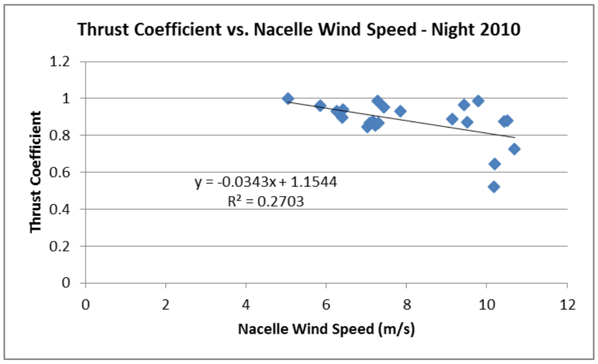

Figure 8: Relation between thrust coefficient and nacelle wind speed for 2010 data during specific night hours.

4.2 Wake Interactions

4.21 Single Wake Interactions

The results from the single wake interaction analysis are shown below on Figure 9. The largest power drop (70%) occurred when the interacting turbines were approximately 7.4 rotor diameters apart. As the distance between the two turbines increased, the power ratio increased. Beyond about 14 rotor diameters, the power ratio exceeded 1.0 at 4 of 5 locations observed. The median normalized power ratio had a maximum of 1.4 when the distance between the interacting turbines were approximately 24.7 rotor diameters. Wake width approximations (+/-5 degrees) occuring at yaw angles of 190° were provided by Russ Doorenbos (Figure 13). In this figure, each wake is 5°, and the distance from each turbine to the ring created by the directional points (start of the angle) is 423 meters. A total of 335 individual wake interactions, or an average of 42 interactions per data point, were used to create Figure 9. There were a total of 197 interactions that contributed to the data points whose mean values were greater than 1.

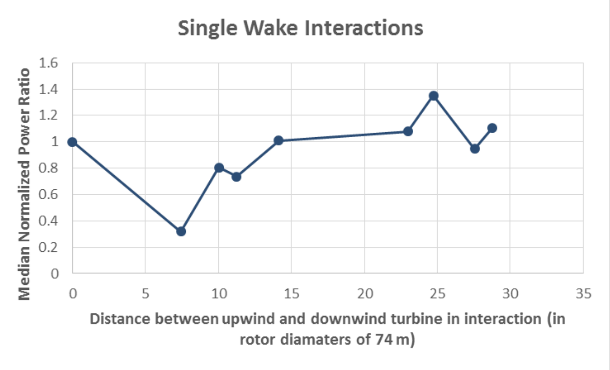

Figure 9: Relation between the median normalized power ratio and the distance between the upwind and downwind turbines in specific single wake interaction cases.

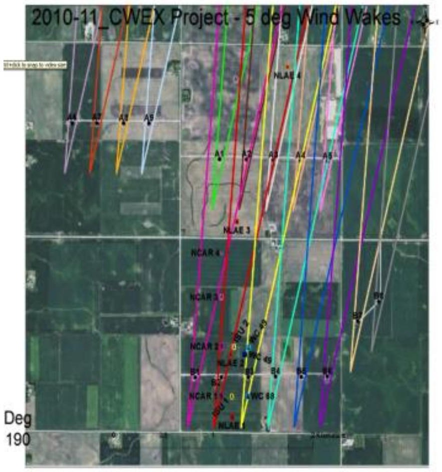

Figure 10: Wake animations showing the interaction of particular turbine wakes when yaw angles are at 190°. Figure provided by Russ Doorenbos.

4.22 Multiple Wake Interactions

For larger distances between turbines and more oblique angles between wind directions and turbine lines individual downwind turbines are affected by wakes of more than one turbine. Power ratio for Turine A5 for multiple wakes from numerous distances are shown in Figure 10. As for single wakes, power ratios exceeding 1.0 are observed, with a maximum value of 1.45 occuring at a rotor diameter of about 23.5 rotor diameters. A total of 405 individual wake interactions (average of 51 per data point) were used to construct Figure 10. A total of 153 interactions contributed to the data points whose values were greater than 1.

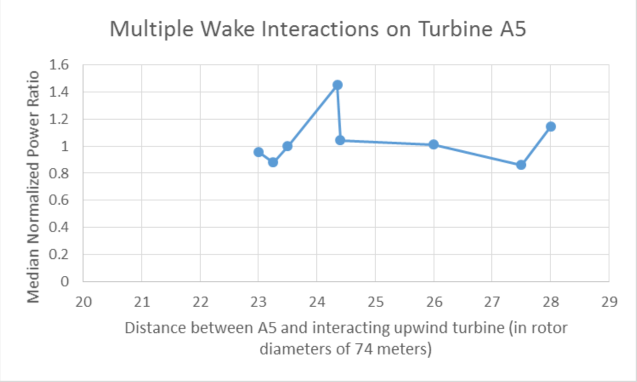

Figure 10: Relation between the median normalized power ratio and the distance between the upwind (turbine A5) and downwind turbines in specific multiple wake interaction cases.

5. Analysis and Interpretation

5.1 Power Output

Our results on the effects of wakes on the power output down a single line of turbines agree with the results of Flowers (2012) for onshore turbines. The greatest drop in power occurs at the second turbine in line, regardless of the time of day or wind direction. As the wind flows further through the system of turbines, the power output does not drop off continually, but instead seems to gradually “recover”. By the time the wake had passed over the sixth turbine in line (B6), power output levels were approximately 60% of the original power output levels at the leading turbine. In addition, our results in Figure 4 confirmed that there is a greater power drop when the wind hits the lead turbine “head-on”, as opposed to indirectly.

These results are consistent with the study of an offshore wind farm by Barthelmie and Jensen (2010), which concluded that the initial drop in a line of turbines is strongest, and although secondary drops may occur, power and wind speed both recover somewhat with distance down the line of turbines. For offshore turbines, Barthelmie et al. (2007) report a power ratio of less than 0.20 at the first downwind turbine in a multi-turbine line. In contrast to the results from larger, offshore wind turbines, the decline in power and wind speed at the central Iowa wind farm was relatively lower and recovered with less distance.

Our day power output vs. night power output analysis revealed that there is more variation in wind speeds and power drops during the evening hours as opposed to daylight hours. Figure 6 shows that during the day, power output levels dropped by approximately 40% at the second turbine in the line and recovered to about 60% of the original power output when the wake reached the final turbine in line (B6). This is contrasting to the evening hours, which showed a more substantial 65% power drop between the first and second turbines in line and only recovered to a little over 40% of the original power output at the end of the turbine line (turbine 6). This diurnal power output difference is due to a variation in atmospheric conditions. During the daytime, the atmospheric boundary layer is well-mixed with little shear and strong turbulence, while during the nighttime, minimal turbulence is found, but there is considerable shear across the rotor disk region and above.

5.2 Thrust Coefficient

Turbulence caused by the wake effect is a function of the thrust coefficient. Wind turbine rotor performance is usually characterized by its power and thrust coefficients, C_p and C_T, respectively. Our calculations of the thrust coefficient were relatively close to the theoretical value of 8/9, or 0.88. When our thrust coefficient values and nacelle wind speed values were plotted against one another, however, no direct relationship was apparent. This is most likely due to the fact that our wind speeds do not represent freestream airflow as they are measured behind the blades. Further research should be conducted on the thrust coefficient using wind speeds that accurately represent freestream airflow.

5.3 Wake Interactions

Figures 9 and 10 provide the first known reports of wind power ratios exceeding 1.0 for turbines in the wake of the reference turbine. These results were from a limited set of observations over only summer months. However, observed values for multiple cases from both single and multiple wakes add confidence that such conditions can occur.

A further analysis of the single wake interaction events (Figure 9) that gave power ratios greater than 1.0 revealed that approximately 56% of these interactions occurred during the nighttime hours of 2000 – 0800 LST (02 UTC – 14 UTC). On average, the wind speeds at the downwind turbine were less than wind speeds at the upwind turbine. All of the upwind wind speeds were above the specified turbine cut-in wind speed of 3 m/s.

The same analysis was conducted for the multiple wake interaction events (Figure 10) that gave power ratios greater than 1.0. Contrary to the single wake interactions, approximately 48% of the events where power ratios exceeded 1.0 occurred during the nighttime hours of 2000 – 0800 LST (02 UTC – 14 UTC). During these conditions, wind speeds at the upwind turbine remained between 4-9 m/s. An in-depth analysis of wind speeds that accompany such events and additional information about the atmospheric conditions that accompany such events is needed and would be suitable for future research endeavors.

6. Conclusions

Wind turbines interacting via the wake generated by the rotating blades greatly impacts the power output at a wind farm. Our results confirm the results of previous studies (Flowers 2012) concluding that wakes have the most severe impact on power generation during periods of low wind speed and when the wind direction flows directly from one turbine to the next.

This analysis provides the first known reports of wind power ratios exceeding 1.0 in the wake of the reference turbine. The fact that these conditions occurred for both our single and multiple wake analysis provides evidence that these events can and do happen. In order to characterize these specific events, further research should be conducted on the atmospheric conditions that occur during these events. A better understanding of the interaction of wakes will have a profound impact on meteorological forecasts used to predict turbine power output and the development of more efficient wind farm layouts.

Additional research ideas include: characterizing the interaction of wakes between turbines at opposite ends of a utility-scale wind farm, analyzing the effects of large utility-scale wind farms on local atmospheric conditions and identifying the specific atmospheric conditions that cause power ratios to exceed 1.0.

Acknowledgements

Support for this research was provided by a National Science Foundation Research Experience for Undergraduates site program in Wind Energy Science Engineering and Policy (WESEP) grant number EEC-1063048 at Iowa State University.

References

Barthelmie, R.J., K. Hansen, S.T. Frandsen, O. Rathmann, J. G. Schepers, W. Schlez, J. Philips, K. Rados, A. Zervos, E. S. Politis, and P. K. Chaviaopoulos, 2009: Modeling and measuring flow and wind turbine wakes in large wind farms offshore. *Wind Energy*, **12**, 431-444. DOI: 10.1002/we.348.

Barthelmie, R.J., and L. E. Jensen, 2010: Evaluation of power losses due to wind turbine wakes at the Nysted offshore wind farm. *Wind Energy*, **13**, 573-586. DOI: 10.1002/we.408.

Barthelmie, R. J., G. C. Larsen, S. T. Frandsen, L. Folkerts, K. Rados, S. C. Pryor, B. Lange, and G. Schepers, 2006: Comparison of wake model simulations with offshore wind turbine wake profiles measured by sodar. *J. Atmos. Oceanic Technol.*, **23**, 888–901. DOI: 10.1175/JTECH1886.1.

Barthelmie, R.J., S. Frandsen, N. Nielsen, S. Pryor, P. Rethore, and H. Jørgensen, 2007: Modelling and measurements of power losses and turbulence intensity in wind turbine wakes at Middelgrunden offshore wind farm. *Wind Energy*, **10**, 517-528. DOI: 10.1002/we.238. 10, 217-228.

Flowers, M. E, 2012: Comparison and analysis of turbine wake interaction. [Available online at http://www.meteor.iastate.edu/windresearch/wesepreu.html].

Frohboese, P., C. Schmuck, 2010: Thrust coefficients used for estimation of wake effects for fatigue load calculation. *European Wind Energy Conference and Exhibition 2010*, Warsaw, Poland.

Kulunk, E., 2011: Aerodynamics of Wind Turbines, Fundamental and Advanced Topics in Wind Power, Dr. Rupp Carriveau (Ed.), ISBN: 978-953-307-508-2, InTech, Available from: http://www.intechopen.com/books/fundamental-and-advanced-topics-in-wind-power/aerodynamics-of-windturbines

Rajewski, Daniel A., and Coauthors, 2013: Crop Wind Energy Experiment (CWEX): Observations of Surface-Layer, Boundary Layer, and Mesoscale Interactions with a Wind Farm. *Bull. Amer. Meteor. Soc.*, **94**, 655–672.
DOI: http://dx.doi.org/10.1175/BAMS-D-11-00240.1

Rhodes, M. E. and J. K. Lundquist, 2013: The Effect of Wind Turbine Wakes on Summertime U.S. Midwest Atmospheric Wind Profiles as Observed with Ground-Based Doppler Lidar. Published online at Springerlink.com.
DOI: 10.1007/s10546-013-9834-x

U.S. DOE, 2008: 20% wind energy by 2030: Increasing wind energy's contribution to U.S. electrical supply. U.S. Department of Energy Rep. DOE/GO-102008-2567, 248 pp. www.nrel.gov/docs/fy08osti/41869.pdf.

Wharton, S. and J. K. Lundquist, 2012: Atmospheric stability affects wind turbine power collection. Environmental Research Letters **7** (2012), 9 pp. DOI: 10.1088/1748-9326/7/1/014005.

Wharton, S., J. K. Lundquist, and N. Marjanovic, 2012: Synergistic Effects of Turbine Wakes and Atmospheric Stability on Power Production at an Onshore Wind Farm. Livermore, CA, Lawrence Livermore National Laboratory (LLNL), Technical Report LLNL-TR-524756.

Zhang, W., C.D. Markfort, and F. Porté-Agel, 2012: Wind turbine wakes in a Convective Boundary Layer: A Wind Tunnel Study. *Springer Science + Business Media*, DOI: 10.1007/s10546-012-9751-4.

Appendices

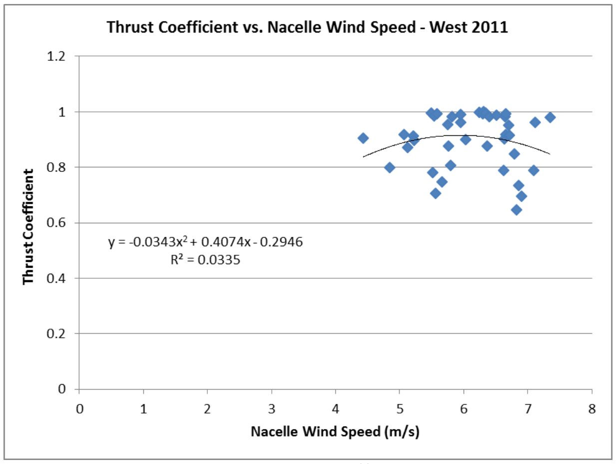

Figure A1: Relation between thrust coefficient and nacelle wind speed for the 2011 westerly direction data. The linear trend line shown here shows no distinct correlation between turbine thrust coefficient and nacelle wind speed.

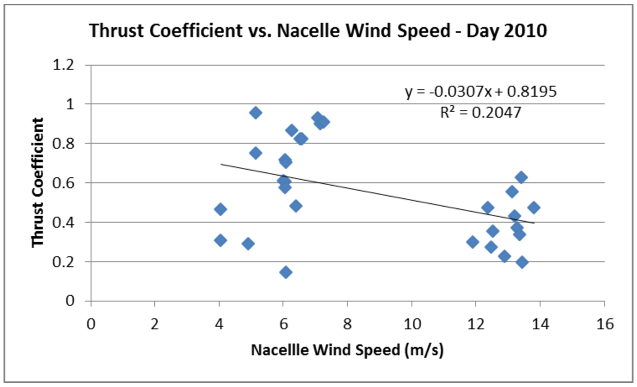

Figure A2: Relation between thrust coefficient and nacelle wind speed for 2010 data during specific day hours.

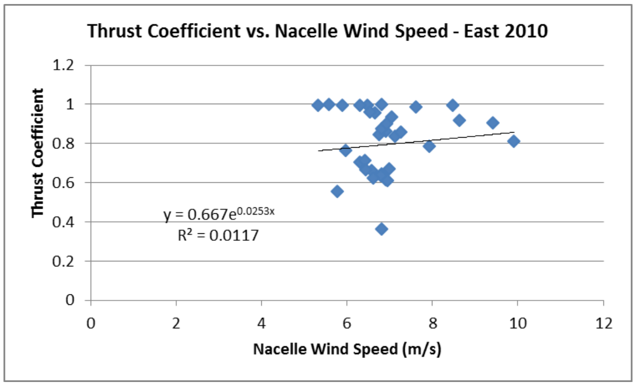

Figure A3: Relation between thrust coefficient and nacelle wind speed for the easterly 2010 data.

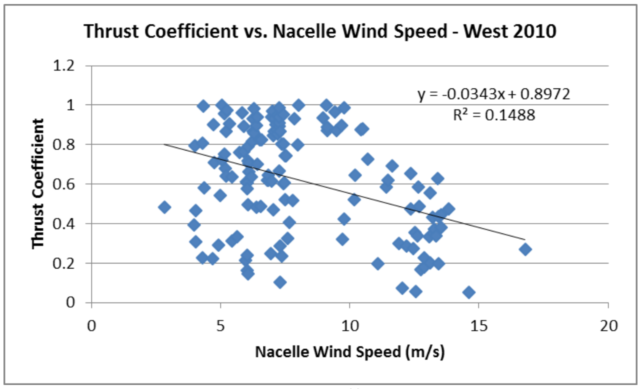

Figure A4: Relation between thrust coefficient and nacelle wind speed for the westerly 2010 data.

Analysis of the Switched Reluctance Generator for Wind Power Operations

ANDREW L. HOFFMAN
Wind Energy Science Engineering and Policy REU, Iowa State University, Ames, Iowa
Mentors: Dr. Dionysios C. Aliprantis and Yanni Li

Abstract

Recent advances in micro-processing and power electronics have made way for re-evaluating the generator operation of the Switched Reluctance Machine (SRM) and implementing its future in wind turbine farms. This pursuit is appealing due to the machine's inexpensive parts, simple design and robust nature. There is an ongoing progression to find optimal solutions for the generator's use in production purposes. In this paper's investigation, Ansoft Maxwell 2D software was used to construct prototypes of the machine and simulate them for torque results. Using Matlab software, torque profiles were produced to examine the machine's average torque and ripple effects. It was found that making small design changes to the stator teeth arcs of a symmetrical SRM can be one way to improve torque production. Although multiple analyses were conducted, it is worthwhile to continue future research in this direction to find optimal results.

---

1. Introduction

Renewable energy has become an advancing field to reduce carbon dioxide emissions. In particular, wind generation can help by contributing clean energy to our worldwide communities. Current research shows that wind generators have the most positive impact on the environment and occupy the least amount of land than any other alternative source besides rooftop solar energy (Nassereddine et al., 2008). In addition, wind generation has short-term construction, a long life cycle, low cost and little maintenance involved. However, there exists a grand challenge for wind generation: the common uses of permanent magnet generators need high torque to operate high power capacities (Nassereddine et al., 2008). One possible solution is the Switched Reluctance Machine (SRM) and utilizing its generator operation, known as the Switched Reluctant Generator (SRG). The machine has simple construction, variable speed operations, robustness, high temperature tolerance, high reliability and low inertia. Additionally, its rotor is absent of coils and magnets (Arifin et al., 2012). The generator operation requires no torque to start. Although there have been drawbacks in its noisiness and nonlinear controls, the electric drive compensates with using micro-processing and highly advanced power electronics to minimize torque, current and voltage ripples (Darie et al., 2009). In this paper I report the modeling of the SRM, its operations and how constructing some nonsymmetrical stator teeth affect average torque.

2. Literature review

Building the SRM is simple in its mechanical aspect but intricate on the electronics side. It contains salient stator and rotor poles with each of the stator poles having wound field coils. The term salient refers to the structures of the poles protruding into the air gap between them. Each field coil is connected in series with their diametrically opposite windings, which forms each independent phase. An external circuit is directly connected to the field coils with a power source connected to the load. Using the right-hand rule, current will feed into the stator windings and create magnetic flux. Fig. 1 shows the 8/6 SRM configuration with one of the 4 stator phases being excited (Arifin et al., 2012).

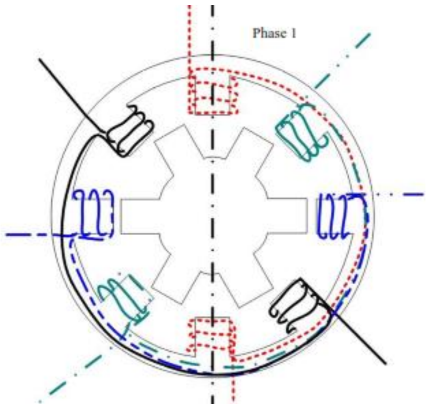

Figure 1. Cross-Section of a 4 phase 8/6 SRM structure

When a stator phase is energized, the rotor's poles will incline to rotate towards alignment with the phase. This is known as the minimum reluctance position

(Miller, 2002). Continual movement is created by sequentially exciting each stator phase. However, if one of the phase coils is unexcited, unbalanced lateral forces will occur in the field lines and may cause mechanical problems (Darie et al., 2009). Depending on where the stator and rotor poles are positioned, the inductance profile will vary from maximum at alignment and minimum when unaligned. The machine operates as a motor when high power switching currents are applied during the increasing inductance profile. This produces positive torque, which is shown by the electromagnetic torque equation:

$$T = \frac{1}{2} i^2 \frac{dL}{d\theta},$$

where the slope of the inductance profile, $\frac{dL}{d\theta}$, increases until maximum at alignment (Arifin et al., 2012). In a wind turbine, the motoring operation will turn the rotor blades through a direct drive or a gearbox. However, when the wind takes control of the blades, switching currents are applied during the decreasing inductance profile to operate the machine as a generator. This creates a braking torque that generates electricity. Table 1 below further explains the switches and how current is applied in motoring and generating operations (Radun, 1994).

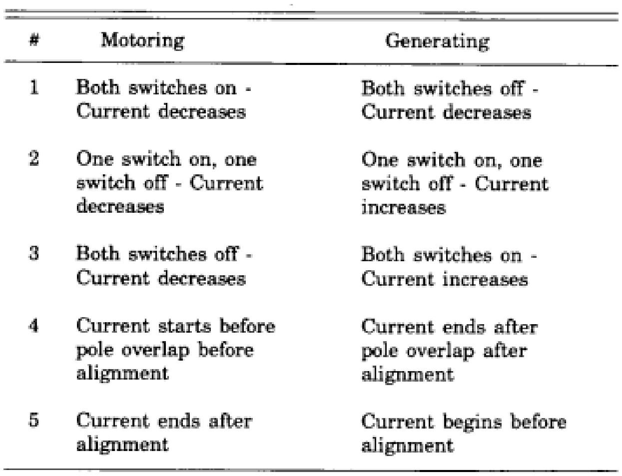

#	Motoring	Generating
1	Both switches on - Current decreases	Both switches off - Current decreases
2	One switch on, one switch off - Current decreases	One switch on, one switch off - Current increases
3	Both switches off - Current decreases	Both switches on - Current increases
4	Current starts before pole overlap before alignment	Current ends after pole overlap after alignment
5	Current ends after alignment	Current begins before alignment

Table 1. Comparison summary of the SRM operations

The generator operation has a similar self-excitation process as the motor. However, the magnetic flux and the rotor's mechanical energy will convert into electrical energy that returns to the grid. This process has been made more controllable due to advanced power electronics switching (Nassereddine et al., 2008). To make the transition between motor and generator operation, a relay is added to the SRM's half-bridge converter. Additionally, firing angles are simultaneously switched on after the rotor and stator poles align. Fig. 2 shows how the general SRM drive would work (Silveira et al., 2009).

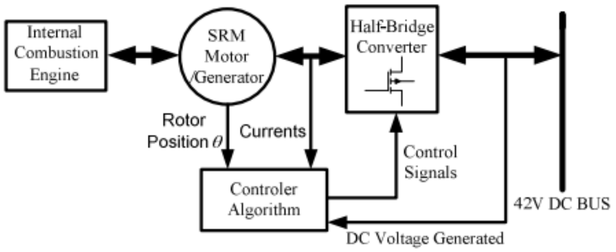

Figure 2. The setup of the overall SRM drive

Although the SRM appears simple to construct, there are limited produced materials and tools available, which means it is ripe for larger innovations. The small air gap and unique concentricity are significant aspects of this machine. It is desirable to have larger amounts of copper turns with higher rated temperature protection. Additionally, an accurate feedback signal is needed for the shaft position used with a specific high-quality sensor or sensorless controller (Miller, 2002).

Research on the air gap, which is an area of space between the rotor and stator teeth, has shown that stator tooth shapes could be slightly sculpted to allow more electromechanical energy conversions within the SRM (Li and Aliprantis, 2013). The idea came from looking at Maxwell's stress tensor theory, which says that the radial and tangential flux work together to create electromagnetic torque production within the air gap. Since the flux usually occurs perpendicular to the surface of the stator teeth, their shape becomes a crucial component. Samples of current waveforms were used to find the optimal stator tooth shape that will minimize torque ripple with marginal effect on average torque (Li and Aliprantis, 2013).

3. Experimental methods

One way to construct and simulate a model of the SRM is using Ansoft Maxwell 2D software. This motor is listed with several other models and contains sets of construction parameters to fill for creation. Following the help document's procedures in Maxwell assisted in building the SRM model. For general data, no frictional loss, no wind loss and a full-voltage circuit were selected. For specific parameters, previous research was used for reference speed, stator teeth dimensions, stator windings and rotor dimensions (Sheth and Rajagopol, 2003). Table 2 displays additional data selected for creating the SRM.

Table 2. Additional SRM parameters

Lead trigger angle	0°
Trigger pulse width angle	120°
Max. current	20 A
Min. current	0 A
Stator/Rotor stacking factor	0.95
Stator/Rotor core length	30.2 mm
Stator/Rotor/Shaft material	Steel 1008
Stator pole embrace	0.449
Thickness of stator's yoke	13.8 mm
Rotor inner diam.	58 mm
Rotor pole embrace	0.392
Thickness of rotor's yoke	13.05 mm
Parallel branches	1
Turns per pole	59
Strands per conductor	2
Wire diameter size	11.674 mm

From previous research, the motor operation was set at constant speed with selected output power, DC voltage, speed and temperature shown in table 3 (Li and Aliprantis, 2013).

Table 3. Solution setup for SRM

Load type	Constant speed
Rated output power	35 W
Rated voltage	10 V
Rated speed	1800 rpm
Operating temperature	75˚ C

After entering the parameters, the 8/6 SRM model is analyzed to produce a list of results with experimental graphs to choose from. The maximum peaks of output power and torque were examined, which were 102 W and 2.82 Nm, respectively. Next, the rated speed parameter was decreased to 500 rpm. This increased maximum output torque to about 4.85 Nm. For maximum output power, the resulting graph shifted to the right and rose to about 107 W. Attention is called to the significant difference between the phase current graphs, where decreasing the rated speed by a factor of 3.6, proportionally, raises the maximum phase current by that same factor. When increasing the rated speed parameter to 3000 rpm, the maximum output power peak rose to nearly 108 W, but the maximum output torque peak lowered to about 2.61 Nm. These speed change results can be confirmed by the air gap power equation:

$$P_a = \omega_m T_e,$$

where ω_m is rotor speed and T_e is electromagnetic torque (Krishman, 2001).

Increasing the output voltage from 10 V to 50 V multiplied the output power by a factor of nearly 5 for all three previously used rated speeds. For example, when voltage was increased to 50 V for the 1800 rpm setup, the maximum output power peak rose to about 479 W. It is noteworthy that, for all three rated speeds, each output torque graph has a different maximum shifted to the left where it appears that starting torque would be required to boost the rotor speed. For example, maximum output torque for rated speed 1800 rpm peaked at about 5.43 Nm.

In changing the wire parameters, the Maxwell 2D software requires that the number of parallel branches must make a factor of the number of stator and rotor poles created. Since 2 is a factor of the 8/6 SRM, the following changes were made: 2 parallel branches, 6 strands of wire and 8.252 mm in diameter for wire size. This resulted in lower output power, lower output torque and two maximum peaks for output power vs. speed. For maximum output power peaks, each one was about 95 W for 655 rpm and 1723 rpm. Output torque had a maximum of 1.39 Nm at 655 rpm, but a smaller ramp up in torque with 0.52 Nm at 1723 rpm. Since the wire size changes appear to make no helpful impact on the motor's energy output, it seems wise to use their initial parameters for simulations.

For producing the electromagnetic simulations, the cross-sectional model of the 8/6 SRM was mirrored about the positive z-axis and the rotor, stator and shaft halves were made uniform. A torque parameter was selected for the rotor and a balloon boundary was created around the cross-section of the SRM. Using the right-hand rule for excitations, each phase winding pair was given opposite current reference directions to point the total force outward from the machine. The directional pattern of the windings for the top half of the model from left to right was negative and positive, respectively. For the bottom half, the cross-section's windings from right to left were positive and negative, respectively. To apply sequential phase excitations, each mirrored side of the 8/6 SRM had its diametrically opposite phase winding excited proportional to each other. To create the motoring operation, the base rotor pole position was aligned with the stator slot area between phase A and B. For the generator operation, the rotor's base pole was offset by 22.5 degrees to align with stator phase A. Li and Aliprantis' (2013) current profile was used for specific rotor positions 0 – 15 degrees to obtain torque results shown in Fig. 3.

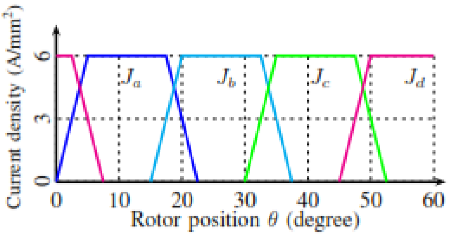

Figure 3. Phase current waveform of the 8/6 SRM

Using previous research from Li and Aliprantis (2013), more experiments were performed in the following order: reducing phase winding areas to 5 degrees and reducing current density peaks in the phase windings to 3 A/mm^2. For a comparison model, a SRM was built from scratch using the software's drawing tools. The machine's stator teeth sides were now aligned with the center axis of the model. Using previous research, the coils' inner and outer radii were drawn to 63.4 mm and 86.6 mm, respectively (Li and Aliprantis, 2013). Fig. 4 shows an example of the machine's symmetric design. Next, the rotor, stator and shaft's material were switched to linear magnetic material with constant relative permeability μ_r = 834.34. The same three previous experiments were conducted using the linear magnetic material.

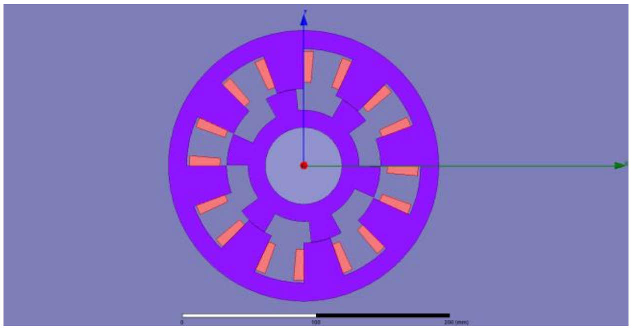

Figure 4. Cross-section view of the manually created SRM

4. Results

After simulating the SRM model, the field lines and magnetic flux density graphs were selected with each of their strongest fields appearing on the positive ends of the third and seventh winding pairs. Over 90% of the flux lines pass the air gap between the stator and rotor. The rest are leaked between adjacent poles, which is normal in realistic situations (Krishman, 2001). Figure A1 shows example results of the SRM's motoring operation in rotor position 0. After creating several designs with rotations to the rotor angle, the simulations were analyzed for torque results. Using Matlab, a positive torque profile was constructed from a collection of 22 rotor positions data points shown in Figure A2 (Li and Aliprantis, 2013). The resulting torque average was about 203 Nm with a large torque ripple produced in the first five rotor positions. When phase winding areas were reduced, average torque dropped to about 81.4 Nm with smaller torque ripple. Additionally, reducing current density by half in the modified winding areas dropped average torque by about a quarter, 23.4 Nm (Figure A3). For comparing the two SRM models, average torque increased to about 33.2 Nm in the symmetric design (Figure A4). In the original SRG, average torque was about -23.4 Nm. This improved to -32.9 Nm in the symmetric design (Figure A5).

For linear magnetic material, average torque was about 301.9 Nm with similar torque ripple effect as the first nonlinear torque profile (Figure A6). When phase winding areas were reduced, the average torque dropped to about 70 Nm with smaller torque ripple. Additionally, reducing current density by half in modified winding areas dropped average torque by about a quarter, 17.5 Nm. For comparing the two SRM models, average torque increased to about 25.3 Nm in the symmetric design. The symmetric SRG's average torque result was about -24.9 Nm.

5. Analysis and interpretation

With nonlinear and linear material, when current density is high, saturation in the iron becomes severe, especially in the teeth region. Figure A2 and A6 show some cases where saturation (torque ripple) is very high. Some of the machine's parameters can be changed to study this saturation phenomenon in the torque profiles. Since current density is defining the excitation, reducing the windings' area will lower the phase current, therefore reducing saturation. In finding the relative permeability of a nonlinear material as a linear approximate, Li and Aliprantis (2013) say the following equation can be used:

$$\mu_r = \frac{B1 - B2}{H1 - H2}$$

where B and H, the magnetic field and magnetizing field, respectively, are selected by the most appropriate values.

Due to the significant differences in average torque found between the pre-model SRM and symmetric SRM, preliminary studies were conducted on how chipping pieces of the stator tooth arcs effect torque production on the symmetrical machine. Using the previous linear magnetic material, the motoring operation was selected for this procedure and a positive torque profile was produced. For analyzing how chipping the tooth shape effects torque results, the stator teeth arcs were carved using cylindrical coordinates from Li and Aliprantis, (2003). Fig. 5 shows an example stator tooth arc that was chipped near the x-axis. Improvements of roughly 8.6% in average torque were produced in comparison to the previous torque profile. However, significant torque ripple increased between rotor positions 3 and 5 (Figure A7).

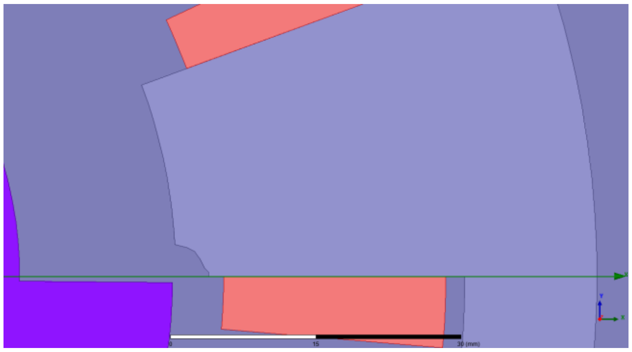

Figure 5. Carved stator tooth arc in the manually created SRM

Two SRG models were also analyzed for how the geometry of stator teeth shapes changes average torque. Figure A8 shows comparison torque profiles with a large change occurring for the carved stator tooth arc case. This may be due to the increase of air gap created from chipping the stator teeth. Additionally, average torque was setback by -9.6%. For more investigation, the carved stator tooth area was reflected to the opposite side of each stator tooth. This resulted in decreasing average torque in the motoring operation by about -16.5%. However, in the generating operation, average torque improved by about 19%.

Next, the machine was analyzed to explore a reality scenario by assuming the rotor would rotate the same previous counter-clockwise pattern as a motor. However, after the last rotor position, a wind variable was added to force the rotor to rotate clockwise back to its base position. Using Matlab, this change in direction created a positive torque profile for the generator that reflected the motor's torque profile with the same average torque. In reality, however, the rotor speed is rotating in the opposite direction, thereby producing negative power that generates electric energy. This can be confirmed by the average power available equation:

$$P = T_m \omega$$

where ω is rotor speed and T_m is average value of the torque derived from:

$$T_m = \frac{N_r}{2\pi} \int_0^{2\pi/N_r} [\sum_{j=1}^{n} \frac{1}{2} \frac{dL_j}{d\theta} i_j^2] d\theta,$$

where N_r is number of rotor poles, n is number of phases, j is phase number, i_j is current phase, θ is rotor position and L_j is inductance of phase j (Darie et al., 2009).

For the last analysis, nonlinear material steel 1018 was constructed and used for the stator, rotor and shaft. Additionally, new carved coordinates were chipped from the stator teeth (Li and Aliprantis, 2013). Average torque results for motoring and generating operations were about 25.1 Nm and -23.2 Nm, respectively, with large torque ripple occurring between rotor positions 5 and 8. In making comparison results, these carved areas were reflected to the opposite side of the stator teeth. Average torque decreased by -4.81% for motoring operation; however, this improved generating operation by about 10.1% and reduced torque ripple (Figure A9 and A10).

6. Conclusions

Ansoft's Maxwell 2D software proved to be a useful tool in creating a symmetrical SRM from scratch to simulate and reflect similar patterns as the pre-model machine had made. Using Matlab software and previous research from Li and Aliprantis (2013), torque profiles were formed and can be improved for desired results. Small changes in the area of the stator teeth arcs were found to reduce torque ripples without significantly decreasing average torque. Future research directed towards optimizing torque production is worth pursuing. After suitable solutions are found, the SRG will become a great investment for wind industries looking to save money on manufacturing costs and time spent constructing generators for their wind farms.

Acknowledgements

Support for this research was provided by a National Science Foundation Research Experience for Undergraduates site program in Wind Energy Science Engineering and Policy (WESEP) grant number EEC-1063048 at Iowa State University.

References

Arifin, A., Ibrahim Al-Bahadly and Subhas Chandra Mukhopadhyay, 2012: State of the art of switched reluctance generator. *Energy and Power Engineering*, **4**, 447-458.

Darie, E., Costin Cepisca and Emanuel Darie, 2009: The use of switched reluctance generator in wind energy applications. *Renewable Energy*, 447-462, doi: 10.5772/7358.

Krishman, R., 2001: Switched reluctance motor drives: modeling, simulation, analysis, design and applications. *Industrial Electronic Series*, 30-83.

Li, Y. and D. C. Aliprantis, 2013: Optimum stator tooth shapes for torque ripple reduction in switched reluctance motors. *IEEE Intern. Elec. Mach. & Drives Conf. (IEMDC)*, Chicago, IL, 1-8.

Miller, T. J. E., 2002: Optimal design of switched reluctance motors. *IEEE Transactions of Industrial Electronics*, **49**, 15-27.

Nassereddine, M., J. Rizk, and M. Nagrial, 2008: Switched reluctance generator for wind power applications. *World Academy of Science, Engineering and Technology*, **41**, 126-130.

Radun, A., 1994: Generating with the switched reluctance motor. *Applied Power Electronics Conference and Exposition*, **9**, Orlando, FL, 41-47.

Sheth, N. K. and K. R. Rajagopal, 2003: Optimum pole arcs for a switched reluctance motor for higher torque with reduced ripple. *IEEE Transactions on Magnetics*, **39**, 3214-3216.

Silveira, A. W. F. V., D. A. Andrade, A. V. S. Fleury, L. C. Gomes, C. A. Bissochi and R. J. Dias, 2009: Generated voltage control of the srm operating as motor/generator. *Power Electronics Conference*, Bonito, Mato Grosso do Sul, 830-835.

Appendix

<u>Simulation results and torque profiles</u>

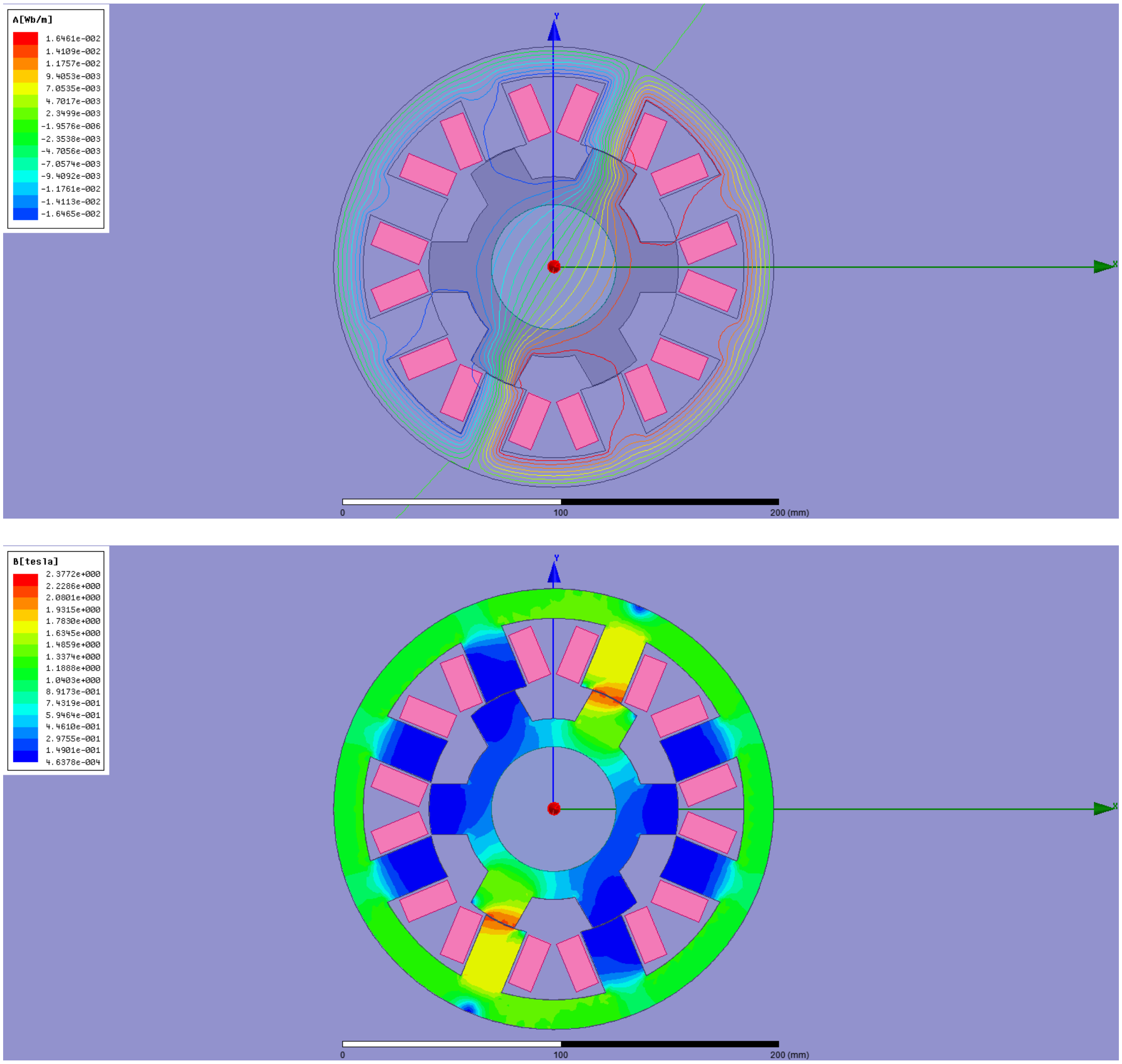

Figure A1. Simulation results of the SRM's motoring operation in rotor position 0 showing field lines and magnetic flux density using nonlinear material steel 1008

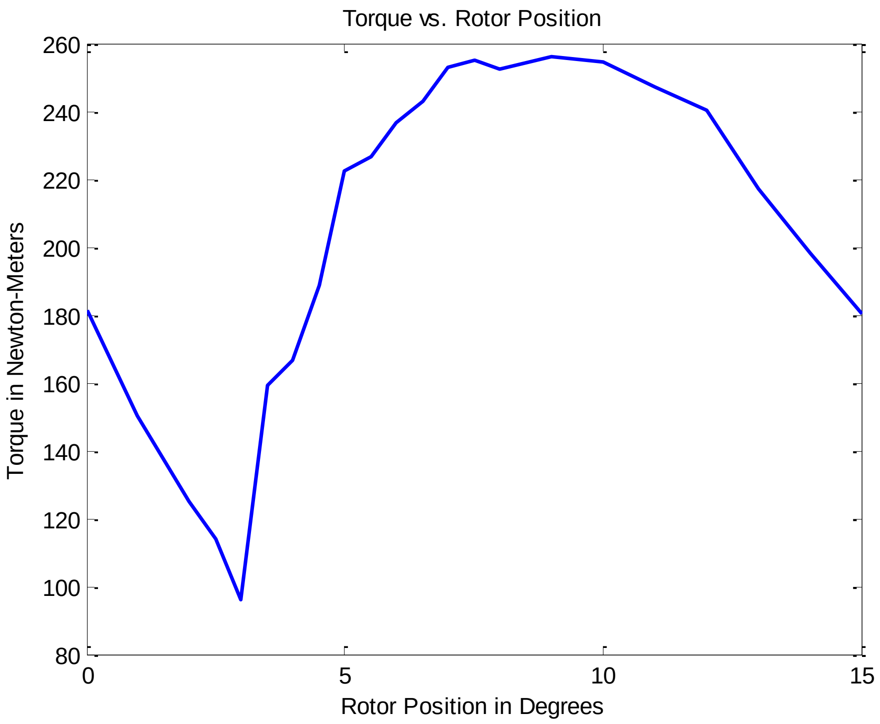

Figure A2. Torque profile of the motoring operation with nonlinear material

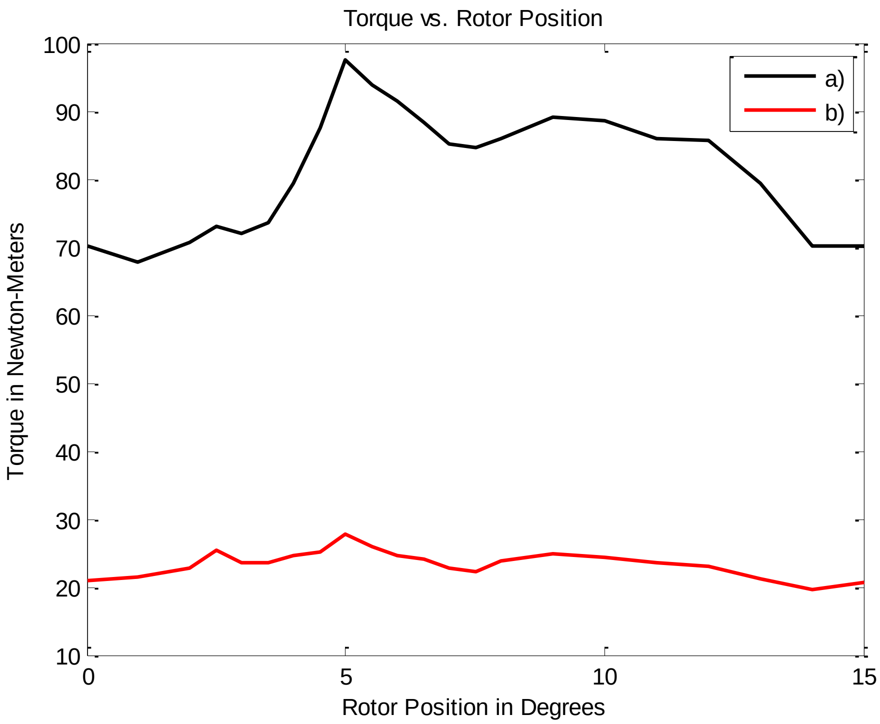

Figure A3. . Comparison torque profiles with a) modified winding areas and b) reduced current density in the modified winding areas

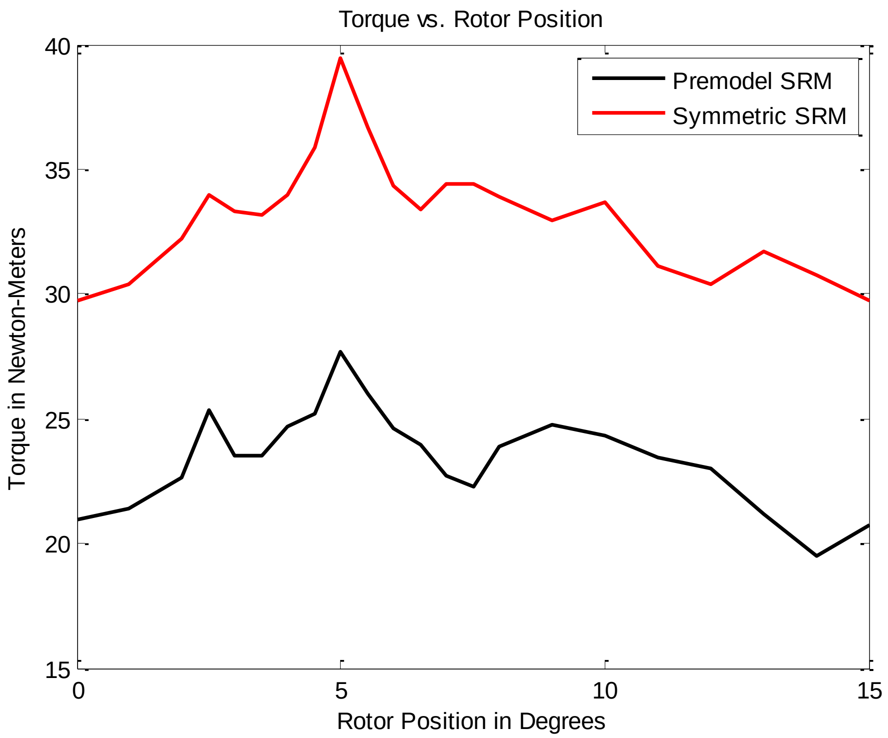

Figure A4. Comparison torque profiles of the two SRM models using nonlinear material

Figure A5. Comparison torque profiles of the two SRG models using nonlinear material

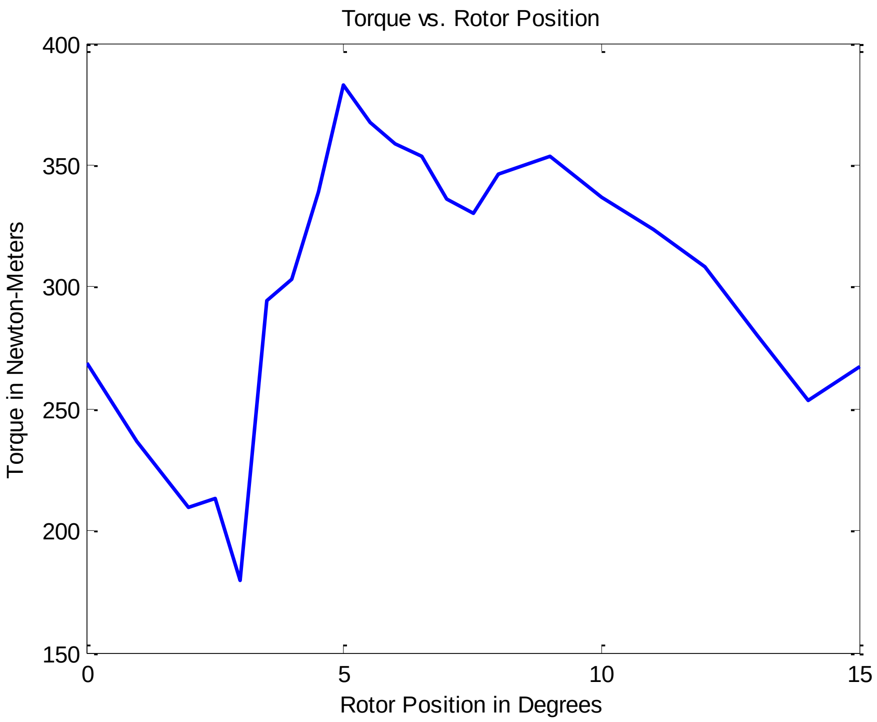

Figure A6. Torque profile of the motoring operation with linear material

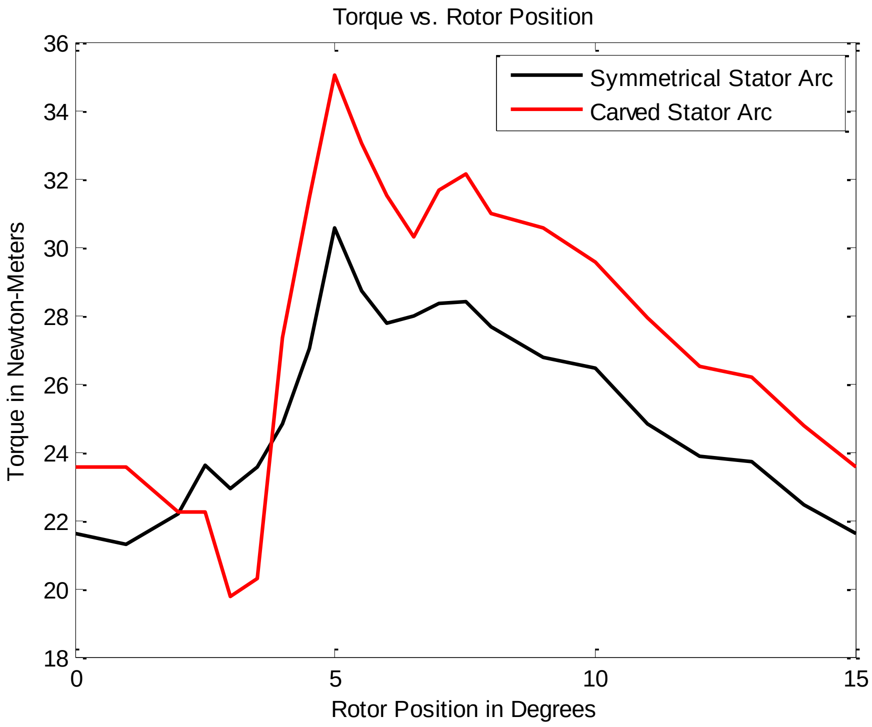

Figure A7. Comparison torque profiles of the two manually created SRM models using linear material with symmetrical stator teeth and carved stator teeth

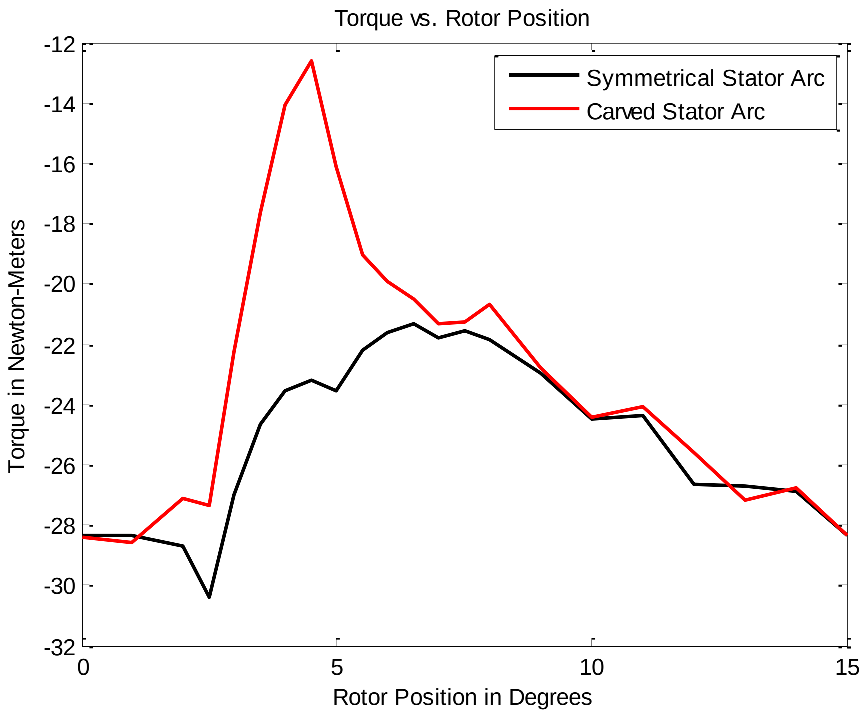

Figure A8. Comparison torque profiles of the two manually created SRG models using linear material with symmetrical stator teeth and carved stator teeth

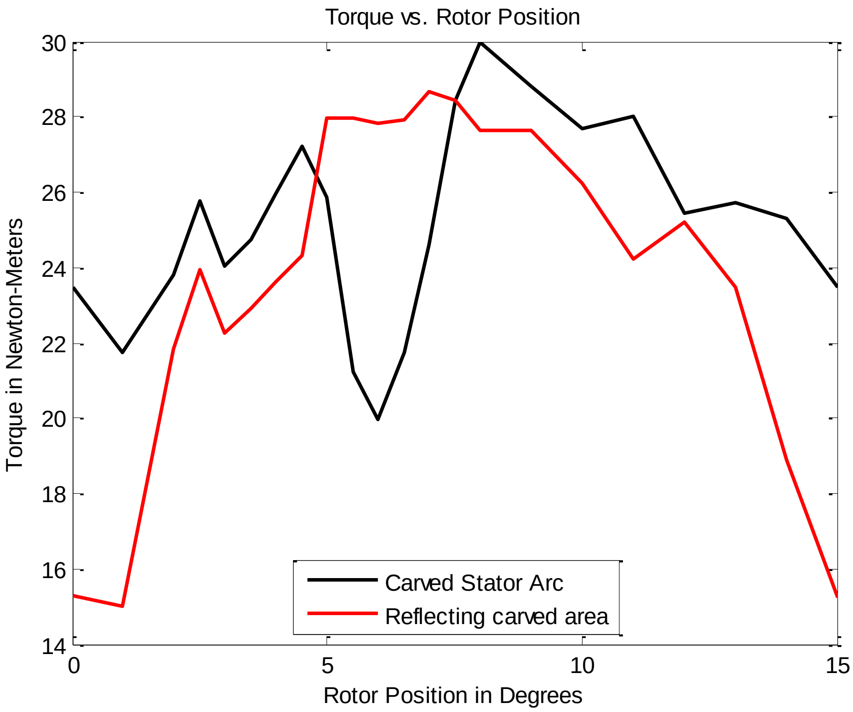

Figure A9. Comparison torque profiles of the two manually created SRM models using nonlinear material steel 1018 with carved stator teeth and reflected carved stator teeth

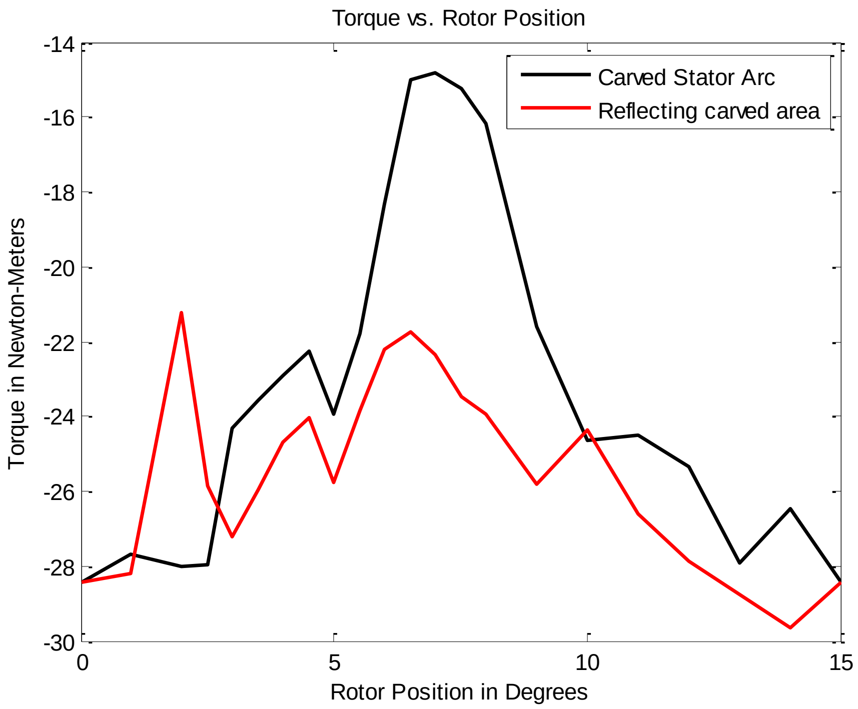

Figure A10. Comparison torque profiles of the two manually created SRG models using nonlinear material steel 1018 with carved stator teeth and reflected carved stator teeth

Use of a Flexible Capacitive Surface Sensor for Wind Turbine Blade Condition Assessment with Comparison of Two Shape Reconstruction Algorithms

VANESSA J. PAN
Wind Energy Science Engineering and Policy REU, Iowa State University, Ames, Iowa
Mentor: Dr. Simon Laflamme

Abstract

As a growing industry, wind energy has many opportunities for research and development to improve the performance of systems involved. Current costs of operation and maintenance are high, so condition-based maintenance (CBM) holds promise in driving down some of these costs. This study of a soft elastomeric capacitor (SEC) sensor explores CBM possibilities for wind turbine blades, which can provide several benefits by continuously monitoring the blades in real-time. To investigate the potential of a SEC sensor network, we apply a load and extract strain data from SEC sensors as well as adjacently placed resistance-based strain gages (RSG) on a simply supported aluminum beam. Deflection equations allow for shape reconstruction of the beam to suggest an algorithm for translating strain to deflection shapes. We compare this method to a polynomial interpolation technique previously performed to identify benefits and limitations of each algorithm. This work confirms the practicality of an SEC sensor network, demonstrating its potential for the future of turbine blade condition assessment. Future work will involve experimentation with a composite blade section to investigate more complex deflection shapes and blade failures.

1. Introduction

As a growing power source in the United States, wind energy relies on the progress of research and development in many facets of its energy production. A major area of development is in operation and maintenance (O&M). The costs of O&M in wind energy can be as high as 75-90% of the investment cost over the lifetime of a turbine (Vachon 2002). To help reduce costs of O&M, concepts of structural health monitoring (SHM) are useful to apply to the idea of condition-based maintenance. Monitoring structures in real-time would enable technicians to prevent structural and mechanical failure in wind turbines to help ensure safe and efficient operation.

Condition-based maintenance (CBM) in structural damage assessment refers to the continuous monitoring of a structure through use of data acquisition and processing in order to facilitate maintenance decision-making before failures occur (Jardine 2006). This approach differs from the classic breakdown-based or time-based methods by instead establishing initial identification of a problem and then addressing it at an ideal instance. With breakdown-based operations, owners or operators would lose the value of potentially reparable blades and critical failure of blades could impose safety hazards. Scheduling unnecessary maintenance also poses added cost to wind farm operations by minimizing the amount of remaining useful life (RUL) with premature replacement of parts (Haddad et al. 2011). Improvements made in wind turbine blade condition assessment would provide many benefits to improving maintenance procedures as well as to reducing costs of wind energy.

Because current methods of condition assessment in civil structures may be difficult or costly to use on turbine blades, Laflamme et al. (2013) have proposed a solution in the form of a *sensing skin*. With the use of a soft elastomeric capacitor (SEC) that acts as a flexible strain gage, CBM applications can be feasible on wind turbine blades. In this paper, we examine how this SEC may contribute to health monitoring of turbine blades through measuring strain on a simply supported aluminum beam. Through analysis of this strain data, the beam-shape deflection can be determined in order to enable condition assessment using the SEC. The next section will review literature regarding condition assessment in order to understand its applications towards use in wind turbine blades.

2. Literature review

Early fault detection in wind turbine blades is critical to large-scale deployment of wind energy technology across the nation. Although manufacturers estimate blade lifetimes to be up to 30 years (Schulz and Sundaresan 2006), blade failure often occurs before this benchmark. The reliability of such estimates is difficult to prove because many turbines have not been in operation for this long. Sources of damage include moisture absorption, fatigue, wind gusts, and lightning strikes—all contributing to blade failure that most often occurs at the root or chord section of blades (Schulz and Sundaresan 2006).

2.1 Wind Turbine Blade Damage Types

Damage types can be classified into three main categories: delamination, adhesive joint cracks, and fiber rupture in laminates (Sørensen et al. 2002). Broken fibers are typically a result of poor laying of the fiberglass material at manufacturing. Similarly, small waves in the material formed after the resin has been set results in structural defects that can become problematic during the lifetime operating cycle of a turbine blade. Other damage types involve debonding of components or cracks in the gel coating of the blade (Debel 2004). Figure 1 depicts a section of a turbine blade labeled with its main elements and Figure 2 shows the most common types of damage that can occur.

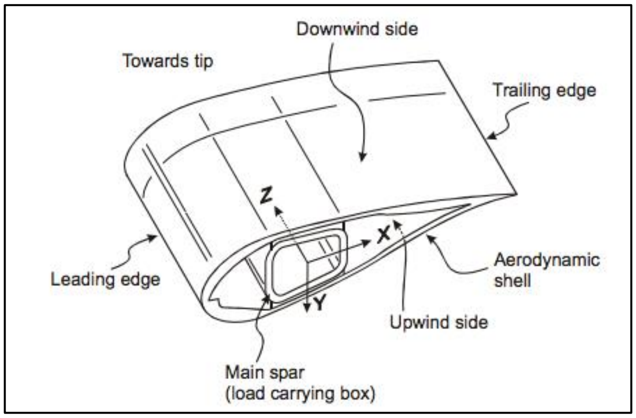

Figure 1 Main elements of a wind turbine blade (Sørensen et al. 2004).

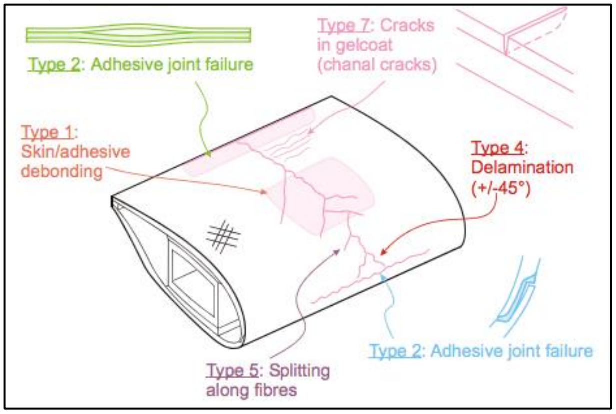

Figure 2 Damage types in wind turbine blades (Sørensen et al. 2004).

2.2 Benefits of condition-based monitoring

Laflamme et al. (2013) and Haddad et al. (2011) identify the major advantages of condition monitoring in wind turbines:

- Avoid catastrophic failure of components
- Minimize cost of unscheduled maintenance or repairs
- Extend lifetime of blades by reducing remaining useful life (RUL)
- Improve safety of wind turbine operations
- Increase flexibility in maintenance planning
- Economically schedule maintenance during times of low wind resource
- Optimize wind resource usage
- Enhance capability of remote monitoring

The failure rates for onshore turbines can be up to six times a year per turbine with capacity greater than 1 MW (Gill et al. 2012). McMillan and Ault (2008) estimate that the typical downtime for a blade outage in an onshore turbine is 30 days based on factors such as component lead-time, spares availability, and availability of appropriately trained technicians. For a new 50-m blade, the total cost is on the order of about $150,000 (Fingersh et al. 2006). By using condition-based maintenance techniques, this cost of replacement could be avoided with early fault detection. Real-time monitoring would allow for suitable maintenance actions to take place before critical failure occurs.

For health monitoring of wind turbines, many methods have been studied and used on gearboxes, generators, or blades. Vergruggen (2003) includes examples such as vibration analysis, physical condition of materials, acoustic monitoring, and strain measurement. If condition-based maintenance is to be integrated into wind turbine blades for diagnosing and prognosing damages, it must be cost-effective and durable. Diagnosis provides information about what the damage is and prognosis forecasts the course of damage over time. With the Laflamme et al. (2013) sensory membrane, both diagnosis and prognosis can be possible by measuring changes in strain.

2.3 Current sensor technology

The current standard for wind turbine maintenance is a combination of both time-based maintenance and breakdown-based maintenance. Typically, individual inspection of turbines is made twice annually and other repairs can be performed as necessary.

Many different sensing technologies are available for structural health monitoring in O&M, each with specific advantages and disadvantages. In order to implement a more efficient method of maintenance in the form of real-time monitoring of blades, principles of nondestructive evaluation (NDE) used for wind turbine manufacturing can also be considered such as ultrasound technology. Table 1 outlines a general organization for the types of sensor technology potentially applicable to condition-based monitoring of turbine blades. The next section will review a suggested sensor technology for turbine blade monitoring.

3. Soft elastomeric capacitor (SEC)

The unique properties of the sensor allow for a wide variety of applications—with characteristics especially suitable for use in turbine blades. The sensor itself is an elastomeric film fabricated from a nanoparticle mix. The SEC contains a capacitor with a thermoplastic elastomer matrix dielectric made of poly-styrene-co-ethylene-co-butylene-co-styrene (SEBS), doped with titanium dioxide to increase material permittivity and robustness to prevent mechanical tampering (Laflamme et al. 2013). The result is a soft, flexible capacitive sensor that resembles biological skin, making it customizable over many uniquely shaped surfaces (Laflamme et al. 2012).

3.1 Sensing method

Similar to conventional resistance-based strain gages (RSG), the sensing skin acts as a capacitive strain gage that links changes in capacitance to changes in strain over

Technology	Sensor type	Description	Advantages	Disadvantages
Piezoelectric	Acoustic emission/pulse-echo	Materials subject to stress or strain emit sound waves due to small structural changes, rate/properties of emissions indicate damage growth	• Unobtrusive • Non-intrusive • Inexpensive	• Some types must be embedded
	Mechanical waves			
	Electromehanical	Electromechanical waves used in conjunction with Lamb waves, impedance technique (exciting vibrations of bonded plates using piezoelectric element as transmitter and receiver of elastic waves) to detect damage		
Optics	Fiber optics/FBG	Based on propagation of light through fiber which is affected by bending of the corrugated materials surrounding the fiber	• High accuracy • Robust • Useful in lifetime prediction	• Expensive since sensors must be placed where deformations occur • Must be embedded during manufacturing
Foil gages	Resistance-based strain gages (RSG)	Metallic foil deforms, changing electrical resistance in order to indicate changes in strain	• High accuracy • Relatively cheap • Simple signal processing	• Expensive to deploy over large surfaces • Not durable on long-term
Flexible gages	Soft elastomeric capacitor (SEC)	Soft elastomeric capacitive sensor measures strain in relation to change in capacitance	• Scalability • Cost-effective • Robust • Easy to install	
Inertial sensors	Accelerometer	Device sensitive to accelerations converts mechanical changes into electrical signals	• Commercially produced in automotive industry—inexpensive	• Signal processing complex • Damage localization complex

Table 1 Sensor options for CBM in wind turbine blades. Sources: Giurgiutiu (2005), Sørensen et al. 2002, Laflamme et al. 2011.

a surface. Any local deformation creates a deviation from a set parameter for capacitance, indicating a crack or surface stress. This strain measurement method of condition assessment relates the change in geometry of the capacitor to a deformation so that real-time monitoring can be carried out with networks of these sensing patches (Laflamme et al. 2012). The sensing skin can thus be deployed over large surfaces such as that of a wind turbine blade to indicate damages such as delamination or cracks.

The capacitance C of a patch is dependent on thickness of the skin d, surface area of the patch A, vacuum permittivity ϵ_0, and polymer permittivity ϵ_M (Laflamme et al. 2012):

$$C = \frac{\epsilon_0 \epsilon_M A}{d}$$

In other conventional O&M practices, one continuously measures certain parameters and compares these data to previous reference data or limits. If a parameter consistently deviates from an expected range, then this indicates a need for repair (Gray and Watson 2009). The same principle may be applied to turbine blades, which are subject to high aerodynamic loads and shear stress.

3.2 Benefits of sensing skin technology

Laflamme et al. (2012) identify many other benefits of this new technology:

- Large scaling capabilities
- Material is inexpensive
- System is cost-effective
- Sensors easy to install
- Simple signal processing
- Robust for long-term use
- Customizable for different surfaces
- Low-powered

An important feature of the SEC is its scalability, which makes it appropriate for turbine applications. Systems of fiber optic networks are currently impractical due to high costs and conventional strain gages cannot be scaled up properly for a system as large as a turbine. The sensing skin would allow for real-time monitoring over large areas without compromising the turbine's structural integrity. Its low cost and robustness also allow for ideal integration into a strain gage sensor network for wind turbines.

4. Experimental methods

4.1 Shape Reconstruction

To relate strain data from the beam-loading experiment to real-time reconstruction of the deflection shape of the beam, an algorithm must be integrated into the structural health management system. Sensors provide curvature data, but there are many methods that might be used to interpret these data and reconstruct the deformation. In addition to the desired application of such algorithms to wind turbine blade condition assessment, methods have been researched for use on helicopters, spacecraft, and structures. Accurate shape-sensing algorithms would enable efficient condition assessment of structures and prognosis of damages.

Studies done on Integrated Vehicle Health Management (IVHM) at NASA Langley Research Center explore the use of the finite element method in structural analysis on aerospace vehicles. Tessler (2013) proposes an inverse finite element method (FEM), which is based on shear deformable shell finite element technology that enables accurate computations of a three-dimensional displacement field for a structure subject to multi-axial deformations. Stress and strain computations are carried out at the element level using the relationships between displacement and strain (Tessler 2013).

The inverse FEM method explored by Tessler and Spangler applies a least squares variational principle, which is discretized using C^0-continuous inverse finite elements that accommodate arbitrarily placed strain-sensor data (Tessler and Spangler 2013). This technique yields a system of linear algebraic equations, allowing for the unknown displacement degrees-of-freedom to be found, thereby predicting structural shape deformations (Cerracchio et al. 2011).

Another proposed approach is a modal transformation technique developed by Bogert et al. (2003) that uses a structure's deformation and strain modes along with discrete strain data to reconstruct the deformed shape. This method relies on a three-step process: deriving modal transformation equations, illustrating the transformation with a closed-form two degree-of-freedom (DOF) problem, and generating the modal transformation using the finite element method (Boger et al. 2003). This algorithm was proven successful through predicting the structural response of a beam under specific static loading conditions.

In the work performed by Laflamme et al. (2013), a simply supported beam equipped with SECs was subjected to various loading conditions to test the capability of the SEC sensor. Shape reconstruction was done by fitting the strain data to a polynomial function and then integrating the strain twice to obtain the deflection curve (Laflamme et al. 2013). Based on a least-squares algorithm performed by Glaser et al. (2012), this method minimizes the objective function that is the summation of the least squares of each strain component. Through a system of equations consisting of strain and position data matrices, a solution is found for the coefficients of the third degree polynomial function that describes the deformation of the beam. The algorithm described in Section 4.2 that we use will be compared to the polynomial interpolation method employed by Glaser et al. (2012).

4.2 Experimental setup

In this experiment, displacement equations are used to predict the deflection using strain sensor data. Classical beam theory recovers the theoretical slope and deflection shape of an aluminum simply supported beam (support-to-support dimensions: 406.4 × 101.6 × 6.35 mm^3). By modifying displacement equations of a uniform cantilever beam, we predict the deformed shape of the simply supported beam equipped with 4 resistance-based strain gages and 4 SEC patches (each SEC with dimensions: 75 × 75 mm^2). See figure 4. This method of shape reconstruction is based on the theories developed by Ko et al. (2007) for the shape reconstruction of beams, tubes, and plates.

The sensors are adhered to the surface of the beam, which is sanded, painted with a primer, and prepared for adhesion with the application of a JB Kwik epoxy. As illustrated, the sensors are placed on the underside of the beam with the load, P, acting downwards on the top of the beam. This network of SECs consists of a 1 × 4 array of sensors placed adjacently to a 1 × 4 array of RSGs for comparison.

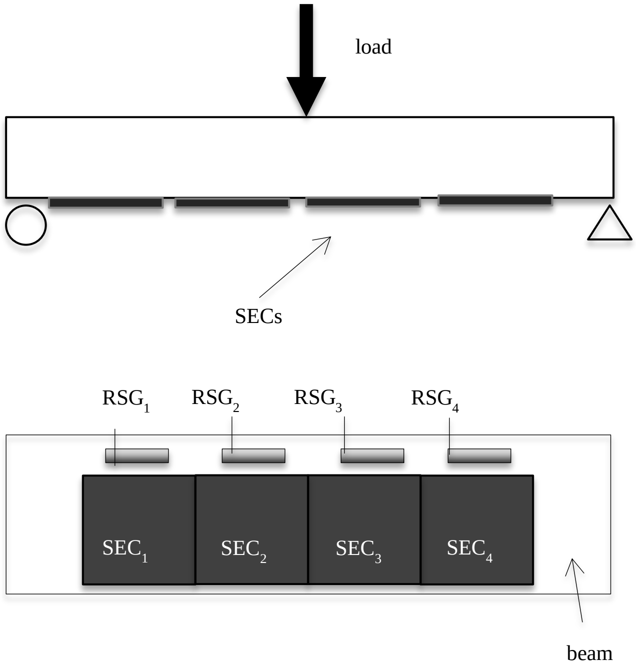

Figure 3 Experimental setup and underside view of sensor array.

The load is applied with a hand operated hydraulic test system with data from the SECs acquired with an off-the-shelf data acquisition system at a sampling rate of 28.0 Hz. The strain gage data is acquired using a Hewlett-Packard 3852 data acquisition system sampled at 1.7 Hz. We subject the beam to a dynamic load with increasing rate to test the sensors and their ability to track strain history.

4.3 Experimental algorithm

4.3.1 Slope equations

First, the moment-strain relationship in a uniform cantilever beam is used to relate the beam bending in terms of strain, $\varepsilon(x)$, and the half depth of the beam, c. The term y represents the vertical displacement of the beam and x is the corresponding axial location along the length of the beam.

$$\frac{d^2y}{dx^2} = \frac{\varepsilon(x)}{c}$$

The slope equation that describes the slope of the beam's deformation between two adjacent sensors, x_{i-1} and x_i, is found through integrating the above equation:

$$\tan\theta(x) = \int_{x_{i-1}}^{x} \frac{\varepsilon(x)}{c}dx + \tan\theta_{i-1};\ x_{i-1} \le x \le x_i$$

Assuming the bending moment *M(x)* to be a piecewise-linear function, we write this local moment equation in terms of strain as

$$\varepsilon(x) = \varepsilon_{i-1} - (\varepsilon_{i-1} - \varepsilon_i)\frac{x - x_{i-1}}{\Delta l};\ x_{i-1} < x < x_i$$

Substitute the strain equation into this slope equation and integrate to obtain the generalized equation for the slope at each sensor location.

$$\tan\theta_n = \frac{\Delta l}{2c}(\varepsilon_{n-1} + \varepsilon_n) + \tan\theta_{n-1}$$

Note that because the beam is symmetrically loaded, the slope $\tan\theta_0$ is derived and used for subsequent calculations of slope at each sensor station:

$$\tan\theta_0 = -\frac{\Delta l}{24c}(6(3\varepsilon_1 + 2\varepsilon_2 + \varepsilon_3) + \varepsilon_4)$$

4.3.2 Deflection equations

After estimating the theoretical slope at each strain gage location is calculated, the beam deflection can be found by integrating the slope equation as shown:

$$y(x) = \int_{x_{i-1}}^{x} \tan\theta(x)\,dx + y_{i-1};\ x_{i-1} \le x \le x_i$$

For n sensing stations, this operation yields:

$$y_n = \frac{(\Delta l)^2}{6c}\left[(3n-1)\varepsilon_0 + 6\sum_{i=1}^{n-1}(n-i)\varepsilon_i + \varepsilon_n\right] + n\Delta l \tan\theta_0$$

In our case, $\varepsilon_0 = 0$ at the left end of the simply supported beam.

5. Results

The plots below show comparisons of individual SEC and RSG sensor strains (µε) over time measured in seconds.

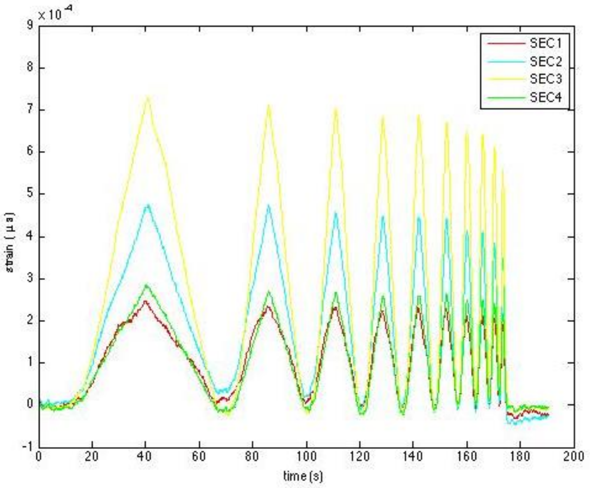

Figure 4 Strain history for four SEC sensors.

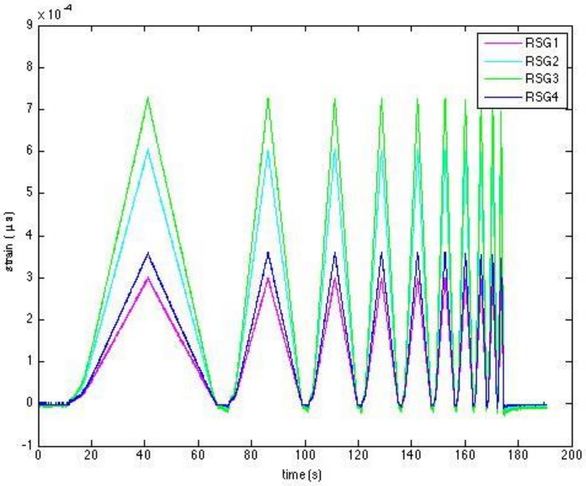

Figure 5 Strain history for four RSG sensors.

The comparative plot shown in Figure 7 shows the analytical reconstruction calculated by Laflamme et al. for the data set using the Euler-Bernoulli beam theory, deflection shapes given by the SECs/RSGs using the polynomial interpolation method, and the deflection shapes given by the SECs/RSGs using the displacement theory method.

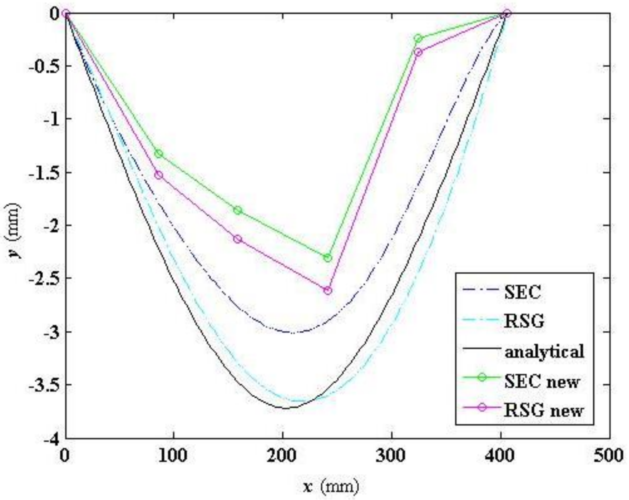

Figure 6 Comparative plot showing deflection shapes using displacement equation algorithm (marked lines labeled "SEC new" and "RSG new") in comparison to polynomial interpolation method (dashed and solid black lines) used by Laflamme et al.

Figure 7 (a)-(d) provide direct comparison between each individual SEC sensor and the corresponding RSG sensor to demonstrate the ability of the SEC sensors to provide the same accuracy as RSGs.

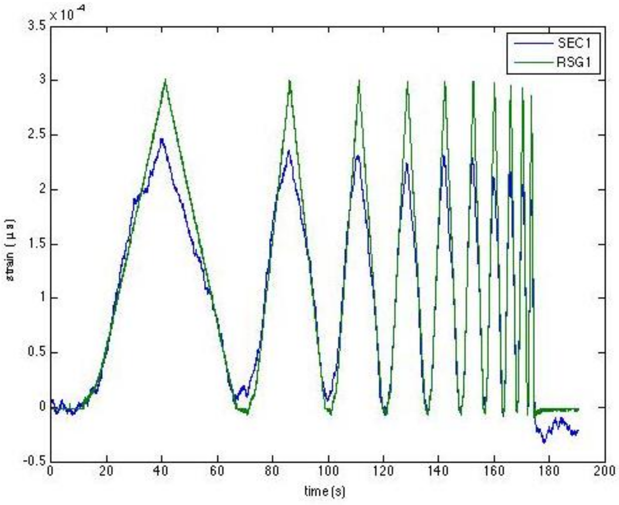

(a)

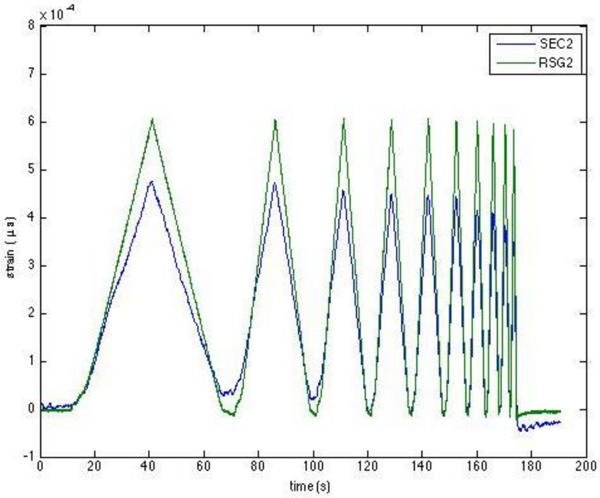

(b)

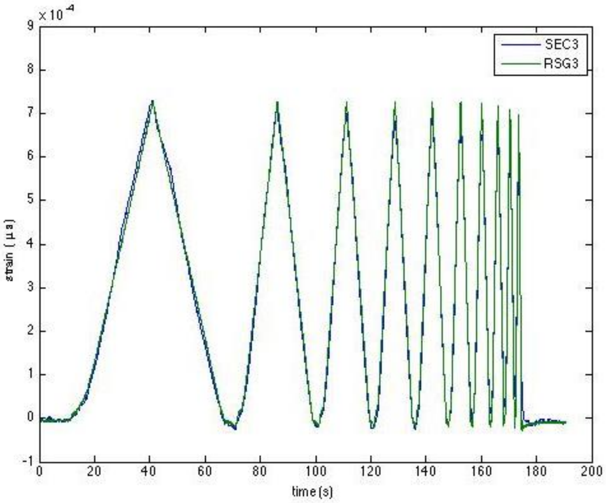

(c)

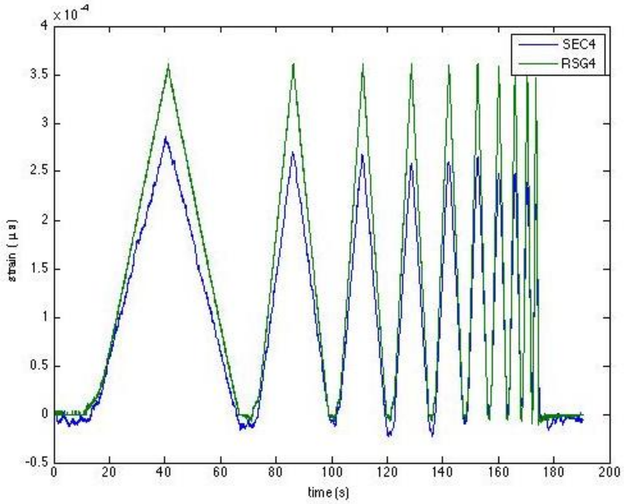

(d)

Figure 7 Strain history comparisons for (a) SEC_1 vs. RSG_1 (b) SEC_2 vs. RSG_2 (c) SEC_3 vs. RSG_3 (d) SEC_4 vs. RSG_4

6. Analysis and interpretation

Figure 4 and 5 show the comparisons of strain history between sensor types on the beam as it is subjected to a dynamic load. Given our assumption that our load was applied symmetrically and our sensors were aligned uniformly along the axes beneath the beam, sensors 1 and 4 for both SECs and RSGs should have the same strains as well as sensors 2 and 3 respectively in theory. For SECs 1 and 4 this can be verified graphically, but the discrepancy between the strain data given by SEC 2 and SEC 3 suggest that the load may have been applied off-center or the placement of the SECs was not symmetric.

In Figure 6, the side-by-side comparison of shape reconstruction solutions of both algorithms is shown for the time 40 seconds. The polynomial interpolation method provides a smooth curve that fits the data to this elliptical shape. We observe that the experimental algorithm's RSG solution is close to the analytical solution and the SEC solution slightly underestimates the deflection.

The nature of the deflection theory method causes our experimental solution to be more rigid since it calculates the slope of the beam at each sensor and then integrates it to obtain this deflection coordinate. The limitations of this method are observed graphically in comparison to the results produced by Laflamme et al. Two main sources of this discrepancy might be slight asymmetries in the placement of sensors or off-center application of the load.

To demonstrate the potential of SECs to produce strain data of similar precision to RSGs, the SEC sensors' data are each plotted against RSG's strain history. Based on our experimental configuration of the 1 × 4 arrays of each sensor type, we can assume that they will produce similar results in these strain versus time plots. The plots show that the SECs underestimate the strain in comparison to the RSGs in general but this can be accounted for with the use of a thicker layer of epoxy for the SEC adhesion that leads to a delay in its response.

7. Conclusions

Through previous experimentation and analysis of the presented data set, we can verify that a sensor network of SECs would be appropriate for application to CBM for wind turbine blades. With limited scalability of RSGs and high costs of fiber optic sensing systems, SECs provide a solution to feasibility of large-scale CBM operations. Work with the SEC sensors done by Laflamme et al. reviews possible reasons for strain underestimation in comparison to RSGs: parasitic capacitance from wires, complexity in measuring small changes in capacitance using off-the-shelf data acquisition systems, impurities in sensor fabrication, and/or inconsistencies during the manual installation (Laflamme et al. 2013). For future work on SEC sensor applications, these problems can be addressed accordingly.

The shape reconstruction algorithm presented in this paper did not produce results as precise as those produced with the polynomial interpolation method, but still offers valuable insight for shape reconstruction algorithms specific to SECs. To further research on shape reconstruction using SECs, other algorithms can be tested such as those listed in Section 4.1. Modified experimental conditions can also be tested such as the beam specimen material, configuration of sensor array, or load placement on simply supported, clamped, and cantilever beams.

To facilitate the use of SEC sensor networks in CBM for wind turbine blades, similar tests can be done on blade sections to observe the unique behavior of blade deformation since it has a composite fabrication. Furthermore, Laflamme et al. suggest that SEC sensors may be used for crack detection and localization in addition to shape reconstruction applications. SEC sensors possess many qualities that make them optimal for use on turbine blades. As the wind energy industry continues to grow, CBM technologies become more pertinent to wind energy infrastructure. SECs provide a basis for condition assessment and hold potential for CBM operations in wind turbine health monitoring.

Acknowledgements

Support for this research was provided by a National Science Foundation Research Experience for Undergraduates site program in Wind Energy Science Engineering and Policy (WESEP) grant number EEC-1063048 at Iowa State University.

References

Bogert, P.B., E. Haugse, and R.E. Gehrki, 2003: Structural shape identification from experimental strains using a modal transformation technique. *44th AIAA/ASME/ASCE/AHS Structures, Structural Dynamics, and Materials Conference*, Norfolk, Virginia. 10.2514/6.2003-1626.

Cerracchio, P., M. Mattone, M. Di Sciuva, and A. Tessler, 2011: Dynamic shape reconstruction of three-dimensional frame structures using the inverse finite element method. *National Aeronautics and Space Administration, Langley Research Center*. [Available online at http://www.congress.cimne.com.]

Debel, C.P., 2004: Identification of damage types in wind turbine blades tested to failure. *Materialeopførsel og skadesanalyse*. DMS, Lyngby: 123-127.

Farrar, C. R., and N. A.J. Lieven, 2007: Damage prognosis: the future of structural health monitoring. *Philosophical Transaction of the Royal Society A: Mathematical, Physical and Engineering Sciences* 365.1851: 623-632.

Fingersh, L., M. Hand, and A. Laxson, 2006: Wint turbine design cost and scaling model. *National Renewable Energy Laboratory Technical Report*. NREL/TP-500-40566.

Gill, S., B. Stephen, and S. Galloway, 2012: Wind turbine condition assessment through curve copula modeling. *IEEE Transactions on Sustainable Energy*. 3(1) [Available online at http://www.ieeexplore.ieee.org.]

Giurgiutiu, Victor, 2005: Structural health monitoring with piezoelectric wafer active sensors. *16th International Conference of Adaptive Structures and Technologies ICAST-2005.*

Glaser, R., V. Caccese, and M. Shahinpoor, 2012: Shape monitoring of a beam structure from measured strain or curvature. *Experimental mechanics*. 52(6): 591-606.

Gray, C. S., and S. J. Watson, 2009: Physics of failure approach to wind turbine condition based maintenance. *Wind Energy*. 13(5), 395-405.

Haddad, G., P. Sandborn, and M. Pecht, 2011: Using real options to manage condition-based maintenance enabled by PHM. *IEEE Conference on Prognostics and Health Management (PHM)*, Montreal, QC.

Jardine, A., D. Lin, and D. Banjevic, 2006: A review on machinery diagnostics and prognostics implementing condition-based maintenance. *Mechanical Systems and Signal Processing.* 20(7), 1483-1510.

Ko, W.L., W.L. Richards, and V.T. Tran, 2007: Displacement theories for in-flight deformed shape predictions of aerospace structures. *NASA Dryden Flight Research Center*. NASA/TP-2007-214612.

Lading, L., M. McGugan, P. Sendrup, J. Rheinländer, and J. Rusborg, 2002: Fundamentals for remote structural health monitoring of wind turbine blades—a preproject, Annex B-Sensors and non-destructive testing methods for damage detection in wind turbine blades. *Risø National Laboratory, Roskilde.* Risø-R-1341(EN).

Laflamme, S., H. S. Saleem, C. Song, B. Vasan, R. Geiger, D. Chen, M. Kessler, N. Bowler, K. Rajan, 2013: Sensing skin for condition assessment of civil structures. *Proceedings of Structural Health Monitoring 2013*.

Laflamme, S., M. Kollosche, J. J. Connor, and G. Kofod, 2012: Robust flexible capacitive surface sensor for structural health monitoring applications. *Journal of Engineering Mechanics* [Available online at http://www.ascelibrary.org/doi/pdf/10.1061/(ASCE)EM.1943-7889.0000530.]

Laflamme, S., H.S. Saleem, B.K. Vasan, R.L. Geiger, D. Chen, M.R. Kessler, N. Bowler, and K. Rajan, 2013: Soft elastomeric capacitor network for strain sensing over large surfaces. (Paper submitted for peer review to IEEE/ASME Transaction on Mechatronics).

McMillan, D. and G.W. Ault, 2008: Condition monitoring benefit for onshore wind turbines: sensitivity to operational parameters. *Renewable Power Generation, IET*. 2(1), 10.1049/iet-rpg:20070064.

Nishio, M., T. Mizutani, and N. Takeda, 2009: Structural shape reconstruction with consideration of the reliability of disturbed strain data from a Brillouin-scattering-based optical fiber sensor. *Smart Mater. Struct.*, 19(3), 035011.

Schulz, M.J., and M.J. Sundaresan, 2006: Smart sensor system for structural condition monitoring of wind turbines. *National Renewable Energy Laboratory*. NREL/SR-500-40089.

Sørensen, B.F., L. Lading, P. Sendrup, M. McGugan, C.P. Debel, O. J.D. Kristensen, G. Larsen, A.M. Hansen, J. Rheinländer, J. Rusborg, and J. D. Vestergaard. 2002: Fundamentals for remote structural health monitoring of wind turbine blades—a preproject. *Risø National Laboratory*. Risø-R-1336(EN).

Sørensen, B.F., E. Jørgensen, C.P. Debel, F.M. Jensen, H.M. Jensen, T.K. Jacobsen, and K.M. Halling, 2004: Improved design of large wind turbine blade of fibre composites based on studies of scale effects (Phase 1). *Summary report from Risø National Laboratory, Denmark*.

Tessler, A., 2013: iFEM: Inverse Finite Element Method. *NASA*. [Available online at http://ifem.larc.nasa.gov/].

Tessler, A., 2007: Structural analysis methods for structural health management of future aerospace vehicles. *Key Engineering Materials*. [Available online http://www.scientific.net/KEM.347.57.]

Tessler, A. and J. Spangler, 2004: Inverse FEM for full-field reconstruction of elastic deformations in shear deformable plates and shells. *Proceedings of Second European Workshop on Structural Health Monitoring*. [Available online at cs.odu.edu.]

Vachon, W. 2002: Long-term O&M costs of wind turbines based on failure rates and repair costs. *American Wind Energy Association Windpower Annual Conference.* [Available online at http://www.debenhamenergy.com.]

Vasquez, S.L., A. Tessler, C.C. Quach, E.G. Cooper, J. Parks, and J.L. Spangler, 2005: Structural health monitoring using high-density fiber optic strain sensor and inverse finite element methods. *NASA Langley Research Center*. NASA/TM-2005-213761.

Vergruggen, T.W. 2003: Wind turbine operation & maintenance based on condition monitoring. WT_OMEGA *Final Report number* ECN-C-03-047 ECN, Energy Research Center of the Netherlands.

An Experimental Investigation of Dual-Rotor Wind Turbines and the Effects of Rotation Direction

COLTON BOEHM
Wind Energy Science Engineering and Policy REU, Iowa State University, Ames, Iowa
Mentors: Dr. Hui Hu, Ahmet Ozbay, and Wei Tian

Abstract

An experimental study was conducted to investigate the effects counter-rotating wind turbines can have on power production, flow characteristics in the wake, and the dynamic wind loads on the turbine. All experiments for the study were performed in the Aerodynamic/Atmospheric Boundary Layer (AABL) Wind Tunnel located at the Aerospace Engineering Department of Iowa State University using 1:350 scaled down model wind turbines. The Atmospheric Boundary Layer wind was kept constant (the streamwise velocity and turbulence intensity during free flow were measured at hub height to be 4.87 m/s and 11.6%, respectively) throughout the study in order to measure and compare a counter-rotating (i.e., the downstream rotor rotates in the opposite direction of the upstream rotor) wind turbine to a single rotor horizontal axis wind turbine (HAWT) as well as a co-rotating (i.e., the downstream rotor rotates in the same direction of the upstream rotor) wind turbine. Each configuration was tested individually (alone in the wind tunnel) as well as in a tandem arrangement (one turbine behind another turbine) with different distances between the two turbines. It was found that both counter-rotating and co-rotating designs would have slower streamwise velocities and enhanced turbulence levels behind the wind turbine when compared to the single rotor design. The co-rotating blades also produced higher azimuthal velocity speeds than a single rotor, while the counter-rotating blades generated almost no velocity in that direction. Yuan et al. (2013) showed that when the two single rotor wind turbines have counter-rotating blades, the azimuthal velocity behind the upstream turbine will create a positive pre-rotating effect on the second one, while co-rotating rotors create a negative pre-rotating effect. The positive effect will result in greater lift on the second turbine while the negative effect will cause more drag to it. The counter-rotating rotors can extract the extra kinetic energy from the azimuthal velocity in the wake of the upstream wind turbine while the co-rotating rotors cannot. As a result of this effect, the wind turbines with counter-rotating rotors in this study proved to be able to extract about 53% more power than the HAWT individually and up to 42% more while in a tandem arrangement. For the tandem wind turbines, the power output benefits of counter-rotation were found to increase as the distance between them grew. It is recommended that a cost analysis be done for counter-rotating wind turbines to evaluate their feasibility. Further research should also be conducted to investigate the stresses that counter-rotating blades will have on downstream wind turbines.

---

1. Introduction

Wind energy has gathered increasing attention in recent years as one of the most promising clean and renewable energy sources today. The U.S. Department of Energy has established a scenario to have 20% of U.S. electricity generation from wind energy by 2030 (U.S. Department of Energy, 2008). This has led to much research to increase overall efficiency of wind turbines and wind power generation in general.

Despite recent improvements, increasing turbine efficiency remains a priority. A single rotor wind turbine (SRWT) cannot extract all available wind energy, and consequently leaves a significant amount in its wake. One way of obtaining some of this energy is by adding a second rotor (back to back configuration) very close in the wake of the front rotor. Also, as the wake behind the upstream turbine rotates in the opposite direction, the counter rotating concept for the added back rotor can be used to capture more of the left over energy. A study done by Yuan et al. (2013) concluded that this was due to a “pre-rotating” effect caused by the upstream rotor. This results in a azimuthal velocity that a counter-rotating rear rotor can exploit while a co-rotating back rotor cannot.

For the experiments in this study, wind turbines with counter-rotating (rotating in opposite directions) rotors were compared to a common SRWT. However, it will also be beneficial to compare aspects of counter-rotation to co-rotation (rotating in the same direction), such as power output, mean axial and azimuthal velocity and turbulence profiles, and aerodynamic forces and moment on the wind turbine.

This paper will discuss further the various effects on power output, wake profile, and dynamic loads caused by adding a second rotor (co-rotating and counter-rotating) on the same turbine behind the nacelle.

2. Literature Review

According to Betz law, the maximum amount of energy that can be taken from the wind by turbines with a single rotor is about 59%. Even so, real single rotor turbines can only convert about 40-50% of the maximum available, leaving up to 60% that can still be captured. A few traditional ways to gain turbine performance are optimizing airfoil characteristics, aerodynamics, and controls as well as using larger blades in general to increase the rotor swept area and therefore the amount of wind that can be harvested. However, many new methods are being investigated in order to increase the efficiency even further.

The idea of adding a second set of blades rotating with the wake of the upstream rotor has produced the concept of a counter rotating wind turbine (CRWT). A number of studies have shown a significant increase in power output when using a CRWT compared to a single rotor design. Appa Technology Initiatives (Appa, 2002) built and tested a prototype 6 kW CRWT in California over a four month period. Their results showed that this CRWT system, when compared to a single rotor wind turbine, could harvest an additional 30% from the same rotor swept area. Also, Habash et al. (2011) conducted a wind tunnel experiment on a downscaled model CRWT and determined that a CRWT design may generate 60% more energy than a similar single rotor system. The counter-rotating concept they used could also reduce cut-in speed while maintaining performance and improving efficiency at lower wind speeds. Design optimizations such as using auxiliary rotors could also help to reduce cut-in speed.

Additionally, Shen et al. (2007) estimated the Annual Energy Production (AEP) for a CRWT, equipped with two Nordtank 500 kW rotors, and a similar SRWT with rotor radii of 20.5 m on the island of Sprogø in Denmark. By creating a wind speed distribution, they calculated that the CRWT could produce an increase in AEP of 43.5% when compared to the SRWT. It was also noted that the CRWT system they tested performed especially well in high wind speeds, but the rotational speed should be reduced at low wind speeds.

Wind turbines can be affected in many ways by wakes of another turbine upstream. When two wind turbines are in a tandem arrangement (one behind the other), the downstream turbine will experience considerable velocity deficits as well as enhanced turbulence due to the upstream turbine. Wake will also have an effect on the downstream turbine's power output (due to the velocity deficit) and dynamic wind loading (due to the enhanced turbulence) which tends to reduce the life span of the turbine. These effects get more significant the closer you are behind the upstream turbine. Because of this, wake effects are of much importance when studying CRWT's, as the second rotor is very close to the upstream one and the wake that is created will be different than a traditional SRWT.

Yuan et al. (2013) constructed an experiment using multiple single rotor wind turbines in tandem to compare a co-rotating to a counter-rotating configuration. It was found that when the distance between two tandem turbines was fixed at 0.7D (0.7 rotor diameters), the rear turbine could produce from 10 to 16.9% more power (using a range of resistances) counter-rotating when compared to co-rotating. This confirmed what was expected as the counter-rotating rear turbine will be rotating in the same direction of the front turbine's wake, and subsequently gains more power output. This is due to the pre-rotating effect caused by the upstream turbine's azimuthal velocity, which will increase the angle of attack causing an increase in torque and power output. It was also concluded that the power advantages of counter-rotation was significantly reduced the further away the rear wind turbine was from the front turbine. This was a result of wake recovery, since the induced azimuthal velocity will recover further away from the turbine. They determined that the benefit of counter-rotation would be less than 1% when the distance between the tandem wind turbines is greater than 6D. This means that by the time the wake reached 6D behind the turbine, the induced azimuthal velocity had almost completely recovered.

3. **Experimental Methods**

All experiments were conducted in the Aerodynamic/Atmospheric Boundary Layer (AABL) Wind Tunnel located at the Aerospace Engineering Department of Iowa State University. The closed-circuit wind tunnel has a test section of 45 ft in length, 8 ft in width, and 7.25 ft in height. The maximum wind speed of the wind tunnel is about 85 mph. The wind speed is controlled by varying the rotational frequency of the electric fan that simulates the wind. For these experiments the frequency was kept constant at 5.5 Hz. Chains were lined on the floor of the test section as roughness elements to simulate a velocity and atmospheric boundary layer wind profile.

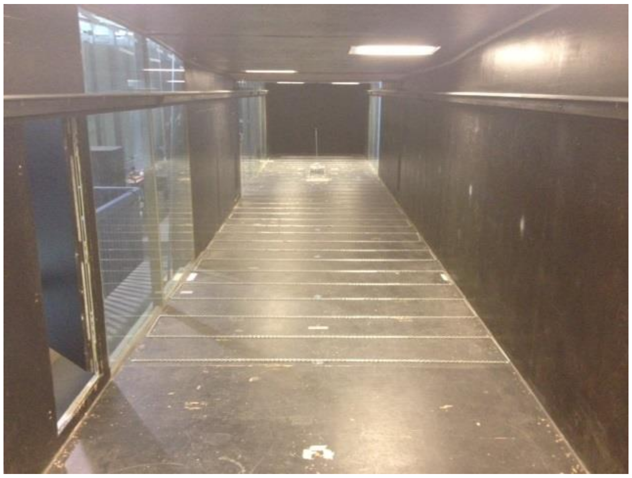

Figure 1. Test section of the wind tunnel with chains as roughness elements

The wind turbine models that were used are 3D printed, 1:350 scaled down versions of a common 2 MW wind turbine modified to include a second rotor. All wind turbine rotors had the same front and back diameter of 10 inches, a pitch angle of 3°, a length between the two rotors of 0.25D (0.25 rotor diameters), and a tower or hub height of 9 inches. Additionally, hollow aluminum rods were used for the turbine towers and installed using a hole in the wind tunnel floor. The hollow aluminum rods were also used for installing DC motors in the turbine nacelles, with the wires travelling through the rod.

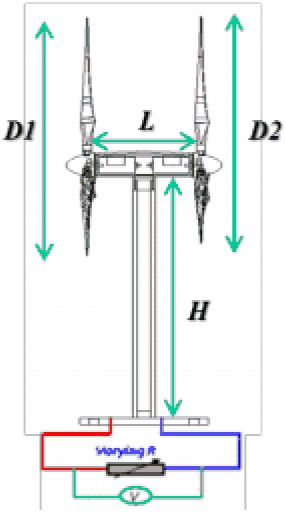

Figure 2. Scale model of a 2 MW turbine modified as a CRWT

For this study, three wind turbine configurations were inspected and compared: a single rotor HAWT, a turbine with a counter-rotating rear rotor (i.e. rotating in the opposite direction of the front rotor), and a turbine with a co-rotating rear rotor (i.e. rotating the same direction as the front rotor). In addition to examining each of these while they were alone in the wind tunnel, each was also put into a tandem arrangement, with both turbines having the same configuration, in order to discover how the downstream wind turbine is affected by the upstream one. The most important data for the tandem case was for the downstream wind turbine. This is because it is essential to see the different wake effects caused by each upstream turbine and which setup might be more efficient.

Various types of data were collected using a few different experimental instruments. The first of these is the wake profile of the wind, measured using a cobra probe. The cobra probe provides instantaneous measurements of three directional components of velocity. Turbulence intensities and Reynolds stresses can also be obtained from real-time measurements. The flow field was measured at different downstream locations in order to comprehend why counter-rotating blades would perform better than the co-rotating configuration. In order to investigate this fully, the flow velocity, turbulence intensities, and Reynolds stresses were all measured and would be analyzed. The cobra probe was fixed on a steel frame for this study and controlled in the vertical direction by a motorized traverse system.

Another data category is electrical power output, measured by small DC motors installed in the wind turbine nacelles. First, a voltage output of each motor was measured while also applying and recording a range of resistances. Once the voltage was measured using an applied resistance in the circuit, power output could be calculated using these two values. By changing the resistance, the power output as well as tip speed ratio could be adjusted. The power outputs for each of the three wind turbine configurations were measured and would be analyzed and compared. By calculating the power output over a range of applied resistances, the optimum power output or efficiency could be found. Additionally, for the tandem case, the wake of the upstream wind turbine is expected to have a great amount of influence on the downstream turbine. Therefore, the power outputs for the downstream turbines were measured and compared in order to better see the upstream turbine's wake effects.

A third parameter recorded is the aerodynamic forces and moments on the wind turbine, measured by a JR3 Force/Moment sensor. This sensor was mounted underneath the wind tunnel floor at the base of the wind turbine tower and recorded three dimensional components of both force and moment. The sampling rate for all force and moment measurements was set to 1.0 KHz with a sampling time of 5 minutes to insure accuracy. As with power output, forces and moments were measured for each of the three turbine configurations as well as for the tandem arrangements of each. However, the forces and moments were only measured at the resistance with optimum power output. These measurements give more understanding to the different effects of co-rotating and counter-rotating blades.

The fourth and last data type collected is the blade rotational speed using an optical tachometer. By attaching a small piece of reflective tape to one blade, the laser from the tachometer would be redirected back every time the blade completes a rotation, thus obtaining its rotational speed, which can be used to calculate the tip speed ratio.

4. Results

4.1 Individual Wind Turbine

4.1.2 Power Output

For the power measurements, each rotor was applied a range of resistances, as described earlier, in order to find the optimum resistance for peak power output. Once this was done, each of the configurations had the optimum resistance applied and the power output was measured and compared under the same flow conditions. Each back rotor (co- and counter-rotating) was also tested individually without a front rotor to make sure they performed similarly as is expected.

First, each of the two dual-rotor configurations' power output was normalized with the HAWT's as shown in Figure 3. It was found that the co-rotating wind turbine had about a 44% increase in total power output than the HAWT, while the turbine with counter-rotating rotors had about a 53% increase. This increase over co-rotating is because the second rotor in the counter-rotating configuration will be rotating in the same direction as the front rotor's wake, allowing it to harvest more left over energy. As explained before, this is due to the positive pre-rotating effect, allowing the back rotor to use the kinetic energy from the induced azimuthal velocity. These results also show that adding a second rotor, no matter which direction it rotates, will still have a considerable increase in power output.

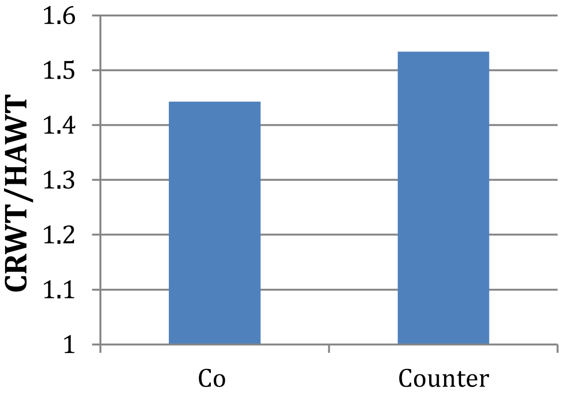

Figure 3. Total power output for each two-rotor configuration normalized with HAWT

Next, the counter-rotating wind turbine was compared directly to the co-rotating one, shown in Figure 4. The total power output was investigated as well as the back and front rotors individually. It was found that the back rotor for the counter-rotating configuration had about a 17% increase over the co-rotating back rotor. Again, this is due to it rotating in the same direction as the front rotor's wake, as opposed to against it as the co-rotating back rotor does. This led to a total power output increase of about 6% for the counter-rotating wind turbine over the co-rotating one. The reason the total increase is lower than the increase of the back rotor is because the front rotor will be harvesting most of the wind turbines energy, and both of the two dual-rotor configurations will have about the same affect on the front rotor, causing it to have a similar power output for each.

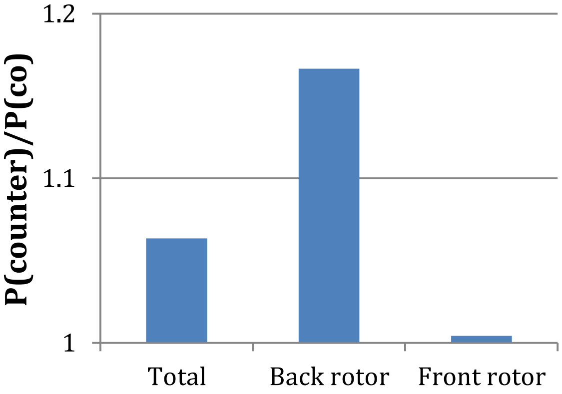

Figure 4. Power outputs for counter-rotating compared to co-rotating configuration

Figure 5 and Figure 6 show the power comparisons for the front and back rotors, respectively. Each value was normalized for when the individual rotor was on the turbine by itself, without the other rotor affecting it. For the front rotor comparison, both rotors performed at about 92% of the alone case. This decrease in power output for the front rotor establishes that attaching the back rotor to the wind turbine will have an effect on the front one, causing it to have slightly less power output than it would have without the back rotor. However, even though the front rotor performs slightly worse, the total power from the wind turbine is still significantly higher due to the back rotor being added. The fact that the front rotor for both co-rotating and counter-rotating configurations has a similar power output shows that the rotation direction of the back rotor will not change the effect it will have on the front rotor.

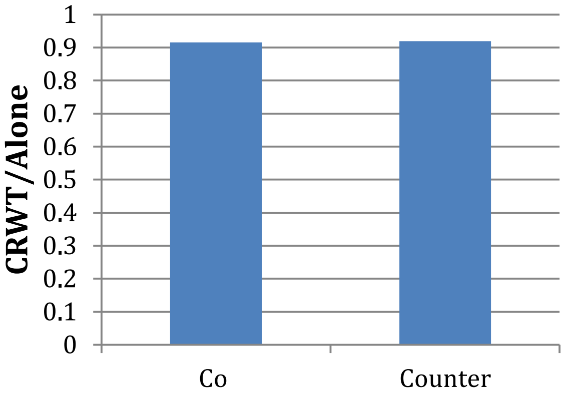

Figure 5. Front rotor power output for each two-rotor configuration normalized with when the rotor is alone

For the back rotor comparison there is a more noticeable difference in the power output for the two rotation directions than the front rotor experienced. This is because the back rotor is in the wake of the front rotor which means it will be significantly affected by the front rotors wake. However, the front rotor is upstream to the back rotor, which is why it experienced very limited effects from the downstream rotor and had a similar power output for both configurations. The figure shows that when the back rotor was co-rotating it harvested about 59% of the power that it did when it was alone on the wind turbine. Additionally, when the rotor was counter-rotating it output around 69% of the power that it did when it was alone. These results confirm that the counter-rotating back rotor has a considerable increase in power output over the co-rotating one. This conclusion can be made because both of the rotors performed similarly while they were alone, meaning that the only thing affecting them while the front rotor was attached was their direction of rotation.

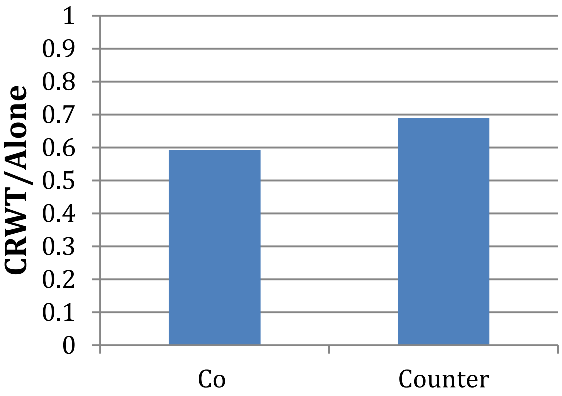

Figure 6. Back rotor power output for each two-rotor configuration normalized with when the rotor is alone

4.1.1 Wake Profile

As described above, the cobra probe was used to measure the velocity profiles in the wake of the wind turbine. For each of the dual-rotor configurations, the front rotor was set to optimum power output by applying the needed resistance. The wake profile of co- and counter-rotating wind turbines, a turbine with a single rotor, and the free flow or free stream (no wind turbine in the wind tunnel) were all measured and compared. The three main components of the wake profile that were measured and analyzed are the streamwise velocity (U-component), azimuthal velocity (V-component or component tangential to the rotor blades), and the turbulence intensity in the U-direction (Iuu).

The first of these measurements, the streamwise velocity, is shown below in Figure 7. A few different plots are shown, each for a different distance behind the lone wind turbine. Each plot shows measurements taken from 1 inch to 30 inches above the wind tunnel floor, normalized with the hub height of 9 inches. Measurements around 20 to 30 inches above the floor are well above the wind turbine and therefore do not see much of its effects, as shown by each data set straightening out and combining. When comparing the HAWT to the dual-rotor configurations, it can easily be seen that the HAWT will almost always have a higher streamwise velocity behind the turbine. This is because when a second rotor is added behind the wind turbine it will be converting more of the wind into energy, which means less wind will be left behind it. However, it can also be seen that as the measurements move further behind the turbine, these differences diminish. This is because the further behind the wind turbine the measurements are taken, the more time the wind has to recover. The results also showed that the co-rotating and counter-rotating rotors had similar data values at all of the distances behind the turbine, meaning the streamwise velocities in their wake were almost the same. However, the streamwise velocities in the wake of the counter-rotating configuration are usually slightly smaller than the values for the co-rotating wind turbine. The counter-rotating blades will convert more wind into power than the co-rotating ones will and, like the difference between the dual-rotor designs and the HAWT, will therefore have slightly slower streamwise wind speeds behind it.

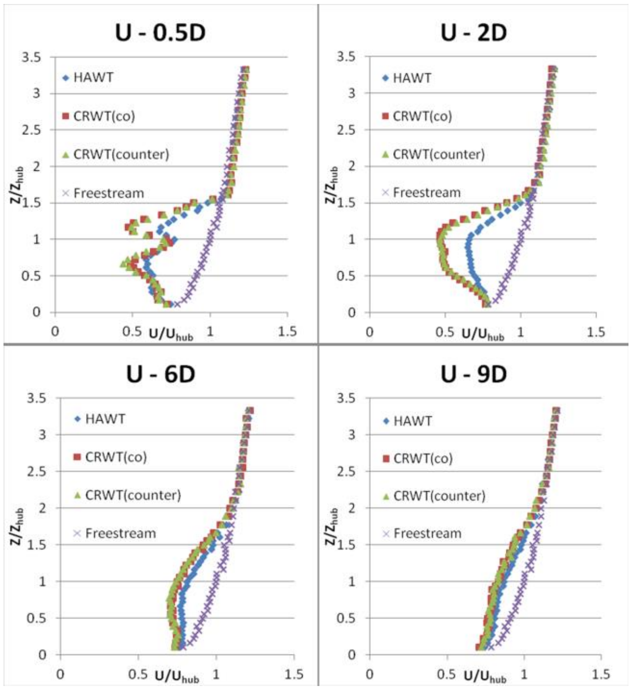

Figure 7. Streamwise velocity (U-direction) profiles at different downstream locations

The next type of measurement is the velocity tangential to the rotor blades, shown in Figure 8 below. Again, there are multiple plots, each taking measurements from the same distances as the streamwise velocity data and ranging from 1 to 30 inches above the wind tunnel floor. Unlike streamwise velocity, however, there is a very noticeable difference in azimuthal velocity when comparing the two dual-rotor configurations. For the measurements that were close behind the wind turbine (0.5D and 2D), the counter-rotating blades had little to no azimuthal velocity behind them, while co-rotating blades had high velocity values behind them. This is due to the nature of counter-rotating blades. As explained before, the wind behind the front rotor will be rotating opposite to the rotor rotation. This means that when the back rotor is rotating with the wind (counter-rotating), it will try change the wind rotation direction again, but the outcome of this only levels the wind back out to having almost no tangential velocity. On the other hand, when the downstream rotor is rotating in the same direction as the upstream one, the opposite happens and the wind is rotated faster in the same direction as the upstream turbines wake. Since the co-rotating back rotor will rotate the wind faster in the same direction, it was found to have a greater azimuthal velocity than even the HAWT configuration. Additionally, it can be seen that there are two peaks in the azimuthal velocity above and below the hub height, one positive and one negative. The reason for this is that the wake behind the HAWT and co-rotating wind turbine will be rotating in a circle. This means that under the hub height the wind will be moving in the opposite direction that it will above the hub height, causing one of the directions to be positive and the other negative. It should also be noted that the second peak just above the hub height is greater than below the hub height is due to higher wind speeds experienced by the upper section of the rotor at higher altitudes in the atmospheric boundary layer flow.

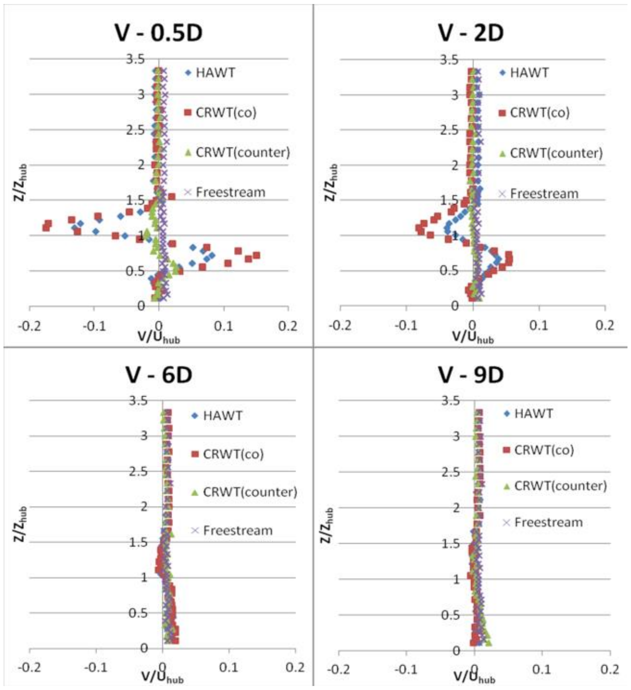

Figure 8. Azimuthal/Tangential velocity (V-direction) profiles at different downstream locations

The last component of the wake profile that was measured is the turbulence intensity, shown below in Figure 9. Each plot is similar to the first two components measured with the same distances behind the wind turbine and heights above the floor. It can be seen that both of the dual-rotor setups almost always had higher turbulence intensity than the turbine with a single set of blades. The values for the CRWTs are similar to the HAWT's at very near wake (0.5D). This is because the flow directly behind the wind turbine will be the most turbulent, making it hard to see many differences between any of the configurations. When a wind turbine experiences more turbulent flow it will have higher fatigue loading on it which results in a shorter life expectancy for the turbine. This means that the more turbulent flow behind a CRWT can cause greater adverse effects on any downstream wind turbines. However, higher turbulence also promotes turbulent mixing thus making the wake recover faster. It can be seen that the CRWT velocity deficit recovery rate is higher between 2D and 6D compared to the HAWT.

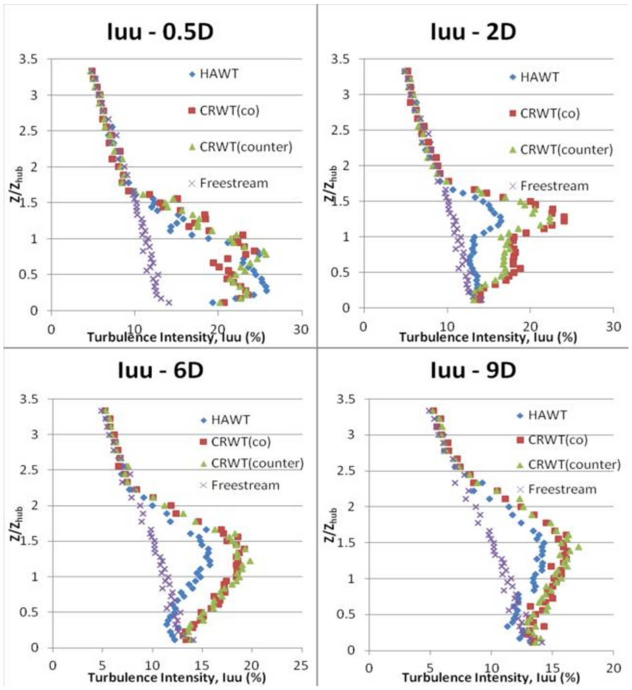

Figure 9. Turbulence Intensity (Iuu) at different downstream locations

4.1.3 Force and Moment

For the force and moment measurements, each rotor was again set to peak power by applying the optimum resistance. For this study, the important values to be compared were the axial force in the streamwise or x-direction and the bending moment about the y-axis.

Figure 10 and Figure 11 show the force and moment measurements, respectively, for each CRWT normalized with the HAWT. Both the co-rotating and counter-rotating systems experienced about 51% more axial force and about 53% more bending moment than the HAWT did. One conclusion from this is that both of the dual-rotor configurations produced similar measurements. From this it can be determined that the rotation direction of the back rotor has little impact on the axial force and bending moment that the whole turbine will experience. A second conclusion is that both CRWTs were shown to have a higher axial loading and bending moment than the HAWT. Higher wind loads may cause a need to increase structural integrity and strength by increasing the tower diameter or foundation strength, which will add to the cost of the wind turbine.

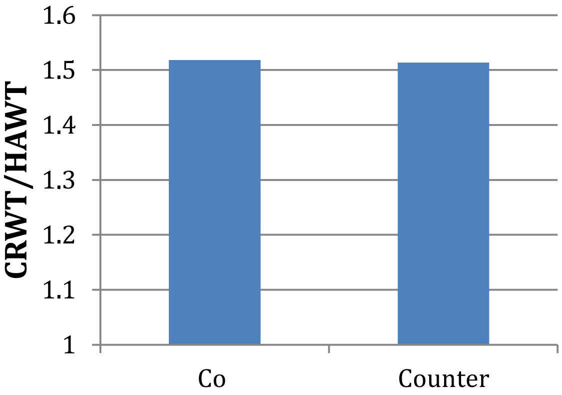

Figure 10. Axial forces for each two-rotor configuration normalized with HAWT

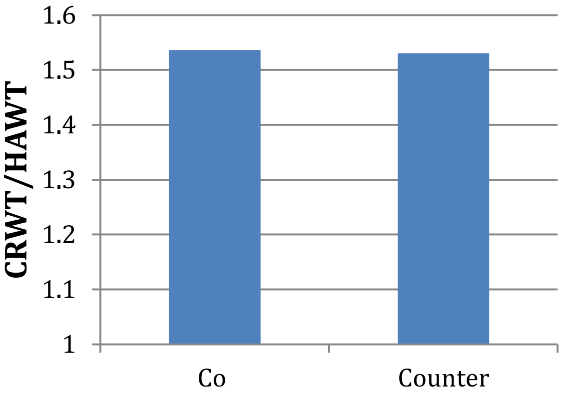

Figure 11. Bending moments for each two-rotor configuration normalized with HAWT

4.2 Wind Turbines in Tandem Arrangement

Similar to the individual tests, each rotor in the tandem arrangement had optimum resistance applied in order to obtain peak power. Measurements were then taken with varying distances between the two turbines. These measurements focused on the power output from the downstream wind turbine individually as well as total power output. Total power output was defined as power from the upstream turbine added to power of the downstream turbine.

Figure 12 shows total wind farm (i.e., two tandem wind turbines) power output of wind turbines that have counter-rotating blades normalized with measurements for the HAWT configuration. For all distances between the two turbines, the counter-rotating configuration was found to always have a higher power output than the tandem HAWTs. At 15D, the CRWTs produced about 42% more power and seems to begin converging to 1.5 times the HAWTs output. This is the largest power output increase because the wind will recover more as it moves farther behind the first wind turbine, leaving more energy to be extracted by the downstream one.

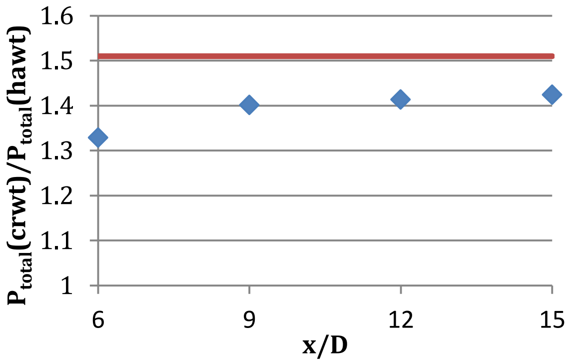

Figure 12. Total wind farm power output of CRWT with different distances between the turbines

Figure 13 shows the power output of the downstream counter-rotating wind turbine in comparison to the downstream HAWT. While it has the total downstream turbine power, it also shows the individual power output of each rotor on the turbine. These results show that the total downstream wind turbine power output for the CRWT can range from about 7-35% more than the HAWT, depending on the distance between the two tandem turbines. Of course, as the turbine is placed farther downstream, it will get more and more efficient due to wake recovery. Although, the benefit that the downstream wind turbine receives due to counter-rotation is not as significant as the power production increase to the full wind farm. This is because the front CRWT is extracting more energy than the HAWT, leaving less wind behind it. Therefore, the downstream turbine will not have as much wind to convert into power for the counter-rotating configuration and cannot perform quite as well as the total wind farm will in comparison.

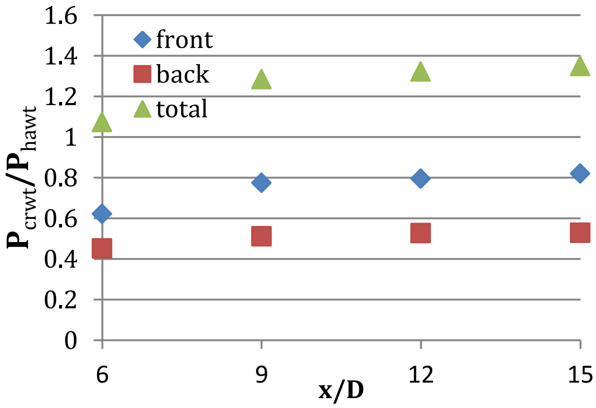

Figure 13. Front rotor, back rotor, and total power output of the downstream CRWT

5. Analysis and Interpretation

In general, the results indicated a significant increase in performance when a second rotor was added behind the nacelle. As hypothesized, when each model wind turbine design was tested alone, the counter-rotating turbine out-performed the others. It was found that the CRWT could produce over 1.5 times the power that a single-rotor HAWT and above 5% more power than the turbine with co-rotating rotors. While this is a significant increase in the power output of an individual wind turbine, the dual-rotors also proved to have a strong effect on the wake characteristics.

However, since both dual-rotor designs were converting more wind into power output than the HAWT, they would also have lower streamwise wind speeds behind the turbine. This difference became less noticeable as measurements moved further behind the wind turbine and, therefore, it would be beneficial to place CRWTs farther apart (when in a wind farm arrangement) to allow the wind more time to recover. Additionally, the counter-rotating rotors almost always had little or no azimuthal velocity in their wake because it exploits the induced azimuthal velocity resulting in an increase in power production while co-rotating blades produced more than the HAWT. This can be beneficial to counter-rotation as azimuthal velocity can negatively affect a downstream wind turbine. Also, both dual-rotor designs typically produced more turbulence behind them than the HAWT. Similarly to streamwise velocity, though, the distinction became less pronounced farther behind the turbine. As the flow becomes more turbulent behind the upstream wind turbine, it can cause the downstream turbine a greater amount of fatigue loading. This will lower the life expectancy of the wind turbine and the structural strength of the turbine may need to be improved. It is also important that higher turbulence will also encourage turbulent mixing, allowing the wake to recover faster.

While these different wake characteristics have an effect on power available and stresses applied to a downstream wind turbine, they can also have an adverse effect to agricultural crops or anything that is on the surface. Rajewski et al. conducted a study looking into the interaction between wind turbines and crop growth on the surface. One conclusion they made was that changes in the wind profile as well as a more turbulent flow caused by wind turbines can alter the micrometeorological conditions of the surface. While the negative effects of this may be variable, counter-rotating wind turbines may enhance these effects, possibly harming items on the surface.

Adding a second rotor to the turbine also caused a change in the aerodynamic forces and moments on the turbine. While each of the dual-rotor wind turbines experienced about the same axial load and bending moment, these values were just above 1.5 times higher than the measurements taken for the HAWT. Like the increase in turbulence behind the CRWT, the increases in forces and moments on the turbine may suggest that the structural strength should be increased.

Lastly, the CRWT also produced a significant increase in power output when in a tandem arrangement. Compared to the single rotor wind turbines, the two turbines together extracted up to 42% more power when the rotors were counter-rotating. The greater the distance was between the two turbines, the better they performed overall, seeming to converge to almost 1.5 times the power harvested by the HAWTs. However, when looking at the downstream CRWT only, it showed to not perform as well as both wind turbines together. This is due to the more significant wake effects of the counter-rotating blades. Although, the downstream wind turbine still converted more wind into power than the HAWT. When the distance between the tandem wind turbines was set to 15D, the downstream turbine provided almost 35% more power than the HAWT. When the distance was set to 6D, though, the benefit was only about 7%.

6. Conclusions

An experimental study was conducted to investigate the effects counter-rotating rotors can have on power production, flow characteristics in the wake, and the dynamic wind loads of a turbine. Experiments for the study were done in an Aerodynamic/Atmospheric Boundary Layer (AABL) Wind Tunnel located at the Aerospace Engineering Department of Iowa State University using scaled down wind turbine models. The results showed that counter-rotating blades on a wind turbine can cause it to harvest a considerable amount more energy from the wind than a traditional single rotor wind turbine. At peak power output, the counter-rotating blades gained a 53% boost to power output over the HAWT that was tested as well as a 6% increase of the co-rotating rotors. While there is a great benefit to power output, the dual-rotor design also has a significant effect on the wake behind the turbine. Changes in velocity profile and turbulence intensities may have negative effects on any turbines that are downstream to a counter-rotating wind turbine as well as crops or anything else that is on the surface. It is suggested that these effects be further researched as well as a cost analysis be completed for adding a second rotor to a wind turbine.

Acknowledgements

Support for this research was provided by a National Science Foundation Research Experience for Undergraduates site program in Wind Energy Science Engineering and Policy (WESEP) grant number EEC-1063048 at Iowa State University. The support from Iowa Alliance for Wind Innovation and Novel Development (IAWIND) and National Science Foundation (NSF) under award number of CBET-1133751 is gratefully acknowledged.

References

Appa, Kari, 2002: Counter rotating wind turbine system,. Energy Innovations Small Grant (EISG) Program Technical Report, California, U.S. [Available online at http://eisg.sdsu.edu/Far/00-09%20FAR%20Appendix%20A.pdf]

Habash, R. W. Y., V. Groza, Y. Yang, C. Blouin, and P. Guillemette, 2011: Performance of a contra rotating small wind energy converter. *ISRN Mechanical Engineering*, Vol.2011 (2011): [Available online at http://www.hindawi.com/isrn/me/2011/828739/]

Rajewski, D. A., Eugene S. Takle, Julie K. Lundquist, Steven Oncley, John H. Prueger, Thomas W. Horst, Michael E. Rhodes, Richard Pfeiffer, Jerry L. Hatfield, Kristopher K. Spoth, and Russell K. Doorenbos, 2012: CWEX: Crop/Wind-energy Experiment: Observations of surface-layer, boundary-layer and mesoscale interactions with a wind farm. Bulletin of the American Meteorological Society, 94, 655-672. doi: 10.1175/BAMS-D-11-00240)

Shen, W. A., V. A. K. Zakkam, J. N. Sørensen, and K. Appa, 2007: Analysis of counter-rotating wind turbines." *Journal of Physics: Conference Series* 75.1 Print.

U.S. Department of Energy, 2008: 20% wind energy by 2030: Increasing Wind Energy's Contribution to U.S. Electricity Supply. DOE/GO-102008-2567.

Yuan, W., A. Ozbay, W. Tian, and H. Hu, 2013: An experimental investigation on the effects of turbine rotation directions on the wake interference of wind turbines. AIAA-2013-0607, *51st AIAA Aerospace Sciences Meeting Including the New Horizons Forum and Aerospace Exposition*, Grapevine, Texas, 07-10 January.

Integrating an Automated Fabric Placement System into the Manufacturing of Wind Turbine Blades

P. SAM COOK
Wind Energy Science Engineering and Policy REU, Iowa State University, Ames, Iowa
Mentors: Siqi Zhu and Dr. M. Frank

Abstract

Manufacturing of a wind turbine blade currently demands an immense amount of human labor during the fabric application process, or layup process, for the composite shell. The intent of this project is to devise a method to better perform the layup process of wind turbine blades. This includes using an already tested and designed method and machine to automate the layup process with a technique called shifting. This machine deforms the fabric in-plane into the shape of an arc in order from the fabric to come in contact with the mold with a curvy contour. However, the system does not have the capability depositing fabric onto an open mold. The research performed in this paper tests the repeatability of the machine as well as a procedure to apply post-shifted fabric to the mold without a large-scale over-head gantry system.

The FARO Edge FaroArm and FARO Laser Tracker ION along with FARO's CAM2 Measure 10 software were used to ensure the accuracy of the results and rule out possible flaws in the shifting machine. The results showed that rolling the fabric with one adhesive location is a viable process in transporting the fabric. The "stretching" and unshifting of the fabric seemed minimal and no major trends were found to mathematically model this process. Future research in automating the rolling process and reducing helical winding could put this technique in the commercial industry.

1. Introduction

A composite is a material made from two or more materials to give it desirable mechanical properties, such as high strength, low weight, fatigue strength, etc. Composite materials are found across a wide array of applications, such as in airplanes, racing vehicles, bathtubs, wind turbines, and many more. These composites provide high strength-to-weight ratio.

Composites can be particle-reinforced or fiber-reinforced, but in either case, they are bound to a matrix. One of the most common composites is concrete. Concrete is a particle-reinforced composite, which combines cement and aggregate, like rock and sand. The cement is the matrix, which is weak mechanically and holds the aggregate in position. When a stress is applied to concrete, rock and sand carry the load instead of the cement alone.

Currently, wind turbine blades are constructed of a fiberglass-reinforced composite. This is a fiber-reinforced composite composed of a fiberglass fabric and resin polymer matrix. The procedure of applying fabric to the mold is called the layup process. There are several techniques that could be used for the layup process to achieve the final infused product. The process used widely in wind energy is vacuum-assisted resin transfer molding (VRTM). VRTM is performed by laying dry fabric into an open mold and then covering it with peel ply and a resin distribution fabric. The stack is then covered by a vacuum bag and sealed to the outer edge of the mold. The resin enters on one side of the mold and pulled through the fabric by a vacuum applied on the other side. The VTRM technique is ideal for large component applications, like wind turbine blades, due to relatively low cost tooling (Daniel, 2006).

Typically, the layup of the fiberglass fabric is performed by human labor when using the VTRM method. This human interaction is a lengthy and hard process to replicate for multiple blades. Due to their high costs, wind turbine blades need to have a high quality assurance between each blade, and catastrophic failure of a blade could be very expensive. If a failure happens, a large crane may have to be transported to site to repair or replace the blade entirely. Automating the layup process could be a viable way to produce a higher quality blade with faster and cheaper results than current methods. This could reduce further maintenance cost and increase the life of the blade. This project focuses on automating the layup process for the wind energy industry.

A methodology and machine were created to perform this task. The research in this paper is intended to test quality repeatability of the machine and continue steps to fully incorporate the automated methodology into the process for manufacturing wind turbine blades.

2. Related Work

The Department of Energy has developed a scenario where wind would provide 20% of U.S. electricity by the year 2030. According to a Lawrence Livermore National Laboratory (2012) flowchart, wind energy accounted for approximately 1.2% of the energy used in 2011. For the 20% scenario to be achieved, manufacturing would have to increase by 20% every year for the next decade and then retain that annual output until 2030 (Department of Energy, 2008). This scenario drives the need for reduced labor content and faster production rates of wind turbine components.

This project will focus on the manufacturing of wind turbine blades. The blades are composed of several sections with several designs. All blades compose of a leading edge and a trailing edge with an outer shell. Inside of the blade is a loading carrying structure, like two spar caps and shear web combination to form an I-beam structure. The load carrying structure is designed differently for each type of blade. Most of these components are made from a fiberglass composite.

There have been many ideas about automating the layup of fiber-reinforced composites. One technique is called *filament winding*. Filament winding involves a rotating mandrel and either a static or one-direction moving platform or roll that holds a continuous band of filament or roll of fabric. The mandrel rotates and as it does so it takes the filament or fabric and it wraps around the shape of the mandrel. This process is usually used on simple geometric shapes.

The advantage of this technique is the high lay-down rates and high repeatability. However, major limitation of filament winding is that concave contours cannot be performed due to the tension that would “bridge” fabric over concave sections (Campbell, 2004).

Another technique, automated tape layup (ATL), is highly used in the aerospace industry. The ATL machines used today are computer-numerical controlled (CNC). A typical configuration could entail a multi-axis gantry with a layup head that follows predefined paths accurately. The system applies a prepreg tape usually of width of 75, 150, or 300 mm (Lukaszewicz et al., 2011). The prepreg tape (usually carbon fiber) is a fiber material that has been impregnated with the resin and is partially cured to give it a tacky texture. These machines are reliable and have a fast enough deposition rate for thin, high value aerospace composites. However, they are too expensive for the use in the wind industry, and do not apply wide enough material fast enough for the thickness of typical wind blades.

One automation system has been in development solely for the manufacturing of wind turbine blades. The company MAG developed a design for a Rapid Material Placement System (RMPS). This system consists of a gantry with multi-axis end effectors capable of spraying coatings, dispensing materials and applying adhesives automatically. The material placement is rated at 3 m/s. A pair of powered brushes follow behind and smooth out the plies while a laser and camera system search for the detection of a wave. The layup is said to be repeatable to within 2 mm with application tolerance of ±5 mm; the concept is visualized in Fig. 1 (Stewart, 2012). This would be an extraordinarily capable machine; however it was never fully developed and put into operation.

Figure 1: MAG RMPS (Stewart, 2012)

3. Solution Methodology

Although all of the above techniques are automated, there is one important aspect that these machines are missing. The systems lay fibrous material into a mold, which are not typically flat and have contour shapes. Since the mold is three-dimensional with a wavy contour, a deformation of the fabric is needed to place it in contact with the mold surface. Current automated systems are not capable of performing a curve with the fabric without an out-of-plane “wave” occurring. A wave will occur when the one side of the fabric has to traverse a shorter or longer distance than the other side, in which the shorter section has “extra” fabric and has no where to go except creating out-of-plane wave. An example used is a curve of an arc in Fig. 2.

Deformations are classified as in-plane and out-of-plane deformations. In-plane deformation is classified by changes to the tow orientation while maintaining contact with the mold surface. Out-of-plane deformation is defined as when the fabric is no longer in contact with the mold or a previous laid fabric. This could be the result of a wave, a wrinkle, or a curl.

Currently in industry, workers use their hands to manipulate the fabric. Instinctively, the workers “steer” the fabric around the shape that is desired. Workers would grasp a section of fabric a considerable length away from each other, and manipulate the shape of the fabric into an arc. Since the two sides of the fabric are the same length and the two sides of the arc are not the same arc length, excess fabric on the smaller radius side would come out of contact with the mold. As the radius becomes smaller, the curvature gets larger meaning that there will be more intense out-of-plane waves. The out-of-plane waves would be detrimental if left unnoticed and still causes quality concerns even at low curvature/small waves. This prompted research for other methods that could be viable in manipulating the fabric needed for the variable shaped contours of composite structures.

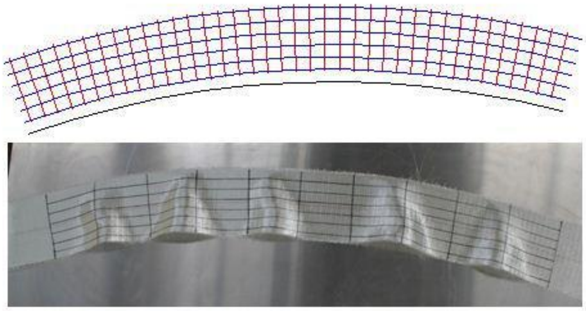

Figure 2: Steering method (Magnussen, 2011)

Manufacturing of the trailing edge of the blade has become one the major difficulties of producing a wind turbine blade. This is due to its complex shape and number of layers of fiberglass, called plies, needed. This sparked the desire to create methods of better manufacturing for this specific subsection of an entire blade. This project will focus on enhancing the manufacturing process of a wind turbine blade's trailing edge portion.

An industry grade material, Saertex 930 g/m^3 unidirectional (UD) fiberglass fabric, was used for this research on the trailing edge. In particular, this unidirectional fabric falls into the category of non-crimp fabric (NCF). The advantage of non-crimp fabric is that all the tows are linear. Woven fabric, unlike NCF, is made in an over-under-over method (basket weaving), which causes tows to be slightly offset from the adjacent tows. This causes a decrease in mechanical properties. The linearity of NCF yields higher strength and flexibility properties than woven fabric and much better fatigue life. Fatigue life is particularly important in a product like a wind turbine blade, which will see over 10 million cycles during a 20 year lifetime spinning on its hub (Ronold et al., 1999).

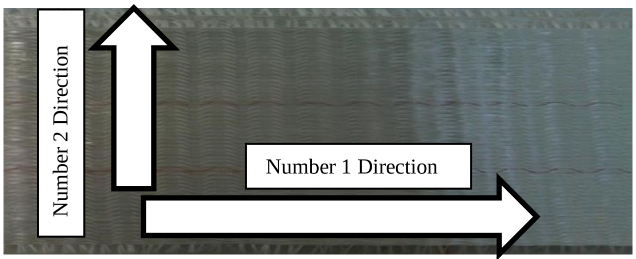

Figure 3: Schematic of Directions

Unidirectional fabric is created when bundles of fibers, also called a tow, are stitched together in the same orientation. The tows that run the length of the fabric are in the "number 1" direction and they are the major load bearing structural tows. Shorter tows running the width, or "number 2" direction of the fabric are cross tows, which stitch the structural tows together and provide minimal strength. The directions are shown in Fig. 3, these directions will be referred to a lot when talking about the fabric.

Two methods have been created in order to perform the deformation needed to place the fabric in contact with the mold. These methods involve manipulating the fabric in a specific direction. The first method is to *shear* the fabric in the "number 1" direction, while the other method is to *shift* the fabric in the "number 2" direction.

The first method, shearing, involves moving tows in the length-wise "number 1" direction. Schlangen (2012) performed this technique by making a Continuous One-Direction Adjustor (CODA) machine shown in Figure 4. This machine had two axles, and on each axle had a particular number of wheels depending on what type of shear was needed to fit the mold. The figure shows two different wheel placements that would create different shear angles. In the figure, Axle 1 had a variable speed while Axle 2 had a constant speed. While the machine was operating, Axle 1, spinning at a slower speed than Axle 2, would push fabric behind the machine. The stationary flattener was used to hold the excess fabric behind the running axles of the machine so that out-of-plane deformations would not occur.

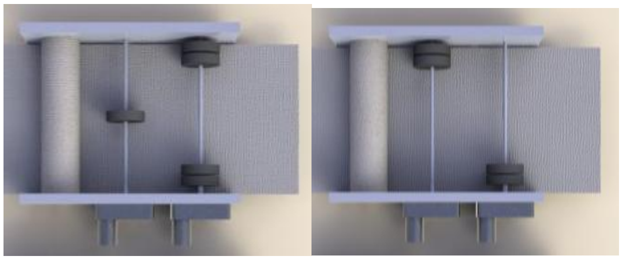

Figure 4: CODA. Different wheel configurations for different shear (Schlangen, 2012)

However, a downside to the shearing method is that it is not capable of executing a constant shear on the fabric, but only a varied shear throughout the length of the fabric. Also, the machine creates an irregular shape at the end, which is no longer perpendicular to the "number 1" direction. This is due to the difference in pulling of the tows, which are no longer at the same point as they were in the beginning. The effect of this non-straightedge is that it would not be effective to automate an entire section due to the cutting of each section to make it appear straight (Schlangen, 2012).

Shifting, the second method, involves performing a manipulation in a direction perpendicular of the shearing technique, the “number 2” direction. To explain this method, Magnussen (2011) used the pin jointed net (PJN) model. The PJN model says that the joint between two fiber directions can be represented as a pin. The angle between the two tow directions is called the shear angle Figure 5.

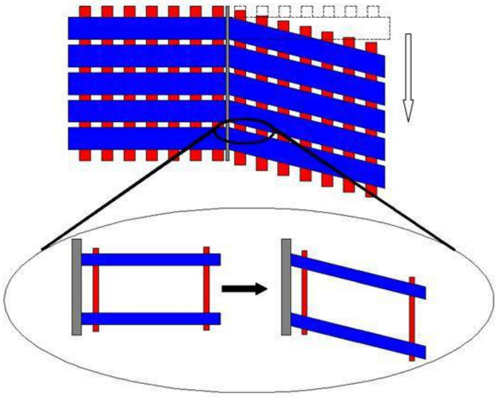

Figure 5: PJN model explaining shifting (Magnussen, 2011)

Using the pin jointed net model, Magnussen (2011) showed that manipulation of the fabric can be done by shaping a rectangular section of fabric into a parallelogram with a prescribed shear angle. This method, called, shifting, is created by clamping a section of fabric at two ends in the “number 1” direction. Then a prescribed shear angle is introduced to the section by moving one clamp parallel to the other in the “number 2” direction. Using the shifting method, out-of-plane deformation is drastically reduced when compared to the steering method. This project focuses solely on the shifting method for composite manufacturing.

Zhu (2013) began to develop an entire shifting machine that would be able to reproduce Magnussen’s methodology. Zhu started to design a shifting head shown in figure 6. The head includes a cylinder for which to place the fabric (figure 6f), front and back pinch rollers to feed the fabric in and out of the machine (figure 6cd), and the two clamps that move in different directions to perform the shift (figure 6ab).

The two clamps are fixed on two linear stages. The spacing clamp moves along the “number 1” direction of the fabric to adjust the length of the section to be shift. After clamping down, the shifting clamp moves in the “number 2” direction to create a prescribed shift angle. To grasp the fabric the top cylinder of each set of pinch rollers move up and down. Pneumatic cylinders controlled by solenoid valves drive the pinching motion. A servo motor drives each of the two linear stages, while the pinch rollers are driven by another servo motor with a timing belt system (Zhu, 2013). The shifting head is connected to a 10-meter by 2-meter gantry system that can move the entire shifting head over that region in six directions.

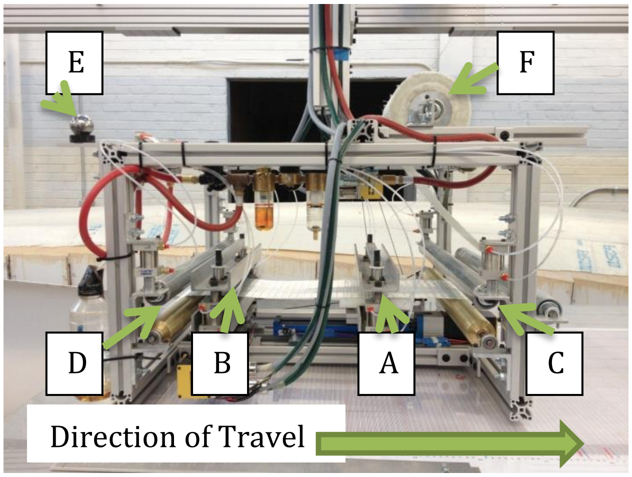

Figure 6: Shifting head (Zhu, 2013). 6a. Spacing clamp. 6b. Shifting clamp. 6cd. Pinch rollers. 6e. Reference sphere. 6f. Fabric roll.

The machine’s shifting procedure is a cycle of motions. First, the spacing clamp (figure 6a) moves to a corresponding position according to the length needed for that particular section. Next the shifting process begins. Both clamps are closed to grip the fabric and both pinch rollers open. As the shifting clamp (figure 6b) moves to perform the shift, the gantry moves the shifting head in the opposing direction to keep the fabric hanging in the same position. At the same time, the spacing clamp moves toward the back roller (figure 6d) to compensate for the length reduction of the shifted fabric. Finally, the clamps open and the pinch rollers closed. The rollers deposit the fabric while the gantry moves forward the length of the newly shifted section to initialize for the next shifted section. This process is repeated to perform multiple shifted sections that form a desired curvature. The process of determining the path for a 2 dimensional part is described in Magnussen’s and Zhu’s Master’s thesis in the Mathematical Model section.

One of the most important questions is: what effect does the shifting approach have on the mechanical properties of the fabric? Magnussen (2011) tested infused sections of fabric that had two linear parts where the shift occurred. Zhu also tested the same sections, however, the fabric he tested where manipulated by the shifting machine. Results from these samples showed that they were not affected by the curvature. This ultimately was the final step to assuring that automating a shifting machine is a viable process.

The current shifting machine is capable of depositing onto a table and not a three-dimensional mold. In order for the fabric to be placed onto the mold, one of either two things must happen. One, a gantry system the size of the mold would have to be created so that the shifting head could move directly above the mold. Or, the fabric could be deposited onto a flat table and then the shifted fabric would have to be picked up by some means and transported to the mold. The first method, a large-scale gantry that would need to be 4+ times larger, could prove to be a more costly option and is currently under research by Zhu. Therefore, the intent of the research presented is to devise a method for transporting the fabric.

Before developing a procedure, the following question must be answered:

> How repeatable is the shifting machine at placing fabric at a desired location for multiple plies?

This question will be evaluated in section 4.1, while the procedure for post-shifted fabric is discussed in section 4.2. These are crucial to determine if the automated shifting system is to be commercialized.

There are two different approaches that have been previously considered for the post-shifted fabric. The fabric could be transported to the mold by folding the layers in half multiple times and carried or by sliding the layers on a lightweight platform of the same size. Both of these are not practical due to the unintentional deformation of the fabric and the large platform that would be needed.

It is noted; however, that when the fabric arrives in the factory, it is packaged as a roll. Putting the fabric onto a roll could be the most feasible possibility. The machine could shift the fabric, be rolled onto a core, and then taken to the mold and rolled back out. This method will be the topic presented in section 4.2 and the latter part of this paper.

4. Experimental Methods

In order to insure accurate results, the components in the shifting head need to be in precise alignment with the over-head gantry. Using the FARO Edge arm, an articulated coordinate-measurement machine (CMM), the front and back pinch rollers, shifting and spacing clamps, and both sides of the fabric roll bracket were aligned to within a tolerable orientation of ±1° of perfect parallelism too the YZ plane of the gantry. The coordinate system of the programing code of the gantry is shown in figure 7. This axis will be used as a reference for the experiments in this research.

4.1 Shifting Machine Layup Repeatability

The purpose of the shifting machine is to deposit layers of plies on top of each other in the prescribed location and orientation that would be needed for the final product. To test this, the following procedure was executed: the machine is given a prescribed curvature that it would need to shift, the machine shifts ply 1, then the fabric is cut at the end of the shifted section. This sequence is repeated for all subsequent plies. The distance between each ply is measured at different locations at a constant distance interval apart.

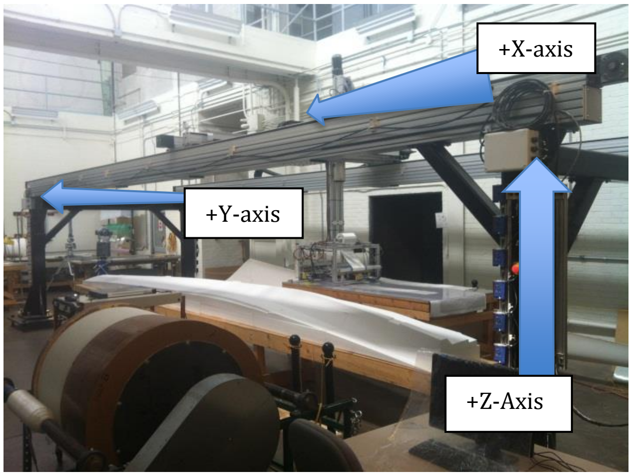

Figure 7: Gantry coordinate system: Directions of positive axes

The curve that was used had 6 shifted sections with two straight sections on the end. The length of each section was 200 mm and each had a different shift angle. The shift angles were -15, -9, -3, 3, 9, and 15 degrees as shown in Figure 8.

As testing began, it was observed that the fabric had a tendency to move to one side of the machine. It was decided to run the machine to deposit fabric in order to find the fabric's natural resting place in the machine. A line was drawn on the platform of the spacing clamp. At the beginning of each new layer or trial, the fabric is placed on this line to ensure that the machine is the only cause of movement that the fabric experiences.

The initial plan to test the repeatability was to run the machine for five layers. After each layer, the gantry would be commanded to offset by a prescribed number. The initial offsets were to be 3mm, 6mm, and 9mm. However, after the first test, an observation showed that each ply was off by a significant distance more than the offset.

It was determined that initial first non-shifted sections were at fault for the significant distance between plies. This was because if the first sections weren't parallel with the underlying ply, then the fabric would be offset by an angle. As the machine traversed it's normal distance, the offset error would be higher due to this slight angle. To compensate for this fact, there would no offset, 0 mm, and a large offset, 10 mm in the positive y-direction.

A FARO Laser Tracker was used to measure the gantry's initial and final position to ensure the precision of the gantry had no effect on the machine's repeatability. The reference sphere for the Laser Tracker was placed in the position in figure 6e. The shifting head's exact

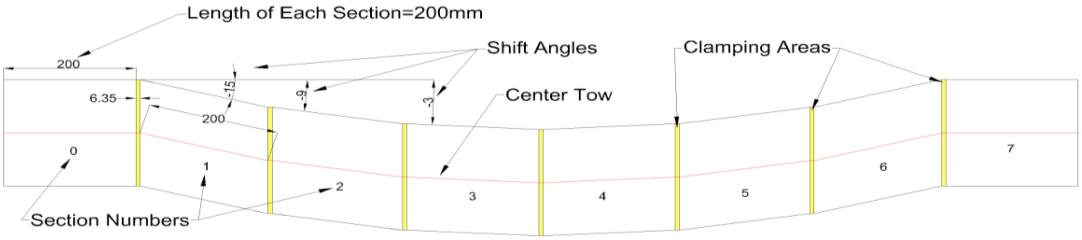

Figure 8: Curve used during testing (Zhu 2013)

position was recorded at the beginning and end of each shifting session.

For each ply in each trial, the beginning section needed to be the same. The fabric was cut so that 400 mm of fabric was hanging out of the shifting head. The location of ply 1 was difficult to determine since there was no ply below it to compare its position on. For ply 1, the fabric was lifted off the table and allowed to fall naturally. Once the fabric fell onto the table in its "natural" position, the edge of the fabric on the positive side of the y-axis was marked on the table to compare with the other plies that would be laid (this was only done for the 10 mm offset).

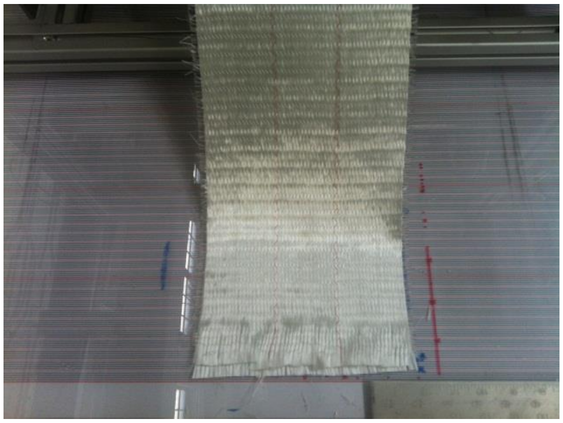

Figure 9: Shifting machine layup repeatability. Each ply is on directly on top on one another for the 0 mm offset.

To begin the shifting sequence, the program was instructed to execute automated motion. After ply 1 was shifted, the fabric was cut 400 mm away from the rear pinch rollers. The machine was then instructed to return to the initial position at the beginning of the ply. If needed, the gantry was instructed to move a prescribed distance in the +Y-direction. This distance would be the desired offset for ply 2. Like before, the edge of ply 2 on the positive edge of the y-axis was marked on the table. The length of the ply that was resting on the table was measured with caliper and adjusted to the necessary offset of each experiment.

The distances between the plies 1 and 2 were measured with calipers at 7 locations with a distance of 200 mm between each location. The first location was approximately 100 mm before the first shifted section. The same procedure was followed for plies 3-5 with measuring the newest laid ply to the one directly below it at the same locations as before. If the ply was laid perfectly where it should have then in should have moved in the positive Y-direction, meaning you measure the distance on the side of the ply of the negative Y-axis. If not, and the current ply over lays the ply underneath, then the side of the ply on the positive Y-axis is measured. This value will be negative since the ply went in the negative Y-direction.

4.2 Rolling Post-Shifted Fabric

The goal of the preliminary tests was to decide how the final process of the procedure would begin. The preliminary experiments were all tested with straight sections. The majority of the experiments were done with a "what would happen if" attitude. During the preliminary testing, the distances between the each ply at each location was measured using calipers. The positive axes for these experiments, shown in figure *** (same as below), were opposite of the gantry's axis system so that they were easy to interpret and these results would not be related to the shifting head gantry. Besides the two preliminary tests, the other experiment's axes were aligned with the gantry's axis system.

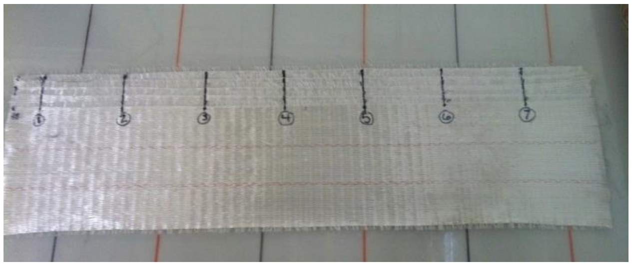

Figure 10: First Experiment Setup

During the first experiment, five plies were laid with an arbitrary offset. Seven locations were marked on the fabric with 125 mm between locations. The first location was at 43 mm from the beginning of the fabric. A straightedge was laid on the table and marked a straight line down the five plies at each location, shown in figure 10. The distance between each ply was measured from the one on top of it using calipers in both the "number 1" direction and "number 2" direction. The layers were then rolled up with the top layer being in contact with the roll core. This was done in order to easily roll the fabric out onto the mold when finished rolling and not having to flip over the fabric after it had been rolled out. The roll core was 83 mm in diameter. The fabric was then rolled back out, and again, the distance between the plies were recorded. The goal of this test was just to observe what would happen with respect to the ply depositions.

The goal of the second preliminary test was intended to apply an adhesive to plies to observe if less unintentional deformation occurred. There were two adhesive experiments. The first tested an adhesive strip on the two ends of the fabric. The second experiment tested one adhesive strip on the beginning section of the fabric.

The two adhesive tests were the same length, but differed in number of adhesive locations and number of locations where measurements were recorded. The adhesive used in this experiment was 3M™ Super 77™ Multipurpose Spray Adhesive. The first test had 11 locations where measurements were to be recorded. The adhesive was applied to location 1 and 11. The second test, using different fabric, only had 8 measurement locations and the adhesive was applied at the first location. The adhesive was given at least 30 minutes to dry in each test and sprayed on using a 1 in. by 8.5 in. template to control the amount of adhesive. This procedure was similar to the first experiment. The distance between the plies were measured using calipers and rolled onto the same 83 mm core.

Lastly, the final testing involved rolling the fabric on a larger roll, 505 mm in diameter. Shifted fabric was tested against straight, unshifted fabric. The procedures for both of these were the same. The FARO Edge FaroArm recorded the measurements in the CAM2 Measure 10 software for this section. To produce coordinated results, the table was used as the plane for the XY plane in the software. Also, a line and a point were measured for the +Y-axis and the origin. For final testing, there would be one adhesive location using 3M™ Super 77™ Multipurpose Spray Adhesive. The adhesive would be sprayed on using a temple that was 1 inch by 8.5 inches.

The shifted fabric produced in section 4.1 was used in this experiment with the curve seen in figure 8. Since the fabric was not perfectly offset from experiments in 4.1, each ply needed to be moved carefully in order not to induce any unintentional deformation. The plies were moved to an approximate 10 mm “tapered” offset that would give easy view of the results and so that a ply would not move under another ply in the process of rolling. Ply 1 was the ply that was fully in contact with the table on the bottom and ply 5 was the fully exposed ply on the top. Figure 11 shows an ideal setup for the shifted fabric.

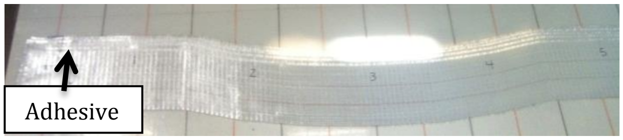

Figure 11: Shifted fabric with five plies with a “tapered” offset of approximately 10 mm.

To conduct precise results, a T-square was aligned with the edge of the table. A line was drawn in the lengthwise direction onto the table on both ends with a constant distance from the edge of the table. This was done so that the lines draw onto the fabric would be orthogonal to the edge of the table. The bottom of the top fabric was placed on this line; this line will be referred to as the *level line*. A straight line in the “number 2” direction was drawn with a color pencil at different places of the fabric to mark the adhesive location (A), +Y-axis, and the measurement locations (1-5), shown in figure 12 and 13. When using a permanent marker, the ink would “bleed” down a fiber. Therefore, these were not used in the entire drawing of the straight line. However, a fine tipped permanent marker was dotted on each color pencil line on each ply at each location. This would cause the ink from the marker to “bleed” down the tow in the “number 1” direction creating an “X” like in figure 13. The probe of the FaroArm would be measured at this “X” before and after rolling the fabric. Using the fine tipped marker, the origin was also marked on the +Y-axis with the same method.

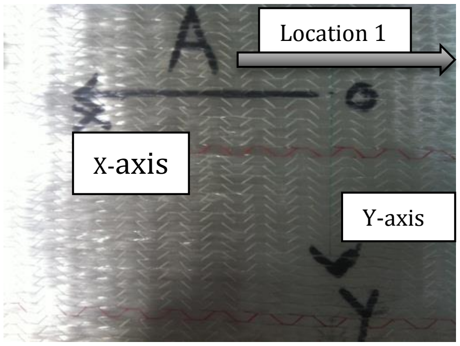

Figure 12: Coordinate system of final testing. X-axis, Y-axis, and Origin (O) are shown. The X-axis is thicker because it was not used in the alignment of the coordinate system.

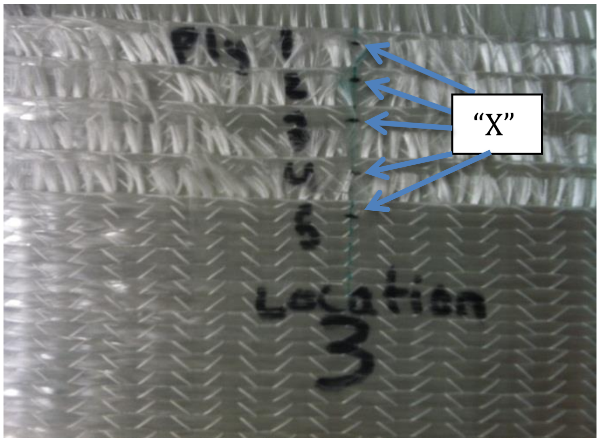

Figure 13: “X” spots where the measurements would be recorded. Notice the small black lines on the vertical green line.

The length of each ply was approximately 2.1 m in the X-axis direction. The adhesive was located at the 100 mm mark and the +Y-axis was marked at 150 mm. The first measurement location was at 350 mm with an interval of 400 mm between each location. The last measurement location, location 5, was at 1950 mm. The axes for the final testing were aligned with the gantry as shown in figure 13.

The roll core used in this experiment is shown in figure 14 was 505 mm in diameter. A large roll core was used because the change in radius would be smaller. When rolling the fabric, the cross tows were made exposed on the roll. This was done so that the roll could be carried over the mold and the fabric could be place directly onto it instead of having to flip over the entire fabric once rolled back out.

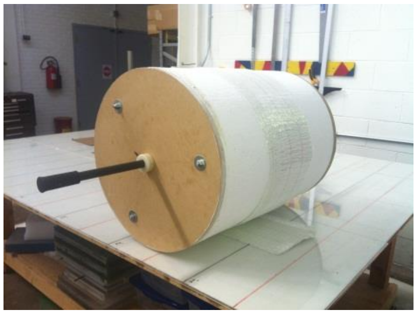

Figure 14: Roll Core (505 mm, foam center)

The overall procedure for the final testing of the effects of rolling straight and shifted fabric was:

1) Offset the fabric approximately 10 mm away from each other and the bottom of the fabric is on the level line.
2) Spray adhesive at the adhesive location using the 1 in. by 8.5 in. template and wait 30 minutes for the adhesive to dry.
3) Mark the fabric where the +Y-axis, origin, and where measurement location would be, as described above.
4) Measure the table as a plane, +Y-axis as a line, and the origin as a point. Use these to create the coordinate system within the CAM2 Measure 10 software.
5) Measure the points with the FaroArm from each ply at each location. This will give the X and Y position of each point.
6) Roll the fabric onto the 505 mm diameter roll core. Ply 5 being in contact with the roll core. Starting at location 1 where the adhesive is located, attempt to roll the fabric continuously on top of same tow.
7) Roll the fabric in the opposite direction so that the fabric lays in the same orientation as before. If the fabric does not lie back on the level line, move both sides so that they are aligned being careful not to add any deformation.
8) Repeat steps 4 and 5 to get the final X and Y positions.

To ensure the measurements from the software were correct, the following checklist was used to validate the data.

1) Y-axis location increases in number for increasing number of ply at each location
2) The distance between each location is 400 mm or approximately 400 mm.
3) The change in distance between each ply at each location is less than 20 mm.

If one of these were not met, then an error in the coordinate system could be the problem. It is important to have the fabric on the level line and to have the +Y-axis/origin to be measured with the T-square aligned with the edge of the table, shown in figure 15.

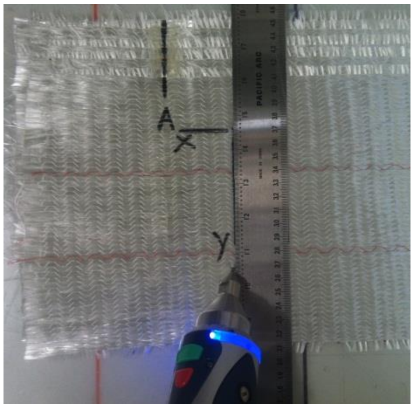

Figure 15: Use the T-square to get a straight Y-axis

5. Results

The first tests showed the accuracy of the shifting machine. For these results the normal Y-axis on the graphs are the change in distance in millimeters, while the X-axis is the distance from the beginning that the measure was taken in millimeters.

The positions between the plies were measured at the locations as described in section 4.1. Once ply 1 was laid down, the distance between ply 1 and ply 2 was measured. Since in this test there was no offset of the machine, the fabric was expected to be 0 mm away from the bottom layer (directly on top). This expected position was called the nominal position. The distance that the ply was measured was added to the previous distance(s) to find if it fell on the nominal position. The nominal position was directly on top of ply 1. For example, if the distance between ply 3 and 4 was -5, and the distance between ply 1-ply 2 and ply 2-ply 3 were both 2. Then ply 4 would be 1 mm away in the -Y-direction (-5+2+2=-1). The nominal position for each graph is the zero value on "Y-axis", the closer it is to the zero value the better quality it has.

Three trials of tests were conducted for each of the two offsets (0 mm and 10 mm). The three trials are shown in Fig. 16.

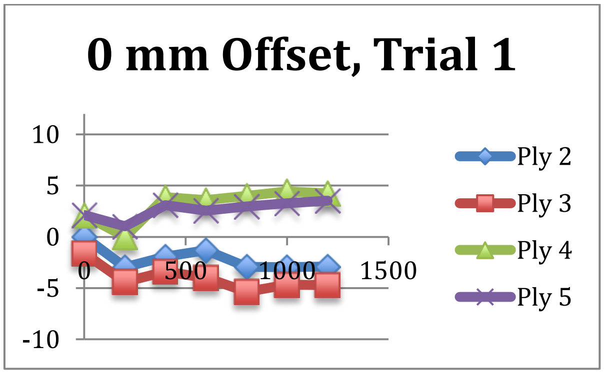

Figure 16: 0 mm offset results, Trial 1-3. The zero on the Y-axis is the expected nominal position. 16a: 0 mm offset, Trial 1

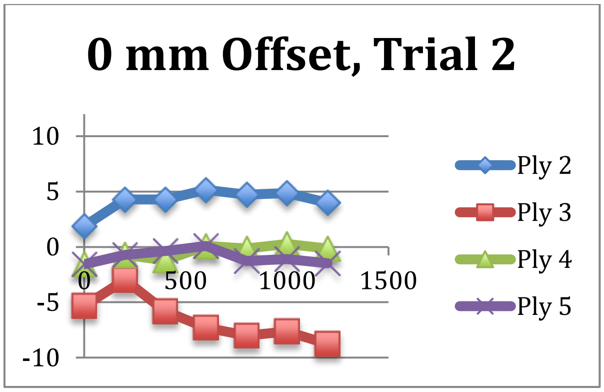

Figure 16b: 0mm Trial 2

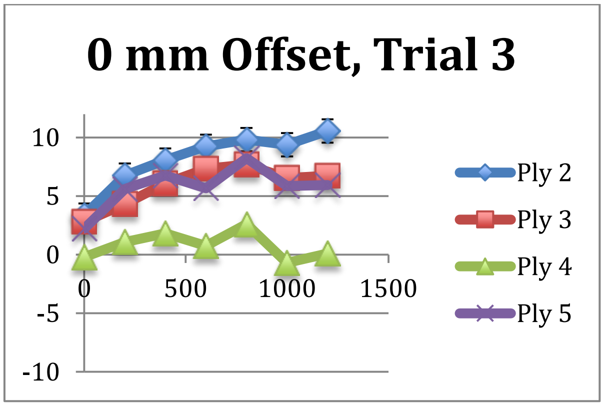

Figure 16c: 0mm Offset, Trial 3

There was some phenomenon noted when taking the measurements. One example is that creating an arc from the table to the back pinch roller like seen in Fig. 17. The fabric made this shape then instantly fell under its own weight as the length increased. This phenomenon occurred in the 0 mm Offset in Trial 1.

The fabric also seemed to be moving a distance in the "number 1", X-axis direction. This movement was usually just a fraction of a millimeter, in some cases in moved around 2 mm.

The initial and final positions of the shifting machine were measured by the FARO Laser Tracker. From one cycle of laying down a ply to another cycle, the shifter had moved a fraction of a millimeter. This is significantly good since the machine moves over 2 m in the process.

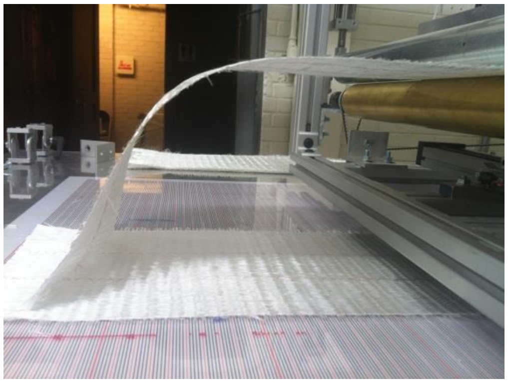

Figure 17: Arc building up behind the shifter as fabric is being deposited

The 10-mm offset data was more significant than the 0-mm offset. This could be due to variability of the "starting angle" of the fabric. As the length of the fabric got longer, so did the ply's position from the nominal. The starting straight section had a 10-mm offset, but this could be perfected less than the 0-mm offset. The data from the 10 mm offset is seen in Fig. 18.

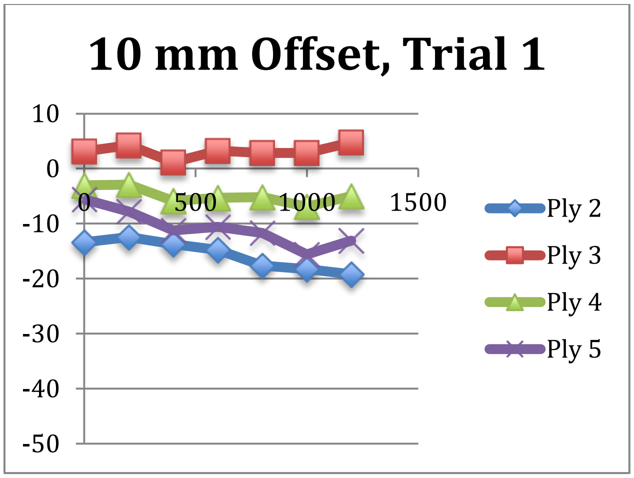

Figure 18: 10-mm offset, Trial 1-3. 18a: 10 mm-offset

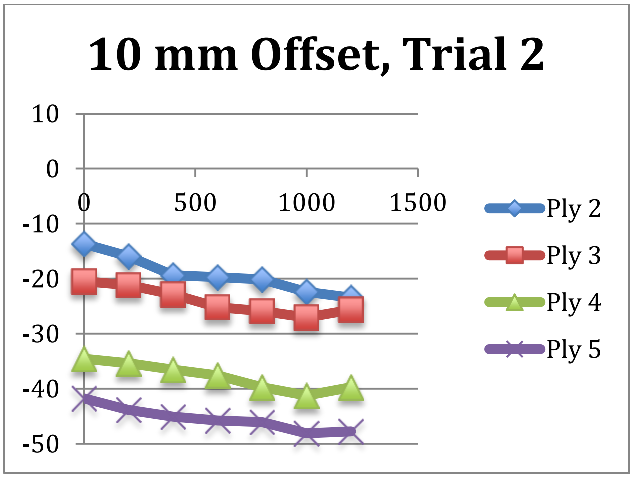

Figure 18b: 10 mm Offset

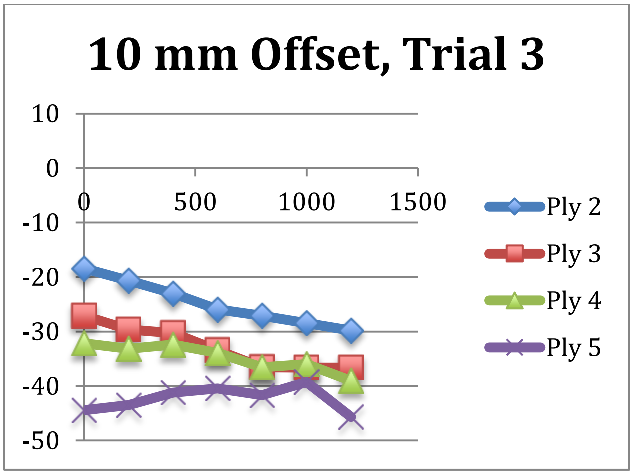

Figure 18c: 10-mm ffset

A new roll of fabric was used for the 10 mm offset, same Saertex 930 g/m^3, and another phenomenon happen in this section, shown in figure 19. The phenomenon has been called *curl*. There has been no evidence that it has any effect on the fabric. It appears that this happens only to certain rolls of fabric, and the cause is unknown.

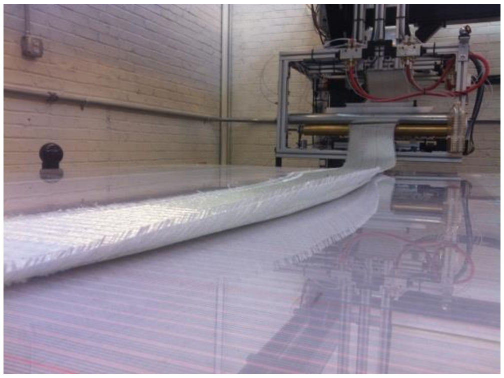

Figure 19: Curl Phenomenon. Unknown cause, unknown effects

Similar to the 0 mm offset, Laser Tracker recorded the initial and final positions. This experiment it recorded the movement of the Y-axis 10 mm offset. The difference between the initial points of each ply was measured against its neighboring ply. Each ply had a Y-axis offset in the range of 10 ±.4 mm.

It was believed that with starting 400 mm of fabric out of the back of the machine was causing the variability in the distance from the ply's nominal position. To test if this was concern one trial was ran with having the fabric start in the machine. About only 30 mm of fabric was sticking out from the pinch rollers, figure 20. Since the fabric did not have a beginning curve/tendency to lie onto the table if would form an arc like described before in figure 17. Therefore, some human interaction had to occur to push down the beginning section of the fabric. The results of the test are shown in figure 20. There was no offset in this test.

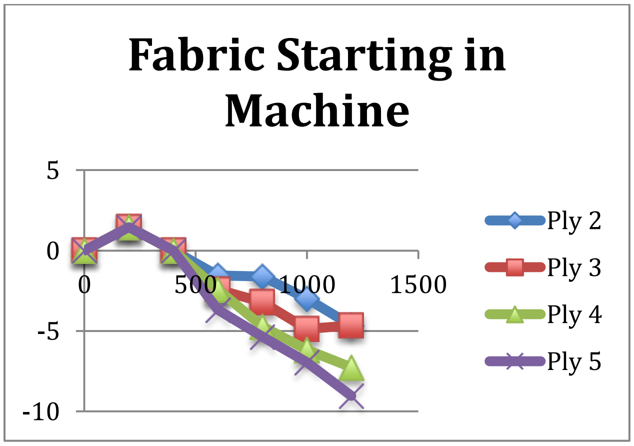

Figure 20: Entire fabric beginning in the machine with no offset.

This was the first test to have fairly consistent data that was on top of one another. Leaving the fabric in the machine at the beginning of the shifting process could make the process more reliable. It is a possibility that the shifter has a high reliability, but the human interaction is what causes the error. This was the last testing of the shifting machine's repeatability.

The next sequence of tests was to test the process of rolling the fabric onto a core and to measure the effects. Figure 21 shows the effect of the spreading of the fabric in the "number 2" direction. The values in the table are absolute values of what was measured, since there was not an axis setup for preliminary tests. Likewise, Fig. 22 shows the absolute change in the "number 1" direction with respect to the ply that was on top.

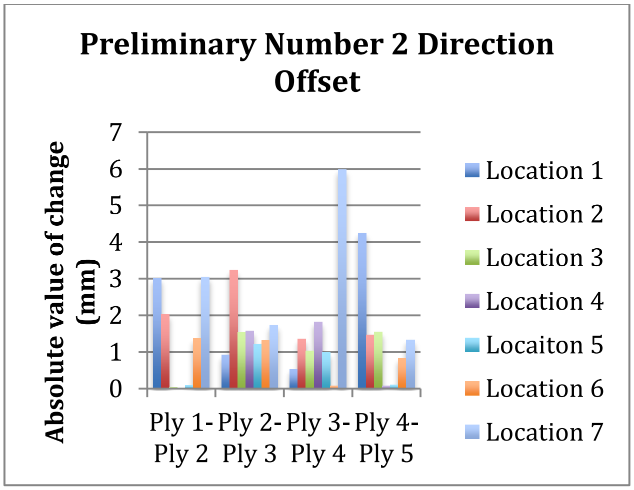

Figure 21: "Number 2" change in distance

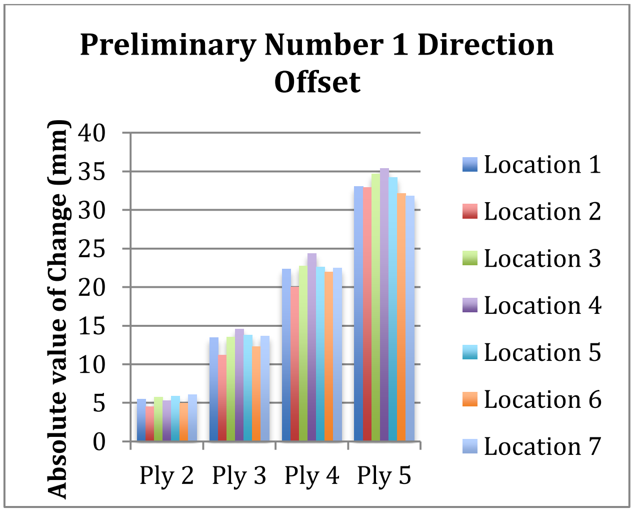

Figure 22: "Number 1" direction change with respect to ply 1.

The values for the "number 2" direction are random and have no correlation. However, for the of the "number 1" direction are similar. This is expected because they are the same ply and since they were straight section they would not be much stretching of the fabric. An observation of the "number 1" direction movement is shown in figure 23 as a staggering line that was once straight as seen in figure 10.

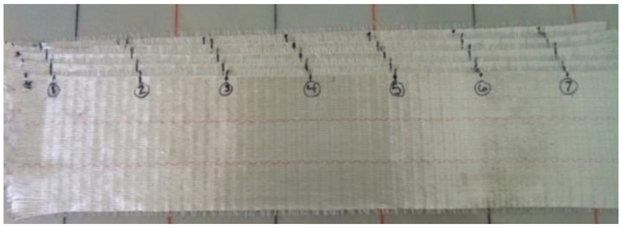

Figure 23: Effect of rolling in the "number 1" direction. Straight lines before, staggered afterwards**.**

To stop the "number 1" direction movement, it was considered to place an adhesive on the fabric. Two adhesive tests were made to observe this. The first had two adhesive locations. While and after rolling the fabric onto the 83 mm core, a wave formed on both ends of the fabric. These waves were identical in height as seen in figure 24 and 25.

Figure 24: Two adhesive test showing both waves at the ends of the fabric within the adhesive

The wave hit a critical amount that it caused the fabric rear the adhesive to spread apart leaving a gap between the tows. Since this is detrimental for the structure of the fabric no measurements were recorded.

The next test was with one adhesive. There were 8 locations in this test with the adhesive at location 1. The "number 2" direction offset was much less in this test, shown in figure 26, than the first test.

Figure 25: Wave at the beginning of the fabric

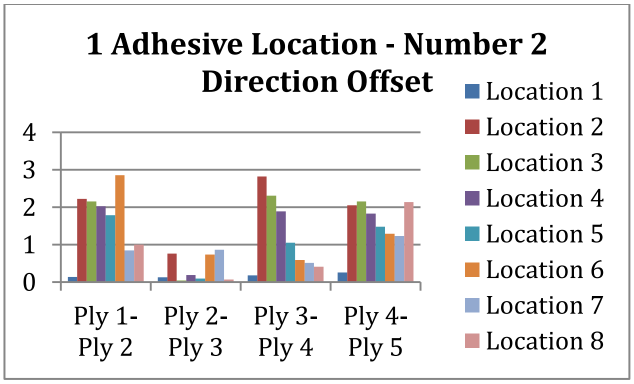

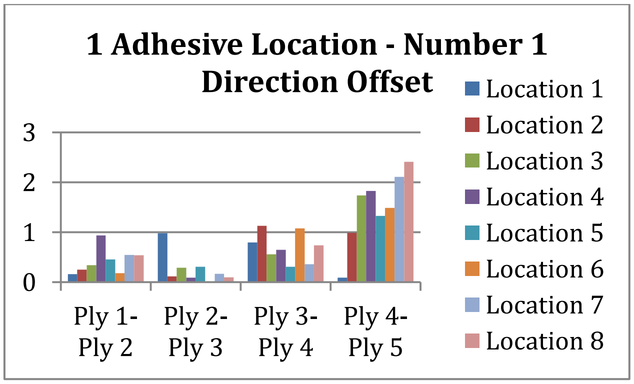

Figure 26: Distance between plies in the “number 1” direction

This showed that using one adhesive location provides the less unintentional deformation and would be used in the final testing.

The final testing involved rolling straight fabric and shifted fabric both being the same horizontal length with the exact same setup as described in section 4.2. This testing involved a coordinated system to record measurements (section 4.2, figure 12 for reference). Shifted and straight fabrics were graphed showing the *fanning effect* and *the stretching/shrinking effect*. The fanning effect can be described like opening a folding hand fan such as seen in figure 27.

Figure 27: Folding hand fan describes how the fabric behaves “pinned” at one end (www.dhgate.com)

The results for the straight fabric are shown below. The fanning effect is shown in figure 28. The stretching/shrinking effect is shown in figure 29. If the value is negative, then the fabric was stretching (expanding). If the value is positive then it is moving toward the positive X-axis and thus shrinking (decreasing) in length. The figures listed below have a Y-axis marked in distance in millimeter. The X-axis shows where that distance occurred, between two plies (fanning) or for one ply (stretching/shrinking).

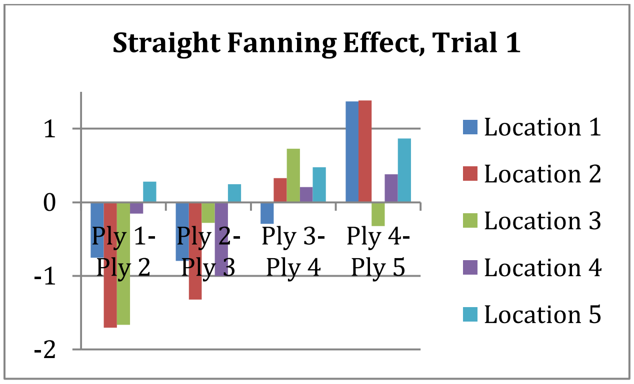

Figure 28: Straight fabric testing showing fanning effect. 28a: Trial 1

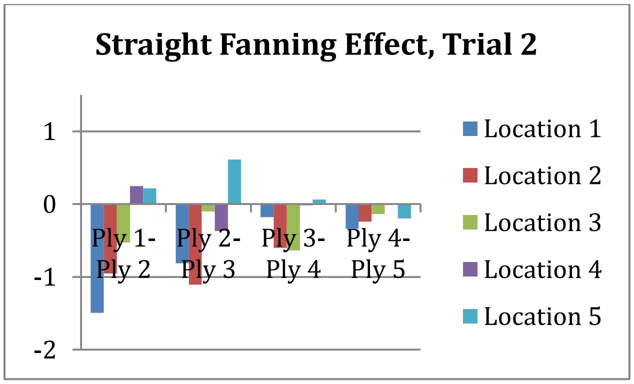

Figure28b: Trial 2

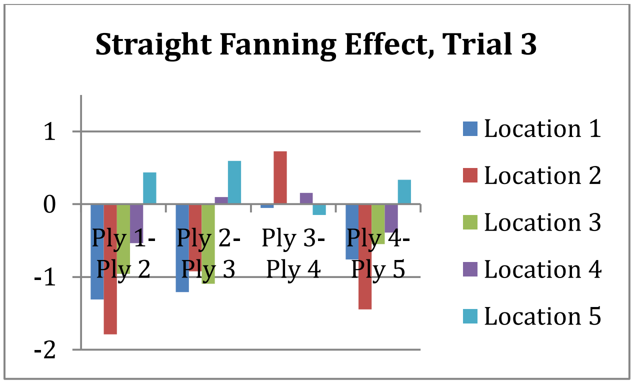

Figure 28c: Trial 3

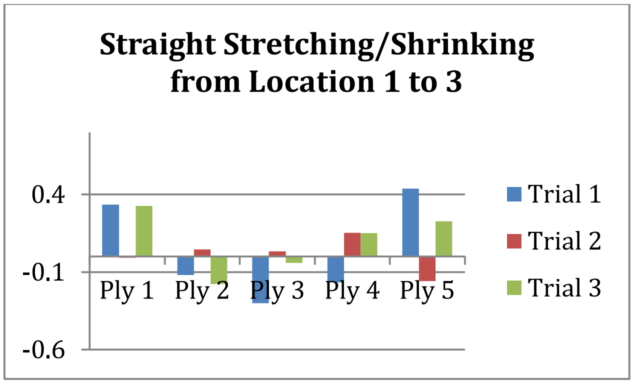

Figure 29: Straight fabric testing showing stretching/shrinking effect. 29a: Stretching/shrinking from location 1 to 3

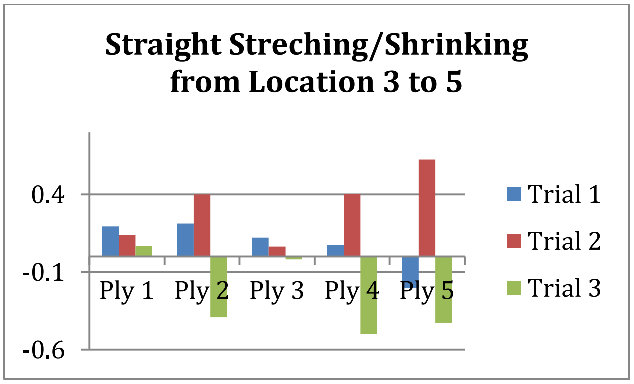

Figure 29b: Stretching/Shrinking from location 3 to 5

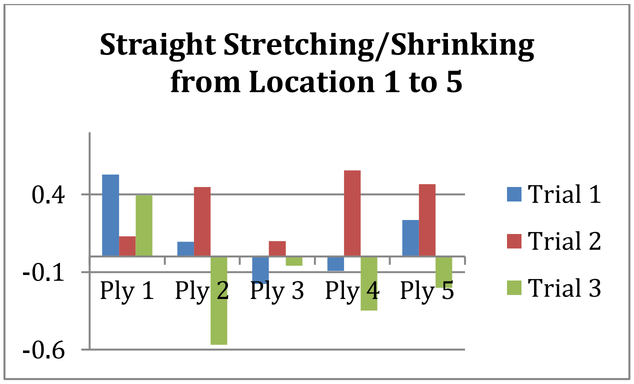

Figure 29c: Stretching/shrinking from location 1 to 5

Next, the shifted fabric was tested using the same experimental methodology. In the same order, the fanning effect is shown in figure 30 and the stretching/shrinking effect is shown in figure 31.

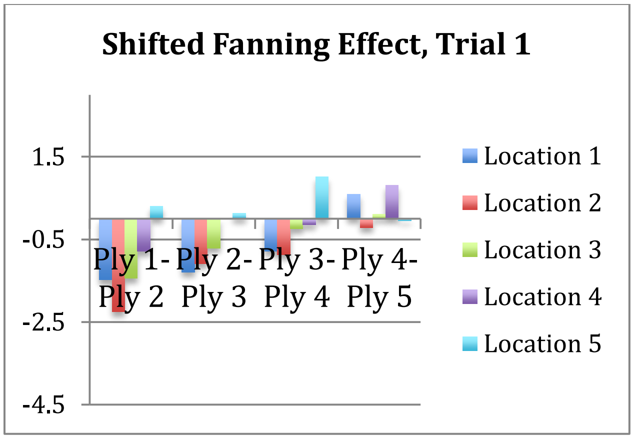

Figure 30: Shifted fabric testing showing fanning effect. Trial 1

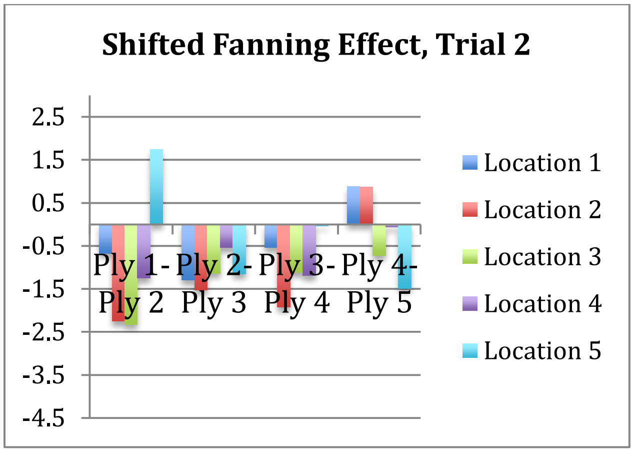

Figure 30b: Trial 2

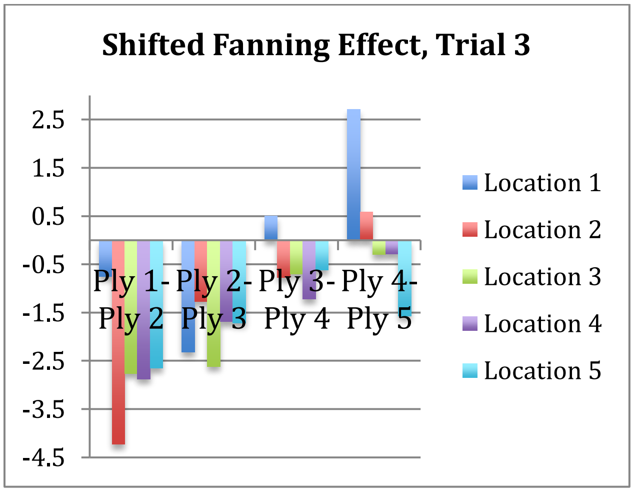

Figure 30c: Trial 3

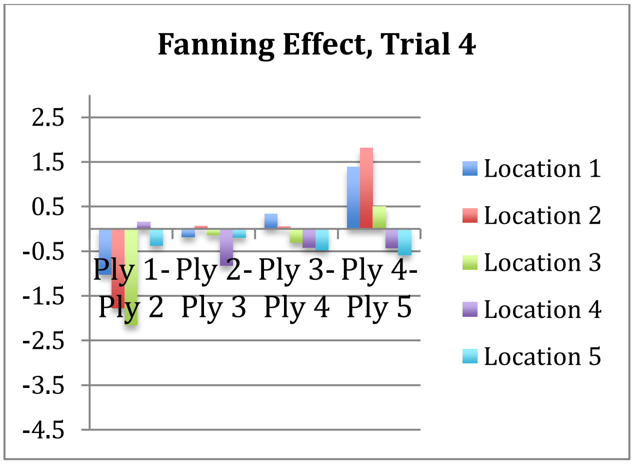

Figure 30d: Trial 4

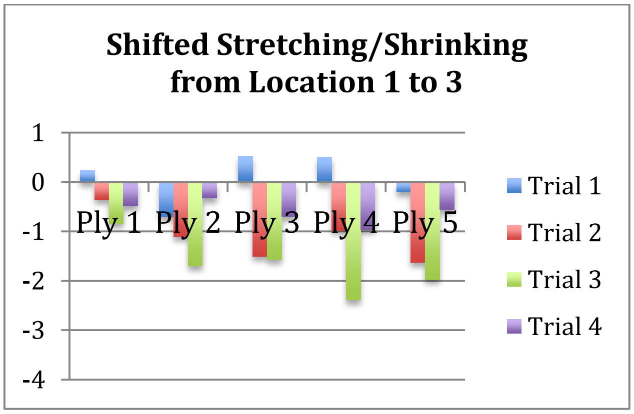

Figure 31: Shifted fabric testing showing stretching/shrinking effects. 31a: Stretching/shrinking from location 1 to 3

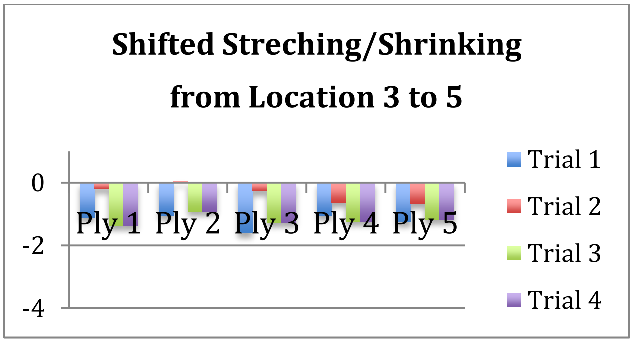

Figure 31b: Stretching/shrinking from location 3 to 5

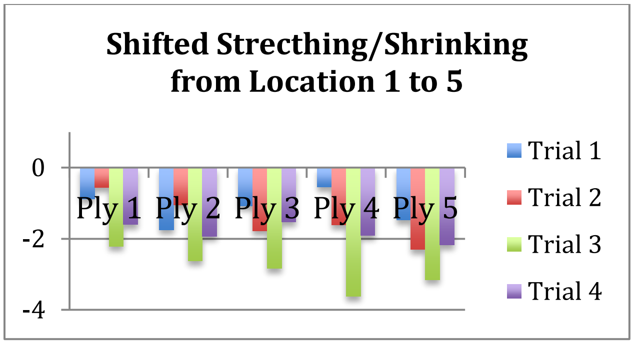

Figure 31c: Stretching/shrinking from location 1 to 5

When rolling the fabric off the roll, a wave occurred near the adhesive strip similar to wave that occurred during the adhesive testing (figure 32). Since this wave would not be allowed in a product, it needed to be smoothed out. The 505 mm diameter core of the roll was rolled over the wave to flatten it to the table. Do this; it caused an in-plane deformation in ply 1 near the adhesive (figure 33).

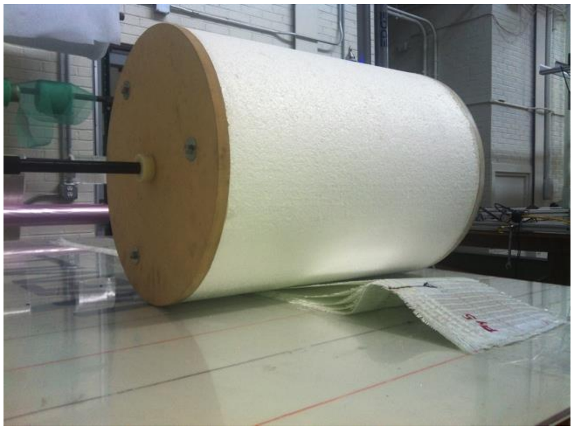

Figure 32: Wave forming at adhesive strip during the process of unrolling

Figure 33: Outline of Ply 1. In-plane deformation after smoothing out by rolling

6. Analyses and Interpretation

For the machine repeatability, the results were assuming that ply 1 was correct. If not, then the other plies should behave like the others if there was a correlation. From Figs. 16 and 18, the plies move in the same trend as a group but are consistently off for each trial. Since they are a group, the error could be between ply 1 and ply 2. It was hard to determine the starting position of ply 1, so this ply could be off and the others could be right. In the figure, the plies would be grouped on top of each other away from the nominal line if the system was perfect except ply 1. The nominal line is the zero line. This could be the case for the results in Figs 16 and 18. However, the lines do not overlay directly on top of each other and some error was happening.

The 0 mm offset had a maximum incorrect offset of 10.84 ± 2 mm. The 10 mm offset had a maximum incorrect offset of 26.03 ± 3 mm. This shows that having a beginning gantry offset from the last ply creates more error in laying down the fabric. This may be human error, because the results that noticed when leaving the first section of fabric in the machine before it starts the automated sequence. When having no fabric on the table when the machine starts its sequence, the machine has more consistent data and lower error.

The test of fabric starting in the machine had better results than the previous tests (Fig. 20). In some composite designs there is a tolerance of ±5 mm. Since the plies stayed in a smaller group, the maximum incorrect offset of this test was 4.39 mm. This puts the fabric within the tolerable range. Therefore, if the machine were to always use this technique then it would need a device to push the fabric down to the surface of the table so that it does not form an arc. A concept of a ramp has been proposed. This ramp would have a roller at the end of the ramp to place the fabric onto the table. The roller would be controlled by the belt system already installed for the pinch rollers. Only when using this technique the system places the fabric in a tolerable position. Otherwise, there is too much error; most likely human error.

The procedure for rolling the fabric was tested next.
A large core was selected for the reason that the change in the "number 1" direction would be smaller. This is represented in the formula for arc length below.

$$S = r_i \theta_i$$
$$S = r_{i+1} \theta_{i+1}$$
$$r_i / r_{i+1} = \theta_{i+1} / \theta_i$$

"S" is the arc length and it is constant for each ply since its length does not change, the letter "i" is the number of ply, and θ is the angle of the arc sector with respect to the center of the roll. This formula shows how the ratio of radii is compared to the ratio of angle, which when unrolled in a linear change in the "number 1" direction.

The preliminary tests were tested to find the most accurate method that caused the least amount of unintentional deformities. Therefore, the one adhesive location strip was used in the final testing. This helped the plies from falling off of the roll separately when unrolling the fabric.

The final testing showed that there was a movement in the "number 2" direction called fanning. The data had statistically no correlation. When comparing the straight fabric to the shifted fabric, the straight fabric had a maximum fanning of -1.8 mm (straight, trial 3, location 2, ply 1-ply 2), while the shifted fabric had a maximum fanning of -4.23 mm (shifted, trial 3, location 2, ply 1- ply 2). The location that received the most movement was at location 2. The negative values mean that the plies were spreading apart. As previously stated, a tolerance of ±5 mm would pass in this situation.

The fanning effect is believed to be the result of *helical winding*, such as the thread on a screw or bolt. If the fabric is not wound exactly on top of itself or the roll is at an angle from the Y-axis like in Fig. 34, the fabric could lose some contact with the roll since in has a finite width. This could explain the fanning effect and further research could prove/disprove this theory. If that is the case, then an automated system could be created to roll the fabric more precisely than a human could.

Figure 34: Dramatic example of helical winding. The fabric does not stay at the same place on the roll for straight fabric.

There was also observed to be movement in the "number 1" direction. This movement would be the result of the fabric stretching and unshifting the curve or shrinking resulting in increasing the curvature. The stretching/shrinking effects were observed over three sections from location 1 to 3, location 3 to 5, and the entire fabric from location 1 to 5. The majority of the movement was in the –X-direction, meaning the fabric wan unshifing and expanding in length (stretching).

The straight fabric had little/no movement in the X-direction, “number 1” direction. The largest movement was 0.63 mm in the area between location 3 and 5 on Trial 2 of the straight fabric. This number might only be as large as it is because of the difficulty to pin point the measurement location on each ply. As for the shifted fabric, the average stretching of location 1 to 3 was -0.83 mm and the average stretching of location 3 to 5 was -1.00 mm. Comparing the averages of the stretching for the same area for the shifted and straight fabric (0.049 mm for location 1 to 3 and 0.051 mm for location 3 to 5 for straight fabric), the stretching had a difference of 0.879 mm for location 1 to 3 and 1.051 mm for location 3 to 5. This results in a total of 1.93 mm change in distance after rolling from location 1 to 5. This value is within the ±5 mm tolerance. However, if the length of the ply were to change then the stretching/shrinking value is expected to change also, which could result in an out of tolerance result.

7. Conclusions

The primary adjective of this research was to develop a procedure for automating the layup process for the trailing edge mold of wind turbine blades for commercial use. Since the mold is three-dimensional with a wavy contour, a deformation of the fabric is needed to place it in contact with the mold surface. A shifting machine was developed to perform an in-plane deformation that would minimize out-of-plane deformation. Currently, the shifting machine is not capable of depositing fabric directly onto the mold surface. Therefore, a methodology was developed to transport the fiberglass fabric to the mold. This research focused on the rolling and testing of Saertex 930 g/m^3 unidirectional fiberglass fabric.

The rolling of fabric is a feasible way of transporting fabric deposited from the shifting machine to the mold of wind turbine blade. Currently, the added errors from the shifting machine and the ones that occur during rolling would go over the standard average tolerance for wind turbine blades. However, if the shifting machine was improved by using a device such as a ramp that would control the position then its precision could be increased.

Most of the error when rolling the fabric occurred in the width-wise direction, “number 2” direction. This so-called *fanning effect* could be the result of *helical winding*. Helical winding is believed to occur when the fabric does not align with itself when completely wrapped around the core of the roll. The fanning effect had a maximum movement of 4.23 mm.

To prevent helical winding, an automated system could be created that would wind the fabric on the core and ensure that the fabric was aligned correctly on the roll.

The second effect that occurred on the shifted fabric was the *stretching/shrinking* of the fabric. This movement in the “number 1” direction was measured from three areas; location 1 to 3, location 3 to 5, and location 1 to 5. Statistically, the difference between location 1 to 3 and location 4 to 5 were insignificant and both cause approximately the same amount of movement. The overall average change from location 1 to 5 was -1.93 mm. It is a concern that as the length of the test sections increased that the amount of stretching will also increase. Future research should look at increasing the length of the plies up to the required amount used in the actual mold to see if the length of the plies is related to the expansion of length of the fabric after rolling and unrolling.

Acknowledgements

Support for this research was provided by a National Science Foundation Research Experience for Undergraduates site program in Wind Energy Science Engineering and Policy (WESEP) grant number EEC-1063048 at Iowa State University.

References

Campbell, F. C., 2004: *Manufacturing Processes for Advanced Composites*. Kidington: Elsevier Advanced Technology. 517 pp.

Daniel, I. M. and O. Ishai, 2006: *Engineering Mechanics of Composite Materials* (2nd ed.). New York: Oxford University Press, Inc. 411 pp.

Department of Energy (DOE), Energy Efficiency and Renewable Energy, 2008: *20% Wind Energy by 2030: Increasing Wind Energy’s Contribution to U.S. Electricity Supply* (DOE/GO-102008-2567)

Lukaszewicz, D.H.-J.A., et al., 2011: Composites: Part B (pp. 997-1009). The engineering aspects of automated prepreg layup: History, present, and future. ACCIS. University of Bristol. Bristol, UK. 12 pp.

Lawrence Livermore National Laboratory, Department of Energy, 2012: Estimated U.S. Energy Use in 2011. Data based on DOE/EIA-0384 (2012). [Available online at http://flowcharts.llnl.gov/content/energy/energy_archinve/energy_flow_2011/LLNLUSEnergy2011.png]

Magnussen, Corey J., 2011: A fabric deformation methodology for the automation of fiber reinforced polymer composite manufacturing. M.S. Thesis, Department of Mechanical Engineering, Iowa State University, Ames, IA. 45 pp.

Schlangen, Luke A., 2012: A methodology for the automation of dry fabric layup for fiber reinforced polymer composite manufacturing. M.S. Thesis, Department of Industrial Engineering, Iowa State University, Ames, IA. 29 pp.

Stewart, Richard, 2012: Wind turbine blade production - new products keep pace as scale increases. Reinforced Plastics, Volume 56, Issue 1, pp.18-25

Ronold, Knut O., et al., 1999: Reliability-based fatigue design of wind-turbine rotor blades, Engineering Structures, Volume 21, Issue 12, pp. 1101-1114.

Zhu, Siqi, 2013: An automated fabric layup machine for the manufacturing of fiber reinforced polymer composite. M.S. Thesis, Department of Industrial Engineering, Iowa State University, Ames, IA. 65 pp.

Modeling Precipitation Induced Gel-Coat Surface Erosion with Application to Wind Turbine Blades

JENNA M. KOESTER
Wind Energy Science Engineering and Policy REU, Iowa State University, Ames, Iowa
Mentors: Dr. John Jackman and Huiyi Zhang

Abstract

The past decade has seen incredible growth in the wind industry. With a massive installation of new technology, old problems surface as new problems. In the case of wind turbine blades, the epoxy resin gel coating experiences long term erosion from a number of sources. This study focuses particularly on erosion due to rainfall. Numerical simulation and probability estimation were used to analyze the erosion of the gel coat and averages over several time periods provided the appropriate analysis. Results were inconclusive, with an incubation period much larger than anecdotal expectations for impact damage. Recommended future research is two pronged: First, a physical laboratory stress test should be produced to compare to theoretical results. Second, incorporate other potential collision damages that may accelerate the damages to the gel coat surface.

1. Introduction

Both government and private sector have a vested interest in developing a diverse alternative energy portfolio. Wind energy has contributed to the growing sector of renewables. In fact, the U.S. Department of Energy (DOE) has developed a scenario to increase total wind energy electricity contribution to twenty percent of U.S. consumption by 2030. This is an aggressive goal - one that requires public and private partnerships to propel the wind industry into the competitive market.

Current estimates for the lifetime of wind turbines are around twenty years but many professionals and academics express skepticism, believing that mechanical and electrical failures will shorten the lifespan of the turbines by several years (Renewable Energy Foundation). Aging wind turbines require regular operations and maintenance (O&M) attention in order to ensure efficiency and functionality. Preventative maintenance and structural health monitoring are essential processes to the upkeep of wind turbines. Some components of the wind turbine are physically more accessible and therefore have a thorough inspection and repair process. Likewise, some components are difficult to monitor and are therefore at risk of premature failure. Turbine blades are among the largest individual components of a wind turbine yet the industry has not developed a cost effective method to scan the blades for cracks, impingements, and other surface damages.

Turbine blades are made of fiberglass and epoxy resin. Once cured, they are coated with gel (polyester) coating or a primer and paint layer. For the purpose of this study, we will assume the surface to be a gel coating of homogenous thickness and the composite substrate is semi-infinite. The coating is meant to protect the fiberglass and resin from moisture. Therefore, cracks and indentions on the surface have potential to destroy the structural integrity of the fiberglass composite by allowing moisture to weaken the bonds.

Rain damage is slow but constant. The ability to forecast rainfall and record data associated with the precipitation allows researchers to closely follow the potential erosion on the surface of a wind turbine. Identifying the degree of damage over time gives the wind industry a time frame in which it may be necessary to re-coat the gel coat surface. The purpose of this study is to adapt and apply a model of homogeneous surface erosion by George S. Springer to the gel-coat erosion of a wind turbine blade.

2. Literature review

The problem of gel coat erosion is not new—several studies over the past forty years have attempted to model erosion in its various forms. The earliest studies addressed erosion on the surfaces of naval vessels and aircrafts. At high speeds, rains and other particles can be particularly damaging to the gel coating. Gone undetected, the erosion could reach the substrate layer and ultimately cause catastrophic structural damage to the vehicle.

Chamis addresses the degradation of composite materials on a ply-by-ply basis. Grundwurmer, et al. (2007) addresses gel coat erosion on metallic surfaces for aeronautic structures in a *Science Direct* paper. Though the models developed in each of these studies are not suitable for wind turbine application, they illustrate the value of understanding how and when gel coat surfaces degrade.

Bargmann, et al. (1992) identifies three distinct phases of erosion with gel coats: incubation, acceleration/deceleration, final stationary stage of constant erosion. Springer, et al. (1974) illustrates the process with an erosion curve from experimental results:

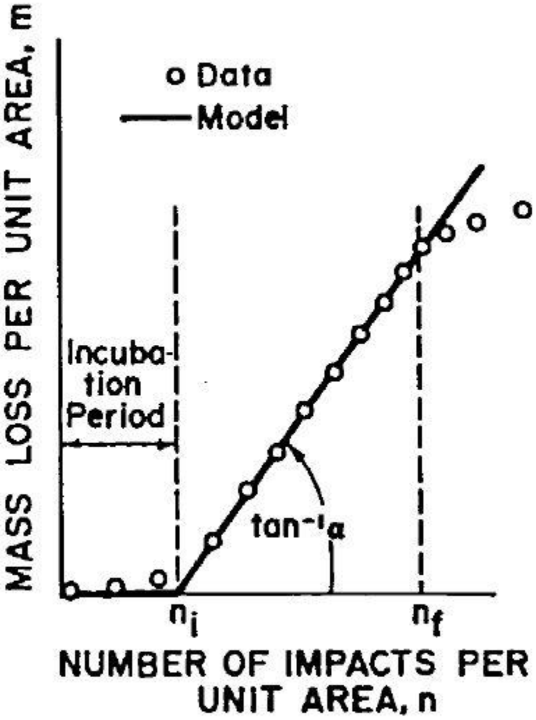

Figure 1. Degradation Phases (Springer, et al. 1974)

Homogenous coatings have material characteristics that vary according to chemical makeup. These characteristics determine unique impact ratios and time scales for each phase of erosion.

Springer, et al. (1974), reviews and models the damaging effects of rain on the thin coatings of aircrafts. The coating studied was homogenous and similar to the gel coating used to cover the composite material of blades. Mass removal of the coating due to droplet impingement over time was calculated and plotted to reveal a linear relationship after an incubation period, n_i, of negligible erosion. Springer, et al. also focused on the damage to the substrate as a result of coating degradation. Substrate damage will not be considered in this particular study.

According to Springer, surface erosion is caused by sound wave propagation. The force impingement causes a wave approximately the same speed as the speed of sound in the respective material. Angle of impact delegates the distribution of waves, thus making the impact pressures slightly varied across surfaces. A large sampling size of raindrops compensates for the angle differences.

Springer's model of surface stresses from droplets during the incubation period was based on Miner's rule (Springer et al., 1974):

$$\frac{f_1}{N_1} + \frac{f_2}{N_2} + \cdots + \frac{f_q}{N_q} = a_1 \tag{1}$$

ƒ represents the number of cycles the surface is subjected to threshold stress levels and N is the total lifetime in terms of overstress cycles. Using this property of gel coating along with data on rainfall (droplet size, velocity, intensity), Springer (1976) defined ƒ and integrated from the ultimate tensile strength σ_u to the endurance limit σ_I. The following equation helps define the constant, α_1:

$$a_1 = \frac{\pi d^2}{4} P n_i (1 - 2v) \left[\frac{\sigma_u^{b-1} - \sigma_I^{b-1}}{4(b-1)\sigma_u^b}\right] \tag{2}$$

The "knee" of the fatigue curve is defined by the gel coated material. On a logarithmic scale, 10^{b2}, corresponds to this break in the fatigue curve. Knowing b_2, b can be calculated using the following formula:

$$b = b_2 / \log_{10}\left[\frac{\sigma_u}{\sigma_e}\right] \tag{3}$$

Knowing α_1, the total number of impacts per unit area is determined. The strength parameter, *S*, and the stress from impinging droplets, P, complete the equation for total impingement:

$$n_i^* = a_1 \left(\frac{S}{P}\right)^{a_2} \tag{4}$$

When plotted on a logarithmic curve, a_1 and a_2 are estimated using a line of best fit. In the case of a homogeneous medium, the determination for both a_1 and a_2 were based upon several different studies on varying homogeneous materials. The following figure illustrates the logarithmic linear relationship that reflects this relationship.

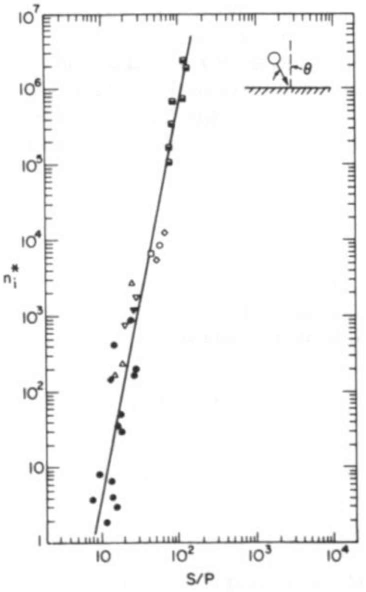

Figure 2. Experimental trend relating incubation period to the Strength to Pressure ratio (Springer 1974)

Thus, the measure for number of impacts in an incubation period follows as:

$$n_i = \frac{8.9}{d^2}\left(\frac{S}{P}\right)^{5.7} \tag{5}$$

Strength, S, is defined as:

$$S = \frac{4\sigma_u(b-1)}{1-2v} \tag{6}$$

Where b is defined by equation (3), ultimate tensile strength is defined in the appendix, and v (dimensionless) is defined by the Springer text.

Pressure at surface, P, is defined as:

$$P = \rho_L C_L V cos\theta \quad (7)$$

Where ρ_L is the density of water, C_L is the speed of sound through water, V is the speed of the turbine blade, and θ is the angle between the blade and the raindrop.

Equations (2)-(7) were adapted from Springer's 1976 text, *Erosion by Liquid Impact*.

3. Rain Data Analysis

The primary method of investigation in determining the erosion of rain on the gel coat surface is a mathematical model adapted from George S. Springer's text, *Erosion by Liquid Impact* (1976).

Scenarios were determined using a model as calculated by Springer. (1976). Springer's model relies on the propagation of sound waves through the homogeneous surface medium. In the case of a wind turbine blade, this medium is a polyester gel-coating protecting a fiberglass composite. The first phase of rain erosion is the "incubation period," or the time in which no measureable erosion occurs. At the end of the incubation period, mass loss begins. Assuming that any amount of mass loss compromises the coating, it could be assumed that the gel coat has incurred enough wear to require maintenance attention. The period of mass loss will not be calculated in this particular model Thus, the model below describes the incubation period and its relationship to regional rain data and epoxy resin gel coating.

To replicate rain erosion, rain data from Cedar Rapids, IA was compiled every day from July 2007 to July 2013. All days were treated as statistically independent events such that the hourly prediction of rainfall was not related to the previous hour. The data provides intensity (mm/hr) while the summary table provides typical raindrop sizes by Law and Parsons (1943) in Table 1. The exponential mean from the distribution of intensities was compared to the drop diameter associated with the rain intensity. The drop diameter assumes that the droplet is composed of 50% small drops and 50% large drops. This combined droplet size was used in the model. Table 2 summarizes the relationship of drop size to terminal velocity.

Rain Intensity I (mm/hr)	**Drop Diameter d (mm)**
0.25	0.77
1.27	1.14
2.54	1.27
12.7	1.73
25.4	2.15
50.8	2.38
101.6	2.67
152.4	2.75

Table 1. Intensity and droplet size (Springer (1976) adapted from Law and Parsons 1943)

Drop Size (mm)	**Terminal Velocity (m/sec)**
0.5	2.06
1	4.03
1.2	4.64
2	6.49
2.6	7.57
4	8.83

Table 2. Terminal velocity of raindrops (Horstmeyer 2008)

Five years of data were collected for hourly rainfall intensities. Collectively, the five years of rain data were treated as a binomial probability. The probability of rainfall in an hour was unrelated to intensity. For each hour of the model, the probability of rainfall occurring was generated.

The incubation period simulation depends on the number of impacts accumulated over a finite timed interval without removing mass from the gel coat. For each hour, the probability of duration or either rainfall or dryness was also generated. A clock function kept track of total hours necessary for incubation period to occur. Figures (3) and 4) below show the distribution of lengths for each circumstance: continuous precipitation period or continuous dry period.

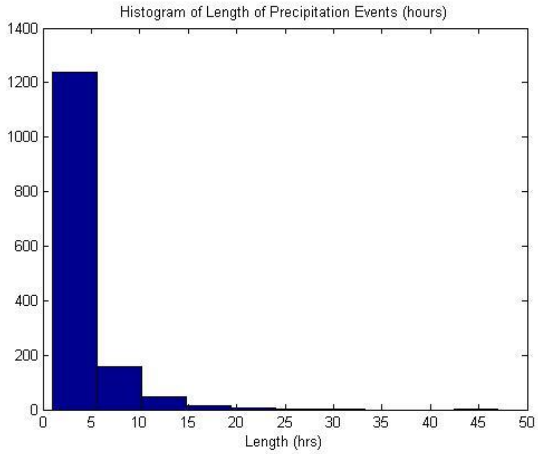

Figure 3. Exponential distribution of length of precipitation events

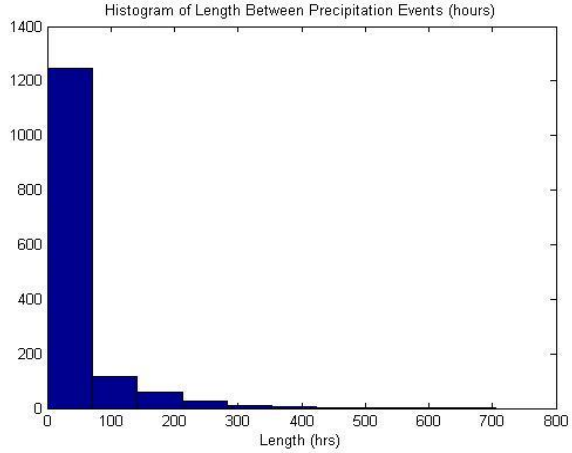

Figure 4. Exponential distribution of length of intervals between precipitation events

This experimental procedure can be replicated using any regional rainfall data.

The calculation to determine incubation period from equation (5) was determined using characteristic values for epoxy resins. Since the leading edge of the wind turbine blade rotates such that its velocity exceeds the terminal velocity of the rain droplet, the model will use the velocity of blade for calculations of surface pressure. Furthermore, since the leading edge of the blade would feel the force of the raindrop one third of the rotation, an assumption is made to factor this decrease in force by 0.33 to compensate for rotational discrepancy.

The total hours input into the model and outputs an incubation period. The Springer model requires the following variables to solve for incubation period: ultimate tensile strength, σ_u; equivalent dynamic stress, σ_e; density of liquid, ρ_l; speed of sound through liquid, C_l; speed of sound through surface, C_s; velocity of droplet, V; knee in fatigue curve, b_2. The strength and pressure parameters are calculated using equations (6) and (7).

The following figure again shows the exponential nature of rain intensities (mm/hr):

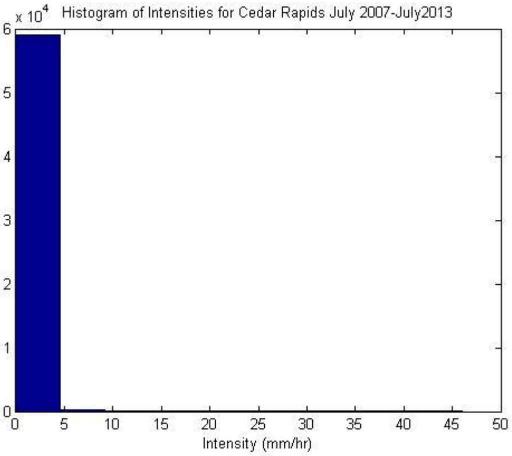

Figure 5. Exponential distribution of rainfall intensities

The exponential mean of the intensity distribution is multiplied by the area of impact. Multiplied by q, the number of impacts per m^3, the impacts per hour value was derived.

$$q = 530.5 \frac{I}{V_t d^3} \tag{8}$$

Given the calculated impingements of the incubation period and the constant value impact per volume, a temporal estimate for incubation period can be determined.

See Appendix for relevant variables.

4. Results

The binomial probability that it will rain in any given hour is 0.0802. Fig. 3 and Fig. 4 represent the probability of duration of rain event and duration of dry event, respectively. The exponential mean, μ, for the two data sets were $\mu_{precip} = 3.2 \pm 0.2$ hours and $\mu_{noprecip} = 37 \pm 2$ hours.

The average drop size, according to the Fig. 5 distribution, was $\mu_{intensity} = 0.153 \pm 0.001$ mm/hr. Using Tables 1 and 2, terminal velocity and drop size were determined such that $q = (4.41 \pm 0.03) \times 10^{10}\ impacts/m^3$.

The incubation period impact resulted in a theoretical value of 8.39 x 10^{16} impacts/m^2. Divided directly into the erosion model, an incubation period of 217 years is determined. Entered into the rain data and time stepped model, the incubation period is on the order of thousands of years.

5. Analysis and interpretation

Given that the marked lifetime of a wind turbine is twenty years and gel coat maintenance becomes a problem within ten years, rain damage cannot be attributed to the erosion of the gel coat. An appropriate analysis of the model would require a physical simulation that could accelerate the incubation period proportionally to the modeled period.

6. Conclusions

At this stage of the model development, the Springer model is not applicable to the erosion of gel coating on wind turbine surfaces. There are several other factors besides rain damage that may contribute to the weakening of the gel coat during the incubation period. Pitch angle, rotation of the rotor blade, and large impacts (birds, hail stones, etc.) may cause a marked increase in weakening of the epoxy resin bonds. The incorporation of these factors may increase accuracy of the incubation period model.

Continuation of this experiment would require a physical sample to compare against the model and eventually, incorporating larger collisions with the consistent rainfall.

Acknowledgements

Support for this research was provided by a National Science Foundation Research Experience for Undergraduates site program in Wind Energy Science Engineering and Policy (WESEP) grant number EEC-1063048 at Iowa State University.

References

AWEO, cited 2013: Size specifications of common industrial wind turbines, GE 1.5s. [Available online at http://www.aweo.org/windmodels.html].

BAMR, cited 2013: Speed of Sound through Materials. [Available online at http://www.bamr.co.za/velocity%20of%20materials.shtml].

Bargmann, H.W., 1992: The mechanics of erosion by liquid and solid impact. *International Journal of Solids and Structures*, **29**, 1685-1698.

Chamis, C.C., 2006: Composite erosion by computational simulation. *Society for the Advancement of material and Process Engineering*, Long Beach, CA, NASA.

Department of Energy, 2008: 20% wind energy by 2030. Energy Efficiency and Renewable Energy Rep. DOE/GO-102008-2567, 1-2.

Engineering Toolbox, cited 2013: Speed of Sound. [Available online at http://www.engineeringtoolbox.com/sound-speed-water-d_598.html].

Erkal, A., D. D'Ayala, and L. Sequeira, 2012: Assessment of wind-driven rain impact, related surface erosion and surface strength reduction of historic building materials. *Building and Environment*, **57**, 336-348.

Ferro, cited 2013: UltraSandable gelcoat [Available online at http://www.ferro.com/Our+Products/Specialty+Plastics/Liquid+Coatings+and+Dispersions/Products+and+Markets/Ultra+and+SuperShield+gelcoat/UltraSandable+gelcoat.htm].

Gründwurmer, M., O. Nuyken, M. Meyer, J. Wehr, and N. Schupp, 2007: Sol-gel derived erosion protection coatings against damage caused by liquid impact. *ScienceDirect*, **263**, 318-329.

Gurit, cited 2013: T-Gel 130 Epoxy Tooling Gelcoat System. [Available online at http://www.gurit.com/tgel-130.aspx].

Horstmeyer, S.L., cited 2013: Summary Table-Typical Raindrop Sizes. [Available online at http://www.shorstmeyer.com/wxfaqs/float/rdtable.html].

Iowa Environmental Mesonet, cited 2013: Archived data. [Available online at http://mesonet.agron.iastate.edu/archive/].

Renewable Energy Foundation cited 2013: *Wear and Tear Hits Wind Farm Output and Economic Lifetime.* [Archived online at http://www.epaw.org/documents.php?lang=en&article=in8]].

Springer, G.S., C Yang, P.S. Larsen, 1974: Analysis of rain erosion of coated materials. *J. Composite Materials*, **8**, 229-252.

Springer, G.S., 1976: *Erosion by Liquid Impact*. John Wiley & Sons.

Zhang, H., 2013: A feasibility study of a computer-based wind turbine surface flaws inspection method. M.S. Thesis, Dept. Industrial Engineering, Iowa State University, Ames, IA. 50 pp.

Appendix

Variable	**Value**	**Source**
σ_u	49.98 (N/mm^2)	Ferro
v	0.3 (mm^3/mm^3)	Springer
ρ_L	1000 (kg/m^3)	engineering toolbox
ρ_S	1200 (kg/m^3)	Gurit
C_L	1481 (m/s)	engineering toolbox
C_S	2650 (m/s)	BAMR
V	81 (m/s)	AWEO
b_2	20.9	Springer